Fluid Mechanics for Biomedical Applications: Weakly Viscoelastic Electrospray, Flow Focusing and Collapsible Channel Models.

SERGIO BLANCO TREJO

PhD Thesis

2022

Fluid Mechanics for Biomedical Applications: Weakly Viscoelastic Electrospray, Flow Focusing and Collapsible Channel Models.

A dissertation submitted by
Sergio Blanco Trejo
to the Department of Aerospace Engineering and Fluid Mechanics
in partial fulfilment of the requirements for the degree
Doctor of Philosophy
in the subject of Fluid Mechanics

Advisor: Prof. Dr. Alfonso Miguel Gañán Calvo
Co-Advisor: Prof. Dr. Miguel Ángel Herrada Gutiérrez

Abstract

Three different research topics are discussed in this thesis: i) weakly-viscoelastic electrospray, ii) the emergence of whipping effect on the Flow Focusing technique, and iii) fluid-structure interaction (FSI) phenomena implementing a 2D collapsible channel model. i) A systematic, theoretical comparison of a Newtonian fluid, and a non-Newtonian one modelled using an Oldroyd-B model was performed, resulting in a better understanding of how the properties of this type of material influence aspects such as meniscus shrinking, the agreement with a 1D-slenderness model, or the minimum flow rate value defining the boundary between electrospray and electrospinning. ii) In order to use Flow Focusing for some applications (e.g. XFEL), chaotic oscillations on the jet, known as whipping, must be avoided. A stability map for axisymmetric and lateral perturbation modes was obtained and compared to previous experimental data, examining the effect of different nozzle geometries on the emergence of the whipping effect and jetting-to-dripping configuration physical boundary. iii) In the last paper, the implemented model overcame some limitations presented in other 2D collapsible channel models, leading to the system's global stability analysis using a non-negligible membrane thickness and large deformations on the flexible wall segment. The multiplicity of solutions and their *folding points*, and the quantification of the effect of physical parameters such as wall thickness and inertia values on the emergence of self-excited oscillations were investigated.

Contents

List of Figures

Dedication

A mis padres.

Acknowledgements

Me gustaría comenzar agradeciendo a Alfonso Miguel Gañán Calvo la oportunidad que me brindó de formar parte de su grupo de investigación, y permitir desarrollar mi carrera investigadora bajo su tutela. Gracias por tus críticas constructivas, tu dirección, y por enseñarme a tener una visión mucho más madura de la ciencia.
Miguel Ángel Herrada Gutiérrez, gracias por estar día tras día apoyándome y guiándome en el apartado de simulaciones numéricas. Has sido un auténtico coach que ha influido en gran medida en que diera lo mejor de mi mismo y a sobrepasar mis límites.
Luis Modesto, gracias por tus enseñanzas en el ámbito experimental. Agradezco mucho haber podido aprender junto a ti en mi último período de tesis trabajando en la síntesis de fibras. Esta tesis no habría sido la misma sin vosotros para apoyarme, aconsejarme y formarme.

Peter S. Stewart, muchas gracias por permitirme colaborar junto a ti, tanto telemáticamente como durante mi estancia en la Universidad de Glasgow. Espero que volvamos a charlar mientras tomamos café.
José Pérez Rigueiro, agradecerte tu acogida en tu grupo de investigación durante mi visita al Centro de Tecnología Biomédica de Madrid. Desde el primer momento me hicisteis sentir uno más de vosotros. Espero de corazón que nuestros caminos se vuelvan a cruzar algún día.
Jose María Montanero, ha sido un placer colaborar junto a ti y tu grupo de investigación en los artículos sobre Flow Focusing y Electrospray.

A nivel institucional, me gustaría dar las gracias al Gobierno de España por mi beca FPI. Mi gratitud también va para el Programa de Doctorado de Ingeniería Mecánica y Organización Industrial. Agradecer también el excelente ambiente de trabajo en el Departamento de Ingeniería Aeroespacial y Mecánica de Fluidos. En concreto, a Paco, Julio, Elena, Bea, Alonso, Carmen y Eulalia. Especialmente me gustaría darle las gracias a Paco. Desde el

momento en que empecé mi tesis, te preocupaste de hacer un hueco para mí, apoyarme en mis momentos más difíciles, aconsejarme, y ayudarme a recobrar las fuerzas para seguir cuando pensaba que no podía más. Gracias por creer en mí durante todo este viaje. No solo me voy con un título de doctor, también me llevo conmigo un verdadero amigo.

A mis compañeros del Departamento de Matemática Aplicada I y el Departamento de Arquitectura y Tecnología de Computadores de la Universidad de Sevilla: Pedro Real Jurado, Helena Molina y Fernando Díaz del Río. Vosotros me enseñasteis mucho más que topología algebraica, me transmitisteis lo divertida que puede llegar a ser la investigación sin por ello perder rigor. También a mis compañeros del IBIS Juan Francisco Martín y José Gómez-Feria, por darme la oportunidad de aprender y colaborar con ellos en el ámbito del procesamiento de señales médicas. A mi profesor de Tecnología Industrial del IES Ramón del Valle-Inclán Ángel Valero. Gracias por transmitirme tu pasión por la ciencia.

Por último, quisiera dar las gracias a mis padres, a quienes se lo debo todo: por estar en mis momentos más oscuros y enseñarme que al final siempre acaba saliendo el sol, por transmitirme los valores que me han convertido en la persona que soy, enseñarme qué es lo realmente importante en la vida y sobre todo, a no rendirme nunca y sacar fuerzas para levantarme.
Gracias por creer siempre en mí, por vuestros abrazos y por vuestro apoyo incondicional. GRACIAS.

Chapter 1

Introduction

1.1 Introduction

Fluid mechanics is an omnipresent discipline in healthcare technology, from drug production and drug delivery to the implementation of biomechanical models, the synthesis of biomaterials or the development of diagnostic techniques. These advances have required an understanding of the physical parameters and boundary conditions that govern processes such as the ejection and rupture of micron-sized capillary jets, under what conditions is possible to obtain aerosols with characteristic droplet size, or at what point a turbulent phenomenon within a blood vessel or the collapse of the channel itself can take place, which could have a negative impact on a person's health.

This thesis aims to contribute to some aspects of fluid mechanics phenomena directly applicable to healthcare developments, through three different studies involving flow-surface and flow-structure interactions, including the stability of those flows: (I) Electrospray, (II) Flow Focusing and (III) the flow in collapsible channels. Firstly, in the following section, the fundamental physical and mechanical concepts related to liquid ejection configurations and flow stability will be briefly discussed.

In that endeavour, dimensional analysis is a key tool to assess the relationship among the multiplicity of physical parameters, providing ways to rationalize the information on the dominance of specific effects, actions or boundary conditions in a given configuration. Some of the most commonly used non-dimensional parameters are those in Table 1. Therefore, depending

Table 1.1: Dimensionless numbers

Name	Expression	Physical interpretation
Reynolds	$Re = \frac{\rho u L}{\mu}$	Relates the inertial forces to viscous forces.
Weber	$We = \frac{\rho v^2 L}{\sigma}$	Relates the inertial forces to surface tension.
Bond	$Bo = \frac{\Delta\rho g L^2}{\sigma}$	Relates the gravitational forces to the surface tension.
Ohnesorge	$Oh = \frac{\mu}{\sqrt{\rho\sigma L}} = \frac{\sqrt{We}}{Re}$	Relates viscous forces to inertial forces and surface tension.
Deborah	$De = \frac{t_c}{t_p}$	Relates relaxation to observation times.

on the value of some of these parameters (the *dominant* or relevant ones), we will be able to predict how the fluid will behave or what configuration it will adopt for certain imposed boundary conditions.

In the formation of jets, the Weber (We) and Ohnesorge (Oh) numbers play a fundamental role. The capillary velocity v_c is defined as that for which We, relating kinetic energy to surface tension as $We = \rho v^2 L/\sigma$, is equal to 1. The value $We = 1$ (or close to unity) often appears related to critical configurations. For a jet to be stable, the convective velocity should be larger than v_c in order to prevent perturbations from travelling upstream towards the source of the jet. Additionally, Oh gives information about the ratio of viscous to surface tension stresses by $Oh = \frac{\mu}{(\rho\sigma a)^{1/2}}$. This parameter is related to the viscosity-induced delay of the growth rate of disturbances which eventually lead to the break up of the jet into drops.

Each configuration in its steady-state exhibits a specific behaviour under given disturbances. In general, the complexity of that behaviour of dynamical response has an obvious dual origin: (i) the complexity of the disturbance, including its spectra of frequencies, wavelengths and amplitudes, and (ii) the intrinsic response of the system to each frequency and spatial distribution of amplitudes of the disturbance. When the amplitude is (sufficiently) small, the system usually exhibits a behaviour fundamentally dictated by the same frequency of the disturbance. That behaviour is termed a *normal mode* when it is not influenced by other frequencies, and exhibits a specific wavelength or spatial distribution of amplitudes. In this case, the spatiotemporal Fourier decomposition (discrete or continuous depending on the extension of the system)

of the disturbance univocally determines the system response.

Certain configurations of a system may eventually exhibit a non-linear response to an arbitrarily small perturbation for a range of values of a given parameter. That non-linear response necessarily alters the state of the system before the disturbance. The system may or may not recover its initial state after the perturbation disappears, which defines the parametric ranges of instability that characterise the general behaviour of the system.

Stability analysis in fluid-dynamic problems has been a discipline of great interest since the XIX century [48], and especially since the 90s, for its predictive potential related to the system bifurcations and breakdown, as for example the dripping-to-jetting transitions in steady capillary ejection or the capillary jet breakup.

In this thesis, we focus on *global* linear stability analyses. These are carried out by linearising the system equations, formulating the general solution as a steady solution plus the linear response of the system to small-amplitude perturbations that are normal in the time domain as $e^{(i\omega t)}$, where $\omega = \omega_r + i\omega_i$ stands for complex frequency, and global in the spatial domain, which using cylindrical polar coordinates can be expressed as $\Phi(r,z)$ for a 2D domain, and as $\Phi(r,\theta,z)$ for a 3D domain. In the 3D case, such perturbations can be decomposed into azimuthal modes: $\Phi^{(j)}(r,\theta,z) = \Phi_{2D}(r,z)e^{(im\theta)}$, where m stands for azimuthal wavelength, $\Phi^{(j)}$ stands for any variable of the problem, and (r, z,θ) is a cylindrical coordinate system where the z-axis coincides with the base flow symmetry axis. By imposing the boundary conditions along with the hydrodynamic equations of the problem, it is possible to determine the spatial structure of each linear mode and the dispersion relationship that gives the eigenfrequency ω of a mode with azimuthal wavenumber m as a function of the physical parameters of the system.

Generally, global stability applies to the cases where the hydrodynamic length is of the order of or much smaller than the dominant disturbance, yielding patterns of motion called global modes. These depend inhomogeneously on two or three spatial directions, in which harmonic oscillations appear with the same complex frequency ω and a fixed phase relation. In this way, it is possible to separate time-dependent and spatial variables and analyse how these respond to perturbations. These global modes are computed as the eigenfunctions of the linearized Navier-Stokes operator as applied to a given base flow,

which will be asymptotically stable in the case where all of the eigenvalues are stable in the half-plane, that is, when they all exhibit an imaginary part $\omega_i < 0$. If this condition is fulfilled, any small-amplitude disturbance applied to the system will decay exponentially as time tends to infinity.

Global stability analysis is therefore an ideal tool to characterize the dynamic nature of flows with a free surface, such as the ejection of liquid from a source into open or bounded domains. In particular, we focus on those configurations which exhibit steady-state solutions with axial symmetry, e.g. in the form of ejected capillary jets or liquid ligaments. There are essentially three types of configurations covered in this thesis:

- Dripping: The liquid ligament breaks up into droplets in a region close to the emitting orifice. The obtained droplets will usually exhibit a radius larger than the orifice.
- Jetting: The liquid ligament moves downstream convectively beyond the orifice. Eventually, the ligament will break up into droplets at a characteristic distance which will be larger than the diameter of the orifice due to Raleigh instabilities.
- Tip streaming: It is characterized by the presence of a nearly static meniscus with a characteristic length sufficiently large compared to the diameter of the ligament, and a conical shape tapering into a liquid ligament that can be a steady jet, or it may break up into droplets. In this case, the sizes of the ejections involved are much smaller than the device orifice.

Both in the case of electrospray and Flow Focusing, it is of great interest to know under which operating regimes a steady jet leads to the emission of spray droplets (jet-to-spray, in the case of electrospray) and to the controlled emission of droplets (jetting-to-drip, in the case of Flow Focusing). A more specific description will be given later on, but as a first approximation, a jet is considered to be in a stationary jet regime when:

- The liquid meniscus is globally stable.
- The emitted jet is convectively unstable.
- The resulting droplets after breakage are of the same order than the jet diameter.

In this regime, an axisymmetric cusp-shaped liquid meniscus of density ρ, viscosity μ and surface tension σ leads to the formation of a jet with an emission flow rate Q. While the meniscus geometry is maintained in nearly-static equilibrium by surface tension between the liquid and the environment (typically air), the kinetic energy and viscous extensional forces play a fundamental role in the jet: their relative weight compared to surface tension, especially around the meniscus cusp, undergo significant changes along the jet development region in the axial direction. Thus, although the jet radius depends on the distance to the meniscus, it often reaches an uniform value R just near the breakup region. The dimensionless parameters Reynolds, Weber and capillary numbers characterize the behaviour of the jet.

$$We = \frac{\rho Q^2}{\pi^2 R^3 \sigma}, \quad Re = \frac{\rho Q}{\pi R \mu}, \quad Ca = \frac{We}{Re}, \tag{1.1}$$

After this introductory section, the two technologies on which this thesis focuses are presented.

1.2 Electrospinning/Electrospray

In 1897, Rayleigh began his first investigations into this technique, which was studied in greater detail by Zeleny [55] in 1914, to later be patented in 1934 by Formhals. In the electrospray dispersion technique, a high-intensity electric field is used to eject a liquid in the form of a jet that eventually, by the action of viscosity and surface tension, break up into spherical droplets. To impose an electric field, a high-potential difference V between the liquid to be ejected, commonly known as dope, and a collector is required. The dope is loaded onto a stainless steel tube, such as a needle, and is supplied continuously by a syringe pump. To prevent electrical attraction from influencing the planned trajectory, a dielectric medium must be placed between the tube and the collector. As the voltage applied to the system increases, a charge accumulation process begins at the fluid's surface, resulting in Maxwell stresses. Due to the balance of Maxwell and surface tension stresses at the surface, a so-called Taylor cone will begin to form at the tip of the tube over a range of voltages (see figure, 1.1).

Taylor's theoretical, no-emission, equipotential, semi-infinite conical solution results from the perfect balance of Maxwell stresses and surface tension

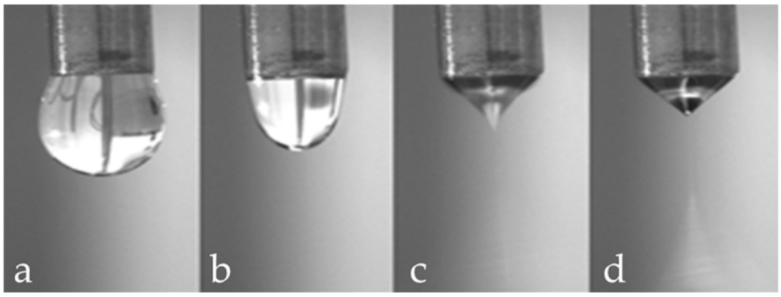

Figure 1.1: Accumulation charges process and the formation of a Taylor cone, and the later ejection by electrical repulsion. a) Droplet pending on the needle due to the effect of surface tension. b) As voltage increases, the spherical shape of the liquid is affected as accumulated charges on the lower surface are being attracted. c) A greater increase of voltage leads to the formation of a Taylor cone. d) Further increase of voltage, produce the emission of the liquid due to Coulomb repulsion, which eventually breaks up into droplets [15].

for a surface with zero hydrostatic pressure:

$$\frac{\sigma}{R\tan(\alpha_T)} = \frac{\varepsilon_0}{2}E_{n,T}^2 \tag{1.2}$$

where R is the spherical coordinate radius, ε_0 vacuum permittivity and $E_{n,T}$ is the normal electric field on the cone.

This, combined with an axial component of the electric field, allows charges to migrate from the cone's surface toward the collector, dragging some of the fluid with them. The length of the liquid layer that responds to the attraction induced by the electric field is known as the Debye length, and it is governed by the electrical conductivity of the fluid utilised. In figure 1.2, a sketch of all the involved parameters is shown.

The ejection process will occur only if the kinetic energy obtained by the electrical component exceeds or is on the order of the surface tension, as discussed in the preceding section. From here, the material is expelled through a stretching and thinning process. It will be electrospray when the jet breaks up into droplets or electrospinning otherwise, depending on the continuity of the jet during the process until the liquid reaches the collector [41] (see figure

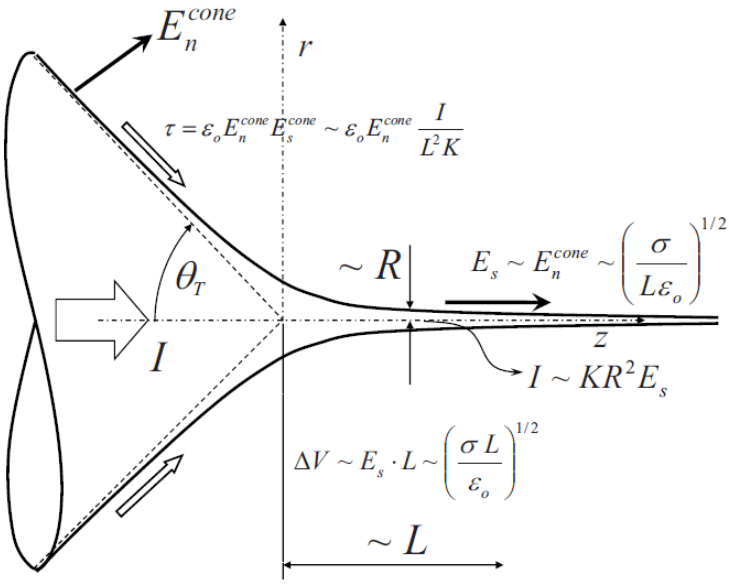

Figure 1.2: Electrospray description and all physical components.E_n is the normal component of the electric field on the jet surface. τ the tangential stress on the jet surface, where E_S and E_n are the tangential and normal components of the electric field on the jet surface respectively. ΔV the difference of potential applied, which is mainly converted into kinetic energy. I and K stands for current intensity and conductivity respectively. L is an axial characteristic length that is small compared to the feeding capillary, and long compared to the jet's radius R. σ stands for the surface tension and ε_0 for electric permittivity. Θ_T is the Taylor's conical solution Reprinted with permission from [23]. https://doi.org/10.1103/PhysRevE.79.066305. Physical review E, 79(6), 066305. Copyright (2022) by the American Physical Society.

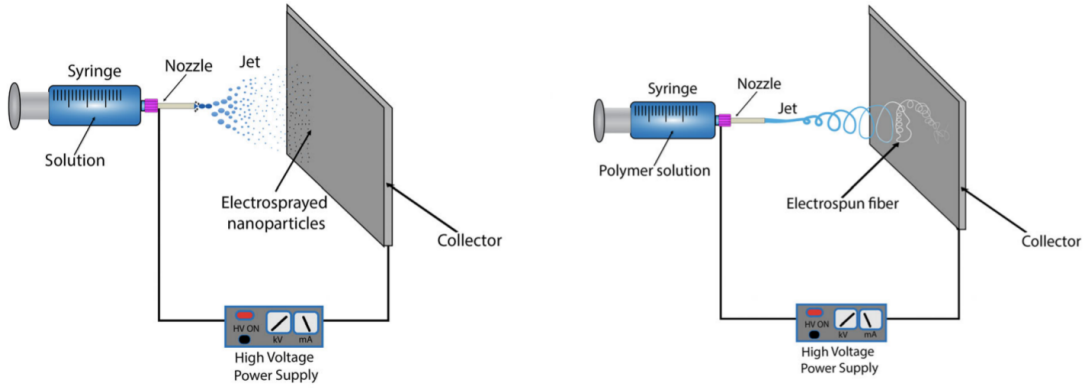

Figure 1.3: Set-up electrospray and electrospinning. On the left figure, perturbations on the jet lead to the break-up into small droplets (electrospray). On the right figure, perturbations give arise to whipping effect, modifying the trajectory of the jet. Figure taken from [34] under licence Creative Commons 4.0 http://creativecommons.org/licenses/by/4.0/.

1.3). The investigation of the parametrical boundaries between these two configurations is critical for optimizing the desired outcomes for each application.

The primary application of electrospray in biomedicine, chemistry, and biotechnology is mass spectrometry. This technique can characterize chemical compounds as well as various types of cells and viruses. Electrospray can also be used for other biomedical applications, such as drug delivery in the form of micro/nano-spheres encapsulation, microbubbles for contrast agents used for biomedical imaging or implants coating for regulating their integration with the surrounding tissue [11].

Electrospinning, on the other hand, enables the development of fibresăfor regenerative therapies. This necessitates a high level of control over their diameter, because reducing diameters increases contact surface with the biological medium, favouring both biocompatibility and biofunctionality and increasing the efficiency of binding sites on cell membrane receptors [2]. Another control parameter is the porosity of the fibre network, which allows chemical species to exchange between cells and the surrounding medium (oxygenation, nutrients, blood vessel growth...). The resulting scaffold resembles the extracellular matrix, which is composed of proteins and carbohydrate polymers known as glycosaminoglycans and serves as a support structure for cells by

forming a mesh. Poly(α-esters) and enzymatically degradable polymers with viscoelastic properties such as elastin, albumin, and fibrin [18] are among the most commonly used materials for biomedial applications [3, 42].

The Oldroyd-B model is one of the most widely used models for viscoelastic materials [45, 49]. This model's behaviour can be explained from two perspectives. On the one hand, it can be viewed as a rubber network of interconnected elastic threads that form and decay according to arbitrary laws [25]. On the other hand, it can be interpreted as a Newtonian-modeled linear elastic spring subjected to the drag of the surrounding fluid [37]. In order to analyse the effect of a liquid with weakly viscoelastic properties when using the electrospray/electrospinning technique, [9] performed a theoretical comparison between a Newtonian case, previously studied by [47], and its non-Newtonian variant.

However, in some applications, high voltage can cause the destruction of a portion of the biological sample or is incompatible due to the material's poor electrical properties. Flow focusing is capable of manipulating such materials for a wide range of applications in the field of health science by using purely mechanical methods. One of its most important applications is the delivery of samples in the XFEL technology process of reconstructing biological structures of molecules.

1.3 Flow Focusing

Flow focusing is based on the interaction of two immiscible fluids. When a given pressure difference ΔP is applied on the focusing fluid, it is large enough to overcome the stresses due to surface tension between the two fluids, creating a virtual nozzle that gives it the shape of a capillary jet at the mouth of a capillary tube, giving rise to a cusp-shaped meniscus. This meniscus appears after a certain distance has been travelled and is influenced by both the presence of favourable pressure gradients and the presence of viscous shear and extensional stresses that cause a constriction in the fluid. The focused fluid begins to elongate as the meniscus forms, and both fluids pass through an orifice located in a plate some distance from the capillary tube's mouth. The diameter of the focused fluid obtained is much smaller than that of the orifice. If the capillary flow is sufficiently stable, a jet of a certain diameter will be formed, which length (on the order of millimetres) will be determined by both the flow

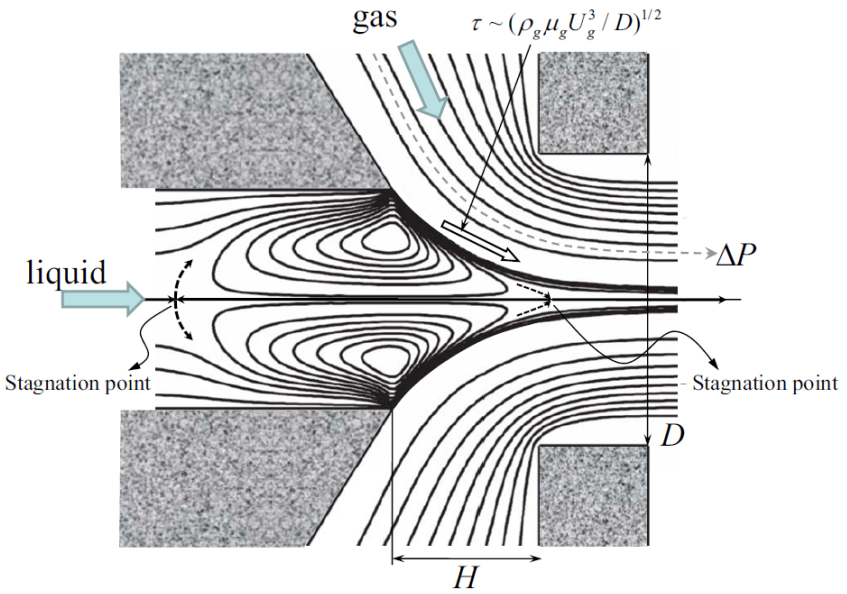

Figure 1.4: Flow Focusing description and all physical components. ΔP is the pressure drop applied to the focusing fluid, D the orifice diameter, τ the tangential viscous stress exerted by the focusing fluid on the meniscus surface and H the capillary-orifice distance. ρ_g, μ_g and U_g are the gas's density, viscosity and velocity respectively Reprinted with permission from [23]. https://doi.org/10.1103/PhysRevE.79.066305. Copyright (2022) by the American Physical Society.

rate and the Reynolds number of the focused fluid. However, as seen in the case of electrospray, there will come a point downstream, at the orifice's outlet, when the surface tension becomes dominant over the kinetic energy of the jet as the pressure values for both fluids decrease, resulting in the emission of bubbles or droplets [22, 40]. A sketch of this configuration is shown in 1.4

The main advantage is that viscous shear stresses are lower than in other techniques, making it easier to manipulate highly sensitive biological material such as cells, DNA, or biomolecules. Contributing to a better understanding of how the fundamental elements of organic nature are organised leads to the development of new therapies, drug synthesis, and knowledge generation for biological pathways such as gene expression and suppression. In the last two decades, there has been an increasing interest in the study of biological samples in the form of crystals, such as proteins [24].

In a numerical study published in 2000, [44] proposed using high-intensity, short-duration pulses of the order of fs to extend the conventional damage barrier (on the order of 200 photons per $Å^2$ with energy of 12keV or a wavelength of 1 Å). This enabled the retrieval of protein structural information just before their interaction with the energy pulse damaged the biological material, combining three aspects: spatial coherence, high-intensity energy peaks, and pulses with a narrow time window. This method was dubbed SFX (Serial Femtosecond Crystallography).

XFEL (X-ray free electron laser) technology [13] is based on the interaction of protein crystals moving in a jet at around 100 m/s with high-frequency X-ray pulses of the order of 4.5 MHz. When the interaction occurs, a diffraction pattern is collected just before the sample is destroyed due to the pulse's high energy. Following the acquisition of several thousand diffraction patterns, they are sequentially sorted by detecting small displacements, and the molecular spatial distribution is computed. Shock waves form during the destruction process, damaging biological material and interfering with data collection by causing pattern distortion. Only one interaction diffraction pattern is ideal (see figure 1.5).

When the laser pulse interaction occurs, the velocity of the water jet or buffer (natural environment of the protein crystals) must be as high as possible to ensure the availability of fresh undamaged sample. To summarise, three factors must be optimised in this pipeline: data diffraction quality, data collected per sample (ideally only one), and experimental ability to reduce collection times.

The jet diameter must be reduced in order to reduce the amount of liquid surrounding the crystals and thus the obstructions in the effect of the samples' diffraction patterns. When using gas-focused liquid methods (GDVN [16] or Flow Focusing)[14], the jet diameter should be in the range of 1 to 5 μm.

Flow Focusing is one of the most widely used mass transport techniques among injectors used in SFX. The diameter of the crystals in the focused liquid is on the order of 50 microns, while the focused fluid allows the ejected diameter to be reduced by an order of magnitude. The main disadvantage of this method is its high sample consumption rate, which is inappropriate for some applications. As tipically the liquid flow rate is greater than 10 micro-

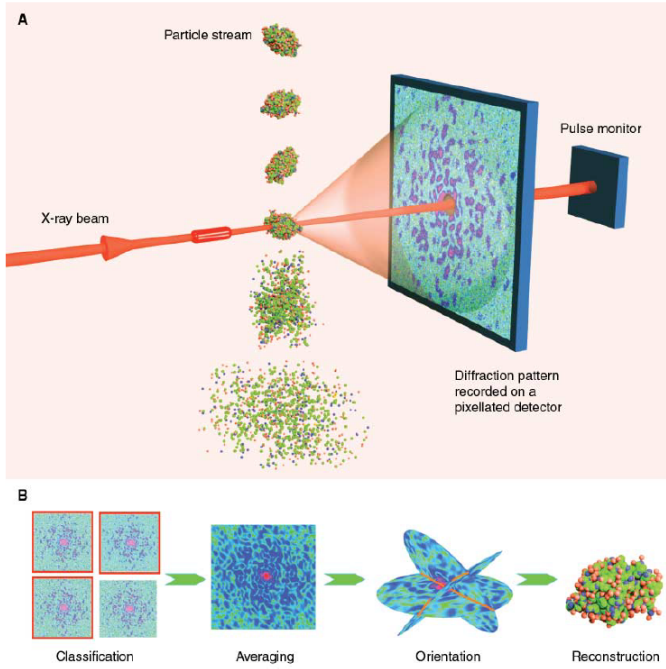

Figure 1.5: The XFEL pipeline is depicted schematically. The diffraction patterns are collected, and after computationally analysing the Bragg peaks, the orientation of the molecules can be recalculated. After several hundred repetitions, the molecular crystal structure of the biological particle can be reconstructed [21].

liters/min, it can consume tens of milligrammes of microcrystals in order to get a full data set. However, progress has been made in reducing the consumption required by these systems.

As the Weber number for a constant jet-mode increases, the resulting jet diameter decreases and instabilities increase due to periodic perturbations. This type of research, in which physical parameter values can be used to predict the configuration of the downstream jet, leads to the calculation of stability regions. The regions where global instabilities can be reached after increasing the pressure drop beyond a limit point for a fixed flow rate, characterised by a chaotic movement of the jet that changes the orientation of its symmetry axis continuously at a given point downstream, must be avoided for proper performance and resource optimization.

The whipping effect is classified into two types: convective and absolute. Convective whipping is defined by jet oscillations beyond the discharge orifice with no downstream consequences. When nozzles are used instead of the traditional configuration, absolute whipping occurs, and lateral oscillations can occur. As a result, SFX technology must account for this phenomenon, which has become a critical point in its proper performance because, under certain conditions, whipping causes the jet to make contact with the nozzle wall. In [10], authors hypothesised that the growing of the dominant linear lateral mode ($m=1$) could be responsible for the growing of lateral oscillations, leading to absolute whipping, as observed in [1].

1.4 Biomechanical models

Numerical models for the kinematic and dynamic analysis of biomechanical systems are critical in areas such as high-performance sports, rehabilitation, diagnosis, implants designing, and surgical planning. One of its main strengths is the analysis of various physical variables that may influence an individual, allowing it to provide personalised therapies and accurate diagnostics by adapting the implemented model to patient-specific cases. Originally, such predictions relied on approximations based on animal tests [5] or the use of corpses.

Different research groups have widely used so-called lumped-models, with

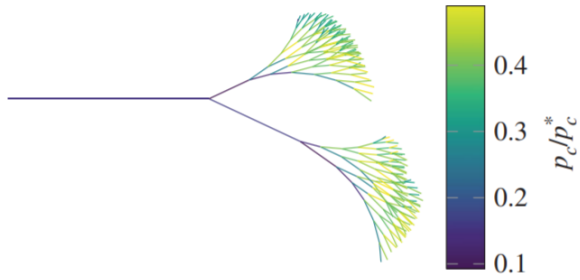

Figure 1.6: The relationship between transmural pressure across the airways and the pressure required to collapse the airways. On the left side we find the trachea, and on the right side the bronchioles [26].

Wiendkessel's models standing out [46, 54]. These models rely on blood vessel network modelling as electronic components (see figure 1.7). Different elements and configurations can be used depending on the characteristic to model (compliance, inertia, or energy loss). Approaches based on CFD (Computational Fluid Dynamics) are becoming more common, allowing the use of biomedical images of patients to define specific geometry and boundary conditions [19] (see figure 1.8).

The analysis of flexible channel models was the focus of this thesis [12, 28, 53]. The ability of these models to perform simplifications of channel deformation and analyse fluid-structure interaction (FSI) phenomena, as well as collect in greater detail some of the most important characteristic properties of a given segment of the vascular network, such as small wall deformations, boundary layer detachment, and conduit collapse, is their main feature.

The shell model is one of the most widely used due to its simpler consistent approximation. The Kelvin-Voigt viscoelastic model, in which the total strain is proportional to the strain and the time derivative of the strain, has shown good agreement with experimental data from animals [5] and humans [4] for the flexible membrane, allowing features such as wall hysteresis to be captured.
Flexible channel models, on the other hand, might be computationally expensive, therefore *ad-hoc* simplifications can be applied. For example, the linear elasticity assumption is reached by assuming that the artery wall is homogeneous and considering sufficiently small deformation gradients and displacements. Other assumptions include a small vessel thickness, which may allow

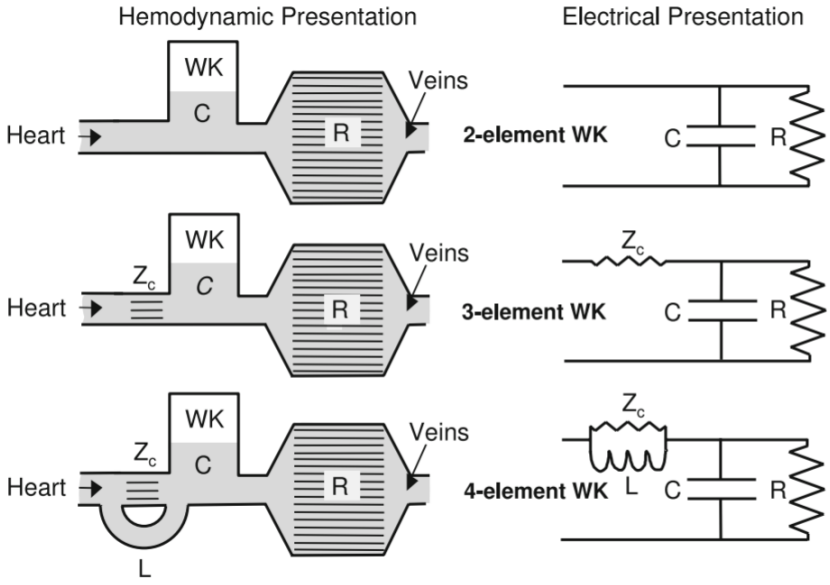

Figure 1.7: Windkessel models of various components for blood vessel simulations based on their electronic analogy. Figure taken from [54] under Creative Commons 2.0 license https://creativecommons.org/licenses/by/2.0/.

for a simplified transition from a 3D to a 2D shell model. Furthermore, assuming an unbranched cylindrical geometry leads to cylindrical shell models. It is possible to convert a shell model to a membrane model if the bending stiffness of the channel is ignored [12]. However, as the thickness of the membrane approaches (or matches) the radius of the duct, or when dealing with large deformations on the flexible membrane domain, the accuracy of these models decreases.

In a system with constant control parameters, self-excited oscillations occur when a stable solution does not exist or becomes unstable [39]. Models based on self-excited oscillations and flexible membrane conduits can analyse the frequency response as well as the system's local and global stability.
They have been used to quantify the severity of conditions such as pulmonary wheezing (see figure 1.6) [26], or cases of apnea. They can detect aneurysms or the emergence of oscillations in the coronary veins during open heart surgery in blood vessels, and it can detect urea flow insufficiencies in the urethra. Furthermore, these models, aid in the development of groundbreaking medical devices such as artificial hearts, voice cord prosthesis, and intra-aortic bal-

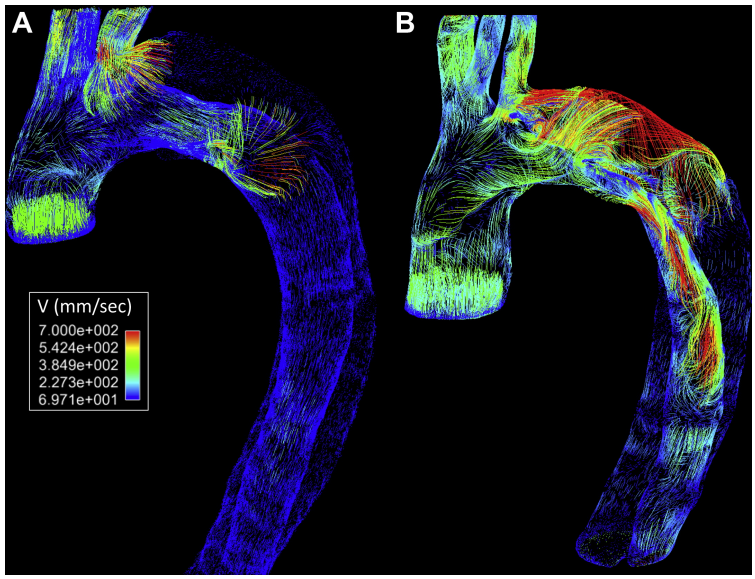

Figure 1.8: Flow velocity maps of aortic dissection thoracic segments showing blood acceleration through dissection tears and subsequent impingement on the far aortic wall. A, Aortic dissection characterised by a stable transaortic diameter. B, Aortic geometry exhibiting rapid expansion [50]. Use license number: 5335030997292. DOI: 10.1016/j.jvs.2015.02.048

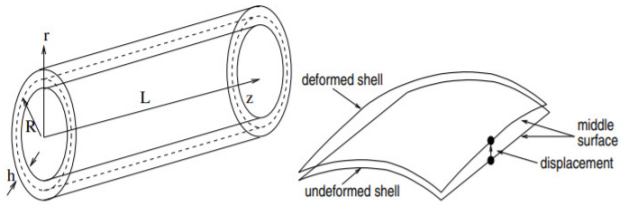

Figure 1.9: Left: Cylindrical shell model where R is the middle surface radius, h the thickness of the shell and L the length. Right: Deformed and not deformed shell states along its displacement [12].

loons.
When the transmural pressure falls below a certain level, any physiological conduit through which a fluid circulates is prone to collapse. This phenomenon will occur in some cases in small vessels, such as capillaries, where the Reynolds number is low, and in others in larger vessels where it is high. In the latter case, a correlation between the occurrence of self-excited oscillations and duct collapse has been studied, as in the case of wheezing or Korotkoff sounds [35].

Depending on the desired degree of detail in the models [27], we can find:

- 1D: These are simplified models, mostly *ad-hoc*. Their accuracy is adequate for describing phenomena such as wave propagation, choking, and transitions between subcritical and supercritical flows.

  However, when compared to some experimental models, 1D models exhibit accuracy errors. This is observed in both the case of viscous dissipation for high Reynolds number flows and the coupling with the local pressure per area ratio, because they are not obtained from higher order systems. These disadvantages lead to deficiencies in the description of the system's energy losses. In addition, some unstable modes may be ignored when performing a global stability analysis of the system due to low resolution in the results.

- 2D (Bounded flows): In this type of model, the solid and fluid domains are treated in such a way that they are coupled to each other, allowing for a more detailed description of when the system can exhibit self-excited oscillations. It entails simulating the conduct with a finite length and a segment of it replaced by a membrane/beam subjected to longitudinal tension. This model is implemented in two ways: by imposing a specific flow or by imposing an external pressure on the flexible segment (see figure 1.10). This increased resolution can deal with instabilities that appear when, for example, a specific longitudinal stress value T applied to the flexible membrane is low enough or Re is high enough [39]. They are also able to capture vorticity phenomena inside the channel. Nevertheless, when dealing with unsteady systems, the membrane's thickness is tipically considered asymptotically thin, reducing the scope of the analysis. In order to overcome this limitation, [33] implemented a 2D numerical model based on the implicit resolution of the system's governing equations, and the use of an elliptical meshing for capturing large deformations on the membrane.

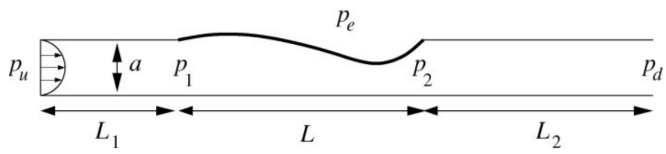

Figure 1.10: 2D collapsible channel model sketch [27].

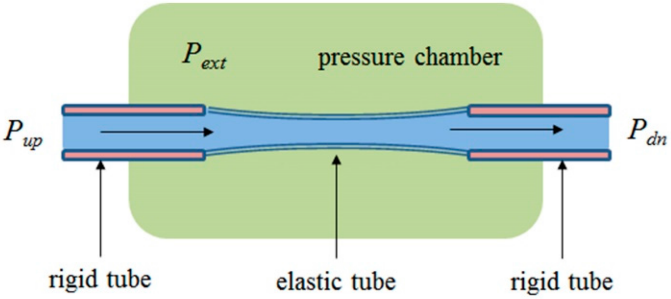

Figure 1.11: Starling resistor set-up diagram [43].

- 3D: These models describe with more detail the collapse of the channel, allowing both small and larger deformations. The way the channel can be obstructed may not be axisymmetric, resulting in a non-linear flow and pressure relation, where flow limitations may be solely due to viscous effects. This model sub-category can also be used to collect hysteresis phenomena on conduct spatial locations. Its main backdraw, is that for some implementations they might be computationally expensive.

The Starling-Resistor is commonly used in experimental studies of self-excited oscillations. They proposed the original configuration. The system consists of an elastic segment anchored at its ends to rigid conduits and enclosed in a pressurised chamber at constant pressure P_{ext}. The flow is controlled by adjusting the pressure difference between the upstream Pup and downstream P_{dn} ducts. The Reynolds number, which is usually in the 10^2-10^4 range, is imposed by selecting the diameter of the duct. The pressures at the elastic region's entrance and exit p_1 and p_2 are controlled by the use of valves (see figure 1.11).

Buckling occurs in the flexible region when external pressure is applied in the absence of flow (i.e., when $p_u = p_d$), adopting an elliptical configuration.

If the region is sufficiently short, two elliptical lobes may appear. Additional increases in the p_e translate into a reduction in cross-sectional area in this configuration. In the case of elastic rings, a relationship between transmural pressure and cross section can be established using thin-shell theory. 3D models (based on nonlinear shell theory) can predict phenomena such as axial pre-stress and subcritical buckling instabilities [29].
When a fluid flows inside the duct and an external pressure is applied to it p_e, the channel narrows in the downstream zone of the elastic region. There are several options based on this configuration. One of them is to investigate the maximum flow limit by varying the pressure drop between p_1 and p_2 while maintaining the transmural pressure constant $(p_1 - p_e)$.

Bertram and colleagues [6, 7], investigated on self-excited oscillations and established their existence at different frequency bands and the dependency on the physical parameters of the elastic material, as well as exhibiting hysteresis phenomena and the interaction between the system's modes. Self-excited oscillations's frequencies can be related to fluttering effects depending on their values. In terms of inertia, low-frequency values correspond to low inertial values in the elastic solid, whereas high-frequency values correspond to increased inertial effects.

1.5 Numerical method used in the thesis

Professor Herrada's numerical method was employed in papers I, II, and III [30]. The algorithm implements the equations that govern the problem and its boundary conditions using the Matlab symbolic tool, and calculates the relevant derivatives evaluating them at each time step in a much simpler and less computationally expensive manner than other approaches found in the literature.

As stated in the first section of this manuscript, fluid-dynamics problems are divided into two parts: One of them entails subjecting the stationary flow defined by the non-linear equations to small perturbations and analysing the corresponding eigenmodes of the linearized problem. The non-linear evolution is calculated from the initial conditions in the other part. This second part, in particular, requires the formulation of the problem's derivatives, which can become tedious depending on the scenario, and this is the main advantage that this numerical method can provide.
Therefore, a solution $U(x,t)$ can be decomposed as the sum of a stationary

term $U_0(x,t)$ and a transitory one $\xi\ U_p(x,t)$ where ξ is a constant. From the premise of considering U_p small enough relative to U_0, it must necessarily be fulfilled that $\xi << 1$. Under this framework, it is possible to linearize the problem equations, obtain a normal decomposition of the eigenmodes, and compute the linear response of the system when perturbed:

$$U_p(x,t) = \sum_{i}^{N} \psi_i(x).e^{\omega_i t} \tag{1.3}$$

where each mode calculated ψ_i will have a certain frequency ω_i. To ensure system stability, all calculated modes must have an imaginary frequency $\omega_i < 0$, so that the exponential attenuates in time. On the contrary, if there were at least one mode with a frequency $\omega_i > 0$, it would imply a growth of U_p, in which case the system diverges from its stationary solution.

To compute the eigenmodes ψ_i, the linearized equations are derived analytically, and then the discrete eigenvalues problem is solved. This allows the problem's nonlinear evolution and linear stability to be calculated using the same algorithm.

The steps followed by the algorithm are:

- Formulation of the problem: First, a mapping of the domain coordinates and the modeling-dependent parameters is performed. A set of equations in the form $F_K(t,\xi,\eta;u_1,u_2,...,u_J) = 0$ where $\xi(x,y;t)$ and $\eta(x,y;t)$ represent the coordinate transformation from the real domain (x,y) to the numeric domain; P represents the physical parameters of the problem, and u_j the set of all variables, including their partial derivatives and the unknowns of the problem. When formulating the problem, both the number of equations F_K and the number of unknowns u_J must match. Prior to executing the numerical simulations, all the partial derivatives of the F_K functions with respect to the u_J variables are symbolically calculated, understanding by variables both the unknowns and their partial derivatives.

- Problem discretization: The mesh points are defined in the numerical domain (ξ,η), calculating the corresponding values of the variables in each of the mesh points at each time step At this point, the necessary placement matrices are computed in order to evaluate the problem's partial derivatives. It should be noted that since the numerical domain is not

time-dependent, neither the placement matrices are. The evaluated mesh points are then converted to a 1D matrix. The derivative with respect to time is computed using the second-orderăregressive finite difference method.

- Symbolic Jacobian: Following the spatiotemporal discretization, the mesh points and unknowns are rearranged in a 1D vector. It is possible to define the symbolic Jacobian in such a way that both the equations and the unknowns are described in the numerical model by taking into account the corrections of the spatial and temporal derivatives and applying the pertinent relationships between the variables and their derivatives in symbolic format.

- Newton-Raphson iterations:At each point of the numerical domain, the equations defined in the preceding steps are solved iteratively. In each step, the symbolic Jacobian is first evaluated at each point in the domain, and then its inverse is calculated to determine the value of the unknowns.

- Global modes: Following the same strategy as described in the previous steps, it is possible to create a symbolic Jacobian matrix J, in a way that allows both the calculation of the basic solution, and another Jacobian matrix J_0 for the perturbation. The problem would be defined as $U = U_0 + \varepsilon e^{-i\omega t}\delta u$, being U a problem variable, U_0 the base solution and δU the solution corresponding to the spatial disturbance, and ω the complex eigenfrequency. Based on the defined parameters, the objective will be to calculate both the eigenfrequency and the eigenmodes. The main difference between this and the previous procedure is that in this case, we will have a Q_0 matrix whose elements are the partial derivatives of the variables in the problem with respect to time. Finally, the problem of calculating eigenmodes and eigenfrequencies would be described as $J_0^{(p,q)}\delta U^{(q)} = i\omega Q_0^{(p,q)}\delta U^{(q)}$.
  An example of global stability calculation using the variables employed in paper II of this thesis is shown below:

$$U(r,\theta,z;t) = U_b(r,z) + \varepsilon\hat{U}(r,z)e^{-i\omega t+im\theta} \tag{1.4}$$

$$V(r,\theta,z;t) = \varepsilon\hat{V}(r,z)e^{-i\omega t+im\theta} \tag{1.5}$$

$$W(r,\theta,z;t) = W_b(r,z) + \varepsilon\hat{W}(r,z)e^{-i\omega t+im\theta} \tag{1.6}$$

$$p(r,\theta,z;t) = p_b(r,z) + \varepsilon\hat{p}(r,z)e^{-i\omega t+im\theta} \tag{1.7}$$

$$F(\theta,z;t) = F_b(z) + \varepsilon\hat{F}(z)e^{-i\omega t+im\theta} \tag{1.8}$$

, where $\varepsilon << 1, \{\hat{U},\hat{V},\hat{W},\hat{p},\hat{F}\}$ stands for eigenmode spatial dependence and $\omega = \omega_r + i\omega_i$ is the eigenfrequency and m is the azimuthal wave number.

For further formality, the reader is referred to the article [30].

Chapter 2

Thesis structure

This thesis consists of 3 articles published in high impact journals:

- Blanco-Trejo, S., Herrada, M. A., Gañán-Calvo, A. M., & Montanero, J. M. (2019). Electrospray cone-jet mode for weakly viscoelastic liquids. Physical Review E, 100(4), 043114.
  Journal Impact Factor 2.296, Q1 (9/55 in category of Physics, Mathematical), Source: Journal Citation Reports (JCR Year 2019).

- Blanco-Trejo, S., Herrada, M. A., Gañán-Calvo, A. M., Rubio, A., Cabezas, M. G., & Montanero, J. M. (2020). Whipping in gaseous flow focusing. International Journal of Multiphase Flow, 130, 103367.
  Journal Impact Factor 3.186, Q2 (45/135 in category of Mechanics), Source: Journal Citation Reports (JCR 2020).

- Herrada, M. A., Blanco-Trejo, S., Eggers, J., & Stewart, P. S. (2022). Global stability analysis of flexible channel flow with a hyperelastic wall. Journal of Fluid Mechanics, 934.
  Journal Impact Factor 3.627, Q1 (4/34 in category of Physics, Fluids and Plasmas), Source: Journal Citation Reports (2020).

In paper I, a theoretical comparison was made between the use of a Newtonian fluid and a non-Newtonian one in the electrospinnig/electrospray technique. The analysis of the system's response at the global stability level, as well as other aspects such as meniscus shape, provides information on how fluids with weakly viscoelastic properties can affect the use of these fluids (e.g. biopolymers and hydrogels).

In paper II, the Flow Focusing technique was employed to investigate the system's regions of stability for the axisymmetric ($m = 0$) and lateral ($m = 1$) modes. Understanding these stability regions enables optimization of operating conditions in applications like XFEL. The geometry of the nozzle and the system's response at the energy level were also studied.

In paper III, 2D collapsible channel model with a Neo-Hookean membrane of non-negligible thickness, is employed to investigate the frequency response considering the impact of inertial effects and flexible membrane's thickness, while exploring the system's global stability in terms of the physical parameters of the system, such as the external pressure and pre-tension applied over the flexible membrane, or the liquid computational domain's Reynolds number, resulting in the definition of maps of stability regions. In addition, the multiplicity of solutions (and their *folding points*), and the characteristics of the self-excited oscillation's limit cycle were subjected to analysis.

The following sections will present all of the governing equations and boundary conditions implemented in the simulations, as well as the considerations and used data, followed by a description of the main results from each paper. Finally, the conclusions of each research will be presented, as well as potential future directions. A full version of each published paper can be found at the end of this manuscript for more information.

2.1 Objectives

Due to the interdisciplinary nature of this thesis, each paper describes a particular topic, with knowledge development to enhance biomedical technology serving as a common denominator.

2.1.1 Paper I: Electrospray cone-jet mode for weakly viscoelastic liquids

Newtonian models have been widely used to study the behaviour of the electrospinning/electrospray technique. However, there was no comprehensive study in the literature of how the occurrence of weakly viscoelastic effects affected the system's response, particularly at the global stability level, providing information and delimiting the boundary between electrospinning and

electrospray. A systematic comparison was carried out using 1-octanol as the fluid, analising the following aspects:

- Proposal of a viscoelastic model in electrospinning/electrospray with which to study the behaviour of non-Newtonian fluids using an adaptation from Newtonian model adding the consideration of the Oldroyd-B model.
- Geometric, electrical and weakly viscoelastic fluid flow pattern characterization.
- Study of global stability of the system, defining operating regions for Newtonian and non-Newtonian fluids.
- Agreement quantification with 1-D slenderness model.
- Effect of polymer relaxation time on critical flow rate.

2.1.2 Paper II: Whipping in gaseous flow focusing

Previous research had allowed for the theoretical investigation of the global stability of Flow Focusing configurations by implementing models with different geometries and performing global stability analysis for the axisymmetric mode (azimuthal number *m=0*). On an experimental basis, [1] carried out an experimental exploration of the axisymmetric and lateral (azimuthal number *m=1*) modes. The primary goal of this paper, was to identify the regions of stability for the modes *m=0* y *m=1*. Specifically, instabilities in the mode *m=1* would be associated with the emergence of *whipping*, phenomenon to avoid in the molecular digitization protocol. The fluid used was 5-cSt silicone oil. Therefore, the objectives of this paper were:

- Theoretical analysis of the geometric influence of the nozzle in the calculation of global stability.
- Exploration of the Flow Focusing configuration (dripping, jetting and whipping) in terms of the values of applied pressure difference ΔP and flow rate Q.
- Quantification of surface disturbances for mode *m=1*.
- Comparison of the theoretical results with the previous experimental research carried out by [1].

- Experimental validation of the theoretical obtained results (Professor Jose María Montanero's group, Universidad de Extremadura).

2.1.3 Paper III: Global stability analysis of flexible channel flow with a hyperelastic wall

Shell models are useful for describing the deformation and frequency response of collapsible biomechanical duct systems (vocal cords, blood vessels, airways...). These models are typically based on taking into account a membrane of negligible thickness in relation to the duct diameter, as well as minor duct deformations. The authors' model overcomes these limitations by employing a deformable hyperelastic solid model of significant thickness under pretension, based on the works of [52] and [28], by implicit solving the equations and boundary conditions without performing any simplification. The flexible solid's inertial effects and how the membrane's thickness value affected the occurrence of self-excited oscillations have also been considered. This research is intended to lay the groundwork for future biomechanical models based on physiological duct networks. The specific goals were:

- Analysis of the global stability of the system as a function of the thickness of the membrane, the inertia of the deformable solid, the external pressure, the Reynolds number and the longitudinal pre-stress to which the membrane was subjected.
- Exploration of the existence of multiple solutions and characterization of the *folding points*.
- Comparison with the results obtained by [28], used as a benchmark.
- Analysis of the frequency response to small disturbances.
- Analysis of limit cycles and other phenomena, such as detachment of the boundary layer and emergence of vorticity within the two-dimensional channel.

Chapter 3

Paper I: Electrospray cone-jet mode for weakly viscoelastic liquids

3.1 Equations

A constant voltage V is applied to a cylindrical capillary. The capillary is pushed up near to a planar grounded electrode at a distance of H. A steady flow rate Q of liquid is injected through the capillary. Inside the capillary, the flow has fully evolved, resulting in a parabolic Hagen-Poiseuille velocity profile upstream at a distance L_n from the capillary's outlet. The triple contact line is anchored R_i away from the capillary axis. The ambient medium is a perfect dielectric gas with no dynamic effects. The gravitational Bond number takes sufficiently small values for the gravity effects to be inconsequential. A sketch of the system can be seen in 3.1. The properties of the leaky-dielectric Oldroyd-B liquid are characterized by the density ρ, zero-shear viscosity μ_0, stress (polymer) relaxation time $\widetilde{\lambda_s}$, retardation time $\widetilde{\lambda_r}$, surface tension γ, electrical permittivity ε_i, and electrical conductivity K. As the outer domain is considered vacuum or gas, the only parameter characterizing its electrical influence is its permittivity ε_0.

The mass conservation and momentum equation are defined as:

$$\nabla . v = 0 \tag{3.1}$$

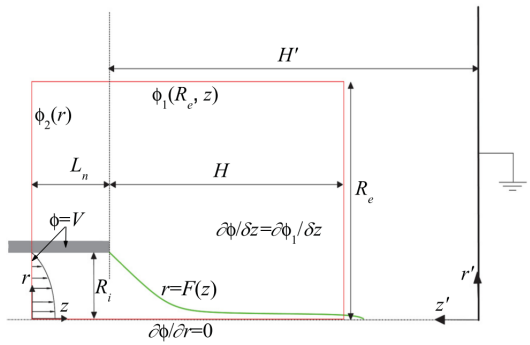

Figure 3.1: Problem sketch. The red square delimits the numerical domain.

$$\frac{\partial v}{\partial t} + v.\nabla v = -\nabla p + \nabla.T \tag{3.2}$$

where $v(r,t) = u(r,z,t)e_r + w(r,z,t)e_z$ is the dimensionless velocity and $p(r,z,t)$ is the reduced pressure. T corresponds to the extra stress tensor T in the Oldroyd-B model, being the sum of the solvent contribution and that due to the presence of polymers:

$$(1+\lambda_s^* G)T = Oh_0(1+\lambda_r^* G)[\nabla v + (\nabla v)^T] \tag{3.3}$$

, where $\lambda_s^* = \widetilde{\lambda}_s/t_c$ is the stress relaxation time defined in terms of the capillary time[20], G[A] the upper convective derivative operator, $Oh_0 = \mu_0(\rho R_i \gamma)^{-1/2}$ the Ohnesorge number, $\lambda_r^* = \lambda_s^* \mu^{(s)}/\mu_0$ the dimensionless retardation time, and $\mu^{(s)}$ the solvent viscosity.

As in the majority of the viscoelastic liquids, the solution viscosity increases as polymer is added to the solvent, $\mu^{(s)} << \mu_0$, leading to $\lambda_r^* \simeq 0$.

In the implemented leaky-dielectric model the bulk net free charge is assumed to be negligible. Thus, the inner and outer potentials ϕ^i and ϕ^o corresponding to the liquid and gaseous domain obey the Laplace equation:

$$\phi_{zz}^{i,o} + \phi_{rr}^{i,o} + \phi_r^{i,o}/r = 0 \tag{3.4}$$

The subscripts r and z correspond to the partial derivatives with respect the radius and length across z-axis.

The free surface location is defined by the equation:

$$r = F(z,t) \tag{3.5}$$

Total current intensity I, computed as the sum of the contributions due to the bulk conduction I_b and the surface convection I_s:

$$I_b(z) = 2\pi\alpha\chi \int_0^{F(z)} E_z^i(r,z) r dr, \quad I_s(z) = 2\pi F(z)\sigma(z)v_s(z). \tag{3.6}$$

where E_z^i is the axial component of the inner electric field and $v_s(z)$ is the free surface velocity.

The following temporal dependence allows the computation of the linear axisymmetric global modes:

3.2 Boundary conditions

In order to compute the eigenvalues from the jetting regime for the analysis of the global stability analysis, a boundary in the downstream direction is setted and applied outflow boundary conditions at the cutoff of the computational domain. The bond number is low enough to neglect gravitational effects.

The boundary conditions at the surface are defined by the following expressions:

- Kinematic compatibility condition:

$$\frac{\partial F}{\partial t} + F_z w - u = 0 \tag{3.7}$$

- Balance of normal stress at both sides of the surface.

$$p + \frac{F F_{zz} - 1 - F_z^2}{F(1+F_z^2)^{3/2}} + n.T.n = \frac{\chi}{2}[(E_n^o)^2 - \beta(E_n^i)^2] + \chi\frac{\beta-1}{2}(E_t)^2 \tag{3.8}$$

- Balance of tangential stress at both sides of the surface.

$$t.T.n = \chi\sigma E_t \tag{3.9}$$

where n is the outward normal vector, $\chi = \varepsilon_0 V^2/(R_i\gamma)$ is the electric Bond number, E_i and E_o correspond to the inner and outer electric fields, t is the unit vector tangential to the free surface meridians, and σ the superficial charge

density. The right-hand sides of the equations are the Maxwell stresses resulting from both the accumulation of free electric charges at the interface and the jump of permitivity across that surface.

The electric field at the free surface and the surface charge density are computed as:

$$E_n^i = \frac{F_z\phi_z^i - \phi_r^i}{\sqrt{1+F_z^2}}, \quad E_n^o = \frac{F_z\phi_z^o - \phi_r^o}{\sqrt{1+F_z^2}} \tag{3.10}$$

It must be noted that the continuity of the electric potential across the free surface ($\phi^i = \phi^o$) has been considered.

$$E_t = \frac{-F_z\phi_z^o + \phi_z^o}{\sqrt{1+F_z^2}} = \frac{-F_z\phi_r^i + \phi_z^i}{\sqrt{1+F_z^2}} \tag{3.11}$$

$$\sigma = \chi(E_n^o - \beta E_n^i) \tag{3.12}$$

Surface charge conservation at $r = F(z,t)$:

$$\frac{\partial\sigma}{\partial t} + \nabla_s.(\sigma v) = \chi\alpha E_n^i \tag{3.13}$$

where ∇_s is the tangential instrinsic gradient along the free surface, and $\alpha = K[\rho R_i^3/\gamma\varepsilon_0^2]^{1/2}$ is the dimensionless electrical conductivity.

Hagen-Poiseuille velocity profile prescribed at entrance of the liquid domain $z = 0$:

$$u = 0, \quad w = 2\mathscr{Q}(1-r^2) \tag{3.14}$$

where $\mathscr{Q} = Q/(\pi R_i^2 v_c)$.
Fixed potential in the capillary wall

$$\phi^i = \phi^o = 1 \tag{3.15}$$

No-slip boundary conditions in the capillary wall:

$$u = w = 0 \tag{3.16}$$

The triple contact line is anchored at the end of the capillary:

$$F = 1 \quad z = L_n \tag{3.17}$$

Standard regularity conditions on the symmetry axis:

$$\phi_r^i = u = w_r = 0 \tag{3.18}$$

Outflow conditions at the end of the computational domain $z_e = H + L_n$:

$$u_z = w_z = F_z = \sigma_z = 0 \tag{3.19}$$

At $r = R_e$ the analytical solution for the far-field electric potential is imposed:

$$\phi_1(r', z') = \frac{-K_v}{log(4H')} log\left\{ \frac{[r'^2 + (1-z')^2]^{1/2} + (1-z')}{[r'^2 + (1-z')^2]^{1/2} + (1+z')} \right\} \tag{3.20}$$

where r' and z' are cylindrical coordinates whose origin is at the intersection between the symmetry axis and the grounded planar electrode, and K_v is a dimensionless variable depending on H'.

At $z = 0$ and $1 < r < R_e$ a logarithmic drop of voltage is applied:

$$\phi_2 = 1 - [1 - \phi_1(r_e, z'_e)] \log r / \log R_e, \quad z'_e \equiv H' + L_n \tag{3.21}$$

At $z = z_e$ for both the liquid and gas domain:

$$\phi_z = (\phi_1) z \tag{3.22}$$

The geometrical parameters in the computational domain had the following values: $H = 12$, length of the feeding capillary $L_n = 1.5$, the distance between the two electrodes $H' = 20$, and a radial distance of the outer boundary from the symmetry axis $R_e = 6$

3.3 Dimensionless and characteristic parameters

The following characteristic parameters were defined as: the characteristic radial length $d_o = [\gamma \varepsilon_o^2 / (\rho K^2)]^{1/3}$, axial length L of the cone-jet transition $L \sim d_0 Q_r$, axial velocity $v_o = [\gamma K / (\rho \varepsilon_o)]^{1/3}$, electric relaxation time $t_o = \varepsilon_o / K$, electric field $E_o = (\gamma^2 \rho K^2 / \varepsilon_o^5)^{1/6}$ and current intensity $I_o = \gamma \rho^{-1/2} \varepsilon_o^{1/2}$ in terms of the electrodynamic properties of the fluids exclusively. The residence time t_r in the cone-jet transition region scales as $t_r \sim L / v_0 \sim d_0 Q_r / v_0$, and the fluid particle accelerates from negligible velocity up to the jet speed $v_j \sim v_0$

within the cone-jet transition region. The axial strain rate $\dot{\varepsilon}$ in the critical region scales as $\dot{\varepsilon} \sim v_j/L \sim v_0/(d_0 Q_r)$.

Five dimensionles parameters can be formed with the following parameters introduced before: the relative permittivity $\beta = \varepsilon_i/\varepsilon_o$, the electrohydrodynamic Reynolds number $\delta_\mu = \rho v_o d_o/\mu_0 = [\gamma^2 \rho \varepsilon_o/(\mu^3 K)]^{1/3}$, the dimensionless stress relaxation time $\lambda_s = \widetilde{\lambda}_s/t_0 = \widetilde{\lambda}_s/(\beta d_0/v_0)$, the dimensionless retardation time $\lambda_r = \widetilde{\lambda}_r/\widetilde{\lambda}_s$, and the relative flow rate $Q_r = Q/Q_o$, where $Q_o = v_o d_o^2 = \gamma\varepsilon_o/(\rho K)$.

The minimum flow rate stability limit can be defined as a function of the following parameters: $Q_{rmin} = Q_{rmin}(\beta, \delta_\mu, \lambda_s, \lambda_r)$, where $Q_{rmin} = Q_{min}/Q_o$ and Q_{min} is the minimum flow rate.
$Q_{rmin} \sim \beta$ as in the Newtonian inviscid (polarity-dominated) limit $\beta\delta_\mu >> 1$. Due to this, the residence time in the cone-jet transition becomes $t_r \sim d_0\beta/v_0 = t_0$. The dimensionless stress relaxation time $\lambda_s = \widetilde{\lambda}_s/t_0$ can be integrated as the Deborah number (the stress relaxation time $\widetilde{\lambda}_s$ measured in terms of the residence time t_r in the critical cone-jet region), the axial strain rate sclaes as $\dot{\varepsilon} \sim v_0/(d_0\beta) = t_0^{-1}$, and λ_s can be regarderd as the Weissenberg number (the strain rate times the stress relaxation time).
The diameter ratio $\Lambda = 2R_i/d_0 = 2[\rho K^2 R_i^3/(\gamma^2)]^{1/3}$, where R_i is the radius of the triple contact line anchored at the feeding capillary end.

The problem variables were made dimensionless with the triple contact line radius R_i, the liquid density ρ, the surface tension γ, and the applied voltage V. All of them yield the characteristic time, velocity, pressure and electric field such that $t_c = (\rho R_i^3/\gamma)^{1/3}$, $v_c = R_i/t_c$, $p_c = \gamma/R_i$ and $E_c = V/R_i$ respectively.
The governing equations are formulated in terms of the dimensionless numbers $\{Oh_0, \lambda_s^*, \lambda_r^*, \beta, \chi, \alpha, \mathscr{Q}\}$. By combining properly, leads to the set $\{\beta, \delta_\mu, \lambda_s, \lambda_r, Q_r\}$:

$$\delta_\mu = \alpha^{-1/3} Oh_0^{1/2}, \quad \lambda_s = \alpha\beta^{-1}\lambda_s^*, \quad \lambda_r = \alpha\beta^{-1}\lambda_r^*, \quad Q_r = \pi\alpha\mathscr{Q}.Oh_0 = \mu_0(\rho R_i\gamma)^{-1/2}, \tag{3.23}$$

Because the electric relaxation time t_0 is substantially shorter than the capillary one t_c, the dimensionless conductivity $\alpha = \beta t_c/t_0$ assumes values much higher than unity.

This implies that $\lambda_s >> \lambda_s^*$. It is noticeable that λ_s measures better the effects due to viscoelasticity as it takes into account the time for the polymer

to relax to its coiling state in terms of the residence time t_0 in the stretching region.
Most polymeric solutions have substantially higher zero-shear viscosities than their comparable solvents. As a result, we shall use $\lambda_r^* \simeq 0$ in our computations.

3.4 Computational domain

The inner (liquid) and outer domains were mapped onto two quadrangular domains through a coordinate transformation. The computations were performed discretizing the governing equations by means of the following meshing: $n_{z_i} = n_{z_o} = 500$ for both the inner and outer axial spatial domain respectivelly, and solved using fourth-order finite difference. On the other hand, for the radial direction $n_{r_i} = 10$ for inner domain, and $n_{r_o} = 101$ for the outer domain using Chebysheb spectral collocation points.

3.5 Fluid properties

The employed liquid for the numerical simulations was 1-octanol, whose physical properties are: $\rho = 827 Kg/m^3$, $\mu = 7.20 mPa.s$, $\gamma = 23.5 mN/m$, $K = 9.0$x 10^{-7}, $\beta = 10$, $\delta_\mu = 2.29$. All the simulations were performed considering $\chi = 7.92$. The Newtonian and non-Newtonian fluids had as relaxation time $\lambda_s = 0$ and $\lambda_s = 2.656$ respectively, being the retardation time $\lambda_r = 0.0926\lambda_s$.

3.6 Results

The acquired results were based on a systematic comparison of the Newtonian fluid and the weakly viscoelastic fluid, analyzing the repercussion of the non-Newtonian component (polymer relaxation time).

3.6.1 Fluid pattern

Firstly, the fluid pattern obtained in the steady solution exhibited a significant difference, specially at the meniscus region, where a shrink respecting to the Newtonian case can be observed (see figure 3.2). In both cases, for

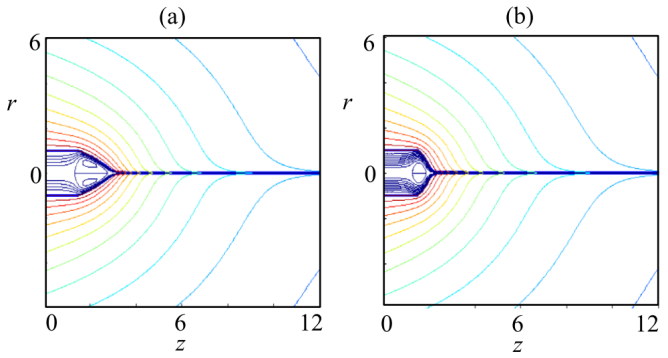

Figure 3.2: Base flows for $\beta = 10$, $\delta_{mu} = 2.29$, $\chi = 7.92$, $Q_r = 7.72$, and $\lambda_r = 0.0926$. (a) $\lambda_s = 0$ and (b) $\lambda_s = 2.656$. Streamlines and equipotential lines are represented by lines in the inner and outer domains.

small enough flow rates, recirculations cells appear in the cone region. Such recirculation suffers a shrink in the non-Newtonian liquid as well.

3.6.2 Global stability analysis

The maximum and minimum flow rates were determined by computing the global stability of both fluids. It was discovered an interval for Newtonian fluid solutions that were stable and ruled by the same dominant eigenvalue. In the case of the viscoelastic fluid, however, the maximum flow rate was obtained, but the minimum flow rate could not be obtained due to the computational complexity of the problem, i.e. numerical instabilities due to the nature of the simulations. Interestingly, for a flow rate of $Q_r \simeq 10$, the weakly viscoelastic fluid exhibits a jump in the dominant eigenmode, explaining the change in oscillation frequency.

3.6.3 Fluid stress and electric fields

In the cone-jet transition region, fluid particles are subjected to intense extensional flow, with velocities increasing from low values to jet speeds. This phenomenon stretches the dissolved polymers in the liquid, which after a timescale λ_s* tend to recover their coiling state. When the timescale is large enough in comparison to the axial strain state, the polymers avoid relaxation and instead stretch across the cone-jet region. More precisely, when $\dot{\varepsilon}\lambda_s^* > 1/2$. In order to analyse this aspect, the strain rate $\dot{\varepsilon}$, and the two contribu-

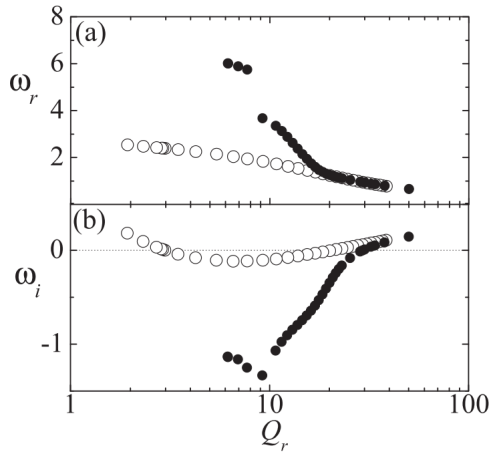

Figure 3.3: Real (a) and imaginary (b) part of the eigenvalue responsible for instability as a function of Q_r. The results were calculated for $\beta = 10$, $\delta_\mu = 2.29$, $\chi = 7.92$, $\lambda_r = 0.0926\lambda_s$, and $\lambda_s = 0$ (open symbols) and $\lambda_s = 2.656$ ($\lambda_s^* = 0.108$)(solid symbols)

tions to the extra stress tensor by the solvent and the polymeric components: $T_{zz}^{(s)} = Oh_s \partial w/\partial z (Oh_s = \mu_s(\rho R_i \gamma)^{-1/2})$ and $T_{zz}^{(p)} = T_{zz} - T_{zz}^{(s)}$ respectively along the symmetry axis were measured. The figure 3.4 shows the results of such comparisons.

As shown in the figure 3.5, $\dot{\varepsilon}\lambda_s^* > 1/2$ in the cone-jet transition region, where the polymer stress experiments an increment. Conversely, for values of $z \gtrsim 2.6$ the strain rate falls while $T_{zz}^{(p)}$ and $T_{rz}^{(p)}$ decay exponentially, and the latter takes small but non-negligible values.
Comparing the tangential and normal components of the inner and outer electric fields at the free surface for the Newtonian and non-Newtonian fluids, E_n^o is approximately three times larger than βE_n^i in both cases in the cone-jet transition region. This implies that the superficial charge is not fully relaxed to its local electrostatic value within that region. Regarding the outer normal component E_n^o, in the Newtonian cone-jet transition region larger values than the viscoelastic case are noticeable. This fact hints that the energy transmitted by the dominant shear electric stress to the liquid is larger in the absence of elasticity. The fact that E_n^o presents similar values in both fluids downstream, hints that the transported amount of superficial charge density is essentially the same.

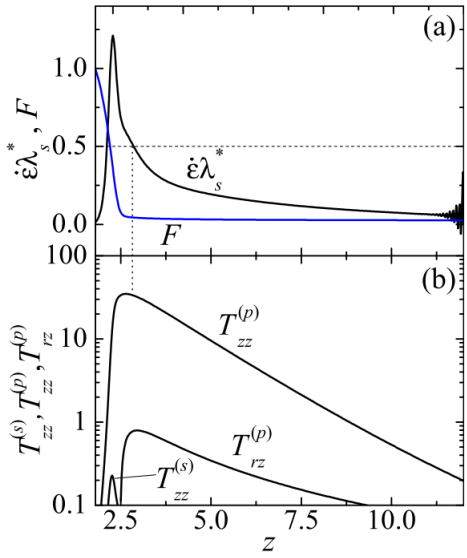

Figure 3.4: (a) Free surface position F and strain rate $\dot{\varepsilon}$ as a function of the axial position z. (b) Components $T_{zz}^{(p)}$ and $T_{rz}^{(p)}$ of the polymeric stress tensor and solvent contribution $T_{zz}^{(s)}$ as a function of the axial position z. The results were calculated for $\beta = 10$, $\delta_\mu = 2.29$, $\chi = 7.92$, $Q_r = 7.72$, $\lambda_r = 0.0926\lambda_s$ and $\lambda_s = 2.656(\lambda_s^* = 0.108)$.

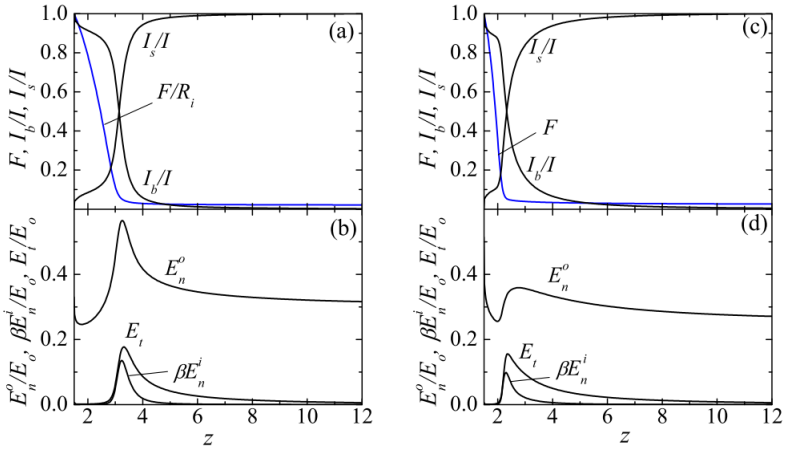

Figure 3.5: (a) and (c) Free surface position F, bulk current intensity I_b and surface current intensity I_s as a function of z. (b) and (d) Tangential E_t and normal components E_n^i and E_n^o of the inner and outer electric fields at the free surface. The results were calculated for $\beta = 10$, $\delta_\mu = 2.29$, $\chi = 7.92$, $Q_r = 7.72$, $\lambda_r = 0.0926\lambda_s$, and $\lambda_s = 0$(left) and $\lambda_s = 2.656(\lambda_s^* = 0.108)$(right)

3.6.4 1D slenderness momentum suitability

The slenderness 1-D model for the momentum equation in the z-direction:

$$\frac{\chi}{2}[(E_n^o)^2 - \beta(E_n^i)^2]_z + \chi\frac{\beta-1}{2}[(E^t)^2]_z + \frac{2\sigma E_t}{F} = (\frac{1}{F})_z + (\frac{Q^2}{2F^4})_z + \frac{6Oh_sQ}{F^2}(\frac{F_z}{F})_z + \frac{1}{F^2}[F^2(T_{rr}^{(p)} - T_{zz}^{(p)})]_z \tag{3.24}$$

, Electrostatic, polarisation, and electric tangential forces per unit volume are found on the left side of the equation, while surface tension, inertia, solvent viscosity, and polymeric stress are found on the right.

All of the contributions of the involved forces, listed below, are depicted in the figure 3.6:

- The **electric tangential force** is the most important implied force in both fluids, especially in the Newtonian case, affecting not only the emission region but also the emitted liquid thread.

- Although minor, the **electrical suction** component aids in the shaping of the cone-jet transition region to produce liquid ejection. It only prevents flow behind the cone-jet transition region in the Newtonian case.
- Two phenomena occur in both Newtonian and viscoelastic fluids when it comes to the **polarisation force**. On the one hand, the fluid is pushed forward of the cone-jet transition region, while on the other, it opposes liquid ejection behind that point.
- Analyzing the impact of the **surface tension** component, for the viscoelastic fluid constitutes the main energy sink in the cone-jet transition region. This is due to the dissolved polymers' resistance to their movement along the liquid ejection, which stretches them.
- In the non-Newtonian fluid, the **polymeric stress** exhibits a maximum absolute value larger than that of the **electric tangential force**, what provides solid evidence for the importance of polymeric axial stress even when weakly viscoelastic effects are considered.

3.6.5 Current and diameter

In the case of the diameters, the larger the value of the shear electric stress the larger the diameter of the emitted jet. Because of this, Newtonian diameters are smaller than viscoelastic ones. As can be seen in the following figure 3.7, in the Newtonian case diameters do not scale as $Q_r^{1/2}$.
On the other hand, in the case of the convected electric current, this is greater in the Newtonian case because of its velocity presents larger values than the non-Newtonian one. For the Newtonian fluid is observed that intensity values does scale as $I/I_0 \sim Q_r^{1/2}$.

3.6.6 Minimum flow rate vs stress relaxation time

This is probably one of the most interesting obtained results, because of its usage in several applications where the smallest and continuous droplets generation (or smallest jet diameter) is pursued (see figure 3.8). In the ratio $\lambda_r/\lambda_s = \mu^{(s)}/\mu_0$, the value of viscosity μ_0 was held constant in all computations. The minimum flow rate is notoriously affected by weakly viscoelastic effects. The appearance of polymeric forces in the cone-jet transition region can be interpreted as the stabiliser effect. Such polymeric forces, combined

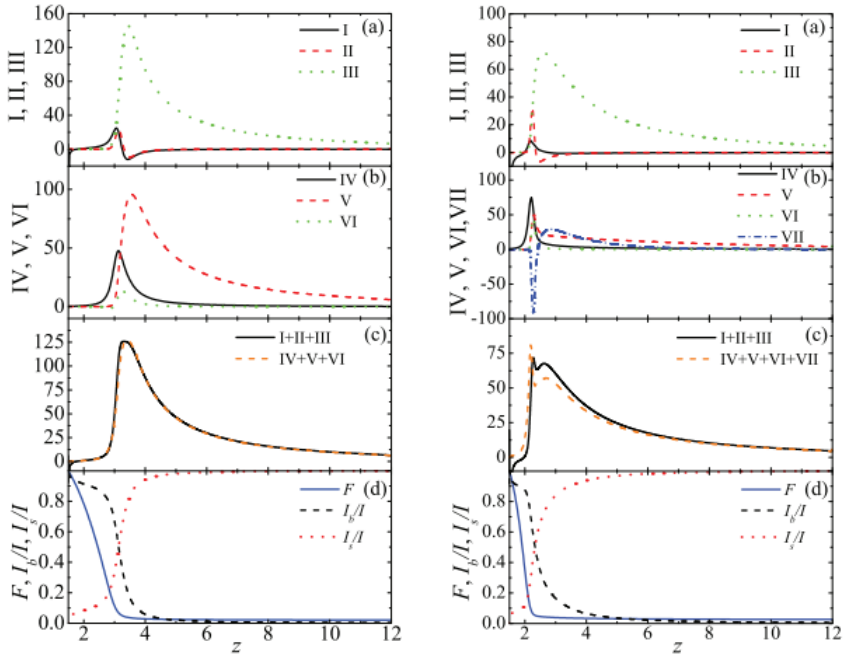

Figure 3.6: Graphs a)-c) show every force contribution of the 1D slenderness model. In the graph d) it has been plotted free surface position F, bulk current intensity I_b and surface current intensity I_s as a function of the axial position z. The shown results were calculated using $\beta = 10$, $\delta_\mu = 2.29$, $\chi = 7.92$, $Q_r = 7.72$, $\lambda_r = 0.0926\lambda_s$ and $\lambda_s = 0$ (for the left graph) and 2.656 ($\lambda_s^* = 0..108$)(right graph).

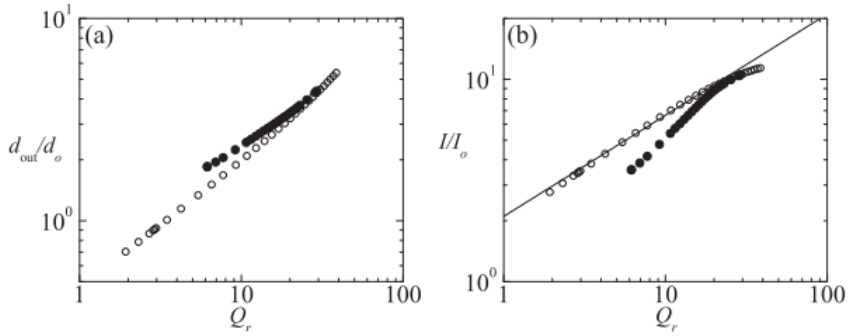

Figure 3.7: a) Jet diameter d_{out}. b) Current intensity I. Cases were computed using $\beta = 10$, $\delta_\mu = 2.29$, $\chi = 7.92$, $\lambda_r = 0.0926\lambda_s$, and $\lambda_s = 0$ for open symbols and 2.656 ($\lambda_s^* = 0.108$) for solid symbols. The line in the right graph is the law $I/I_0 = 2.1Q_r^{1/2}$.

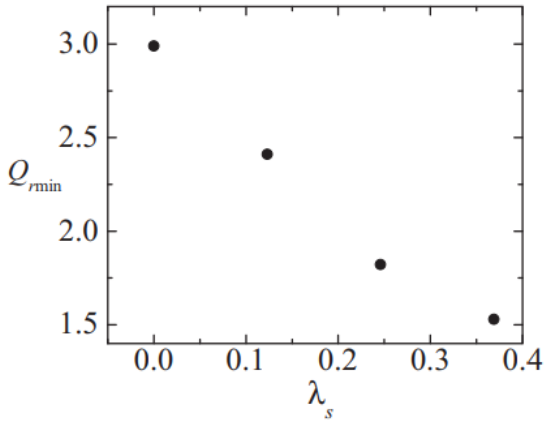

Figure 3.8: Q_{rmin}, dimensionless flow rate at the minimum flow rate stability, as a function of λ_s, the stress relaxation time. The results were obtained using $\beta = 10$, $\delta_\mu = 2.29$, $\chi = 7.92$ and $\lambda_r = 0.0926\lambda_s$.

with shear electric stress, promote liquid pushing throughout this region, assisting in overcoming resistance forces. Once this region is gone, polymers obstruct the liquid movement in the opposite direction of shear electric stress, which drives the fluid particle movement and increases its velocity.

Chapter 4

Paper II: Whipping in gaseous flow focusing

4.1 Equations

A liquid of density ρ_l and viscosity μ_l is injected through a feeding capillary of radius R_1 at a constant flow rate Q. The feeding capillary is located inside a converging-diverging nozzle at a distance H from the nozzle neck, whose diameter is D. A pressure drop Δp is applied to a gas stream of density ρ_g and viscosity μ_g. The gas stream stretches the liquid meniscus that hangs on the edge of the capillary end due to the action of the surface tension σ. In the steady jetting regime, the meniscus tip emits a liquid microjet, which crosses the nozzle coflowing with the outer gas stream.

$$\frac{(rU^{(j)})_r}{r} + \frac{V_\theta^{(j)}}{r} + W_z^{(j)} = 0 \tag{4.1}$$

$$\begin{aligned} \rho^{\delta_{jg}}(U_t^{(j)} + U^{(j)}U_r^{(j)} + V^{(j)}\frac{U_\theta^{(j)}}{r} + W^{(j)}U_z^{(j)} - \frac{V^{(j)2}}{r}) = \\ -p_r^{(j)} + \mu^{\delta_{jg}} Oh[\frac{(rU_r^{(j)})r}{r} + \\ \frac{U_{\theta\theta}^{(j)}}{r^2} + U_{zz}^{(j)} \\ -\frac{U^{(j)}}{r^2} - \frac{2V_\theta^{(j)}}{r^2}], \end{aligned} \tag{4.2}$$

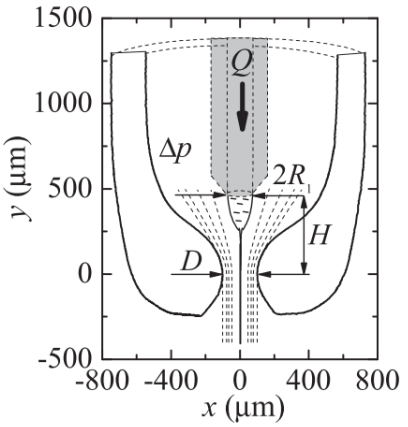

Figure 4.1: Geometry used by [1]. $R_1 \simeq 75\mu m$, $D \simeq 200\mu m$ and $H \simeq 440\mu m$.

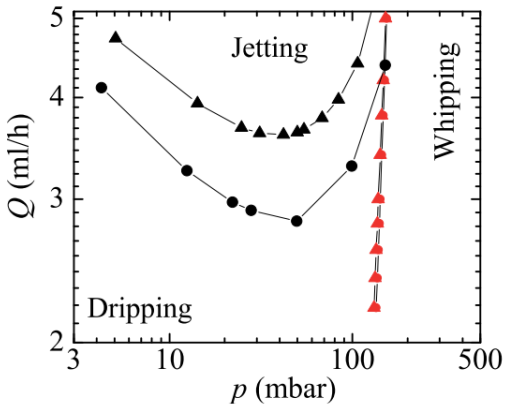

Figure 4.2: Numerical domain of the problem. The grey region shows the position of the feeding tube for $440\mu m$.

$$\rho^{\delta_{jg}}\left(V_t^{(j)}+U^{(j)}V_r^{(j)}+\frac{U^{(j)}V^{(j)}}{r}+V^{(j)}\frac{V_\theta}{r}-W^{(j)}V_z^{(j)}\right)= \\ -p_\theta^{(j)}+\mu^{\delta_{jg}}Oh[\frac{(rV_r^{(j)})r}{r}+ \\ \frac{V_{\theta\theta}^{(j)}}{r^2}+V_{zz}^{(j)}-\frac{V^{(j)}}{r^2}-\frac{2U_\theta^{(j)}}{r^2}], \tag{4.3}$$

$$\rho^{\delta_{jg}}(W_t^{(j)}+U^{(j)}W_r^{(j)}+V^{(j)}\frac{W_\theta^{(j)}}{r}+W^{(j)}W_z^{(j)}=-p_z^{(j)}+\mu^{\delta_{jg}}Oh[\frac{(rW_r^{(j)_r})}{r}+ \\ \frac{W_{\theta\theta}}{r^2}+W_{zz}^{(j)}, \tag{4.4}$$

where U, V and W stand for the three velocity components. The superscripts j denote the involved fluids (liquid and gas), while the subscripts r, t and z denote the partial derivatives respecting to each variable. p is the pressure, $\mu=\mu_g/\mu_l$ is the viscosity ratio of the fluids, $\rho=\rho_g/\rho_l$ is the density ratio of the fluids, δ_{km} is the Kronecker delta and $Oh=\mu_l(\rho_l\sigma R_1)^{-1/2}$ is the Ohnesorge number.

4.2 Boundary conditions

Kinematic compatibility condition at the free surface position $r=F(\theta,z;t)$:

$$F_t-U^{(j)}+\frac{F_\theta}{F}V^{(j)}+F_zW^{(j)}=0 \tag{4.5}$$

$$\tau_n^{(l)}=\tau_n^{(g)},\tau_{t1}^l=\tau_{t1}^g,\tau_{t2}^l=\tau_{t2}^g, \tag{4.6}$$

where $\tau_n^{(l)}$, τ_{t1}^l and τ_{t2}^l are the sum of the capillary pressure, hydrostatic pressure and viscous stress on the two sides of the free surface, and the subindexes n, t_1 and t_2 denote the normal and two tangential directions. The expressions of such stresses are given below:

$$\tau_n^{(j)} = p^{(j)} - \nabla.e_n - \frac{2\mu^{\delta_{jg}} Oh}{C_n^2}\left\{ U_r^{(j)} + F_z(F_z W_z^{(j)} - U_z^{(j)} - W_r^{(j)}) - \frac{F_\theta}{F}\left[-\frac{F_\theta}{F^2}(U^{(j)} + V_\theta^{(j)}) + \frac{U_\theta^{(j)}}{F} + V_r^{(j)} - \frac{V^{(j)}}{F} - F_z\left(V_z^{(j)} + \frac{W_\theta^{(j)}}{F} \right) \right] \right\} \tag{4.7}$$

$$\tau_{t1}^{(j)} = \frac{\mu^{\delta_{jg}} Oh}{C_n C_t}\left\{ 2F_z(U_r^{(j)} - W_z^{(j)}) + (1 - F_z^2)(W_r^{(j)} + U_z^{(j)}) - \frac{F_\theta}{F}\left[V_z^{(j)} + \frac{W_\theta^{(j)}}{F} + F_z\left(\frac{U_\theta^{(j)}}{F} + V_r^{(j)} - \frac{V^{(j)}}{F} \right) \right] \right\} \tag{4.8}$$

$$\tau_{t2}^{(j)} = \frac{\mu^{\delta_{jg}} Oh}{C_n^2 C_t}\left\{ \frac{2F_\theta}{F}\left[U_r^{(j)} - (1 + F_z^2)\frac{U^{(j)} + V_\theta^{(j)}}{F} + F_z(F_z W_z^{(j)} - U_z^{(j)} - W_r^{(j)}) \right] + \left(1 + F_z^2 - \frac{F_\theta^2}{F^2} \right)\left[\frac{U_\theta^{(j)}}{F} + V_r^{(j)} - \frac{V^{(j)}}{F} - F_z\left(V_z^{(j)} + \frac{W_\theta^{(j)}}{F} \right) \right] \right\}, \tag{4.9}$$

where C_n, C_t and C_θ are functions of the instantaneous free surface shape given by the equations:

$$C_n = \left(1 + \frac{F_\theta^2}{F^2} + F_z^2 \right)^{1/2}, C_t = (1 + F_z^2)^{1/2}, C_\theta = \left(1 + \frac{F_\theta^2}{F^2} \right)^{1/2}. \tag{4.10}$$

In addition, $e_n = \frac{1}{FC_n}[(F_\theta sin\theta + F cos\theta)e_r - (F_\theta cos\theta + F sin\theta)e_\theta - FF_z e_z]$ is the outward unit vector perpendicular to the free surface and

$$\nabla.e_n = \frac{1}{FC_n} + \frac{1}{FC_n^3}[\frac{F_\theta}{F}(\frac{F_\theta}{F} + 2F_z F_{\theta z}) - C_t^2 \frac{F_{\theta\theta}}{F} - C_\theta F F_{zz}] \tag{4.11}$$

is the local mean curvature.

Anchorage condition impossed at the edge of the feeding capillary:

$$F = 1 \tag{4.12}$$

No-slip boundary conditions on all solid surfaces:

$$v = 0 \tag{4.13}$$

Periodic boundary conditions in the angular direction are imposed for all variables.
Hagen-Poiseuille velocity distribution:

$$U^{(l)} = 0 \tag{4.14}$$

$$W^{(l)} = 2v_e(1-r^2)(v_e = Q/(\pi R_1^2 v_c)) \tag{4.15}$$

Additional considerations:

- Uniform velocity profile at the inlet sections $z = 0$ of the liquid and gas domains respectively.
- Uniform pressures at the outlet sections of the gas and liquid domains.
- The liquid outlet pressure equals that of the gas plus the capillary pressure.
- The pressure drop Δp applied to the gas stream is calculated as the difference between the value averaged over the inlet section and that imposed at the outlet section.
- The steady and axisymmetric base flow is characterized by the velocity and pressure fields $v_b(r,z) = U_b(r,z)e_r + W_b(r,z)e_z$ and $p_b(r,z)$, as well as by the distance $F_b(z)$ between a surface element and the z axis.

4.3 Dimensionless and characteristic parameters

The variables were made dimensionless with the capillary radius R_1, liquid density ρ_l and the surface tension σ leading to the definition of the characteristic time $t_c = (\rho_l R_1^3/\sigma)^{1/2}$, characteristic velocity $v_c = R_1/t_c$ and characteristic pressure $p_c = \sigma/R_1$. The velocity $v^{(j)}(r,z,\theta;t) = U^{(j)}(r,z,\theta;t)e_r + V^{(j)}(r,z,\theta;t)e_\theta + W^{(j)}(r,z,\theta;t)e_z$ and the pressure $p^{(j)}(r,z,\theta;t)$ fields verify the Navier-Stokes equations defined before.

4.4 Computational domain

The governing equations are discretized in the transformed radial direction η using n_η^l=13, n_η^g=40 Chebysheb collocation points in the liquid and gas domain respectivelly. The transformed axial direction *xi* was discretized using fourth-order finite differences and n_ξ^l=n_ξ^g=1201 equally spaced points.

4.5 Fluid properties

5-cSt silicone oil focused by air. The values of this liquid were a density $\rho_l = 917 Kg/m^3$, viscosity $\mu_l = 4.60 mPa.s$, superficial tension $\sigma = 19 mN/m$, and Ohnesorge number $Oh = 0.11$.

4.6 Results

4.6.1 Comparison with previous experiments

A more complex geometry than the proposed by [1] was studied on the experimental part of this paper by Jose María Montanero's group (UEx).

The reason for this, is to improve the focusing effect produced by the gaseous stream in the neck. Unfortunately, the mesh generation was not current enough in the solid region, so simulations were performed using [1] geometry. In this work, we investigated the similarities between the experimental results, and the results of global stability analysis obtained by our computations. For detecting the boundaries in the stability maps, the values of ΔP and Q were changed in a way that allowed the tracking of the modes, since each dominant mode exhibited similar frequency values for small changes in the physical variables. For *m=0*, keeping a given value of ΔP, Q was increased or decreased until a growth factor of zero was reached, while for *m=1* a vice versa strategy was carried out.

- Modes *m=0* y *m=1* using H=350 μm: Using this geometrical value, it was verified a good agreement between simulations and [1]'s experiments, with exception of a region of discrepancy that is attributed to an optical distortion in the measurement. Another point of disagreement was the nozzle deviation from the feeding capillary, which could be explained by the thickness of the feeding capillary versus the zero value used in the simulations. Analyzing the behaviour of these modes, it

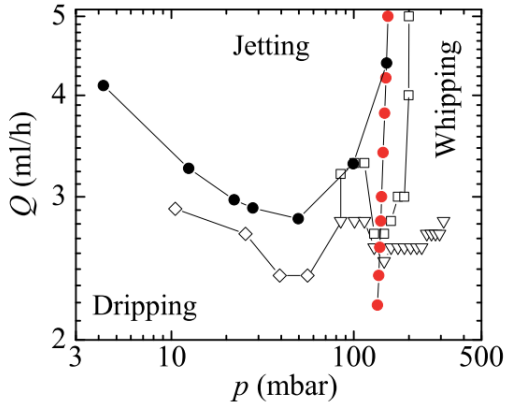

Figure 4.3: Stability map of the different regions experimentally studied by [1] using 5-cSt silicone oil. In the experiments, the open diamonds, squares, and triangles correspond to the jetting-to-dripping, jetting-to-whipping, and whipping-to-dripping transitions. The black and red solid circles show the marginally stable flows under *m=0* and *m=1* perturbations, respectively, calculated numerically for H = 350 μm.

is possible to predict jetting-to-dripping and jetting-to-whipping transitions, as well as quantify which values of Q and ΔP give rise to regions with a positive growth rate, resulting in whipping. Either decreasing the value of Q or increasing ΔP led to a more unstable *m=0* and *m=1* eigenvalue. The ΔP value was specially determinant in the jetting-to-whipping transition, for the jetting-to-dripping transition, the Q values take precedence over the effect of ΔP, which causes the transition to occur with lower or higher Q values (see figure 4.3).

- Influence of H (capillary-to-neck distance) on the global modes. $H = 350\mu m$ vs $H = 440\mu m$: As illustrated in the diagram 4.4, changes in this parameter have a significant impact on the *m=0* mode, leading to a change in the stability map. On the other hand, in the case of *m=1*, only a slight change is appreciated.

- Free surface deformation: analyzing how *m=1* was affecting to the free surface, it was shown that there is a growth when capillary distance is increased. In all analysed cases, the shape after perturbation was very similar (see figure 4.5).

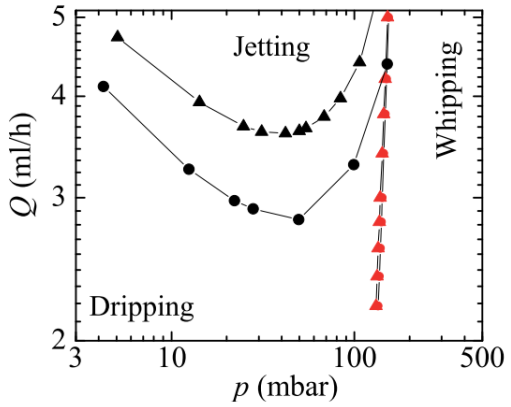

Figure 4.4: Marginally stable flows under *m=0* (black symbols) and *m=1* (red symbols) perturbations calculated numerically for 5-cSt silicone oil focused with the nozzle used by [1]. The circles and triangles correspond to H = 350 and 440 μm, respectively.

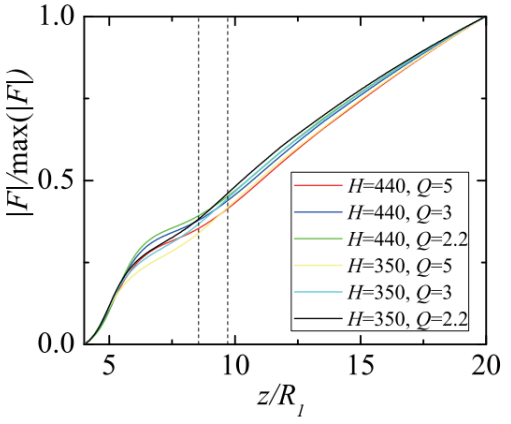

Figure 4.5: Magnitude of the free surface perturbation amplitude, $|\hat{F}(z)|$ corresponding to the mode *m=1* for the marginally stable flows in the simulations. The results were normalized using the maximum value for each case. In the labels the capillary-to-neck distance (μm) and flow rate (ml/h) are indicated. The positions of the nozzle neck are marked by dashed lines.

4.6.2 Effect of the nozzle shape

All distances were made dimensionless with the capillary radius R_1:

- Influence of the α parameter in the global stability analysis: In contrast with the influence of the H parameter, the shape in front of the neck has a strong repercussion on the emergence of whipping (m=*1*). The nozzle's shape convergence was implemented using the following formula:

$$S(z) = R_0 - (R_0 - D/2)exp[-\alpha(z - L_l)^2]. \tag{4.16}$$

  Whipping is suppressed as the convergence rate increases, which explains why whipping is rare in the classical plate-orifice configuration. As for the varicose mode, it depends on the analysed region of the stability map. For ΔP values ranging from $\Delta P \approx 70 mbar$ there is no noticeable change, but looking from this value to higher, it seems like $m = 0$ starts becoming more unstable as the convergence increases.

- Mode dominance and possible coexistence of dripping and whipping (modes interaction): If the varicose mode is dominant, the jet will eventually exhibit a dripping transition. If the whipping instability is dominant, the filament will oscillate at the free surface. According to the observed results, a dripping configuration at the jet tip may be appreciated during a whipping effect. This can occur if the growth rates of both modes reach similar levels at the same time.

- Free surface perturbation: The results (figure 4.6) show a very similar behaviour to that shown previously. In the region where $z/R_1 \approx 7.5$ differences are greater between the flow rates Q employed in the simulations.

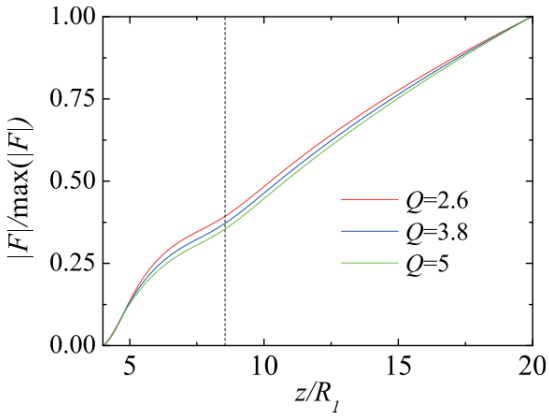

Figure 4.6: Magnitude of the free surface perturbation amplitude, $|\hat{F}(z)|$, corresponding to the mode *m=1* for the marginally stable flows in the simulations. The results have been normalised using the maximum value for each case. The labels show the flow rate in millilitres per hour. The position of the nozzle neck is indicated by the vertical dashed line.

Chapter 5

Paper III: Global stability analysis of flexible channel flow with a hyperelastic wall

5.1 Equations

A planar rigid (two-dimensional) channel of uniform internal width h is owing an incompressible Newtonian fluid. An interior section of length L is removed from the channel's rigid upper wall and replaced by a pre-tensioned elastic solid of (initially) uniform thickness e, which is subjected to a passive external gas at uniform pressure P_{ext}. The external gas load and fluid traction can both deform this elastic wall. The lengths of the rigid sections upstream and downstream of the compliant segment are L_1 and L_2, respectively. The flow is driven by a specified upstream flux q in this case, whereas the fluid pressure at the downstream end of the channel can be set to zero without losing generality (see figure 5.1).

The fluid domain Ω_1 is described by the planar coordinates $x = xe_x + ye_y$ where x parametrises the lower wall of the channel, with x = 0 at the intersection between the upstream rigid segment and the compliant segment, while y parametrises the direction normal to the entirely rigid wall pointing into the fluid (in the plane of the channel). The solid domain Ω_2 is measured relative to a reference configuration parametrised by the coordinates $X = Xe_x + Ye_y$ where X parametrises the lower surface of the wall and Y parametrises the direction pointing into the wall (in the plane of the channel).
The conservation of mass and momentum equations in the fluid (i=1) and solid

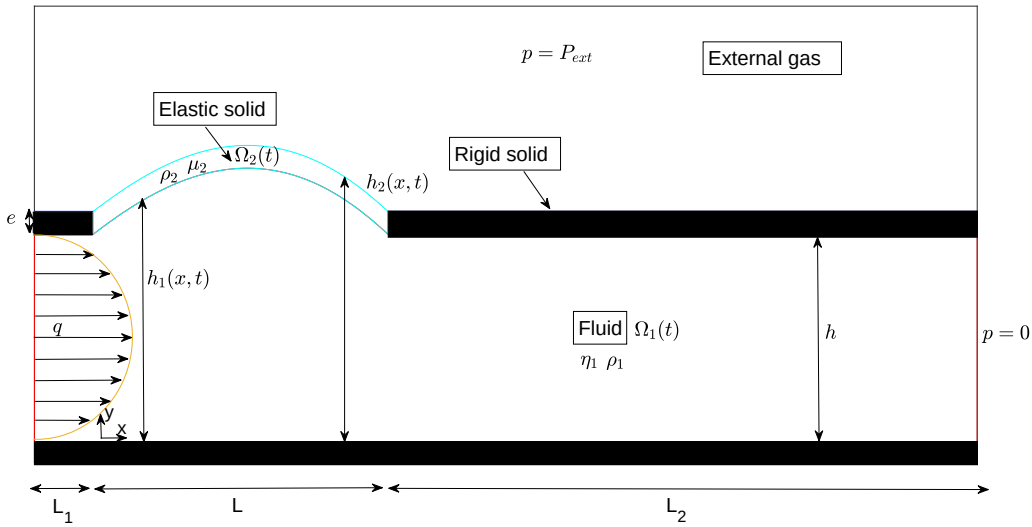

Figure 5.1: A sketch of the the geometry of the bi-dimensional channel.

(i=2) subdomains:

$$\nabla.v_i = 0 \quad (i = 1,2) \tag{5.1}$$

$$\rho_i \left(\frac{\partial v_i}{\partial t} + (v_i.\nabla)v_i \right) = \nabla.\sigma_i \quad (i = 1,2). \tag{5.2}$$

where ρ_i is the density, v_i the velocity field and σ_i is the stress tensor of material $i(i = 1,2)$.

The stress tensor for the region 1:

$$\sigma_1 = -p_1 I + \eta_1(\nabla v_1 + \nabla v_1^T) \tag{5.3}$$

where p_1 is the fluid pressure, I is the identity tensor and η_1 the fluid viscosity.

For the region 2 domain, we consider a neo-Hookean (hyperelastic) solid which has a pre-stress, $\sigma_{2p}^{(0)}$ in the initial undeformed state. The stress tensor is given by [52]

$$\sigma_2 = -p_2 I + \mu_2(F.F^T - I) + F.\sigma_{2p}^{(0)}.F^T \tag{5.4}$$

where p_2 is the solid pressure, μ_2 is the shear elastic modulus, $x(X,t)$ is the position of a material point after deformation of the solid and $F = \partial x/\partial X$ is the deformation gradient tensor. In the initial state, $x = X$ and $F.F^T = I$.
In order to make a connection between the Eularian formulation for the conservation of mass and momentum equations for the solid and the Lagrangian formulation for the elastic stress, we need to determine the deformation generated by transport by the solid velocity v_2. This is achieved using the inverse Lagrangian map $X(x,t)$ [36]:

$$\frac{\partial X}{\partial t} + v_2.\nabla X = 0 \tag{5.5}$$

satisfying that the reference coordinates are invariants under flow.
Given the bi-dimensionality of the problem the material points can be expressed in Cartesian coordinates and so the velocity vectors can be written as:

$$v_i = v_{yi}e_y + v_{xi}e_x \quad (i = 1,2) \tag{5.6}$$

while the stress tensors can be written as:

$$\sigma = \sigma_{yy}e_y \otimes e_y + \sigma_{yx}e_y \otimes e_x + \sigma_{xy}e_x \otimes e_y + \sigma_{xx}e_x \otimes e_x, \tag{5.7}$$

The deformation tensor in the solid can be written as:

$$F = \frac{\partial y}{\partial Y}e_y \otimes e_y + \frac{\partial y}{\partial X}e_y \otimes e_x + \frac{\partial x}{\partial Y}e_x \otimes e_y + \frac{\partial x}{\partial X}e_x \otimes e_x. \tag{5.8}$$

In the initial undeformed position in the solid domain exists an initial longitudinal tension T_0 that leads to an initial stress $\sigma_{2p}^{(0)} = (T_0/e)e_x \otimes e_x$.
By replacing the incompressibility equation in the solid domain based on the velocity field by an expression relating the deformation tensor F [52], we obtain:

$$\det(F) = \left(\frac{\partial y}{\partial Y}\frac{\partial x}{\partial X} - \frac{\partial y}{\partial X}\frac{\partial x}{\partial Y}\right) = 1 \tag{5.9}$$

For modeling the deformation on the solid domain, an implementation of a mapping technique based on the work of [52] was performed. The spatial domain occupied by the fluid $\Omega_1(t)$ is mapped into a rectangular domain, parametrised by Cartesian coordinates ξ_1 and χ_1 for the lower rigid wall and channel inlet:

$$y = f_1(\xi_1, \chi_1, t), \quad x = g_1(\xi_1, \chi_1, t), \quad [-L_1 \le \xi_1 \le L + L_2] \quad x \quad [0 \le \chi_1 \le 1], \tag{5.10}$$

where the shape functions f_1 and g_1 are obtained as a result of the solution of the problem. Using the quasi-elliptic transformation [17], it is possible capturing large anisotropic deformations:

$$g_{22}\frac{\partial^2 f_1}{\partial \xi_1^2} + g_{11}\frac{\partial^2 f_1}{\partial \chi_1^2} - 2g_{12}\frac{\partial^2 f_1}{\partial \xi_1 \partial \chi_1} = Q, \tag{5.11}$$

$$g_{22}\frac{\partial^2 g_1}{\partial \xi_1^2} + g_{11}\frac{\partial^2 g_1}{\partial \chi_1^2} - 2g_{12}\frac{\partial^2 g_1}{\partial \xi_1 \partial \chi_1} = Q, \tag{5.12}$$

where the coefficients take the form:

$$g_{11} = \left(\frac{\partial g_1}{\partial \xi_1}\right)^2 + \left(\frac{\partial f_1}{\partial \xi_1}\right)^2, \quad g_{22} = \left(\frac{\partial g_1}{\partial \chi_1}\right)^2 + \left(\frac{\partial f_1}{\partial \chi_1}\right)^2,$$
$$g_{12} = \frac{\partial g_1}{\partial \chi_1}\frac{\partial g_1}{\partial \xi_1} + \frac{\partial f_1}{\partial \chi_1}\frac{\partial f_1}{\partial \xi_1},$$
$$with$$
$$Q = -\left(\frac{\partial D_1}{\partial \chi_1}\frac{\partial f_1}{\partial \xi_1} - \frac{\partial D_1}{\partial \xi_1}\frac{\partial f_1}{\partial \chi_1}\right)\frac{J}{D_1}, \quad J = \frac{\partial g_1}{\partial \chi_1}\frac{\partial f_1}{\partial \xi_1} - \frac{\partial g_1}{\partial \xi_1}\frac{\partial f_1}{\partial \chi_1}, \quad and$$
$$D_1 = \varepsilon_p \sqrt{\left[\left(\frac{\partial f_1}{\partial \xi_1}\right)^2 + \left(\frac{\partial g_1}{\partial \xi_1}\right)^2\right] \Big/ \left[\left(\frac{\partial f_1}{\partial \chi_1}\right)^2 + \left(\frac{\partial g_1}{\partial \chi_1}\right)^2\right]} + (1 - \varepsilon_p). \tag{5.13}$$

where ε_p is a constant whose values are between 0 and 1 ($\varepsilon_p = 0$ corresponds to the classical elliptical transformation). In our simulations a value of $\varepsilon_p = 0.2$ was employed.

In the case of the elastic solid domain, it was mapped from an initial state Ω_{2o} and from the current state $\Omega_2(t)$ onto rectangular domains, parametrised by Cartesian coordinates ξ_2 and χ_2 for the lower surface of the flexible membrane and the edges in contact with the rigid segments of the channel, by means of non-singular mapping in the form:

$$\begin{gathered} y = f_2(\xi_2, \chi_2, t), \quad x = g_2(\xi_2, \chi_2, t), \\ Y = F_2(\xi_2, \chi_2, t), \quad X = G_2(\xi_2, \chi_2, t), \\ [0 \le \xi_2 \le L] x [0 \le \chi_2 \le 1], \end{gathered} \tag{5.14}$$

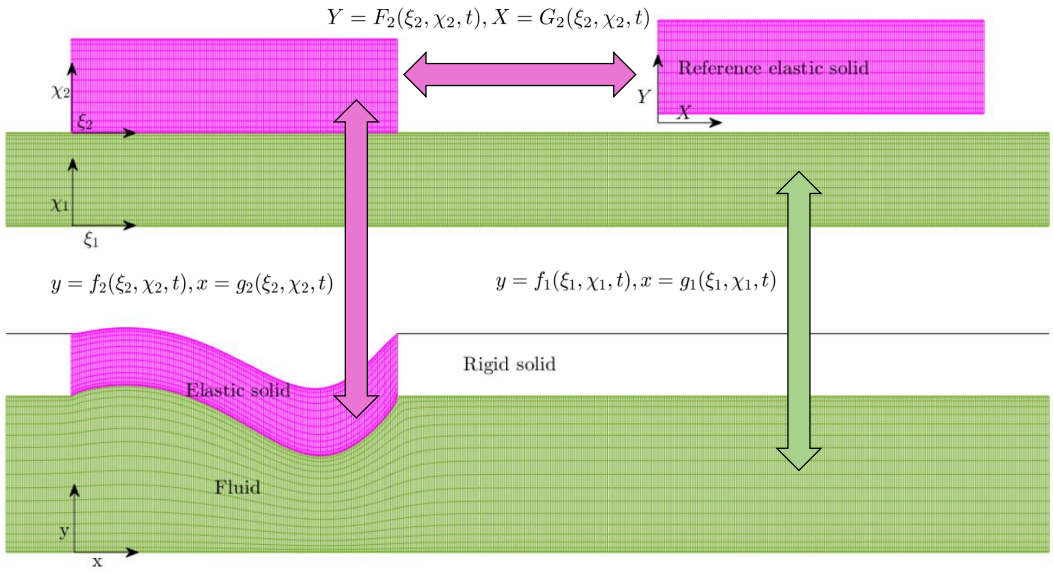

Figure 5.2: Computational domains of the problem and a sketch of the mapping technique employed in the paper.

where f_2, g_2, F_2 and G_2 are (again) obtained as a part of the solution. For computing these functions, it is necessary to use the next equations:

$$g_2 = \xi_2 \tag{5.15}$$

which ensures a direct application of the discretization used for the variable ξ_2 to the variable x, and

$$F_2 = h + e\chi_2 \tag{5.16}$$

the elastic part of the upper channel wall, at its initial state, is a rectangle of uniform width e.

$$g_1 = -L_1, \quad f_1 = h\chi_1, \quad (x = \xi = -L_1) \tag{5.17}$$

5.2 Boundary conditions

Poiseuille profile at the channel entrance, $x = -L_1$:

$$v_{1x} = \frac{6q}{h^3} y(h-y), \quad v_{1y} = 0, \quad (x = -L_1, 0 \leq y \leq h). \tag{5.18}$$

Zero fluid pressure $p_1 = 0$ at the channel exit, $x = L + L_2$. No-slip conditions along the entirely rigid wall:

$$v_{x1} = v_{y1} = 0, \quad (y = 0, -L_1 \leq x \leq L + L_2). \tag{5.19}$$

and the rigid parts of the upper wall:

$$v_{x1} = v_{y1} = 0, \quad (y = h, -L_1 \leq x \leq 0, x \geq L). \tag{5.20}$$

The flexible surface (where the elastic membrane and the fluid interact) is defined as a function of x, avoiding the surface to overturn or expand beyond the range $0 \leq x \leq L$: $y = h_1(x,t)$. Across this interface the velocity field must be continous:

$$v_{x1} = v_{x2}, \quad v_{y1} = v_{y2}, \quad (y = h_1, 0 \leq x \leq L) \tag{5.21}$$

Normal and tangential stresses between the solid and the fluid:

$$n_1.(\sigma_1 - \sigma_2).n_1 = 0, \quad t_1.(\sigma_1 - \sigma_2).n_1 = 0 \tag{5.22}$$

where:

$$n_1 = \frac{e_y - e_x h_{1,x}}{(1 + h_{1,x}^2)^{1/2}}, \quad t_1 = \frac{e_x + e_y h_{1,x}}{(1 + h_{1,x}^2)^{1/2}} \tag{5.23}$$

are normal and tangential vectors to the surface $y = h_1(x,t)$ and subscript x represents a derivative with respect to x. Imposing no deformation along the surfaces where the elastic material is clamped:

$$v_{2x} = v_{2y} = 0, \quad Y = y, \quad X = x, \quad (x = 0, x = L \quad with \quad h \leq y \leq h + e). \tag{5.24}$$

We denote the external surface of the flexible membrane as $y = h_2(x,t), (0 \leq x \leq L)$, imposing that the normal and tangencial elastic stresses are balanced with the external pressure in the form:

$$n_2.(\sigma_2 - P_{ext} I).n_2 = 0, \quad t_2.(\sigma_2).n_2 = 0 \tag{5.25}$$

where:

$$n_2 = \frac{e_y - e_x h_{2,x}}{(1 + h_{2,x}^2)^{1/2}}, \quad t_2 = \frac{e_x + e_y h_{2,x}}{(1 + h_{2,x}^2)^{1/2}} \tag{5.26}$$

are normal and tangential vectors to the surface $y = h_2(x,t)$.

The following boundary conditions are used for ensuring the correct mapping on the solid deformations by the shape functions.
At the channel entrance:

$$g_1 = -L_1, \quad f_1 = h\chi_1, \quad (x = \xi_1 = -L_1). \tag{5.27}$$

At the channel exit:

$$g_1 = L + L_2, \quad f_1 = h\chi_1, \quad (x = \xi_1 = L + L_2). \tag{5.28}$$

On the lower wall we impose:

$$g_1 = \xi_1, \quad f_1 = 0, \quad (y = \chi_1 = 0). \tag{5.29}$$

Different boundary conditions are used for the rigids parts and the flexible surface. For the rigid walls:

$$g_1 = \xi_1, \quad f_1 = h, \quad (-L_1 \leq x = \xi_1 \leq 0, x = \xi_1 \geq L, y = h). \tag{5.30}$$

whilst for the flexible segment:

$$f_1 = f_2, \quad g_1 = g_2, \quad (0 \leq x = \xi_1 = \xi_2 \leq L, y = h_1(x,t), \chi_1 = 1, \chi_2 = 0). \tag{5.31}$$

Finally, for the edges of the rectangle that are in contact with the rigid walls, clamped conditions are used, preventing deformation along the rigid wall:

$$\begin{aligned} g_2 = G_2 = \xi_2, \quad f_2 = F_2 = h + e\chi_2, \\ (x = \xi_2 = 0, x = \xi_2 = L, h \leq y \leq (h+e), 0 \leq \chi_2 \leq 1). \end{aligned} \tag{5.32}$$

5.3 Dimensionless and characteristic parameters

All lengths were made dimensionless using the channel width h, velocities on the mean inlet speed q/h, time on h^2/q, the fluid stress on the viscous scale $\eta_1 q/h^2$ and the solid stress on the elastic shear modulus μ_2. On the other hand, the solutions were characterised by the interface's dimensionless profile between the fluid and solid domains $\hat{h}_{b1} = h_{b1}/h$, the dimensionless

frequency $\hat{\omega} = \omega q/h^2$ and the dimensionless eigenfunction profile of the surface between the fluid and the solid, denoted $\widehat{\delta h_1} = (\delta h_1)/h$. The membrane's profile termed as mode-n, if $\widehat{\delta h_1}$ has n extrema across the compliant segment. The problem is ruled by six dimensionless parameters:

$$Re = \frac{\rho_1 q}{\eta_1}, \quad Q = \frac{\eta_1 q}{h^2 \mu_2}, \quad \frac{\hat{p}_{ext}}{\mu_2}, \quad \hat{T}_0 = \frac{T_0}{h\mu_2}, \quad \hat{e} = \frac{e}{h}, \quad \hat{\rho} = \frac{\rho_2 q^2}{h^2 \mu_2} \tag{5.33}$$

where Re is the Reynolds number, Q the ratio of the viscous stresses in the fluid to the elastic shear stresses in the membrane, $\hat{p}_{ext}$ the dimensionless external pressure, $\hat{T}_0$ the dimensionless longitudinal pre-tension, $\hat{e}$ the dimensionless thickness of the flexible membrane and $\hat{\rho}$ the ratio between the inertial and the elastic forces in the solid. As for geometrical factors, we used:

$$\hat{L}_1 = \frac{L_1}{h}, \quad \hat{L} = \frac{L}{h}, \quad \hat{L}_2 = \frac{L_2}{h}, \tag{5.34}$$

where $\hat{L}_1$ corresponds to the length of the upper rigid wall prior to the flexible membrane, L is the length of the flexible membrane, and $\hat{L}_2$ the length of the upper rigid wall beyond the flexible membrane.

The steady solutions were denoted by using the subscript b. The following formulas were used to calculate the minimal and maximum positions of the flexible membrane deformation:

$$\hat{h}_{min} = min_x\left(\frac{h_{1b}}{h}\right) \quad \hat{h}_{max} = max_x\left(\frac{h_{1b}}{h}\right). \tag{5.35}$$

5.4 Computational domain

Hence, for the liquid domain, the unknowns are f_1, g_1, p_1, v_{1x} and v_{1y} whilst for the solid domain the unknowns are f_2, g_2, p_2, v_{2x}, v_{2y}, F_2 and G_2. The derivates appearing in the governing equations are expressed in terms of ξ, χ and t.

The mapping is applied to the governing equations. For the χ-direction, equations are discretized using $n_{\chi 1}$ and $n_{\chi 2}$ Chebyshev spectral collocation points for both the liquid and the solid computational domain. In contrast, for the ξ-direction, fourth-order finite differences was employed, with $n_{\xi 1}$ and $n_{\xi 2}$ equally spaced points in the liquid and solid domain.

The computations were performed using the following number of nodes:
$n_{\xi 1} = 641$, $n_{\xi 2} = 201$, $n_{\chi 1} = 19$, $n_{\chi 2} = 14$.

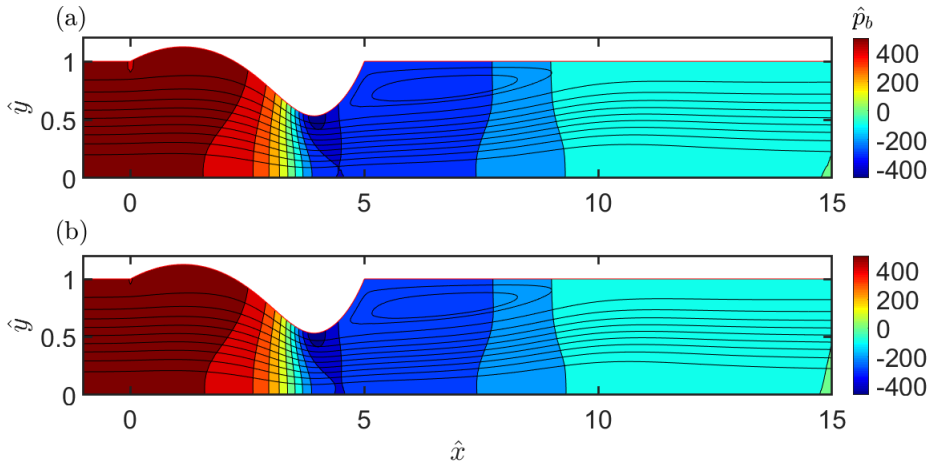

Figure 5.3: Streamlines and pressure contours for the steady solution using. a) authors' model; b) [28]'s model. $\hat{T}_0 = 10$, $\hat{e} = 0.01$, $\hat{\rho} = 0$, $Re = 500$ and $\hat{p}_{ext} = 3.204$.

5.5 Results

5.5.1 Heil's results as a benchmark

An evaluation of the precision of our numerical technique was carried out. For this purpose, we used the steady flow from [28], whose physical values were $\hat{e} = 0.01$ and $\hat{T}_0 = 10$ for the flexible membrane, $\hat{L}_1 = 1$, $\hat{L} = 5$, $\hat{L}_2 = 10$, $Q = 0.01$ (elastic stresses dominate the viscous ones).
Pressure distribution in the liquid domain, the streamlines and the flexible membrane deformation were subjected to analysis. As depicted in figures 5.3 and 5.4, a remarkable agreement was obtained, with minor differences. In figure 5.3, both of them exhibit a recirculating flow separation downstream from the collapsing membrane.

The second comparison was the minimum $\hat{h}_{min}$ and maximum $\hat{h}_{max}$ membrane's position values. For sufficiently large Reynolds numbers, the system admits multiple steady solutions at the same point in the parameter space. In our study, this resulted in three Branches labelled I, II and III, connected by two limit points namely *folding points* (starting-ending points that delimit the frontier between branches of steady solutions) (see figure 5.4).
For computatiing each Branch and its *folding points*, different strategies were followed. For Branches I and III, from initial cases with sufficiently low and

large $\hat{p}_{ext}$ values, respectively, increments (for Branch I) and decrements (for Branch III) were performed until the solutions from the other Branch were detected by monitoring the values of $\hat{h}_{max}$ and $\hat{h}_{min}$ and an abrupt change in the values was observed. For the Branch II steady solutions, an initial case was obtained using a constant $\hat{p}_{ext}$ value while decreasing $\hat{T}_0$ from a high value. A quantitative comparison of the $\hat{h}_{min}$ values for Branch II and III was made by changing the $\hat{p}_{ext}$ values for $Re = 500$ and $Re = 250$. Both showed a very good agreement, with exception of small differences for the higher $\hat{p}_{ext}$ region (see 5.4).

The definition of the applied pre-stress to the flexible membrane was different from [28]. We defined this dimensionless parameter as σ_0, which is directly related to our model through $\sigma_0 = \frac{\hat{T}_0}{\hat{e}}$ (i.e. for a value of $\sigma_0 = 1000$ we used values of $\hat{T}_0 = 10$ and $\hat{e} = 0.01$). All the simulations concerning to this part were performed without considering inertial effects ($\hat{\rho} = 0$).

For cases with a Reynolds number larger that a certain value, namely Re_{cusp}, [28] stated a region that allows the co-existence of multiple steady solutions for the same parameter values (see figure 5.5).

In order to obtain the value of Re_{cusp}, the $\hat{p}_{ext}$ values for each Branch were monitored, detecting the *folding points* of Branches I and III for each Re value (see figure 5.6). This was first performed using large values of Re, and decreasing in each iteration, until the *folding point* of each Branch collapsed in a $\hat{p}_{ext}$ value. It was assessed that starting from a $Re \approx 330$, multiple solutions can be obtained in a range of $\hat{p}_{ext}$ values. In figure 5.6 we can see not only the zone of solution multiplicity, but also the region of stability when self-excited oscillations begin to emerge in the system.

The *folding points* were named as $\hat{p}_{ext1}$ for the limit of the Branch I solutions, and $\hat{p}_{ext2}$ for those solutions of the Branch III. If the $\hat{p}_{ext} > \hat{p}_{ext}1$, the channel will suffer a catastrophic collapse jumping from Branch I to III, whereas for values $\hat{p}_{ext} < \hat{p}_{ext2}$ the channel will recover from the collapsed state, jumping from Branch III into Branch I steady solutions. Figure 5.7 shows a transition from Branch I to III, by increasing incrementally the value of $\hat{p}_{ext}$ from 1.52 to 1.54.

During the collapse of the channel, a boundary layer separation at the end of the flexible membrane is noticeable. A supplementary video showing the process can be reached out at: https://researchdata.gla.ac.uk/1113/. This phe-

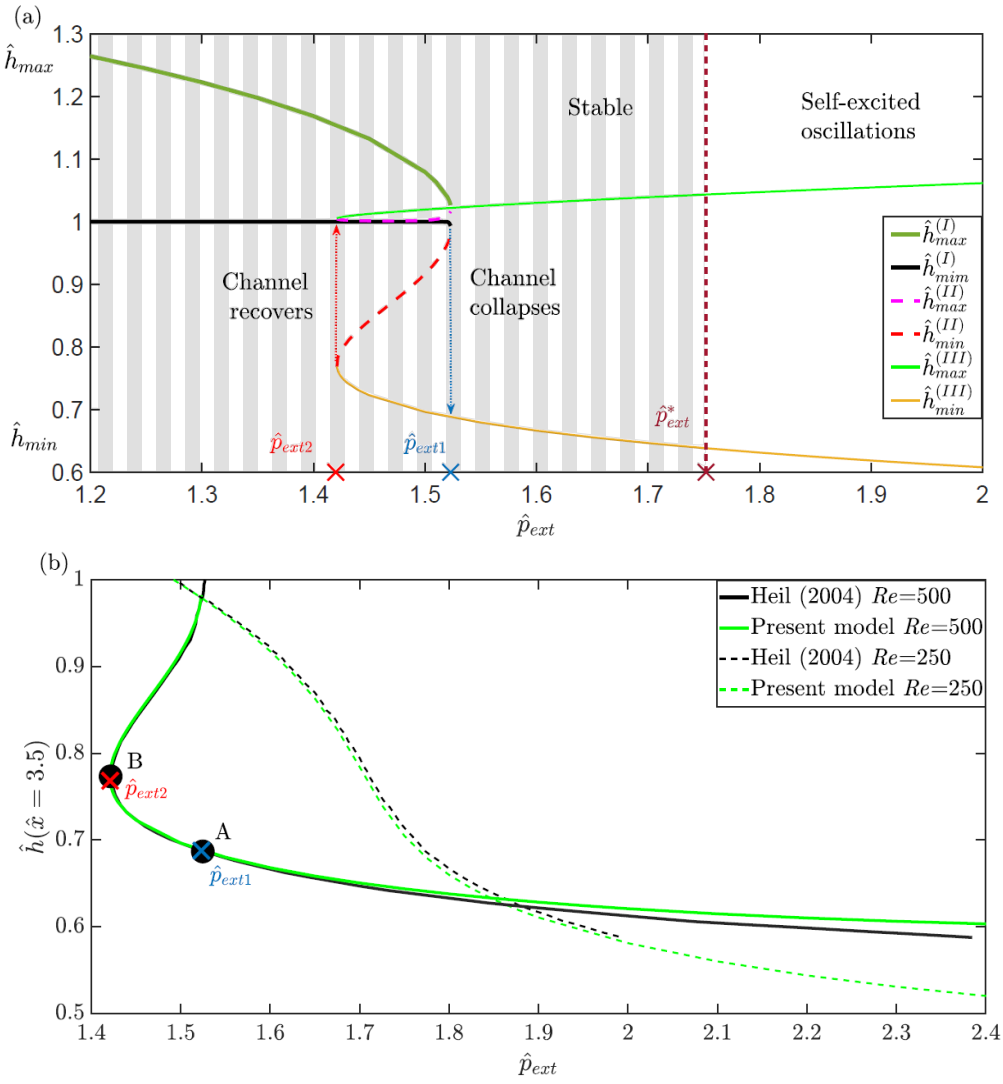

Figure 5.4: a) Maximum ($\hat{h}_{max}$) and minimum ($\hat{h}_{min}$) spatial point of the flexible membrane vs $\hat{p}_{ext}$. *Folding points* are reached for $\hat{p}_{ext1} = 1.52$ for Branch I and $\hat{p}_{ext2} = 1.42$ for Branch III. b)Precision assessment using [28]'s results. Black circles represent [28]'s *folding points* and crosses paper results $\hat{T}_0 = 10$, $\hat{e} = 0.01$ and $\hat{\rho} = 0$.

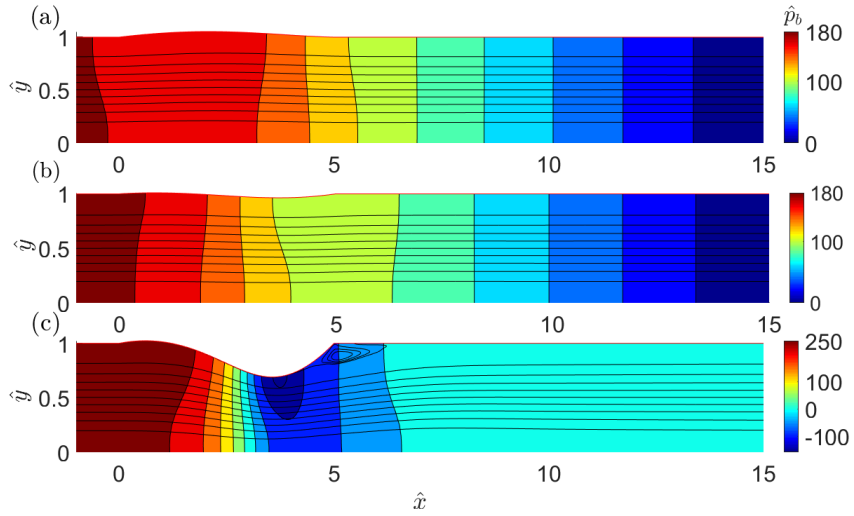

Figure 5.5: An example of multiplicity of solutions. Streamlines and pressure distribution $\hat{p}_b$ inside the channel a) Branch I. b) Branch II. c) Branch III. $\hat{T}_0 = 10$, $\hat{e} = 0.01$, $\hat{\rho} = 0$ and $Re = 500$.

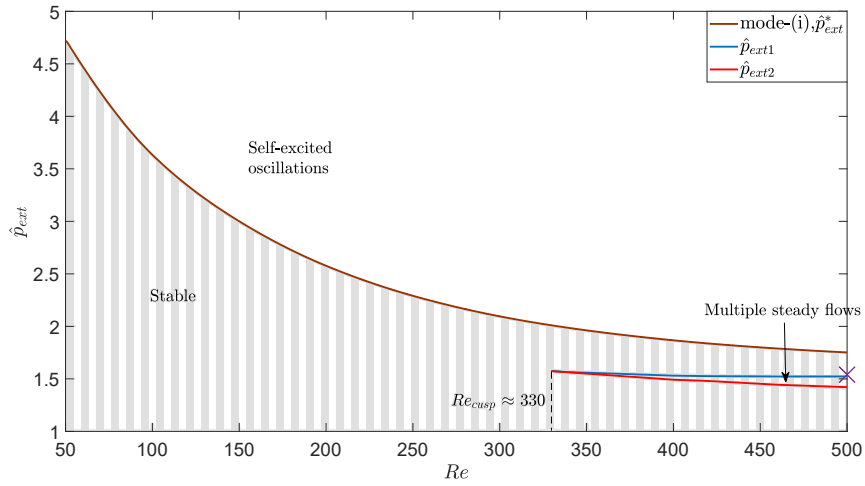

Figure 5.6: Stability analysis along with the representation of multiplicity of solutions starting from a certain value of Re (Re_{cusp}) and within a range of $\hat{p}_{ext}$. The cross at the lower right part indicates the case employed for the boundary layer separation analysis. $\hat{e} = 0.01$, $\hat{\rho} = 0$ and $\hat{T}_0 = 10$.

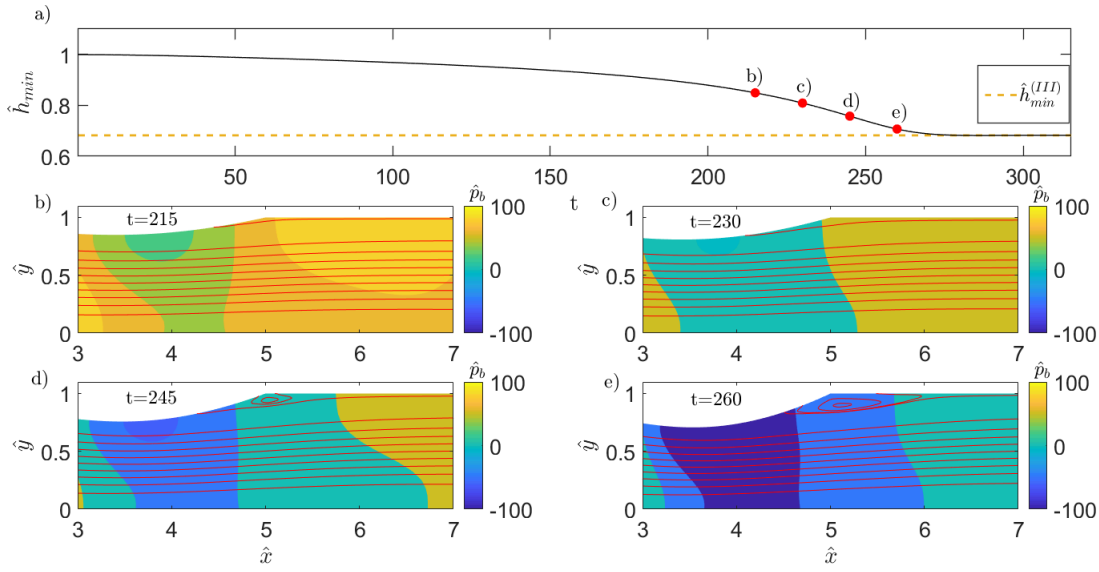

Figure 5.7: Streamlines and pressure contours. a) Timeline representing the evolution of the minimum point ($\hat{h}_{min}$) in the flexible membrane. Red circles from b) to e) hint the cases below. At time $t \approx 230$ boundary layer separation takes place. $\hat{T}_0 = 10$, $\hat{e} = 0.01$, $\hat{\rho} = 0$ and $Re = 500$.

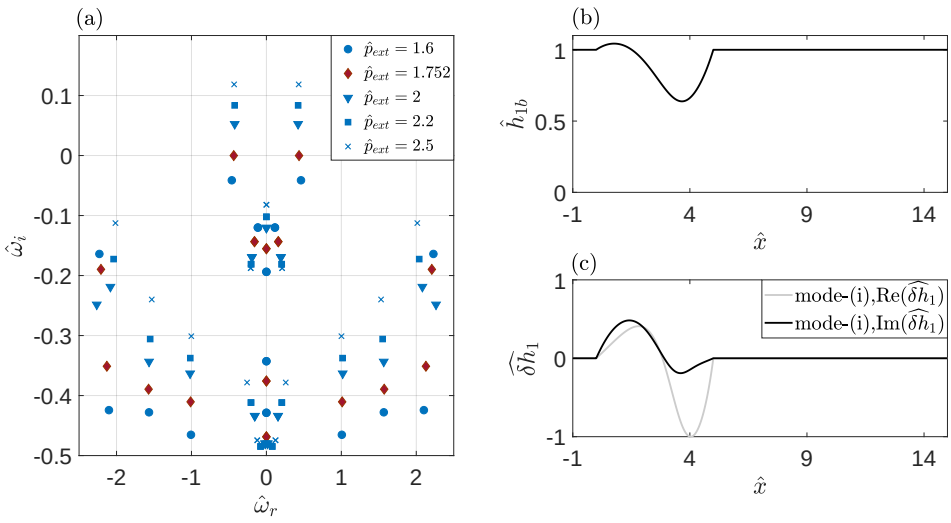

Figure 5.8: a) Eigenvalues spectrum of the global stability analysis. Stability limit is denoted by red diamonds. b) Shape of the interphase. c) Eigenfunction representation for $\hat{p}_{ext} = 1.752$, $\hat{T}_0 = 10$, $\hat{e} = 0.01$, $Re = 500$.

nomenon is similar to vortex breakdown in swirling flows in pipes [38, 31], where also bifurcation diagrams can be employed to describe multiple steady solutions. Since all the computed solutions from the Branch I were stables for $\hat{p}_{ext} > 0$, the $\hat{p}^*_{ext}$ curve was defined by performing the global stability analysis from the Branch III steady solutions.

In figure 5.8, eigenvalues spectrum allows to track the transition from stable to unstable state in the global stability analysis, as $\hat{p}_{ext}$ increases.

5.5.2 Effect of longitudinal pre-stress ($\hat{T}_0$) on the flexible membrane

In this section, we studied the effect of applying a lower value of pre-stress $\hat{T}_0 = 5$ on the membrane, while keeping a width value of $\hat{e} = 0.01$. Figure 5.9 summarizes the main obtained results:

- As Re increases, the unstable region for Branch III steady solutions expands, and the $\hat{p}^*_{ext}$ curve almost overlaps the boundary of the multiplicity solutions region $\hat{p}_{ext1}$.

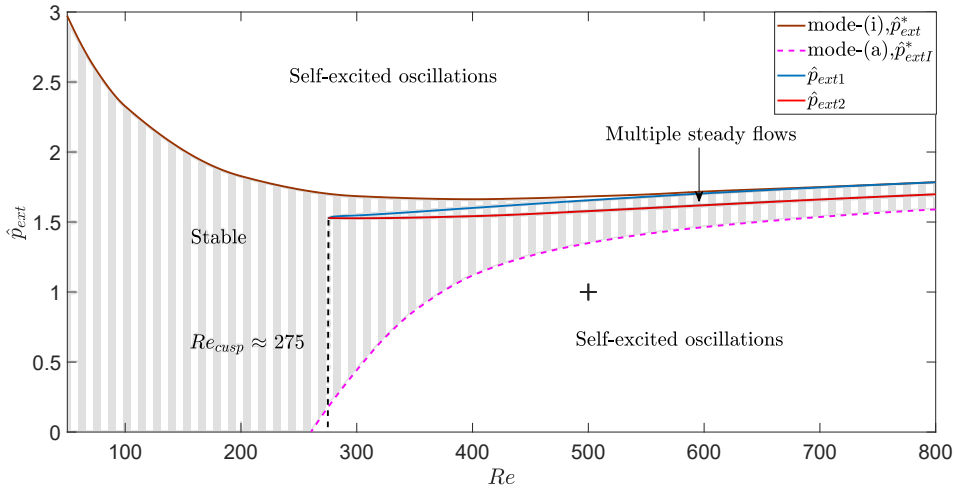

Figure 5.9: Stability analysis along with the representation of multiplicity of solutions from a certain value of Re (Re_{cusp}) and within a range of $\hat{p}_{ext}$. Unlike the previous graph, for sufficiently small value of $\hat{T}_0$ a stability region delimited by $\hat{p}^*_{extI}$ appears. $\hat{e} = 0.01$, $\hat{\rho} = 0$ and $\hat{T}_0 = 5$.

- Branch I introduces a new unstable region, where the system exhibits self-excited oscillations when $\hat{p}_{ext}$ falls below a external pressure value $\hat{p}^*_{extI}$ for a given Re (see figures 5.9 and 5.10).

- Re_{cusp} appears sooner ($Re_{cusp} \approx 275$), leading to an expansion of the multiple steady solutions.

Analyzing the membrane's profile along with the eigenfunctions for the case of neutral stability: $\hat{p}_{ext} = 1.12$, $Re = 400$ and $\hat{T}_0 = 5$ (Branch I), although the membrane was inflated with a simple hump (mode-1) at neutral stability, the eigenfunction was mode-2, which was similar to that of the Branch III (see figure 5.11). This might be related to the specified upstream flux, which suppresses modes that induce large volume changes in the flexible membrane.

The study of limit cycles was another intriguing aspect of Branch I instabilities. This occurred when the $\hat{p}_{ext}$ values fell below a critical threshold ($\hat{p}^*_{extI}$) for a given Re number, away from the upper branch (Branch I) limit point and the region of multiple steady states. Using the values of $Re = 500$, $\hat{p}_{ext} = 1$ and $\hat{T}_0 = 5$, the system's behaviour in the instability region was studied, including the propagation of the hump(s) downstream and upstream along

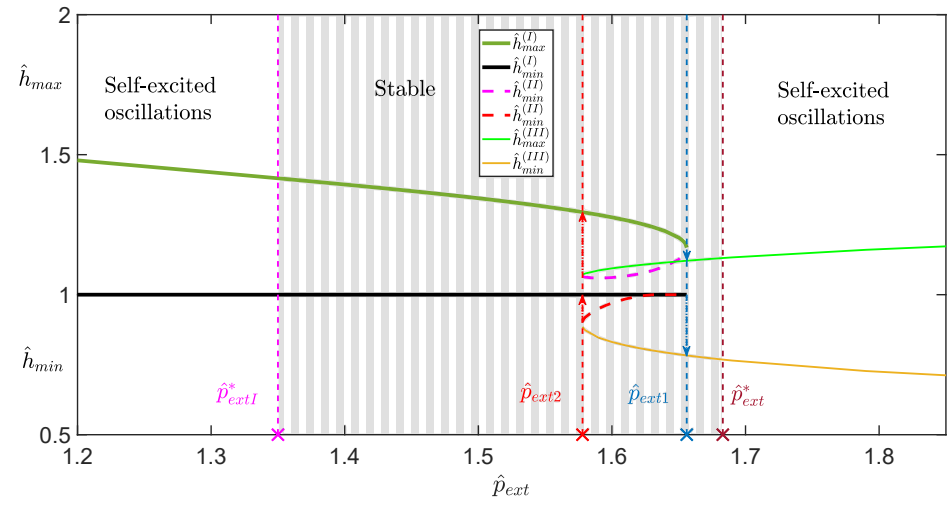

Figure 5.10: Representation of the three Branches. Stability regions are delimited by dashed lines and the *folding points* are marked as $\hat{p}_{ext1}$ for branch I and $\hat{p}_{ext2}$ for branch III respectively.

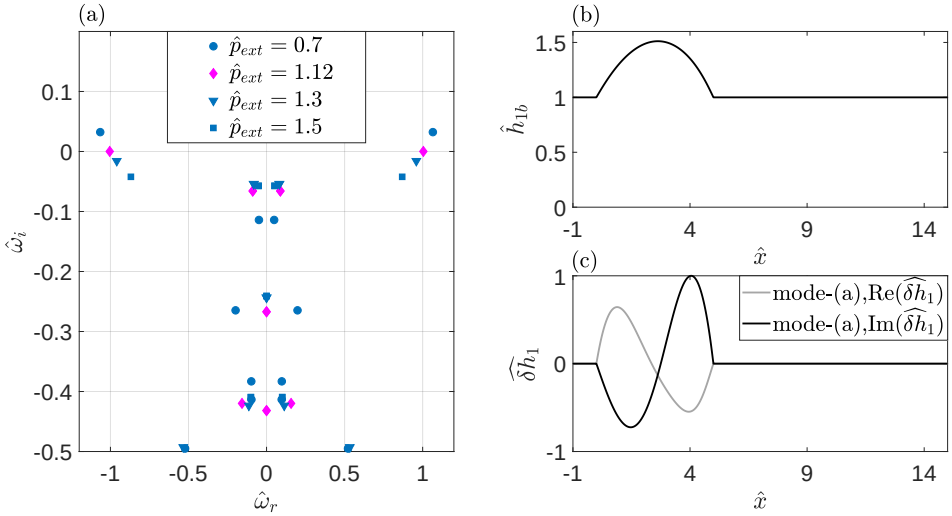

Figure 5.11: Effect of $\hat{p}_{ext}$ on mode-(i). a) Global stability analysis using different values of $\hat{p}_{ext}$. Magenta diamonds depict the marginally stable case. b) Interphase shape. c) Eigenfunction for the case with $\hat{p}_{ext} = 1.12$, $\hat{e} = 0.01$, $\hat{\rho} = 0$ and $\hat{T}_0 = 5$.

the cycle, changes in amplitude, and the shedding of a low pressure vortex close to the downstream rigid segment, which resulted in a vorticity wave (see figure 5.12).

5.5.3 Influence of the membrane's thickness

The dimensionless thickness $\hat{e}$ of the flexible membrane not only has an effect on the global stability of steady solutions, but also on physical parameters such as the $\hat{h}_{min}$ and $\hat{v}_{max} = max_{x,y}(\hat{v}_{1xb})$. For this purpose, we employed fixed values of pre-tension, external pressure and Reynolds number: $\hat{T}_0 = 5$, $\hat{p}_{ext} = 2.98$ and $Re = 50$. This parameter values correspond to a case that is globally unstable (see figure 5.11). As seen in the figure 5.13, the value of $\hat{h}_{min}$ below 1 hints that the channel is collapsed. Increasing the thickness value decreases the $\hat{v}_{max}$ in the channel while the value of $\hat{h}_{min}$ increases.
Increasing the thickness value from $\hat{e} = 0.01$ to $\hat{e} = 2$, is noticeable how as the $\hat{e}$ values become larger, the stable region is reached at a critical value of $\hat{e} \gtrsim 0.08$, and the resonance frequency $\hat{\omega}_r$ starts dropping.

Using a pre-tension value of $\hat{T}_0 = 5$ stability curves for five different values of $\hat{e}$ were obtained,allowing the influence on global stability to be more clearly recognised. For small changes in $\hat{e}$ non-significant changes were reported, but as this value increases and becomes on the order of the channel width ($\hat{e} \sim 1$), the behaviour begins to change noticeably as shown in figure 5.14. For a value of $\hat{e} = 2$, the values of critical $\hat{p}^*_{ext}$ and $\hat{\omega}_r$ saturate as the Reynolds number increases.

5.5.4 The influence of membrane's inertia

We used the same values of pre-tension, external pressure, and Reynolds number to quantify the impact of inertia on global stability: $\hat{T}_0 = 5$, $\hat{p}_{ext} = 2.98$ and $Re = 50$. By continuity, every mode was tracked as the value of $\hat{\rho}$ increased. The analysis reported four different modes as shown in the figure 5.15, with mode-(iv) having the highest resonance frequency $\hat{\omega}_r$. Different values for dominance and frequency were obtained. It was concluded that an increase in membrane inertia resulted in the destabilisation of higher-frequency modes of instability, which eventually dominated the primary global instability as this parameter becomes larger.

A second approach involved the tracking the system's modes, by smoothly changing Re and $\hat{p}_{ext}$ values for different fixed values of $\hat{\rho}$ ($\hat{\rho}$=0,10,50). As

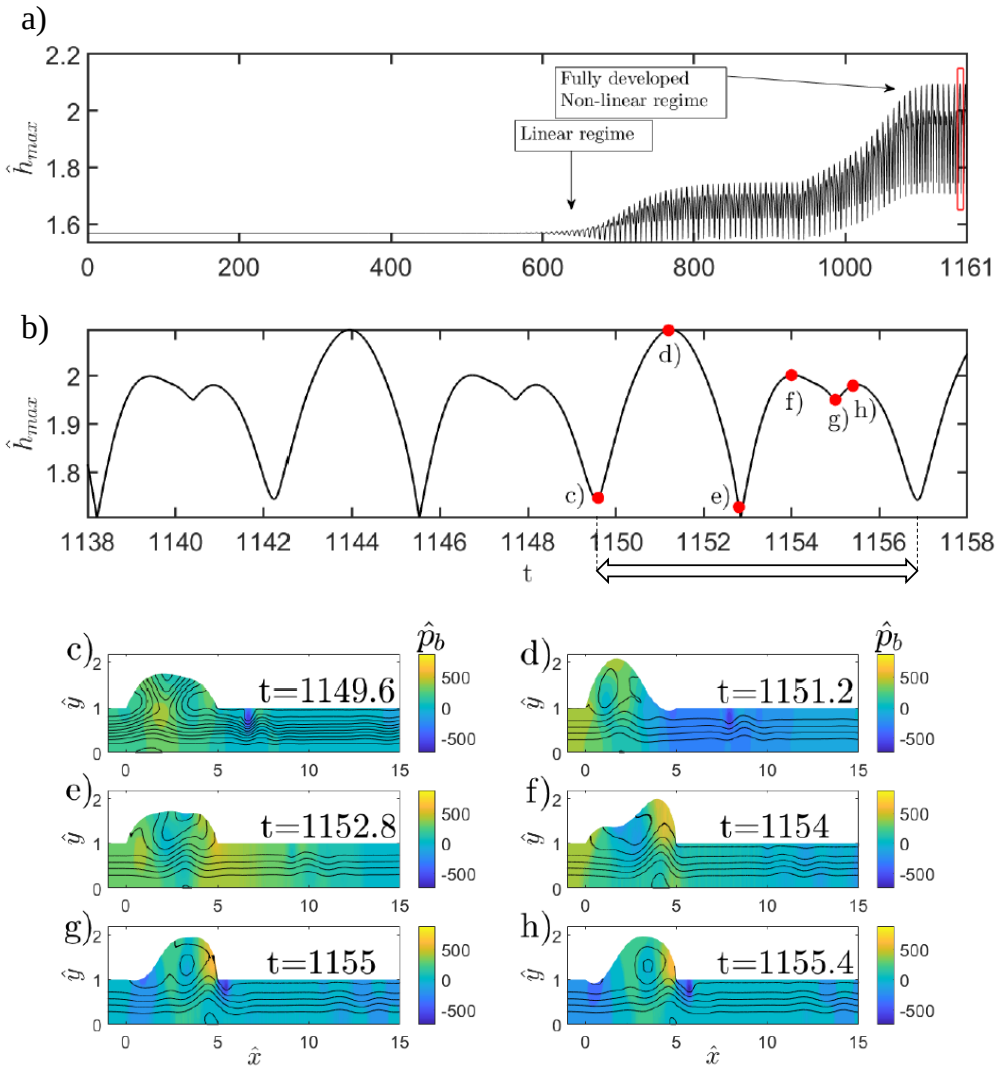

Figure 5.12: a) Representation of the system's evolution from linear regime until to fully developed non-linear regime. b)-h) A time window representing the deformation on the solid and liquid domains for a limit cycle, depicted on a) with a red rectangle. $Re = 500$, $\hat{p}_{ext} = 1$ and $\hat{T}_0 = 5$.

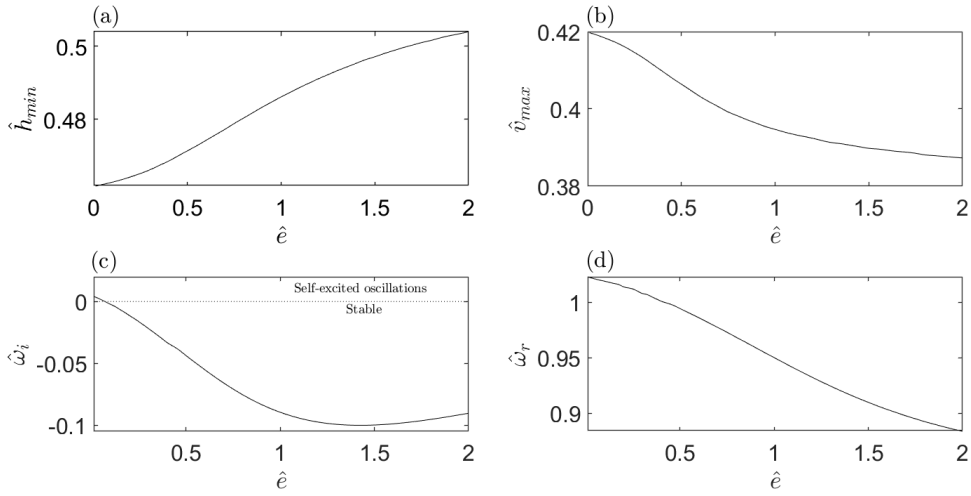

Figure 5.13: Effect of thickness $\hat{e}$ without considering inertial effects ($\hat{\rho} = 0$), for a case with $\hat{T}_0 = 5$, $\hat{p}_{ext} = 2.98$ and $Re = 50$.

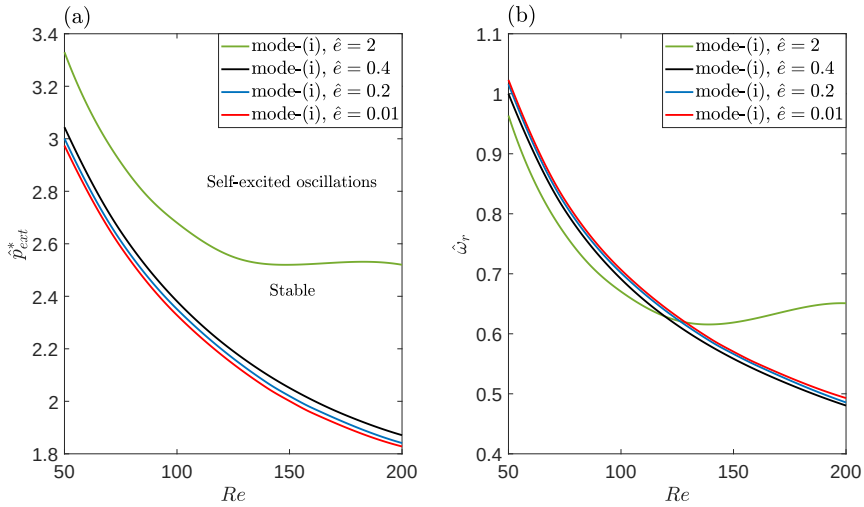

Figure 5.14: Effect of thickness on mode-(i). a) Stability regions. b) Eigenfrequency values.

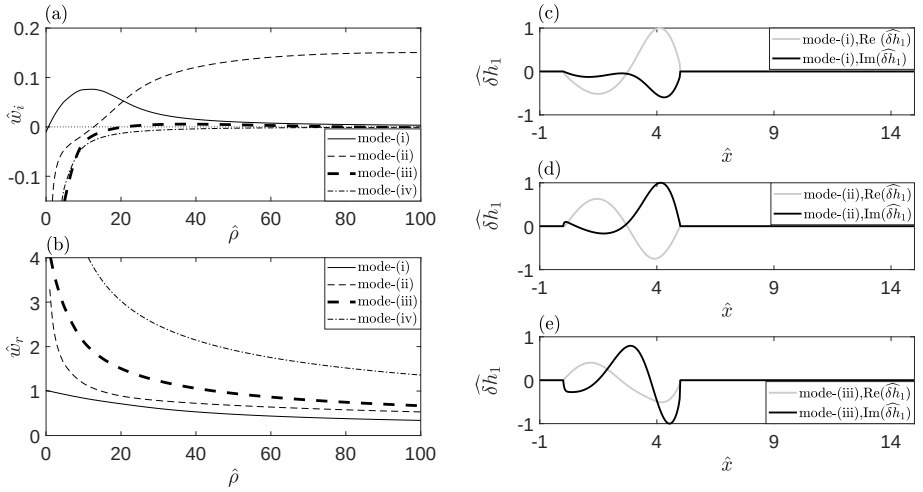

Figure 5.15: Effect of inertia on system's modes. a) Stability regions. b) Eigenfrequency values. c)-e) Eigenfunctions for modes i-iii.

the membrane's inertia increases, the mode-(i) instability region expands, and high frequency modes of instability emerge. Figure 5.16 shows the changes in the stability regions for each inertia value.

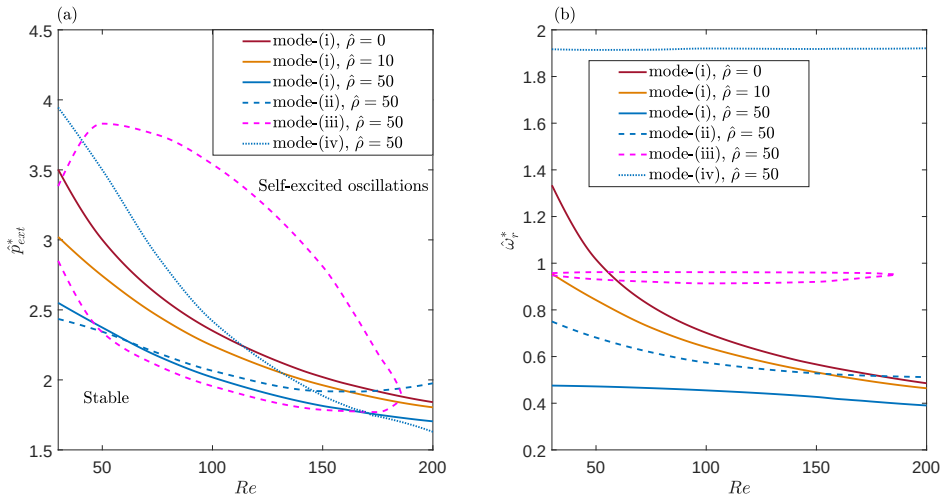

Figure 5.16: Effect of inertia on the system's modes. a) Stability regions. b) Frequency values.

Chapter 6

Conclusions and future work

6.1 Paper I: Electrospray cone-jet mode for weakly viscoelastic liquids

6.1.1 Conclusions

- When the stress relaxation time is of the order of the residence time in the cone-jet region, fluid particles undergo an extensional deformation in that region that is intense enough to cause the dissolved polymers to stretch continuously, preventing relaxation to the coiling state. As a result, the axial polymeric stress becomes much greater than that produced by the solvent viscosity. This axial stress pulls from the liquid, causing it to accelerate much faster than in the Newtonian case. The electrified liquid meniscus contracts as a result of the sudden acceleration. Because the kinetic energy gained by the meniscus from the stretching polymers is lost in the jet region, where they eventually coil, axial polymeric stress does not play a significant role in the final energy balance.

- The shrinkage of the meniscus reduces the outer normal component of the electric field over the free surface while increasing the resistance force provided by surface tension and viscosity in the cone-jet transition region. These effects work together to reduce the speed of the emitted jet in comparison to the Newtonian case.

- The current intensity transported by the viscoelastic liquid is much lower than that calculated in the Newtonian simulation, especially at low flow rates. The fact that the liquid gains kinetic energy from polymeric stress

in the most unstable region seems to explain why the minimum flow rate stability limit is decreasing.

- When a small amount of polymer is added to a Newtonian solvent, the liquid undergoes two significant changes: on the one hand, when fluid particles are deformed at a high enough rate, polymeric stresses form. The zero-shear viscosity, on the other hand, rises.

- The presence of long polymeric chains strongly aligned with the flow is the molecular source of anisotropy, which causes the liquid mechanical response to be non-Newtonian.

6.1.2 Future work

Two factors influence stretching on the cone-jet transition region in viscoelastic liquids: the emergence of Deborah numbers on the order of unity in liquids with stress relaxation times as short as hundreds of microseconds; and the influence of electrical conductivity on both the stretching rate (increases) and the residence time (decreases). The study of the rheological properties of weakly viscoelastic liquids and the performance of a comparison between numerical calculations and laboratory data obtained by observing the slenderness of the viscoelastic meniscus is an intriguing future approach. Such experimental data would be obtained by measuring the fluid's relaxation time.

6.2 Paper II: Whipping in gaseous flow focusing

6.2.1 Conclusions

- The capillary-to-neck distance affects the jetting-to-dripping transition but has no effect on the whipping instability under the conditions considered in [1]. We also investigated the effect of nozzle shape on jetting stability.

- The nozzle convergence rate was studied, which is defined as the inverse of the distance along which the diameter decreases to its smallest value. Whipping is suppressed as the convergence rate increases, which explains why it is much less common in the classical plate-orifice configuration [22].

- The stability map is highly dependent on many parameter conditions, making it impossible to draw broad conclusions. For example, under the conditions considered, the capillary-to-neck distance seems to have no effect on whipping instability.

- The liquid viscosity eliminates the whipping instability and enables the jetting regime for $Q \approx 10$ ml/h.

- The shape of the nozzle's converging part has a significant impact on the response of the liquid jet far away from the discharge orifice. This last result can be explained if we assume that convective whipping occurs due to convection and amplification of lateral waves emitted by small-amplitude oscillations of the liquid meniscus rather than wind-induced destabilisation of the jet downstream. Overall, we can probably conclude that ejector shapes closer to the plate-orifice configuration produce less whipping.

6.2.2 Future work

Although a region of stability for *m=2* was not found in this paper, it may be possible to observe its influence in the fluid jet and even its interactions with modes *m=0* and *m=1* by employing new geometries in the computational domain.

6.3 Paper III: Global stability analysis of flexible channel flow with a hyperelastic wall

6.3.1 Conclusions

- The current implementation overcomes the limitations of other models (elastic shell or membrane) by allowing a non-singular mapping of hyperelastic domain deformation using thicker values for the deformable solid based on Arbitrary Lagrangian-Eularian (ALE). All fields are solved at the same time, resulting in a fully implicit method.

- The model predicts that at least one steady solution will exist for all parameter values. A region of three coexisting solutions will appear for Reynolds numbers greater than Re_{cusp}. Such solutions are linked by a pair of limit points that delimit the transitions between upper and lower

branches, resulting in the channel's collapse or recovery. There is an intriguing analogy between these outcomes and those reported by [38, 31] in swirling flows in pipes and open jets [51].

- In the case of the lower branch, sufficiently large values of Re and external pressure $\hat{p}_{ext}$ cause the system to become unstable. In the case of the upper branch, if the pre-tension value falls low enough, a stability region appears in which external pressure values below a critical point cause self-excited oscillations.

- The fully developed limit cycle exhibits a hump propagating upstream along the deformable segment interacting with the flow imposed upstream, and then being reflected by the rigid segment upstream. The flow then sheds a low pressure vortex, allowing a vorticity wave to enter the downstream rigid segment.

- Analyzing the thickness of the wall without inertia revealed no significant changes in either the steady solutions or the oscillations until the thickness of the compliant segment approaches the channel width. From this point critical pressure is reached at higher values for the same Re, whilst critical frequency values drop. For the maximum thickness considered in our study ($\hat{e} = 2$) both values saturate from a Reynolds number large enough.

- The dimensionless inertia parameter $\hat{\rho}$ describes the strength of the wall inertia compared to the internal elastic stress and an eigen-frequency of the elastic wall compared to the characteristic (inverse) time scale of the flow past the elastic wall. Increasing this parameter not only expands the region of self-excited oscillations, but also promotes the emergence of high frequency modes, which eventually dominate the primary global instability.

6.3.2 Future work

Our hyperelastic definition is based on first-order elasticity, so that the stress is proportional to the gradient of the strain energy function with respect to the strain tensor, and imposing lateral boundary conditions of no displacement along the face of the elastic solid in contact with the rigid wall. It should be noted that our methodology cannot reproduce an elastic beam's resistance to bending because it would require strain gradient (second-order) elasticity, in

which the stress exhibits additional contributions due to the derivative of the strain energy function with respect to the strain gradient tensor. This method necessitates the addition of new boundary conditions, such as enforcing the gradient of the profile at the rigid segment edges.
A 3D collapsible channel model is currently being investigated. This new configuration considers pre-tension over the flexible membrane using two components: longitudinal and perpendicular to the channel. Another innovative aspect is the use of lateral perturbation modes for the global stability analysis of this new setup.

Chapter 7

Bibliography

Bibliography

[1] AJ Acero et al. “Focusing liquid microjets with nozzles”. In: *Journal of Micromechanics and Microengineering* 22.6 (2012), p. 065011.

[2] Seema Agarwal, Joachim H Wendorff, and Andreas Greiner. “Use of electrospinning technique for biomedical applications”. In: *Polymer* 49.26 (2008), pp. 5603–5621.

[3] Gregory H Altman et al. “Silk-based biomaterials”. In: *Biomaterials* 24.3 (2003), pp. 401–416.

[4] Ricardo Armentano et al. “Effects of hypertension on viscoelasticity of carotid and femoral arteries in humans”. In: *Hypertension* 26.1 (1995), pp. 48–54.

[5] Ricardo Luis Armentano et al. “Arterial wall mechanics in conscious dogs: assessment of viscous, inertial, and elastic moduli to characterize aortic wall behavior”. In: *Circulation research* 76.3 (1995), pp. 468–478.

[6] CD Bertram, CJ Raymond, and KSA Butcher. “Oscillations in a collapsed-tube analog of the brachial artery under a sphygmomanometer cuff”. In: (1989).

[7] CD Bertram and J Tscherry. “The onset of flow-rate limitation and flow-induced oscillations in collapsible tubes”. In: *Journal of fluids and structures* 22.8 (2006), pp. 1029–1045.

[8] Christopher D Bertram. “Flow-induced oscillation of collapsed tubes and airway structures”. In: *Respiratory physiology & neurobiology* 163.1-3 (2008), pp. 256–265.

[9] S Blanco-Trejo et al. “Electrospray cone-jet mode for weakly viscoelastic liquids”. In: *Physical Review E* 100.4 (2019), p. 043114.

[10] S Blanco-Trejo et al. “Whipping in gaseous flow focusing”. In: *International Journal of Multiphase Flow* 130 (2020), p. 103367.

[11] Sunil Kumar Boda, Xiaoran Li, and Jingwei Xie. “Electrospraying an enabling technology for pharmaceutical and biomedical applications: A review”. In: *Journal of aerosol science* 125 (2018), pp. 164–181.

[12] Sunica ani et al. “Modeling viscoelastic behavior of arterial walls and their interaction with pulsatile blood flow”. In: *SIAM Journal on Applied Mathematics* 67.1 (2006), pp. 164–193.

[13] Henry N Chapman et al. “Femtosecond X-ray protein nanocrystallography”. In: *Nature* 470.7332 (2011), pp. 73–77.

[14] LMG Chavas, L Gumprecht, and HN Chapman. “Possibilities for serial femtosecond crystallography sample delivery at future light sources”. In: *Structural Dynamics* 2.4 (2015), p. 041709.

[15] Arianna De Mori et al. “3D printing and electrospinning of composite hydrogels for cartilage and bone tissue engineering”. In: *Polymers* 10.3 (2018), p. 285.

[16] DP DePonte et al. “Gas dynamic virtual nozzle for generation of microscopic droplet streams”. In: *Journal of Physics D: Applied Physics* 41.19 (2008), p. 195505.

[17] Yannis Dimakopoulos and John Tsamopoulos. “A quasi-elliptic transformation for moving boundary problems with large anisotropic deformations”. In: *Journal of Computational Physics* 192.2 (2003), pp. 494–522.

[18] Cevat Erisken, Dilhan M Kalyon, and Hongjun Wang. “Viscoelastic and biomechanical properties of osteochondral tissue constructs generated from graded polycaprolactone and beta-tricalcium phosphate composites”. In: *Journal of biomechanical engineering* 132.9 (2010).

[19] Juhana Frösen. “Flow dynamics of aneurysm growth and rupture: challenges for the development of computational flow dynamics as a diagnostic tool to detect rupture-prone aneurysms”. In: *Trends in Cerebrovascular Surgery* (2016), pp. 89–95.

[20] T Funada and DD Joseph. “Viscoelastic potential flow analysis of capillary instability”. In: *Journal of non-newtonian fluid mechanics* 111.2-3 (2003), pp. 87–105.

[21] KJ Gaffney and Henry N Chapman. “Imaging atomic structure and dynamics with ultrafast X-ray scattering”. In: *science* 316.5830 (2007), pp. 1444–1448.

[22] Alfonso M Gañán-Calvo. “Generation of steady liquid microthreads and micron-sized monodisperse sprays in gas streams”. In: *Physical review letters* 80.2 (1998), p. 285.

[23] Alfonso M Gañán-Calvo and José M Montanero. “Revision of capillary cone-jet physics: Electrospray and flow focusing”. In: *Physical review E* 79.6 (2009), p. 066305.

[24] Chris Gisriel et al. “Membrane protein megahertz crystallography at the European XFEL”. In: *Nature communications* 10.1 (2019), pp. 1–11.

[25] Melville S Green and Arthur V Tobolsky. “A new approach to the theory of relaxing polymeric media”. In: *The Journal of chemical physics* 14.2 (1946), pp. 80–92.

[26] AL Gregory, Anurag Agarwal, and Joan Lasenby. “An experimental investigation to model wheezing in lungs”. In: *Royal Society open science* 8.2 (2021), p. 201951.

[27] James B Grotberg and Oliver E Jensen. “Biofluid mechanics in flexible tubes”. In: *Annu. Rev. Fluid Mech.* 36 (2004), pp. 121–147.

[28] Matthias Heil. “An efficient solver for the fully coupled solution of large-displacement fluid–structure interaction problems”. In: *Computer Methods in Applied Mechanics and Engineering* 193.1-2 (2004), pp. 1–23.

[29] Matthias Heil and Tim J Pedley. “Large post-buckling deformations of cylindrical shells conveying viscous flow”. In: *Journal of Fluids and Structures* 10.6 (1996), pp. 565–599.

[30] MA Herrada and José M Montanero. “A numerical method to study the dynamics of capillary fluid systems”. In: *Journal of Computational Physics* 306 (2016), pp. 137–147.

[31] MA Herrada, M Pérez-Saborid, and A Barrero. “Vortex breakdown in compressible flows in pipes”. In: *Physics of fluids* 15.8 (2003), pp. 2208–2218.

[32] Miguel A Herrada et al. “Liquid flow focused by a gas: Jetting, dripping, and recirculation”. In: *Physical Review E* 78.3 (2008), p. 036323.

[33] Miguel Angel Herrada et al. “Global stability analysis of flexible channel flow with a hyperelastic wall”. In: *Journal of Fluid Mechanics* 934 (2022).

[34] Jing Huang, Vasileios Koutsos, and Norbert Radacsi. “Low-cost FDM 3D-printed modular electrospray/electrospinning setup for biomedical applications”. In: *3D printing in medicine* 6.1 (2020), pp. 1–7.

[35] RD Kamm and TJ Pedley. “Flow in collapsible tubes: a brief review”. In: (1989).

[36] Ken Kamrin, Chris H Rycroft, and Jean-Christophe Nave. “Reference map technique for finite-strain elasticity and fluid–solid interaction”. In: *Journal of the Mechanics and Physics of Solids* 60.11 (2012), pp. 1952–1969.

[37] Werner Kuhn. “Über die gestalt fadenförmiger moleküle in lösungen”. In: *Kolloid-Zeitschrift* 68.1 (1934), pp. 2–15.

[38] JM Lopez. “On the bifurcation structure of axisymmetric vortex breakdown in a constricted pipe”. In: *Physics of Fluids* 6.11 (1994), pp. 3683–3693.

[39] XY Luo and TJ Pedley. “A numerical simulation of unsteady flow in a two-dimensional collapsible channel”. In: *Journal of Fluid Mechanics* 314 (1996), pp. 191–225.

[40] José M Montanero and Alfonso M Ganán-Calvo. “Dripping, jetting and tip streaming”. In: *Reports on Progress in Physics* 83.9 (2020), p. 097001.

[41] Juan Fernandez de la Mora et al. “Electrochemical processes in electrospray ionization mass spectrometry”. In: *Journal of Mass Spectrometry* 35.8 (2000), pp. 939–952.

[42] Lakshmi S Nair and Cato T Laurencin. “Biodegradable polymers as biomaterials”. In: *Progress in polymer science* 32.8-9 (2007), pp. 762–798.

[43] Tsutomu Nakada et al. “Aquaporin-4 functionality and Virchow-Robin space water dynamics: physiological model for neurovascular coupling and glymphatic flow”. In: *International Journal of Molecular Sciences* 18.8 (2017), p. 1798.

[44] Richard Neutze et al. “Potential for biomolecular imaging with femtosecond X-ray pulses”. In: *Nature* 406.6797 (2000), pp. 752–757.

[45] James G Oldroyd. “On the formulation of rheological equations of state”. In: *Proceedings of the Royal Society of London. Series A. Mathematical and Physical Sciences* 200.1063 (1950), pp. 523–541.

[46] Frank Otto. “Die grundform des arteriellen pulses”. In: *Zeitung fur Biologie* 37 (1899), pp. 483–586.

[47] A Ponce-Torres et al. “The steady cone-jet mode of electrospraying close to the minimum volume stability limit”. In: *Journal of Fluid Mechanics* 857 (2018), pp. 142–172.

[48] Lord Rayleigh. “On the instability of jets”. In: *Proceedings of the London mathematical society* 1.1 (1878), pp. 4–13.

[49] Michael Renardy and Becca Thomases. “A mathematicians perspective on the Oldroyd B model: Progress and future challenges”. In: *Journal of Non-Newtonian Fluid Mechanics* 293 (2021), p. 104573.

[50] Eric K Shang et al. “Use of computational fluid dynamics studies in predicting aneurysmal degeneration of acute type B aortic dissections”. In: *Journal of vascular surgery* 62.2 (2015), pp. 279–284.

[51] Vladimir Shtern and Fazle Hussain. “Hysteresis in swirling jets”. In: *Journal of Fluid Mechanics* 309 (1996), pp. 1–44.

[52] JH Snoeijer et al. “The relationship between viscoelasticity and elasticity”. In: *Proceedings of the Royal Society A* 476.2243 (2020), p. 20200419.

[53] Peter S Stewart, Sarah L Waters, and Oliver E Jensen. “Local and global instabilities of flow in a flexible-walled channel”. In: *European Journal of Mechanics-B/Fluids* 28.4 (2009), pp. 541–557.

[54] Nico Westerhof, Jan-Willem Lankhaar, and Berend E Westerhof. “The arterial windkessel”. In: *Medical & biological engineering & computing* 47.2 (2009), pp. 131–141.

[55] John Zeleny. “The electrical discharge from liquid points, and a hydrostatic method of measuring the electric intensity at their surfaces”. In: *Physical Review* 3.2 (1914), p. 69.

Chapter 8

Published Papers

8.1 Paper I: Electrospray cone-jet mode for weakly viscoelastic liquids

Authors:
Sergio Blanco Trejo, Miguel Ángel Herrada, Alfonso Miguel Gañán Calvo, and Jose María Montanero.

Paper published in:
Physical Review E Vol. 100 Iss. 4-October 2019
DOI: https://doi.org/10.1103/PhysRevE.100.043114

Electrospray cone-jet mode for weakly viscoelastic liquids

S. Blanco-Trejo, M. A. Herrada, and A. M. Gañán-Calvo
Escuela Técnica Superior de Ingenieros, Universidad de Sevilla, Avda. de los Descubrimientos s/n, E-41092-Sevilla, Spain

José M. Montanero
Departmento de Ingeniería Mecánica, Energética y de los Materiales and Instituto de Computación Científica Avanzada (ICCAEx), Universidad de Extremadura, Avda. de Elvas s/n, E-06071 Badajoz, Spain

(Received 29 May 2019; published 28 October 2019)

We study theoretically the influence of viscoelasticity on the steady cone-jet mode of electrospray for small stress relaxation times. For this purpose, we numerically integrate the leaky-dielectric model together with the Oldroyd-B constitutive relationship and calculate both the base flow and linear eigenmodes characterizing its stability as a function of the governing parameters. We describe the effect of the polymeric stresses on both the cone-jet mode and the minimum flow rate stability limit. There are considerable differences between the Newtonian and viscoelastic electrospray realizations even for relatively small stress relaxation times due to the intense extensional deformation suffered by the fluid particles in the cone-jet transition region The axial polymeric stress shrinks the liquid meniscus and stabilizes it by pushing the fluid particle in the cone-to-jet transition region.

DOI: 10.1103/PhysRevE.100.043114

I. INTRODUCTION

Electrospinning of polymer solutions is a widely used technique for the fabrication of polymer fibers with diameters ranging from tens of microns down to a few nanometers [1]. Several medical areas, like tissue engineering or drug delivery [2], benefit from this technique. Electrospinning produces nanofibers with specific photonic, electronic, magnetic and photocatalytic properties demanded in a number of technical fields. Areas like textile and filter applications have benefited from electrospinning as well [3].

Despite its wide applicability, the liquid ejection in electrospinning is far from being fully understood. Most theoretical studies are based on the 1D (slenderness) approximation for the axial momentum equation [4,5], which allows for a simple description of the balance between the forces driving and opposing the liquid motion. Carroll and Joo [6] conducted a "hybrid" local-global linear stability analysis for low-conductivity viscoelastic liquids in which the axially non-uniform base flow was numerically calculated from the 1D model, and was perturbed with normal modes. The analysis was subsequently extended to highly-conducting polymer solutions [7]. If the stress relaxation time is large enough for the polymer coil-stretch transition to take place in the unperturbed state, then the axisymmetric mode drastically stabilizes. This mode has a capillary and electrical origin for low and high conductivities, respectively. Dharmansh and Chokshi [8] conducted the global linear stability analysis of a low-conductivity Newtonian jet in the framework of the 1D model too. They showed the stabilizing effect of the jet thinning, and attributed that effect to both the variation of the surface charge density and the extensional deformation rate in the base flow. Similar conclusions were obtained when rheological effects were considered [9]. To the best of our knowledge, there is neither analytical nor numerical 2D (axisymmetric) solution of the cone-jet mode in electrospinning. The calculation of the scaling laws for the jet diameter and current intensity commonly applied in electrospray of Newtonian liquids [10] does not have its counterpart in electrospinning either.

Weakly viscoelastic polymer solutions with quasimonodisperse molecular weight distributions exhibit a constant viscosity μ_0 over a wide interval of shear rates (shear thinning can be neglected) and elastic properties that can be approximately quantified by a single characteristic relaxation time $\widetilde{\lambda}_s$ [11]. The Oldroyd-B model [12] is one of the simplest approximations for calculating the total extra stress tensor of this type of non-Newtonian liquids because it assumes a linear relationship between the polymer stress and conformation tensor, and a linear relaxation law for the latter. This simplicity, and the fact that it can be derived from kinetic theory for a fluid filled with elastic beads and spring dumbbells [13], has conferred remarkable popularity upon this model [14]. One of its fundamental limitations is the fact that it does not take into account the finite extensibility of the polymers, and, therefore, it cannot describe phenomena like the appearance of blistering in capillary thinning [15,16].

The Taylor-Melcher leaky-dielectric model [17,18] has been successfully applied to the description of the steady cone-jet mode of electrospray [19–22]. In this approximation, the net free charge accumulates within a very thin Debye layer formed at the free surface, which collects free charge from the bulk at a rate given by a constant electrical conductivity. A natural question is whether this last condition still holds under the anisotropic conditions arising in electrospray with polymer solutions. In this case, the electrical conductivity probably becomes a non-uniform tensorial quantity related to the local value of the polymer conformation tensor, which

accounts for the expected difference between the electrical resistivity along the radial and axial directions of electrospray. Given the absence of experimental measurements to support this or any other correlation, researchers have simply extended the Newtonian leaky-dielectric model to the viscoelastic case by replacing the Newtonian constitutive relationship by the Oldroyd-B or FENE-P model [4,5,9].

The cone-jet mode of electrospray is intrinsically unstable because the breakup of the emitted jet into drops is always an energetically favorable process. The question is whether one can identify a fluid domain portion, which includes an ejected thread long as compared to its diameter, where the flow remains essentially steady. The most accurate approach to address this question is the global linear stability analysis [23]. In this analysis, one asks the system whether small-amplitude perturbations introduced at a given instant in the considered fluid domain decay asymptotically on time in the Eulerian frame of reference. For this purpose, one firstly calculates the axisymmetric stationary solution $U_0(r,z)$ framed within the considered fluid domain, and then obtains the global modes

$$\left\{\delta U^{(k)}(r,z)\,\exp\left[i\left(m\theta-\omega_m^{(k)}t\right)\right]\right\}\quad (k=1,2,\ldots,N)\quad (1)$$

of that base flow. Here, the symbol U represents any hydrodynamic quantity, r and z are the cylindrical coordinates (z is the symmetry axis), and $\omega_m^{(k)}=\omega_{mr}^{(k)}+i\omega_{mi}^{(k)}$ is the eigenfrequency characterizing the temporal evolution of the linear mode with azimuthal number m. If all the growth factors $\{\omega_{mi}^{(k)}\}$ are negative, then any perturbation decays for long times, and the base flow is asymptotically stable [23]. The linear superposition of decaying modes excited by a given perturbation may lead to the short-term growth of that perturbation. In some cases, this effect can destabilize an asymptotically stable flow [24], as occurs in gaseous flow focusing [25]. However, this possibility has not been observed in Newtonian electrospray, where the minimum flow rates predicted by the global stability analysis agree fairly well with the experimental values [21]. Therefore, it is reasonable to identify asymptotic stability with linear stability in the weakly viscoelastic case too.

This work can be regarded as a first attempt to extend the 2D numerical analyses of electrospray for Newtonian liquids [19–22] to weakly viscoelastic fluids. We will study how elasticity influences the flow pattern, meniscus shape, superficial electric field, and both driving and resistant forces arising in the cone-jet mode of electrospray. We will examine the effect of elasticity on the linear stability of this mode under axisymmetric $m=0$ perturbations.

II. THE CONE-JET MODE OF ELECTROSPRAY

To gain insight into the time and spatial scales characterizing the weakly viscoelastic electrospray, we here borrow some well-established results from the Newtonian case. The parameters which essentially characterize the steady cone-jet mode of electrospray are the issued flow rate Q and both the liquid and outer environment properties. The properties of a leaky-dielectric Oldroyd-B liquid are the density ϱ, (zero-shear) viscosity μ_0, stress (polymer) relaxation time $\widetilde{\lambda}_s$, retardation time $\widetilde{\lambda}_r$, surface tension γ, electrical permittivity ε_i, and electrical conductivity K. As can be seen, we assume that the presence of macromolecules does not significantly alter the isotropic character of electric conduction. This approximation applies to viscoelastic solutions whose molecular composition leads to significant mechanical anisotropy but quasi-isotropic ionic diffusion. If the outer environment is either vacuum or a gas, then its dynamical effect on the liquid can be neglected, and the only parameter characterizing its electrical influence is its permittivity ε_o.

There is a narrow interval of the applied voltage V within which the steady cone-jet mode can be established. For this reason, and as a first approximation, one does not regard this quantity as a governing parameter. In the steady cone-jet mode, conduction gives way to dominant charge convection over the liquid surface within the so-called cone-jet transition region [10]. Forces driving and opposing the fluid motion emerge in this critical region, whose size is typically much smaller than that of the electrospray device. Due to the local character of electrospray, the device geometrical features and associated lengths play a secondary role in this phenomenon.

Under the above conditions, one defines the characteristic radial length $d_o=[\gamma\varepsilon_o^2/(\rho K^2)]^{1/3}$, axial velocity $v_o=[\gamma K/(\rho\varepsilon_o)]^{1/3}$, electric relaxation time $t_o=\varepsilon_i/K$, electric field $E_o=(\gamma^2\rho K^2/\varepsilon_o^5)^{1/6}$ and current intensity $I_o=\gamma\rho^{-1/2}\varepsilon_o^{1/2}$ in terms of the electrodynamic properties of the fluids exclusively. Five dimensionless parameters can be formed with the first three characteristic quantities introduced above and the liquid density and viscosity: the relative permittivity $\beta=v_o t_o/d_o=\varepsilon_i/\varepsilon_o$, the electrohydrodynamic Reynolds number $\delta_\mu=\rho v_o d_o/\mu_0=[\gamma^2\rho\varepsilon_o/(\mu^3 K)]^{1/3}$, the dimensionless stress relaxation time $\lambda_s=\widetilde{\lambda}_s/t_o=\widetilde{\lambda}_s/(\beta d_o/v_o)$, the dimensionless retardation time $\lambda_r=\widetilde{\lambda}_r/\widetilde{\lambda}_s$, and the relative flow rate $Q_r=Q/Q_o$, where $Q_o=v_o d_o^2=\gamma\varepsilon_o/(\rho K)$.

The characteristic axial length L of the cone-jet transition region in Newtonian electrospray can be estimated as $L\sim d_o Q_r$ [10], while the liquid velocity in that region scales as v_o. Therefore, the residence time t_r in the cone-jet transition region scales as $t_r\sim L/v_o\sim d_o Q_r/v_o$. The fluid particle accelerates from a negligible velocity up to the jet speed $v_j\sim v_o$ within the cone-jet transition region. Therefore, the axial strain rate $\dot{\varepsilon}$ in the critical region scales as $\dot{\varepsilon}\sim v_j/L\sim v_0/(d_0 Q_r)$ [21].

The minimum flow rate stability limit is probably the most relevant parameter region at the practical level, because relatively monodisperse streams of droplets are produced with their minimum size in that region. The Buckingham π theorem [26] shows that any dimensionless number describing the steady cone-jet mode behavior must be a function of the above-introduced governing parameters. In particular, $Q_{r\min}=Q_{r\min}(\beta,\delta_\mu,\lambda_s,\lambda_r)$, where $Q_{r\min}=Q_{\min}/Q_o$ and $Q_{\min}$ is the minimum flow rate. In the Newtonian inviscid (polarity-dominated) limit $\beta\delta_\mu\gg 1$, a simple scaling analysis shows that $Q_{r\min}\sim\beta$ [27]. Then, the residence time in the cone-jet transition region becomes $t_r\sim d_o\beta/v_o=t_o$. Therefore, and under the conditions mentioned above, the dimensionless stress relaxation time $\lambda_s=\widetilde{\lambda}_s/t_o$ can be interpreted as the Deborah number, i.e., the stress relaxation time $\widetilde{\lambda}_s$ measured in terms of the residence time t_r in the critical cone-jet transition region. In addition, the axial strain rate in that region scales as $\dot{\varepsilon}\sim v_0/(d_0\beta)=t_o^{-1}$, and, therefore,

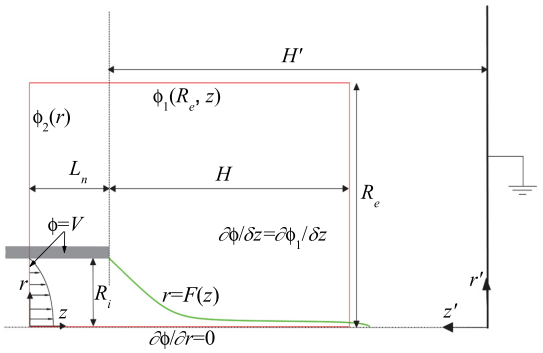

FIG. 1. Sketch of the problem's formulation. The rectangle (red online) denotes the limits of the computational domain.

λ_s can also be regarded as the Weissenberg number, i.e., the strain rate times the stress relaxation time.

When the radial and/or axial dimension of the cone-jet transition region are commensurate with the Taylor meniscus size, the latter may affect some features of the cone-jet mode. In this case, one defines the diameter ratio $\Lambda = 2R_i/d_o = 2[\rho K^2 R_i^3/(\gamma\varepsilon_o^2)]^{1/3}$, where R_i is the radius of the triple contact line anchored at the feeding capillary end. For $\Lambda \lesssim 10^2$, the cone-jet mode stability can be influenced by the feeding capillary size [28]. This may occur, for instance, in the cone-jet mode of nanoelectrospray [29,30].

III. THE LEAKY-DIELECTRIC OLDROYD-B MODEL

In this section, we present the equations defining the leaky-dielectric Oldroyd-B model and describe the numerical method used to calculate both the base flows and their linear stability. In this work, we restrict ourselves to the analysis of the $m = 0$ mode, and, therefore, the model is axisymmetric. Both the model and the numerical method are the natural extensions of those recently used to study the cone-jet mode of Newtonian electrospray [21].

Figure 1 represents the geometrical and electrical configurations considered in the simulations. The red rectangle corresponds to the computational domain. A cylindrical capillary is held at a constant voltage V. The capillary is brought face to face up close to a planar grounded electrode located at a distance H'. A liquid is injected through the capillary at a constant flow rate Q. The flow is fully developed inside the capillary, so that there is a parabolic Hagen-Poiseuille velocity profile upstream at a distance L_n from the capillary's exit. The triple contact line anchors at a distance R_i from the capillary axis. The ambient medium is a perfect dielectric gas whose dynamic effects are neglected. To analyze the global stability of the jetting regime, we set a boundary in the downstream direction and apply outflow (passive) boundary conditions at that cutoff. The gravitational Bond number takes sufficiently small values for the gravity effects to be inconsequential. In what follows, all the quantities are made dimensionless with the triple contact line radius R_i, the liquid density ρ, the surface tension γ, and the applied voltage V, which yields the characteristic time, velocity, pressure and electric field scales $t_c = (\rho R_i^3/\gamma)^{1/2}$, $v_c = R_i/t_c$, $p_c = \gamma/R_i$ and $E_c = V/R_i$, respectively. It must be noted that theses quantities differ from those defined in Sec. II to describe the critical cone-jet transition region because the present model considers the entire fluid configuration.

The (dimensionless) velocity $\mathbf{v}(\mathbf{r}, t) = u(r, z, t)\mathbf{e_r} + w(r, z, t)\mathbf{e_z}$ and reduced pressure $p(r, z, t)$ fields are calculated from the continuity and momentum equations:

$$\nabla \cdot \mathbf{v} = 0, \tag{2}$$

$$\frac{\partial \mathbf{v}}{\partial t} + \mathbf{v} \cdot \nabla \mathbf{v} = -\nabla p + \nabla \cdot \mathbf{T}. \tag{3}$$

The extra stress tensor $\mathbf{T}$ in the Oldroyd-B model can be seen as the sum of the solvent contribution and that due to the presence of polymers, which is given by the Maxwell model [31]. The result is

$$(1 + \lambda_s^* \mathsf{G})\mathbf{T} = \mathrm{Oh}_0(1 + \lambda_r^* \mathsf{G})[\nabla \mathbf{v} + (\nabla \mathbf{v})^T], \tag{4}$$

where $\lambda_s^* = \widetilde{\lambda}_s/t_c$ is the stress relaxation time defined in terms of the capillary time [32], $\mathsf{G}[\mathsf{A}]$ the upper convected derivative operator, $\mathrm{Oh}_0 = \mu_0(\rho R_i \gamma)^{-1/2}$ the Ohnesorge number, $\lambda_r^* = \lambda_s^* \mu^{(s)}/\mu_0$ the dimensionless retardation time, and $\mu^{(s)}$ the solvent viscosity. In most viscoelastic liquids, the solution viscosity considerably increases when the polymer is added to the solvent. For this reason, we will assume that $\mu^{(s)} \ll \mu_0$ and, therefore, $\lambda_r^* \simeq 0$.

In the leaky-dielectric model, the bulk net free charge is assumed to be negligible, and, therefore, the electric potentials ϕ^i and ϕ^o in both the inner (liquid) and outer (gas) domains obey the Laplace equation

$$\phi_{zz}^{i,o} + \phi_{rr}^{i,o} + \phi_r^{i,o}/r = 0. \tag{5}$$

The subscripts r and z here and henceforth denote the partial derivatives with respect to the corresponding spatial variables.

The free surface location is defined by the equation $r = F(z, t)$. The boundary conditions at that surface are

$$\frac{\partial F}{\partial t} + F_z w - u = 0, \tag{6}$$

$$p + \frac{F F_{zz} - 1 - F_z^2}{F\left(1 + F_z^2\right)^{3/2}} + \mathbf{n} \cdot \mathbf{T} \cdot \mathbf{n} = \frac{\chi}{2}\left[\left(E_n^o\right)^2 - \beta\left(E_n^i\right)^2\right] + \chi \frac{\beta - 1}{2}(E_t)^2, \tag{7}$$

$$\mathbf{t} \cdot \mathbf{T} \cdot \mathbf{n} = \chi \sigma E_t, \tag{8}$$

where $\mathbf{n}$ is the unit outward normal vector, $\chi = \varepsilon_o V^2/(R_i\gamma)$ is the electric Bond number, $\mathbf{E}^i$ and $\mathbf{E}^o$ stand for the inner and outer electric field, respectively, $\mathbf{t}$ is the unit vector tangential to the free surface meridians, and σ the superficial charge density. Equation (6) is the kinematic compatibility condition, while Eqs. (7) and (8) express the balance of normal and tangential stresses on the two sides of the free surface, respectively. The right-hand sides of these equations are the Maxwell stresses resulting from both the accumulation of free electric charges at the interface and the jump of permittivity across that surface.

The electric field at the free surface and the surface charge density are calculated as

$$E_n^i = \frac{F_z\phi_z^i - \phi_r^i}{\sqrt{1+F_z^2}}, \quad E_n^o = \frac{F_z\phi_z^o - \phi_r^o}{\sqrt{1+F_z^2}}, \tag{9}$$

$$E_t = \frac{-F_z\phi_r^o + \phi_z^o}{\sqrt{1+F_z^2}} = \frac{-F_z\phi_r^i + \phi_z^i}{\sqrt{1+F_z^2}}, \tag{10}$$

$$\sigma = \chi\left(E_n^o - \beta E_n^i\right). \tag{11}$$

It must be noted that the continuity of the electric potential across the free surface, $\phi^i = \phi^o$, has been considered in Eq. (10).

The free surface equations are completed by imposing the surface charge conservation at $r = F(z,t)$,

$$\frac{\partial\sigma}{\partial t} + \nabla_s\cdot(\sigma\mathbf{v}) = \chi\alpha E_n^i, \tag{12}$$

where ∇_s is the tangential intrinsic gradient along the free surface, and $\alpha = K[\rho R_i^3/(\gamma\varepsilon_o^2)]^{1/2}$ is the dimensionless electrical conductivity.

As mentioned above, the Hagen-Poiseuille velocity profile is prescribed at the entrance of the liquid domain $z = 0$:

$$u = 0, \quad w = 2\mathcal{Q}(1-r^2), \tag{13}$$

where $\mathcal{Q} = Q/(\pi R_i^2 v_c)$. At the capillary wall, we fix the electric potential and impose no-slip boundary conditions, i.e.,

$$\phi^i = \phi^e = 1 \quad \text{and} \quad u = w = 0. \tag{14}$$

The triple contact line is anchored at the end of the capillary:

$$F = 1 \quad \text{at} \quad z = L_n. \tag{15}$$

The standard regularity conditions

$$\phi_r^i = u = w_r = 0 \tag{16}$$

are prescribed on the symmetry axis, and the outflow conditions

$$u_z = w_z = F_z = \sigma_z = 0 \tag{17}$$

are considered at the right-hand end $z_e = H + L_n$ of the computational domain.

The analytical solution for the far-field electric potential [33],

$$\phi_1(r',z') = \frac{-K_v}{\log(4H')}\log\left\{\frac{[r'^2+(1-z')^2]^{1/2}+(1-z')}{[r'^2+(1+z')^2]^{1/2}+(1+z')}\right\}, \tag{18}$$

is imposed at the boundary $r = R_e$. Here, r' and z' are cylindrical coordinates with origin at the intersection between the symmetry axis and the grounded planar electrode (see Fig. 1), while K_v is a dimensionless constant which depends on H'. A logarithmic drop of voltage

$$\phi_2 = 1 - [1-\phi_1(r_e,z_e')]\log r/\log R_e, \quad z_e' \equiv H' + L_n, \tag{19}$$

is applied at the boundary $z = 0$ and $1 < r < R_e$. Finally, the condition

$$\phi_z = (\phi_1)_z \tag{20}$$

is imposed at the right-hand end $z = z_e$ of both the liquid and gas computational domains.

The base flow of the steady cone-jet mode is calculated as the solution of the above equations eliminating the partial derivatives of the unknowns with respect to time. The simulation allows one to obtain the total current intensity I as the sum of the contributions due to the bulk conduction I_b and surface convection I_s. These contributions can be calculated at any axial position z along the cone-jet as

$$I_b(z) = 2\pi\alpha\chi\int_0^{F(z)} E_z^i(r,z)\,r\,dr, \quad I_s(z) = 2\pi F(z)\sigma(z)v_s(z), \tag{21}$$

where E_z^i is the axial component of the inner electric field, and $v_s(z)$ is the free surface velocity. Both the free surface position and current intensity have been calculated and compared with experimental data for 1-octanol, showing good agreement [20].

To calculate the linear axisymmetric global modes, one assumes the temporal dependence

$$U(r,z;t) = U_0(r,z) + \epsilon\delta U^{(k)}(r,z)\,e^{-i\omega^{(k)}t} \quad (\epsilon \ll 1). \tag{22}$$

Here, $U(r,z;t)$ represents any hydrodynamic quantity, $U_0(r,z)$ and $\delta U^{(k)}(r,z)$ stand for the base (steady) solution and the spatial dependence of the kth eigenmode, respectively, while $\omega^{(k)} = \omega_r^{(k)} + i\omega_i^{(k)}$ is the eigenfrequency. Both the eigenfrequencies and the corresponding eigenmodes are calculated as a function of the governing parameters. The dominant eigenmode is that with the largest growth factor. If that growth factor is positive, then the base flow is asymptotically unstable [23]. We restrict our study to the dominant mode, whose eigenfrequency is $\omega = \omega_r + i\omega_i$.

The governing equations are formulated in terms of the dimensionless numbers $\{\mathrm{Oh}_0, \lambda_s^*, \lambda_r^*, \beta, \chi, \alpha, \mathcal{Q}\}$ and those characterizing the rest of boundary conditions. The parameters of the first set can be combined to get the dimensionless numbers $\{\beta, \delta_\mu, \lambda_s, \lambda_r, Q_r\}$ introduced in Sec. II; specifically,

$$\delta_\mu = \alpha^{-1/3}\mathrm{Oh}_0^{1/2}, \quad \lambda_s = \alpha\beta^{-1}\lambda_s^*,$$
$$\lambda_r = \alpha\beta^{-1}\lambda_r^*, \quad Q_r = \pi\,\alpha\,\mathcal{Q}. \tag{23}$$

The dimensionless conductivity $\alpha = \beta t_c/t_o$ takes values much greater than unity because the electric relaxation time t_o is much smaller than the capillary one t_c. This implies that $\lambda_s \gg \lambda_s^*$. It must be noted that the effect of viscoelasticity in electrospray is better quantified by the dimensionless relaxation time λ_s, because it measures the time for the polymer to relax to its coiling state in terms of the residence time t_o in the stretching region.

Most polymeric solutions exhibit zero-shear viscosities much larger than those of their corresponding solvents. For this reason, we will take $\lambda_r^* \simeq 0$ in our calculations. As explained in Sec. II, the influence of the geometrical parameters can be neglected if one takes into account both the locality of the jet emission phenomenon and the secondary role of the electrical potential. In particular, the results are not expected to depend on the length H of the computational domain for sufficiently large values of this parameter. We set $H = 12$ and verified that neither the base flow nor its eigenmodes

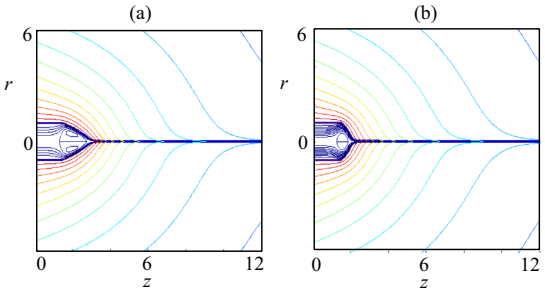

FIG. 2. Base flows for $\beta = 10$, $\delta_\mu = 2.29$, $\chi = 7.92$, $Q_r = 7.72$, $\lambda_r = 0.0926\lambda_s$, and $\lambda_s = 0$ (a) and 2.656 ($\lambda_s^* = 0.108$) (b). The lines in the inner and outer domains correspond to the streamlines and equipotential lines, respectively.

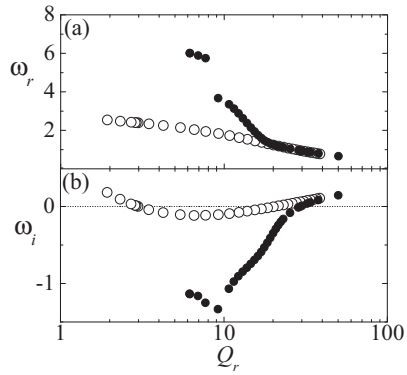

FIG. 3. Real (a) and imaginary (b) part of the eigenvalue responsible for instability as a function of Q_r. The results were calculated for $\beta = 10$, $\delta_\mu = 2.29$, $\chi = 7.92$, $\lambda_r = 0.0926\lambda_s$, and $\lambda_s = 0$ (open symbols) and $\lambda_s = 2.656$ ($\lambda_s^* = 0.108$) (solid symbols).

significantly varied when that parameter was considerably increased. In addition, the length of the feeding capillary was $L_n = 1.5$, the distance between the two electrodes was $H' = 20$, and the radial distance of the outer boundary from the symmetry axis was $R_e = 6$.

We use the numerical method proposed by Herrada and Montanero [34] to solve the model described in this section. The application of that model to the electrospray configuration, as well as its validation for Newtonian liquids, have been recently described by Ponce-Torres *et al.* [21]. The inclusion of the polymeric stresses does not modify any substantial aspect of the numerical method. We refer interested readers to that work for more details of the procedure.

The addition of elastic stresses limits the numerical stability of the algorithm used to find the base flow solution. As mentioned in Sec. II, the strain rate in the cone-jet transition region of Newtonian electrospray scales as $\dot{\varepsilon} \sim\sim v_0/(d_0 Q_r)$. This means that the polymeric stress increases in that critical region as the flow rate decreases. This sets an upper limit to the stress relaxation time for a fixed flow rate, and a lower limit for the flow rate for a fixed stress relaxation time. In addition, the retardation time somehow quantifies the energy dissipation due to the solvent viscosity. Numerical instabilities are damped out by the solvent viscous stresses, which sets a lower limit for the retardation time too.

IV. RESULTS

In this section, we study the effects of viscoelasticity on the electrospray cone-jet mode of 1-octanol ($\rho = 827$ kg/m^3, $\mu = 7.20$ mPa s, $\gamma = 23.5$ mN/m, $K = 9.0 \times 10^{-7}$, $\beta = 10$, $\delta_\mu = 2.29$), whose numerical simulation has been validated experimentally [20,21]. This liquid corresponds to a moderately low-viscosity (polarity-dominated) case. The feeding capillary radius $R_i = 550$ μm is sufficiently large for the jet emission to be regarded as a local phenomenon [21]. All the simulations are conducted for the electric Bond number $\chi = 7.92$. In Figs. 2–7, we examine the effect of viscoelasticity by considering the stress relaxation time $\widetilde{\lambda}_s = 261$ μs, which is sufficiently large to produce noticeable effects, and small enough for the liquid to be considered as a weakly viscoelastic solution [35]. We take the retardation time value $\widetilde{\lambda}_r = 24.2$ μs, which is much smaller than $\widetilde{\lambda}_s$ but sufficiently large to damp out numerical instabilities. The influence of viscoelasticity on the minimum flow rate stability limit is studied in Fig. 8 for different stress relaxation times λ_s while keeping constant the ratio λ_r/λ_s, i.e., for a fixed solution viscosity.

There is a considerable difference between the flow patterns of the Newtonian and viscoelastic cone-jet modes (Fig. 2). When viscoelasticity is added to the electrosprayed liquid, the meniscus shrinks significantly. For sufficiently small flow rates, a recirculation cell appears in the cone. As can be observed, that cell also shrinks in the non-Newtonian case.

Figure 3 shows the real and imaginary parts of the eigenvalue responsible for the instability of the base flow as a function of the flow rate Q_r. In the Newtonian case, there is an interval of flow rates for which the growth rates are negative, which means that the system is asymptotically stable in that interval. The maximum flow rate is roughly ten times the minimum one. The loss of stability at the minimum and maximum flow rates is caused by the same eigenmode. The perturbation responsible for instability grows in amplitude while oscillating with a frequency of the order of the capillary time. We do not observe any bifurcation of the base flow when the numerical solution crosses the stability limits. The lowest flow rate explored for the non-Newtonian liquid was limited by numerical instabilities, as explained in Sec. III. For this reason, the minimum flow rate stability limit could not be reached in this case. The dominant eigenmode in the viscoelastic case changes for $Q_r \simeq 10$, which explains the jump of the oscillation frequency at that flow rate. There is little influence of viscoelasticity on both the maximum flow rate and the oscillation frequency of the mode responsible for the instability.

Fluid particles undergo an intense extensional flow when crossing the cone-jet transition region, where the velocity increases from very small values up to the jet speed. This extensional flow stretches the polymers dissolved in the

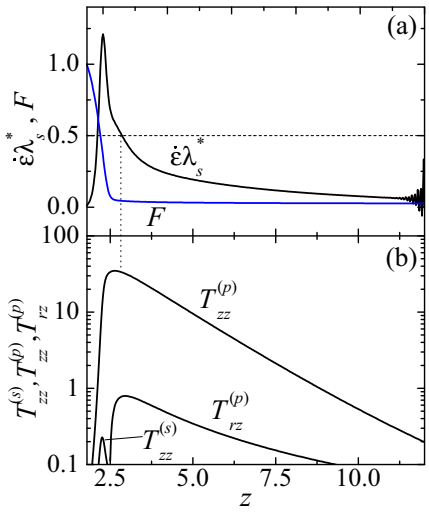

FIG. 4. (a) Free surface position F and strain rate $\dot{\varepsilon}$ as a function of the axial position z. (b) Components $T_{zz}^{(p)}$ and $T_{rz}^{(p)}$ of the polymeric stress tensor and solvent contribution $T_{zz}^{(s)}$ as a function of the axial position z. The results were calculated for $\beta = 10$, $\delta_\mu = 2.29$, $\chi = 7.92$, $Q_r = 7.72$, $\lambda_r = 0.0926\lambda_s$ and $\lambda_s = 2.656$ ($\lambda_s^* = 0.108$).

liquid, which tend to relax to their coiling state on a timescale given by λ_s^*. If this characteristic time is sufficiently large as compared to the axial strain rate, then the stretch-to-coil transition is prevented, and polymers keep on stretching over the cone-jet region. In an uniaxial extensional flow, this occurs for $\dot{\varepsilon}\lambda_s^* > 1/2$. To examine this aspect of the problem, we have measured the strain rate $\dot{\varepsilon}$ and both the solvent $T_{zz}^{(s)} = \mathrm{Oh}_s\, \partial w/\partial z$ ($\mathrm{Oh}_s = \mu_s(\rho R_i \gamma)^{-1/2}$) and polymeric $T_{zz}^{(p)} = T_{zz} - T_{zz}^{(s)}$ contributions to the extra stress tensor along the symmetry axis. Figure 4 shows the results for the case considered in this section. As can be seen, $\dot{\varepsilon}\lambda_s^* > 1/2$ in the cone-jet transition region, which makes the polymer stress sharply increase in that region. For $z \gtrsim 2.6$, the strain rate falls below that critical value mentioned above, and both $T_{zz}^{(p)}$ and $T_{rz}^{(p)}$ decay exponentially. As can be observed, $T_{rz}^{(p)}$ takes relatively small but non-negligible values. The existence of a noticeable off-diagonal stress component of the polymeric stress tensor has also been observed in the later stages of Oldroyd-B filament thinning [36]. The contribution of the solvent viscous stress is hardly noticeable due to the smallness of the retardation time.

Figure 5 compares the tangential and normal components of the inner and outer electric fields at the free surface for the Newtonian liquid and its viscoelastic counterpart. In both cases, E_n^o is around three times larger than βE_n^i in the cone-jet transition region, and, therefore, one can conclude that the superficial charge is not fully relaxed to its local electrostatic value within that region. The outer normal component E_n^o of the electric field in the Newtonian cone-jet transition region takes values significantly larger than those of the viscoelastic case, which indicates that the energy transmitted by the dominant shear electric stress to the liquid is larger in the absence

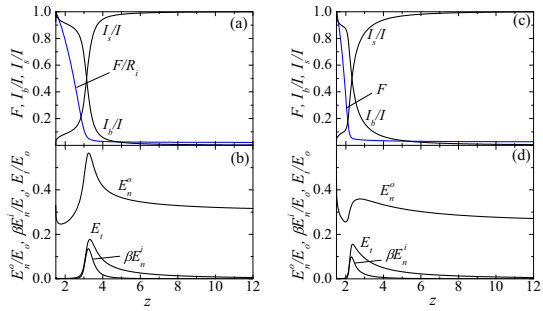

FIG. 5. Free surface position F, bulk current intensity I_b and surface current intensity I_s as a function of the axial position z [(a) and (c)]. Tangential E_t and normal components E_n^i and E_n^o of the inner and outer electric fields at the free surface [(b) and (d)]. The results were calculated for $\beta = 10$, $\delta_\mu = 2.29$, $\chi = 7.92$, $Q_r = 7.72$, $\lambda_r = 0.0926\lambda_s$, and $\lambda_s = 0$ (left) and 2.656 ($\lambda_s^* = 0.108$) (right).

of elasticity. This is linked to the more stretched shape taken by the Newtonian liquid meniscus. The component E_n^o reaches similar values downstream, which means that the superficial charge density transported by the viscoelastic jet is essentially the same as that convected by the Newtonian one.

In the 1D (slender) approximation, the momentum equation in the z-direction becomes [4]:

$$\underbrace{\frac{\chi}{2}\left[\left(E_n^o\right)^2 - \beta\left(E_n^i\right)^2\right]_z}_{\mathrm{I}} + \underbrace{\chi\frac{\beta-1}{2}[(E^t)^2]_z}_{\mathrm{II}} + \underbrace{\frac{2\sigma E_t}{F}}_{\mathrm{III}}$$
$$= \underbrace{\left(\frac{1}{F}\right)_z}_{\mathrm{IV}} + \underbrace{\left(\frac{\mathcal{Q}^2}{2F^4}\right)_z}_{\mathrm{V}} + \underbrace{\frac{6\mathrm{Oh}_s\mathcal{Q}}{F^2}\left(\frac{F_z}{F}\right)_z}_{\mathrm{VI}}$$
$$+ \underbrace{\frac{1}{F^2}\left[F^2\left(T_{rr}^{(p)} - T_{zz}^{(p)}\right)\right]_z}_{\mathrm{VII}}. \qquad (24)$$

The terms of Eq. (24) have been grouped into electric (left-hand side) and hydrodynamic (right-hand side) forces. The addends I, II, and III are generally referred to as the electrostatic, polarization, and electric tangential forces per unit volume, respectively [10]. The terms IV, V, VI, and VII correspond to surface tension, inertia, solvent viscosity, and polymeric stress, respectively.

Figure 6 shows the values taken by all the terms of the 1D model Eq. (24) as a function of the axial position z. The electric tangential force (III) is the main driving force and acts not only in the jet emission region but also along the ejected liquid thread. As mentioned above, this force takes considerably larger values in the Newtonian case. The electrostatic suction (I) supplies much less energy, but it plays a relevant role in shaping the cone-jet transition region to produce the liquid ejection. It hinders the flow behind the cone-jet transition region only in the absence of viscoelasticity. Finally, the polarization force pushes the fluid in front of the cone-jet transition region, while opposes the liquid ejection behind that point in the two cases. Most of the work

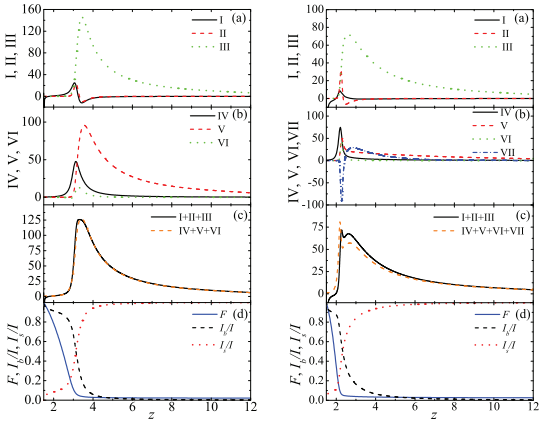

FIG. 6. [Graphs (a), (b), and (c)] Terms I–VII of the slenderness model Eq. (24) as a function of the axial position z. [Graph (d)] Free surface position F, bulk current intensity I_b and surface current intensity I_s as a function of the axial position z. The results were calculated for $\beta = 10$, $\delta_\mu = 2.29$, $\chi = 7.92$, $Q_r = 7.72$, $\lambda_r = 0.0926\lambda_s$, and $\lambda_s = 0$ (left) and 2.656 ($\lambda_s^* = 0.108$) (right).

done by the electric field on the Newtonian liquid converts into kinetic energy. Polymers pull from the liquid while stretching in the meniscus apex, and exert a resistant force throughout the jet as they relax to their coiling state. The pulling exerted by the dissolved polymers increases the liquid acceleration, which flattens the meniscus. For this reason, the surface tension constitutes the main energy sink in the viscoelastic cone-jet transition region, and the 1D approximation provides less accurate predictions in that region [see Fig. 6(c)]. In fact, this model does not even contemplate the off-diagonal polymeric stress $T_{rz}^{(p)}$, which takes smaller but nonnegligible values as compared to those of $T_{zz}^{(p)}$ (Fig. 4). The fact that the maximum of |VII| exceeds the maximum of III reveals the importance of the polymeric axial stress in this flow, despite the smallness of the stress relaxation time.

Figure 7 shows the diameter d_{out} at the outlet section and the current intensity I transported by the liquid as a function of the dimensionless flow rate Q_r for the linearly stable configurations. The diameter of the Newtonian cases is smaller than

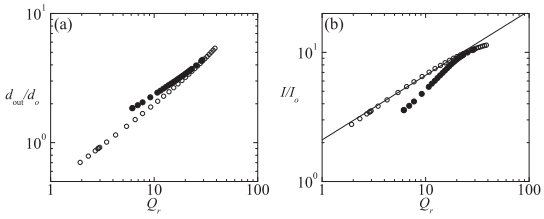

FIG. 7. Jet diameter d_{out} (a) and current intensity I (b) as a function of the dimensionless flow rate Q_r. The results were calculated for $\beta = 10$, $\delta_\mu = 2.29$, $\chi = 7.92$, $\lambda_r = 0.0926\lambda_s$, and $\lambda_s = 0$ (open symbols) and 2.656 ($\lambda_s^* = 0.108$) (solid symbols). The line in the right-hand graph is the law $I/I_o = 2.1Q_r^{1/2}$.

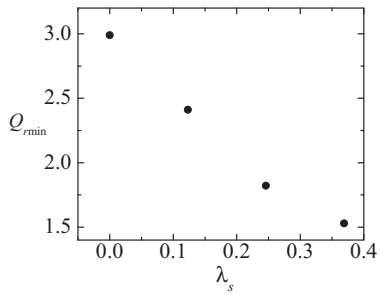

FIG. 8. Dimensionless flow rate Q_r at the minimum flow rate stability limit as a function of the stress relaxation time λ_s. The results were calculated for $\beta = 10$, $\delta_\mu = 2.29$, $\chi = 7.92$, and $\lambda_r = 0.0926\lambda_s$.

those of their viscoelastic counterparts, essentially because, as mentioned above, the shear electric stress is larger in the former case. The diameters do not scale as $Q_r^{1/2}$ in the Newtonian case [10,37] because the jet is still accelerating at the outlet section for large flow rates. On the contrary, the current intensity transported by the Newtonian jet does follow the scaling law $I/I_o \sim Q_r^{1/2}$ [10,37], while it considerably deviates from that prediction when small viscoelasticity is considered. The electric current convected by the viscoelastic jet is smaller than that transported by its Newtonian counterpart because the speed of the former is smaller than that of the latter.

The minimum flow rate stability limit is a very attractive parameter region of electrospray at the practical level because it leads to the continuous production of the smallest droplets while keeping a high degree of monodispersity. The effect of viscoelasticity on the minimum flow rate stability limit is shown in Fig. 8. The ratio $\lambda_r/\lambda_s = \mu^{(s)}/\mu_0$, and therefore the solution viscosity μ_0, were kept constant in all the simulations. Despite the smallness of the stress relaxation time ($\lambda_s = 0.5$ corresponds to $\tilde{\lambda}_s = 49.2$ μs), viscoelasticity significantly reduces the minimum flow rate. This stabilizing effect can be understood in terms of the polymeric force appearing in the cone-jet transition region (Fig. 6). This force collaborates with the incipient shear electric stress in pushing the liquid throughout this critical cone-jet region, which helps the fluid to overcome the resistant forces emerging in that region. The polymeric force hinders the liquid motion beyond the cone-jet transition region, where the fluid particle moves faster driven by the shear electric stress. In this sense, one may say that the liquid borrows energy from the polymeric stress in the most unstable region and returns it when safely moving downstream.

V. CONCLUSIONS

We analyzed theoretically the influence of viscoelasticity on the steady cone-jet mode of electrospray for small stress relaxation times. To this end, we numerically solved the leaky-dielectric model and calculated both the base flow and the eigenmodes characterizing its linear stability as a function of the governing parameters. We selected a well-known

Newtonian electrospray realization and introduced polymeric stresses modeled by the Oldroyd-B approximation. The stress relaxation time was varied to examine the influence of those stresses on the cone-jet mode stability.

When the stress relaxation time is of the order of the residence time in the cone-jet region, fluid particles undergo an extensional deformation in that region sufficiently intense for the dissolved polymers to stretch continuously, preventing their relaxation to the coiling state. As a consequence, the axial polymeric stress becomes much larger than that produced by the solvent viscosity. This axial stress pulls from the liquid, which accelerates much faster than in the Newtonian case. This sharp acceleration makes the electrified liquid meniscus shrink. The axial polymeric stress does not play a dominant role in the final balance of energy because the kinetic energy gained by the meniscus through the action of the stretching polymers is lost in the jet region, where they eventually reach their coiling state. The meniscus shrinkage reduces the outer normal component of the electric field over the free surface, and increases the resistant force offered by both the surface tension and viscosity in the cone-jet transition region. These effects collaborate in decreasing the speed of the emitted jet with respect to that in the Newtonian case. The current intensity transported by the viscoelastic liquid is significantly smaller than that calculated in the Newtonian simulation, especially for small flow rates. The fact that the liquid gains kinetic energy from the polymeric stress in the most unstable region seems to explain the decrease of the minimum flow rate stability limit.

When a small amount of polymers is added to a Newtonian solvent, the liquid experiences two major changes: (i) polymeric stresses arise when fluid particles are deformed at sufficiently high rates, and (ii) the zero-shear viscosity increases. To analyze the effect on electrospray of the first factor exclusively, we compared numerical simulations with and without polymeric stresses for the same values of the Newtonian parameters, including the Reynolds number. The conclusions might be different from those obtained when comparing the electrospray realizations of the solvent and the polymeric solution due to the decrease of the Reynolds number caused by the presence of the polymers.

In the present work, the conduction of electrical charges in the bulk is assumed isotropic. However, one may expect that the presence of macromolecules significantly stretched along the streamwise direction may limit the validity of that assumption in the critical cone-jet transition region. It must be noted that the inclusion of anisotropic and/or inhomogeneous conductivity in the leaky-dielectric model can violate the conservation of volumetric charge ($\nabla \cdot \mathbf{j} = 0$, $\mathbf{j}$ is the current density), which is automatically satisfied for constant scalar conductivity ($\nabla \cdot \mathbf{j} = \nabla \cdot (K\mathbf{E}) = K\nabla \cdot \mathbf{E} = 0$). In other words, the inclusion of an electrical conductivity linked to the state of the dissolved polymers at a given point may require calculating the volumetric charge density in the bulk even if the electric forces are neglected there. The molecular origin of anisotropy that renders the liquid mechanical response non-Newtonian is the same as the one that would make the ionic and thermal mobilities of species present in the liquid anisotropic: the presence of long polymeric chains highly aligned with the flow. One may argue that if non-Newtonian deviations are accounted for in the stress-strain relationship, then deviations from isotropy should be considered in the rest of properties too. However, and given the vast variety of liquid mixtures used in chemical processes and applications, there can be a large range of these mixtures that exhibit stronger mechanical deviations from isotropy than those of electrical properties, which justifies our approach; for example, the cases where ionic species are sufficiently small or electrolytes are used as solvents.

Electrospray stretches violently the fluid particles in the cone-jet transition region. As shown in this work, it can produce Deborah numbers of the order of unity when acting on viscoelastic liquids with stress relaxation times as small as hundreds of microseconds. The residence time (stretching rate) decreases (increases) with the electrical conductivity, and, therefore, one can adjust this parameter to magnify the viscoelastic character of the polymer solution. This offers the opportunity of measuring the extensional rheological properties of weakly viscoelastic liquids. For instance, it is possible (and technically simple) to measure experimentally the slenderness of the viscoelastic meniscus. Then, one can compare it with that calculated numerically as a function of the stress relaxation time to infer the value of this parameter.

ACKNOWLEDGMENTS

This research has been supported by the Spanish Ministry of Economy, Industry and Competitiveness under Grant No. DPI2016-78887, and by Junta de Extremadura under Grant No. GR18175.

[1] D. H. Reneker and A. L. Yarin, Electrospinning jets and polymer nanofibers, Polymer **49**, 2387 (2008).

[2] A. G. Kanani and S. H. Bahrami, Review on electrospun nanofibers scaffold and biomedical applications, Trends Biomater. Artif. Organs **24**, 93 (2010).

[3] S. Agarwala, A. Greinera, and J. H. Wendorff, Functional materials by electrospinning of polymers, Prog. Polym. Sci. **38**, 963 (2013).

[4] C. P. Carroll and Y. L. Joo, Electrospinning of viscoelastic boger fluids: Modeling and experiments, Phys. Fluids **18**, 053102 (2006).

[5] S. Gadkari, Influence of polymer relaxation time on the electrospinning process: Numerical investigation, Polymers **9**, 501 (2017).

[6] C. P. Carroll and Y. L. Joo, Axisymmetric instabilities of electrically driven viscoelastic jets, J. Non-Newtonian Fluid Mech. **153**, 130 (2008).

[7] C. P. Carroll and Y. L. Joo, Axisymmetric instabilities in electrospinning of highly conducting, viscoelastic polymer solutions, Phys. Fluids **21**, 103101 (2009).

[8] Dharmansh and P. Chokshi, Axisymmetric instability in a thinning electrified jet, Phys. Rev. E **93**, 043124 (2016).

[9] D. Dharmansh and P. Chokshi, Stability analysis of an electrospinning jet of a polymeric fluid, Polymer **131**, 34 (2017).
[10] A. M. Gañán-Calvo, The surface charge in electrospraying: Its nature and its universal scaling laws, J. Aerosol Sci. **30**, 863 (1999).
[11] C. Clasen, J. P. Plog, W.-M. Kulicke, M. Owens, C. Macosko, L. E. Scriven, M. Verani, and G. H. McKinley, How dilute are dilute solutions in extensional flows? J. Rheol. **50**, 849 (2006).
[12] J. G. Oldroyd, On the formulation of rheological equations of state, Proc. R. Soc. London **200**, 523 (1950).
[13] R. B. Bird, R. C. Armstrong, and O. Hassager, *Dynamics of Polymeric Liquids* (John Wiley & Sons, New York, 1987).
[14] P. P. Bhat, S. Appathurai, M. T. Harris, M. Pasquali, G. H. McKinley, and O. A. Basaran, Formation of beads-on-a-string structures during break-up of viscoelastic filaments, Nat. Phys. **6**, 625 (2010).
[15] M. S. N. Oliveira and G. H. McKinley, Iterated stretching and multiple beads-on-a-string phenomena in dilute solutions of highly-extensible flexible polymers, Phys. Fluids **17**, 071704 (2005).
[16] C. Clasen, J. Eggers, M. A. Fontelos, J. Li, and G. H. McKinley, The beads-on-string structure of viscoelastic threads, J. Fluid Mech. **556**, 283 (2006).
[17] J. R. Melcher and G. I. Taylor, Electrohydrodynamics: A review of the role of interfacial shear stresses, Annu. Rev. Fluid Mech. **1**, 111 (1969).
[18] D. A. Saville, Electrohydrodynamics: The Taylor-Melcher leaky dielectric model, Annu. Rev. Fluid Mech. **29**, 27 (1997).
[19] F. J. Higuera, Numerical computation of the domain of operation of an electrospray of a very viscous liquid, J. Fluid Mech. **648**, 35 (2010).
[20] M. A. Herrada, J. M. López-Herrera, A. M. Gañán-Calvo, E. J. Vega, J. M. Montanero, and S. Popinet, Numerical simulation of electrospray in the cone-jet mode, Phys. Rev. E **86**, 026305 (2012).
[21] A. Ponce-Torres, N. Rebollo-Muñoz, M. A. Herrada, A. M. Gañán-Calvo, and J. M. Montanero, The steady cone-jet mode of electrospraying close to the minimum volume stability limit, J. Fluid Mech. **857**, 142 (2018).
[22] M. Gamero-Castaño and M. Magnani, Numerical simulation of electrospraying in the cone-jet mode, J. Fluid Mech. **859**, 247 (2019).
[23] V. Theofilis, Global linear instability, Annu. Rev. Fluid Mech. **43**, 319 (2011).
[24] P. J. Schmid, Nonmodal stability theory, Annu. Rev. Fluid Mech. **39**, 129 (2007).
[25] F. Cruz-Mazo, M. A. Herrada, A. M. Gañán-Calvo, and J. M. Montanero, Global stability of axisymmetric flow focusing, J. Fluid Mech. **832**, 329 (2017).
[26] G. I. Barenblatt, *Scaling* (Cambridge University Press, Cambridge, 2003).
[27] A. M. Gañán-Calvo, N. Rebollo-Muñoz, and J. M. Montanero, Physical symmetries and scaling laws for the minimum or natural rate of flow and droplet size ejected by Taylor cone-jets, New J. Phys. **15**, 033035 (2013).
[28] W. J. Scheideler and C.-H. Chena, The minimum flow rate scaling of Taylor cone-jets issued from a nozzle, Appl. Phys. Lett. **104**, 024103 (2014).
[29] J. Carlier, S. Arscott, J.-C. Camart, C. Cren-Olivé, and S. Le Gac, Integrated microfabricated systems including a purification module and an on-chip nano electrospray ionization interface for biological analysis, J. Chromatogr. A **1071**, 213 (2005).
[30] E. M. Yuill, N. Saand, S. J. Ray, G. M. Hieftje, and L. A. Baker, Electrospray ionization from nanopipette emitters with tip diameters of less than 100 nm, Anal. Chem. **85**, 8498 (2013).
[31] D. F. James, Boger fluids, Annu. Rev. Fluid Mech. **41**, 129 (2009).
[32] T. Funada and D. D. Joseph, Viscoelastic potential flow analysis of capillary instability, J. Non-Newtonian Fluid Mech. **111**, 87 (2003).
[33] A. M. Gañán-Calvo, J. C. Lasheras, J. Dávila, and A. Barrero, The electrostatic spray emitted from an electrified conical meniscus, J. Aerosol Sci. **25**, 1121 (1994).
[34] M. A. Herrada and J. M. Montanero, A numerical method to study the dynamics of capillary fluid systems, J. Comput. Phys. **306**, 137 (2016).
[35] P. C. Sousa, E. J. Vega, R. G. Sousa, J. M. Montanero, and M. A. Alves, Measurement of relaxation times in extensional flow of weakly viscoelastic polymer solutions, Rheol. Acta **56**, 11 (2017).
[36] E. Turkoz, J. M. López-Herrera, J. Eggers, C. B. Arnold, and L. Deike, Axisymmetric simulation of viscoelastic filament thinning with the Olroyd-b model, J. Fluid Mech. **851**, R2 (2018).
[37] A. M. Gañán-Calvo, J. M. López-Herrera, M. A. Herrada, A. Ramos, and J. M. Montanero, Review on the physics electrospray: From electrokinetics to the operating conditions of single and coaxial Taylor cone-jets and AC electrospray, J. Aerosol Sci. **125**, 32 (2018).

8.2 Paper II: Whipping in gaseous flow focusing

Authors:
Sergio Blanco Trejo, Miguel Ángel Herrada, Alfonso Miguel Gañán-Calvo, Ángel Rubio, Maria Guadalupe Cabezas, and Jose María Montanero.

Paper published in:
International Journal of Multiphase Flow Volume 130, September 2020, 103367
DOI: https://doi.org/10.1016/j.ijmultiphaseflow.2020.103367

International Journal of Multiphase Flow 130 (2020) 103367

Contents lists available at ScienceDirect

International Journal of Multiphase Flow

journal homepage: www.elsevier.com/locate/ijmulflow

Whipping in gaseous flow focusing

S. Blanco-Trejo [a], M.A. Herrada [a], A.M. Gañán-Calvo [a], A. Rubio [b], M.G. Cabezas [b], J.M. Montanero [b,*]

[a] Departamento de Ingeniería Aerospacial y Mecánica de Fluidos, Universidad de Sevilla, Camino de los Descubrimientos s/n 41092, Spain
[b] Departamento de Ingeniería Mecánica, Energética y de los Materiales and Instituto de Computación Científica Avanzada (ICCAEx), Universidad de Extremadura, E-06006 Badajoz, Spain

ARTICLE INFO

Article history:
Received 13 April 2020
Revised 1 June 2020
Accepted 3 June 2020
Available online 6 June 2020

Keywords:
Gaseous flow focusing
Whipping instability
Global stability analysis
Micronozzles

ABSTRACT

We study both theoretically and experimentally the whipping instability in axisymmetric gaseous flow focusing realized in a converging-diverging nozzle. The lateral oscillation of both the tapering meniscus and emitted jet is explained in terms of the global linear instability of the lateral mode with the azimuthal number $m = 1$. A comparison with previous experiments shows good agreement. The distance between the feeding capillary and the nozzle neck hardly affects the $m = 1$ stability limit for the conditions considered in those experiments. We analyze the influence of the nozzle shape on the parameter conditions leading to whipping. As the nozzle convergence rate (the inverse of the length over which the diameter reduction takes place) increases, the flow becomes more stable under $m = 1$ perturbations. The above results are in marked contrast with those of the axisymmetric mode $m = 0$. For the axisymmetric mode, the minimum flow rate increases with the nozzle convergence rate, while the capillary-to-neck distance has considerable influence on the jetting-to-dripping transition. We also conduct experiments with different nozzles and capillary-to-neck distances to examine the effect of those factors on the stability of the jetting regime. The experiments allow us to distinguish between absolute whipping, in which both the tapering meniscus and the emitted jet oscillate, and convective whipping, in which the jet oscillates while the meniscus remains practically steady. Absolute whipping is observed for water and 1-cSt silicone oil focused with the nozzle with the smallest convergence rate and capillary-to-neck distance. The increase of the liquid viscosity stabilizes the liquid meniscus, producing the transition from absolute to convective whipping. In the high-viscosity case, the oscillation of the emitted jet far away from the discharge orifice is considerably affected by the shape of the nozzle in front of its neck. In fact, the increase of the convergence rate and capillary-to-neck distance eliminates the convective whipping as well. The reduction of surface tension enhances absolute whipping. We explain the appearance of the two types of whipping in terms of the flow pattern induced by the nozzle shape in front of the neck.

1. Introduction

The production of microjets has enormous applications in very diverse fields such as biotechnology, analytical chemistry, pharmacy and food industry, and industrial engineering. These capillary structures are the natural gate to produce drops, emulsions, and capsules on the micrometer scale, in a continuous way, and with a relatively large degree of monodispersity (Eggers and Villermaux, 2008). The so-called tip streaming phenomenon allows for the reduction of the capillary jet diameter down to the micrometer scale while keeping the size of the passages and orifices of the ejector on the scale of hundreds of microns (Montanero and Gañán Calvo, 2020). Several tip streaming configurations can be used to produce very thin liquid jets (Taylor, 1964; Eggers, 1997; Cohen et al., 2001; Collins et al., 2008; Castro-Hernández et al., 2009; Anna and Mayer, 2006). In aerodynamic (gaseous) flow focusing (Gañán Calvo, 1998), the liquid is supplied across a feeding capillary at a flow rate of the order of a few microliters per minute. The feeding capillary is placed in front of a discharge orifice whose diameter is commensurate with that of the capillary. A high-speed gaseous current coflows with the liquid across the discharge orifice. The combination of the pressure drop and viscous shear stress caused by the gaseous current drives the liquid flow, stretching the meniscus attached to the feeding capillary. A thin jet tapers from the meniscus tip and exits the ejector together with the outer gaseous stream. The original plate-orifice flow focusing configuration (Gañán Calvo, 1998) was modified by

* Corresponding author.
E-mail address: jmm@unex.es (J.M. Montanero).

https://doi.org/10.1016/j.ijmultiphaseflow.2020.103367
0301-9322/

DePonte et al. (2008) ten years later by replacing the plate with a borosilicate tube inside which the feeding capillary was introduced. The tube was ended by a fire-shaped nozzle to produce the same focusing effect as that of the plate orifice in the original configuration. DePonte et al. (2008) coined the expression "Gas Dynamic Virtual Nozzle" (GDVN) to refer to this ejector.

Gaseous flow focusing has found applications in very diverse fields. For instance, microparticles of complex structures have been produced by injecting coaxially two immiscible liquid streams (Gañán Calvo et al., 2013). Viscoelastic threads (Ponce-Torres et al., 2016; Hofmann et al., 2018; Vasireddi et al., 2019) for smooth printing and bioplotting (Ponce-Torres et al., 2017) have been produced by applying essentially the flow focusing principle. Ponce-Torres et al. (2019) have recently extruded fibers with diameters ranging from a few microns down to hundreds of nanometers with the gaseous flow focusing spinning method. A gaseous coflow focusing process has been used to produce stimuli-responsive microbubbles that comprise perfluorocarbon suspension of silver nanoparticles in a lipid (Si et al., 2016). In electro-flow focusing (Gañán Calvo et al., 2006), a relatively small voltage is applied to the liquid to charge the droplets, which make them perfect candidates for surface sample desorption (Forbes and Sisco, 2014a; 2014b).

Among the several gaseous flow focusing applications, the serial femtosecond crystallography (SFX) is probably the most important one. In fact, this technology has revolutionized the molecular determination of complex biochemical species by recording single flash diffraction patterns of many individual protein crystals (Chapman et al., 2011). Most experiments in SFX have utilized a liquid microjet to place the sample into the beam focus. The jet must be perfectly steady to ensure a consistent interaction with the X-ray beam, which allows for efficient data collection. The protein crystals are damaged by the beam, and therefore the jet must be sufficiently fast to ensure that the exposed sample exits the interaction region before the next pulse strikes the jet Stan et al. (2016). In fact, a fresh sample must be placed into the beam focus at a rate that matches the arrival of X-ray pulses. This constitutes a severe condition for, e.g., the European XFEL, which produces pulses at frequencies of the order of 10^6 Hz (Wiedorn et al., 2018). The X-ray pulse produces an explosion of the liquid in the interaction region, which must be located sufficiently far from the nozzle exit to avoid a rapid collection of sputtered material from the explosion. In addition, the jet must be as thin as possible to reduce the background diffraction signal. The simultaneous fulfillment of these two last conditions is a difficult task because surface tension shortens the jet as the diameter decreases. In SFX, the jet is usually generated by aerodynamically focusing (Gañán Calvo, 1998; DePonte et al., 2008; Zahoor et al., 2018) a liquid stream with a GDVN-like ejector. The production of long and thin jets imposes severe constraints on the geometrical design of issuing nozzles (DePonte et al., 2008; Beyerlein et al., 2015; Piotter et al., 2018; Wiedorn et al., 2018).

For a given geometrical configuration, the size of the focused jet can be reduced either by decreasing the liquid flow rate or by increasing the pressure drop applied to the gas stream. In the first case, one inevitably runs into an axisymmetric instability leading to the dripping regime (Si et al., 2009; Vega et al., 2010). In the latter case, the steady jetting mode becomes unstable due to the growth of whipping (bending) oscillations (Chigier and Reitz, 1996; Lasheras and Hopfinger, 2000) of the capillary system. In the whipping instability, surface tension has a stabilizing effect, and the destabilizing factor is purely aerodynamic: a perturbation at the jet free surface causes the gas stream to accelerate as it passes a crest, lowering the pressure at that point and encouraging the crest to increase in size (as in wind-generated ripples on a liquid free surface). The analysis of the whipping instability entails certain complexity even for a parallel liquid base flow. In fact, an accurate calculation of the perturbation growth rate requires the consideration of the gas viscosity even for small values of this parameter because the existence of an outer boundary layer significantly affects the instability (Gordillo and Pérez-Saborid, 2005). The problem for non-parallel liquid flows (as those produced by flow focusing) becomes much more complicated due to the cumbersome numerics. However, this analysis is highly relevant to optimize the production of both microdroplets and microfibers from jetting realizations.

In the classical plate-orifice configuration, the whipping instability is found in the jet beyond the discharge orifice, does not propagate upstream, and, therefore, the liquid meniscus remains perfectly steady (convective whipping). On the contrary, when the jet is focused by a nozzle (as happens in SFX) (DePonte et al., 2008), the liquid meniscus can also oscillate laterally (absolute whipping) (Acero et al., 2012). In some cases, those oscillations make the liquid touch the inner wall of the nozzle, which constitutes a serious obstacle in applications. Acero et al. (2012) speculated that the absence of absolute whipping in the plate-orifice configuration might be due to the radial character of the gaseous flow in front of the discharge orifice, which somehow stabilizes the meniscus under bending perturbations. Neither the origin of this phenomenon nor the way to eliminate it has been determined yet.

In the linear global stability analysis (Theofilis, 2011), we calculate the base flow characterizing the steady jetting mode of a certain capillary system. Then, we interrogate the base flow about its response to small-amplitude perturbations (Sauter and Buggisch, 2005; Tammisola et al., 2012; Gordillo et al., 2014; Dharmansh and Chokshi, 2016; 2017). The system evolves asymptotically (i.e., for sufficiently large times) dominated by the mode with the largest growth rate of the eigenfrequency spectrum. If this growth rate is positive, then natural perturbations lead to the base flow instability. Cruz-Mazo et al. (2017) have shown that this occurs to axisymmetric perturbations in gaseous flow focusing for sufficiently large applied pressure drops and flow rates below a minimum value. In this work, we apply the same methodology to explain the whipping instability arising for sufficiently large pressure drops. We hypothesize that the lateral oscillation of the liquid meniscus and/or emitted jet observed in experiments (Acero et al., 2012) corresponds to the growth of the dominant $m = 1$ linear mode. To the best of our knowledge, the non-axisymmetric ($m \neq 0$) global stability analysis has not as yet been applied to any capillary systems. In fact, previous studies of non-axisymmetric perturbations are restricted to local stability analyses, which assume that the base flow is quasi-uniform in the streamwise direction over a distance of the order of the wavelength of the dominant perturbation (Montanero and Gañán Calvo, 2020). This approximation is not valid to examine the dynamical response of the flow focusing meniscus.

In this work, we will study the appearance of the whipping instability in gaseous flow focusing both theoretically and experimentally. In the numerical analysis, the steady base flow will be calculated by solving the non-linear, steady Navier-Stokes equations. Then, the linear eigenmodes will be obtained to examine the response of that flow to small-amplitude perturbations. The parameter conditions leading to whipping are assumed to be those for which the $m = 1$ dominant eigenmode grows on time. In the experimental study, we will determine the parameter conditions for which convective and absolute whipping come up. We will consider different nozzle shapes and capillary-to-neck distances both in the global stability analysis and in the experiments. We will focus on the nozzle convergence rate, defined as the inverse of the distance along which the diameter reduces to its minimum value. The results will show that whipping is suppressed as the convergence rate increases, which explains why whipping

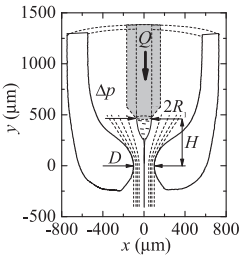

Fig. 1. Axisymmetric gaseous flow focusing. The geometrical configuration corresponds to that used in the experiments by Acero et al. (2012). The values of the main parameters are $R_1 \simeq 75$ μm, $D \simeq 200$ μm, and $H \simeq 440$ μm.

is much less common in the classical plate-orifice configuration (Gañán Calvo, 1998).

The paper is organized as follows. Section 2 presents the governing equations and briefly describes the numerical method. The experimental procedure is explained in Section 3. Section 4 shows both the theoretical and experimental results. The paper closes with some concluding remarks in Section 5.

2. Theoretical method

The gaseous flow focusing configuration considered in this paper is shown in Fig. 1. A liquid of density ρ_ℓ and viscosity μ_ℓ is injected through a feeding capillary of radius R_1 at a constant flow rate Q. The feeding capillary is located inside a converging-diverging nozzle at a distance H from the nozzle neck, whose diameter is D. A pressure drop Δp is applied to a gas stream of density ρ_g and viscosity μ_g. The gas stream stretches the liquid meniscus that hangs on the edge of the capillary end due to the action of the surface tension σ. In the steady jetting regime, the meniscus tip emits a liquid microjet, which crosses the nozzle coflowing with the outer gas stream.

In this section, all the variables are made dimensionless with the capillary radius R_1, the liquid density ρ_ℓ, and the surface tension σ, which yields the characteristic time, velocity and pressure scales $t_c = (\rho_\ell R_1^3/\sigma)^{1/2}$, $v_c = R_1/t_c$, and $p_c = \sigma/R_1$, respectively. The velocity $\mathbf{v}^{(j)}(r,z,\theta;t) = U^{(j)}(r,\theta,z;t)\ \mathbf{e_r} + V^{(j)}(r,\theta,z;t)\ \mathbf{e}_\theta + W^{(j)}(r,\theta,z;t)\ \mathbf{e_z}$ and pressure $p^{(j)}(r,\theta,z;t)$ fields verify the Navier-Stokes equations:

$$\frac{(rU^{(j)})_r}{r} + \frac{V_\theta^{(j)}}{r} + W_z^{(j)} = 0, \tag{1}$$

$$\rho^{\delta_{jg}}\left(U_t^{(j)} + U^{(j)}U_r^{(j)} + V^{(j)}\frac{U_\theta^{(j)}}{r} + W^{(j)}U_z^{(j)} - \frac{V^{(j)2}}{r}\right) = -p_r^{(j)} + \mu^{\delta_{jg}}Oh\left[\frac{(rU_r^{(j)})_r}{r} + \frac{U_{\theta\theta}^{(j)}}{r^2} + U_{zz}^{(j)} - \frac{U^{(j)}}{r^2} - \frac{2V_\theta^{(j)}}{r^2}\right], \tag{2}$$

$$\rho^{\delta_{jg}}\left(V_t^{(j)} + U^{(j)}V_r^{(j)} + \frac{U^{(j)}V^{(j)}}{r} + V^{(j)}\frac{V_\theta^{(j)}}{r} + W^{(j)}V_z^{(j)}\right) = -p_\theta^{(j)} + \mu^{\delta_{jg}}Oh\left[\frac{(rV_r^{(j)})_r}{r} + \frac{V_{\theta\theta}^{(j)}}{r^2} + V_{zz}^{(j)} - \frac{V^{(j)}}{r^2} + \frac{2U_\theta^{(j)}}{r^2}\right], \tag{3}$$

$$\rho^{\delta_{jg}}\left(W_t^{(j)} + U^{(j)}W_r^{(j)} + V^{(j)}\frac{W_\theta^{(j)}}{r} + W^{(j)}W_z^{(j)}\right) = -p_z^{(j)} + \mu^{\delta_{jg}}Oh\left[\frac{(rW_r^{(j)})_r}{r} + \frac{W_{\theta\theta}^{(j)}}{r^2} + W_{zz}^{(j)}\right]. \tag{4}$$

In the above equations, $\rho = \rho_g/\rho_\ell$ and $\mu = \mu_g/\mu_\ell$ are the density and viscosity ratios, δ_{km} is the Kronecker delta, the superscripts $j = \ell$ and g refer to the liquid and gas phases, respectively, the subscripts t, r, and z denote the partial derivatives with respect to the corresponding variables, and $Oh = \mu_\ell(\rho_\ell\sigma R_1)^{-1/2}$ is the Ohnesorge number. It is worth noting that, although the density and viscosity ratios take very small values in gaseous flow focusing, they may significantly affect the lateral (whipping) instability of the steady jetting regime (Gordillo and Pérez-Saborid, 2005; Herrada et al., 2010).

The Navier-Stokes equations are integrated considering the kinematic compatibility condition at the free surface position $r = F(\theta,z;t)$:

$$F_t - U^{(j)} + \frac{F_\theta}{F}V^{(j)} + F_z W^{(j)} = 0. \tag{5}$$

The balance between the normal and tangential stresses on the two sides of the free surface reads

$$\tau_n^{(\ell)} = \tau_n^{(g)}, \quad \tau_{t_1}^{(\ell)} = \tau_{t_1}^{(g)}, \quad \tau_{t_2}^{(\ell)} = \tau_{t_2}^{(g)}, \tag{6}$$

where $\tau_n^{(j)}$, $\tau_{t1}^{(j)}$ and $\tau_{t2}^{(j)}$ are the sum of capillary pressure, hydrostatic pressure and viscous stress on the two sides of the free surface, and the subindexes n, t_1 and t_2 denote the normal and two tangential directions, respectively. These stresses are given by the expressions

$$\tau_n^{(j)} = p^{(j)} - \nabla\cdot\mathbf{e_n} - \frac{2\mu^{\delta_{jg}}Oh}{C_n^2}\left\{U_r^{(j)} + F_z\left(F_z W_z^{(j)} - U_z^{(j)} - W_r^{(j)}\right) - \frac{F_\theta}{F}\left[-\frac{F_\theta}{F^2}\left(U^{(j)} + V_\theta^{(j)}\right) + \frac{U_\theta^{(j)}}{F} + V_r^{(j)} - \frac{V^{(j)}}{F} - F_z\left(V_z^{(j)} + \frac{W_\theta^{(j)}}{F}\right)\right]\right\}, \tag{7}$$

$$\tau_{t1}^{(j)} = \frac{\mu^{\delta_{jg}}Oh}{C_nC_t}\left\{2F_z\left(U_r^{(j)} - W_z^{(j)}\right) + \left(1 - F_z^2\right)\left(W_r^{(j)} + U_z^{(j)}\right) - \frac{F_\theta}{F}\left[V_z^{(j)} + \frac{W_\theta^{(j)}}{F} + F_z\left(\frac{U_\theta^{(j)}}{F} + V_r^{(j)} - \frac{V^{(j)}}{F}\right)\right]\right\}, \tag{8}$$

$$\tau_{t2}^{(j)} = \frac{\mu^{\delta_{jg}}Oh}{C_n^2C_t}\left\{\frac{2F_\theta}{F}\left[U_r^{(j)} - \left(1 + F_z^2\right)\frac{U^{(j)} + V_\theta^{(j)}}{F} + F_z\left(F_z W_z^{(j)} - U_z^{(j)} - W_r^{(j)}\right)\right] + \left(1 + F_z^2 - \frac{F_\theta^2}{F^2}\right)\left[\frac{U_\theta^{(j)}}{F} + V_r^{(j)} - \frac{V^{(j)}}{F} - F_z\left(V_z^{(j)} + \frac{W_\theta^{(j)}}{F}\right)\right]\right\}, \tag{9}$$

where C_n, C_t, C_θ are functions of the instantaneous free surface shape given by the equations

$$C_n = \left(1 + \frac{F_\theta^2}{F^2} + F_z^2\right)^{1/2}, \quad C_t = \left(1 + F_z^2\right)^{1/2}, \quad C_\theta = \left(1 + \frac{F_\theta^2}{F^2}\right)^{1/2}. \tag{10}$$

In addition, $\mathbf{e_n} = \frac{1}{FC_n}\left[(F_\theta\sin\theta + F\cos\theta)\,\mathbf{e_r} - (F_\theta\cos\theta + F\sin\theta)\,\mathbf{e}_\theta - FF_z\,\mathbf{e_z}\right]$ is the outward unit vector perpendicular to the free surface, and

$$\nabla\cdot\mathbf{e_n} = \frac{1}{FC_n} + \frac{1}{FC_n^3}\left[\frac{F_\theta}{F}\left(\frac{F_\theta}{F} + 2F_zF_{\theta z}\right) - C_t^2\frac{F_{\theta\theta}}{F} - C_\theta^2FF_{zz}\right] \tag{11}$$

is the local mean curvature. The anchorage condition $F = 1$ is imposed at the edge of the feeding capillary, while the no-slip boundary conditions $\mathbf{v} = \mathbf{0}$ is prescribed on all the solid surfaces. Periodic boundary conditions in the angular direction are imposed for all the variables.

We impose the Hagen-Poiseuille velocity distribution, $U^{(\ell)} = 0$ and $W^{(\ell)} = 2v_e(1 - r^2)$ ($v_e = Q/(\pi R_1^2 v_c)$), and a uniform velocity profile at the inlet sections $z = 0$ of the liquid and gas domains, respectively. We set uniform pressures at the outlet sections of the gas and liquid domains. The liquid outlet pressure equals that of the gas plus the capillary pressure. The pressure drop Δp applied to the gas stream is calculated as the difference between the value averaged over the inlet section and that imposed at the outlet section.

The steady and axisymmetric base flow is characterized by the velocity and pressure fields, $\mathbf{v}_b(r,z) = U_b(r,z)\ \mathbf{e_r} + W_b(r,z)\ \mathbf{e_z}$ and $p_b(r,z)$, as well as by the distance $F_b(z)$ between a surface element and the z axis. To calculate the linear global modes, one assumes the spatio-temporal dependence

$$U(r,\theta,z;t) = U_b(r,z) + \epsilon\,\hat{U}(r,z)\,e^{-i\omega t+im\theta}, \tag{12}$$

$$V(r,\theta,z;t) = \epsilon\,\hat{V}(r,z)\,e^{-i\omega t+im\theta}, \tag{13}$$

$$W(r,\theta,z;t) = W_b(r,z) + \epsilon\,\hat{W}(r,z)\,e^{-i\omega t+im\theta}, \tag{14}$$

$$p(r,\theta,z;t) = p_b(r,z) + \epsilon\,\hat{p}(r,z)\,e^{-i\omega t+im\theta}, \tag{15}$$

$$F(\theta,z;t) = F_b(z) + \epsilon\,\hat{F}(z)\,e^{-i\omega t+im\theta}, \tag{16}$$

where $\epsilon \ll 1$, $\{\hat{U},\hat{V},\hat{W},\hat{p},\hat{F}\}$ stand for the eigenmode spatial dependence of the corresponding quantities, while $\omega = \omega_r + i\omega_i$ is the eigenfrequency and m is the azimuthal wave number. Both the eigenfrequencies and the corresponding eigenmodes are calculated as a function of the governing parameters for $m = 0$ and 1. The dominant eigenmode is that with the largest growth rate ω_i. If that growth rate is positive, the base flow is unstable under the corresponding axisymmetric ($m = 0$) or lateral ($m = 1$) perturbation.

The global linear stability analysis describes the response of the base flow to small-amplitude perturbations. If the base flow is linearly unstable, the dominant mode grows exponentially with time producing perturbations that leave the linear regime. The present stability analysis does not allow one to predict the system's response in the non-linear phase. However, the growth of an axisymmetric dominant mode is expected to lead to the jetting-to-dripping transition. On the contrary, the growth of the $m = 1$ eigenmode may be saturated by the non-linear terms of the hydrodynamic equations within the experimental field of view. In this case, the linear instability will lead to finite-amplitude lateral oscillations of the liquid system (whipping regime). It is not possible to safely predict the appearance of either convective or absolute whipping in the non-linear regime from the linear stability analysis. For this reason, we will not distinguish between those whipping modes in Section 4.

The theoretical model was solved with a variation of the numerical method described by Herrada and Montanero (2016). The base flow and the corresponding eigenmodes are calculated with the boundary fitted method (Thompson and Warsi, 1982). The hydrodynamic equations are discretized in the transformed radial direction η using $n_\eta^\ell = 13$ and $n_\eta^g = 40$ Chebyshev collocation points (Khorrami, 1989) in the liquid and gas domains, respectively. The transformed axial direction ξ was discretized using fourth-order finite differences and $n_\xi^\ell = n_\xi^g = 1201$ equally spaced points. The grid points accumulate near the free surface (Fig. 2) where the gradients of the hydrodynamic quantities are expected to increase. The accumulation of grid points on the outer side of the free surface is important to accurately integrate the gaseous boundary layer, which plays an important role in the calculation of the $m = 1$ mode (Gordillo and Pérez-Saborid, 2005). We have verified that neither the base flow nor the eigenvalues characterizing the linear modes changed significantly when the number of grid points was increased (Fig. 3). More details of the numerical method can be found elsewhere (Herrada and Montanero, 2016).

Table 1
Physical properties of the liquids considered in our study.

	ρ_ℓ (kg/m^3)	μ_ℓ (mPa · s)	σ (mN/m)	Oh
Distilled water	998	1.00	72	0.0118
1-cSt silicone oil	818	0.818	17	0.0217
5-cSt silicone oil	917	4.60	19	0.11
100-cSt silicone oil	961	96	21	2.14

3. Experimental method

Three flow focusing ejectors were used in the experiments. In each of these ejectors, a tube of radius R_1=100 μm was coaxially located inside a converging-diverging nozzle. We used three nozzles with different shapes but with the same neck diameter D=220 μm. These nozzles were fire-shaped from cut-end borosilicate capillaries (Hilgenberg Gmbh) and optically characterized by the method described by Muñoz Sánchez et al. (2019). Fig. 4 shows the shapes of the nozzles and the inner capillary located at a distance H= 450 μm from the nozzle neck. Nozzles 1 and 2 were fabricated from capillaries of OD 3.3 ± 0.1 mm and ID 2.8 ± 0.1 mm at different heating positions. Nozzle 1 was heated deep in the flame for a short time, while Nozzle 2 was heated in an outer region for a longer time. As can be observed, the nozzles have practically the same neck diameter and shape in the diverging part. However, they exhibit significantly different shapes in front of the neck. In Nozzle 1, the diameter reduction spreads over a long region. The shape of Nozzle 2 is closer to that of the plate-orifice configuration because the diameter reduction occurs over a shorter length. The diameter reduction is large for these two nozzles. For this reason, it involved a large amount of molten material, and, consequently, the necks are long. Nozzle 3 was fabricated from a thinner capillary (OD 2.0 ± 0.1 mm, ID 1.6 ± 0.1 mm) and at an outer heating position. The diameter reduction is smaller in this case, and, therefore, the neck is considerably shorter. The three flow focusing ejectors used in the present study are expected to produce an intense focusing effect, which confers practical relevance upon our results.

In our experiments, the liquid was injected at a constant flow rate Q through the feeding tube by a syringe pump KDS120 (kdScientific). Air was injected across the nozzle with a constant pressure drop Δp. We observed the emitted jet using a CCD camera (AVT Stingray F-125B) equipped with optical lenses and LED backlight. The camera exposure time was reduced to 4 μs to acquired sharp images. The optical magnification was 1.295 μm/pixel. A three-axis translation stage allowed for proper alignment and focusing. All the elements were mounted on a vibration isolation board.

We examined the behavior of distilled water, 1-cSt silicone oil, and 100-cSt silicone oil to analyze the influence on the stability map of both the surface tension and liquid viscosity. The values of the physical properties of the liquids considered in our study are displayed in Table 1. The table also shows the physical properties of 5-cSt silicone oil considered in the theoretical analysis of Section 4, and the value of the Ohnesorge number calculated with the radius R_1=100 μm of the feeding capillary.

The experimental sequence consisted of the following steps. The pressure drop was applied to the air stream. The liquid was injected at a sufficiently large flow rate to establish the jetting

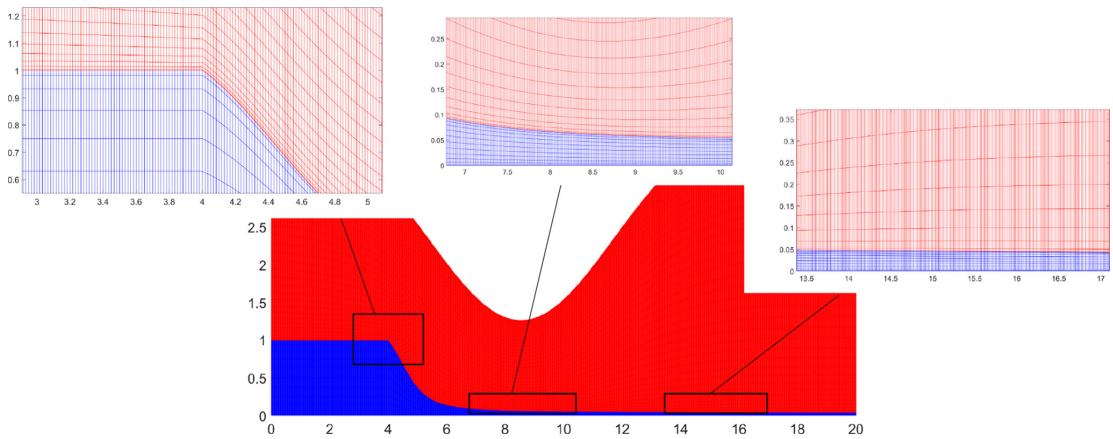

Fig. 2. Details of the grid used in the simulations.

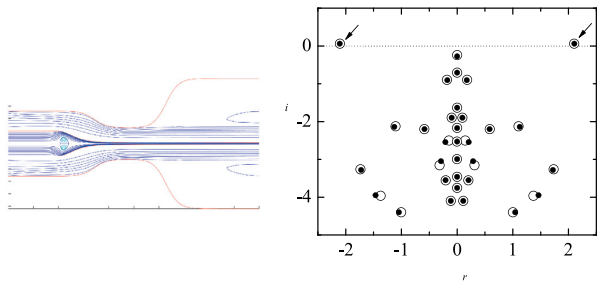

Fig. 3. (Left) Streamlines of the base flow for the nozzle considered in Section 4.1, $H = 440$ μm, $Q = 4.2$ ml/h, and $\Delta p = 154$ mbar. (Right) Spectrum of eigenvalues for $m = 1$. The solid and open symbols correspond to ($n_\xi^\ell = n_\xi^g = 1201, n_\eta^\ell = 11,\ n_\eta^g = 31$) and ($n_\xi^\ell = n_\xi^g = 1201, n_\eta^\ell = 15, n_\eta^g = 40$), respectively.

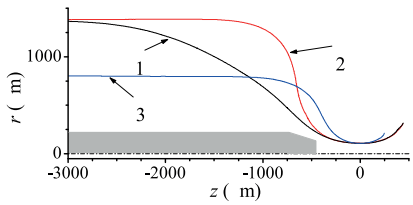

Fig. 4. Inner shape of Nozzles 1, 2, and 3. The grey region shows the position of the feeding tube for $H = 450$ μm.

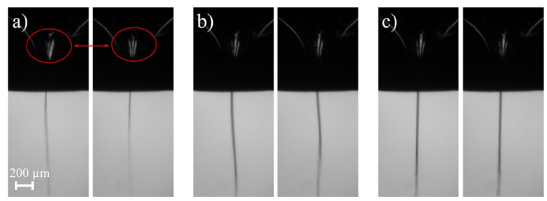

Fig. 5. Absolute whipping (a), convective whipping (b), and jetting (c) in experiments with water. The red circles in (a) indicates the oscillation of the tapering meniscus. (For interpretation of the references to colour in this figure legend, the reader is referred to the web version of this article.)

regime. Then, the flow rate Q was progressively reduced to determine the values corresponding to the transitions between the different regimes. This sequence was repeated for applied pressure drops in the interval $50 \leq \Delta p \leq 300$ mbar.

The images acquired in the experiments were analyzed to determine the regime adopted by the system for each pair of values Δp and Q. As explained in the Introduction, two types of whipping instabilities were distinguished (Acero et al., 2012): convective whipping in which the tapering meniscus remains stable and the emitted jet oscillates laterally, and absolute whipping in which both the meniscus and the jet oscillate. Due to the difficulties inherent to the experiment, we adopted the following simple criterion to identify the above-mentioned regimes. Absolute whipping occurs if some visible section of the meniscus (see the circle in Fig. 5a) oscillates with an amplitude larger than the jet radius. Convective whipping takes place if this oscillation occurs only beyond the discharge orifice (Fig. 5b). Finally, jetting occurs if neither of these conditions applies (Fig. 5c).

4. Theoretical results

4.1. Comparison with previous experiments

As can be observed from the comparison between Figs. 3-left and 4, the focusing geometry in our experiments is more complicated than that considered by Acero et al. (2012). We chose this geometry to enhance the focusing effect produced by the gaseous stream in the neck, which makes the results more interesting at the practical level. However, the mesh generation method used in the numerical simulations fails to adapt to the solid shapes shown in Fig. 4. For this reason, we will limit the comparison

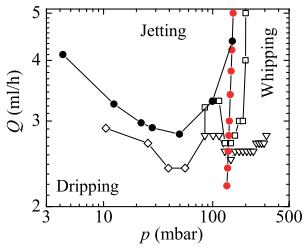

Fig. 6. Stability map obtained from the experiments conducted by Acero et al. (2012) for 5-cSt silicone oil (open symbols). The open diamonds, squares, and triangles correspond to the jetting-to-dripping, jetting-to-whipping, and whipping-to-dripping transitions in the experiments. The black and red solid circles show the marginally stable flows under $m = 0$ and 1 perturbations, respectively, calculated numerically for $H = 350$ μm. (For interpretation of the references to colour in this figure legend, the reader is referred to the web version of this article.)

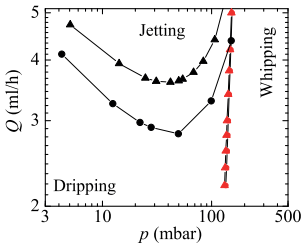

Fig. 7. Marginally stable flows under $m = 0$ (black symbols) and 1 (red symbols) perturbations calculated numerically for 5-cSt silicone oil focused with the nozzle used by Acero et al. (2012). The circles and triangles correspond to $H = 350$ and 440 μm, respectively.. (For interpretation of the references to colour in this figure legend, the reader is referred to the web version of this article.)

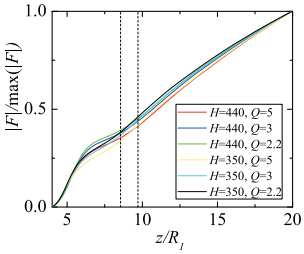

Fig. 8. Magnitude of the free surface perturbation amplitude, $|\hat{F}(z)|$, corresponding to the mode $m = 1$ for the marginally stable flows in the simulations. The results have been normalized with the maximum value for each case. The labels indicate the values of the capillary-to-neck distance and flow rate measured in μm and ml/h, respectively. The vertical dashed lines show the positions of the nozzle neck for the two values of H considered.

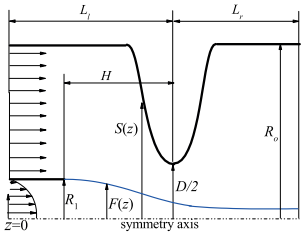

Fig. 9. Sketch of the computational domain.

between theory and experiments to the geometry examined by Acero et al. (2012).

In this section, we assess the accuracy of the linear stability analysis by comparing its predictions with the experimental results of Acero et al. (2012). The numerical domain is that considered by Cruz-Mazo et al. (2017) (see Fig. 4 of that reference), which approximately coincides with the experimental configuration (Fig. 1). The base flow was calculated for a given flow rate and different applied pressure drops. The example in Fig. 3 shows how the drag force exerted by the outer stream causes a recirculation pattern in the liquid meniscus. The existence of this pattern prevents one from safely using 1D approximations or local stability analysis in this problem. We calculated the spectrum of eigenvalues of the modes $m = 0$ and 1 for each of the base flows. The transition from jetting to dripping (whipping) takes place when the growth rate of the dominant $m = 0$ ($m = 1$) mode becomes positive. As can be observed in Fig. 3, $\omega_r \neq 0$ in that case, which means that the instability has an oscillatory character.

Fig. 6 shows the stability map obtained from the experiments of Acero et al. (2012) for 5-cSt silicone oil. The figure also shows the marginally stable numerical realizations under $m = 0$ and $m = 1$ perturbations. In all the cases analyzed, the mode $m = 2$ was stable. Three regimes are distinguished: (i) dripping, (ii) whipping in which only the jet or both the jet and the tapering meniscus oscillate laterally, and (iii) jetting in which both the tapering meniscus and the jet are stable. As explained in Section 2, we here do not make a distinction between convective and absolute whipping owing to the inability of the linear stability analysis to predict the type of whipping that prevails in the non-linear response of the system. The results for $H = 350$ μm agree well with the experimental data, although there is a small region of whipping in the experiments which has not been detected by the global stability analysis. The value of H is slightly smaller than that measured in the experiments ($H = 440$ μm), which may be attributed to an error in the measurement of H caused by the optical distortion produced by the significant curvature of the converging part of the micronozzle. In fact, Acero et al. (2012) conducted their experiments for a large value of H. Montanero et al. (2011) showed that the flow rate at the jetting-to-dripping transition is very sensitive to H as this parameter approaches its maximum value. Therefore, small errors in H can lead to significant errors in the critical flow rate. Another source of discrepancy is the deviation of the nozzle and feeding capillary numerical shapes from their experimental counterparts. In particular, the feeding capillary in the simulations has zero thickness while in the experiment both the thickness and shape of the capillary end may play a significant role. In the global stability analysis, we considered two values of the capillary-to-neck distance H (Fig. 7). As can be observed, the value of H considerably affects the instability transition for $m = 0$ (Montanero et al., 2011), while it hardly alters the flow stability under the $m = 1$ perturbation.

We now analyze the eigenmodes $m = 1$ responsible for the whipping instability. We show in Fig. 8 the magnitude $|\hat{F}(z)|$ of the free surface perturbation amplitude. This amplitude monotonically grows as the distance from the feeding capillary increases. The function $|\hat{F}(z)|$ exhibits approximately the same shape in all the cases, although they probably correspond to experimental realizations of convective and absolute whipping.

4.2. Effect of the nozzle shape

Acero et al. (2012) hypothesized that the appearance of whipping in GDVN ejectors is linked to the axial component of the gas flow induced by the nozzle shape in front of the neck. To analyze the validity of this hypothesis, in this section we study the influence of an increase in the convergence rate of the focusing nozzle

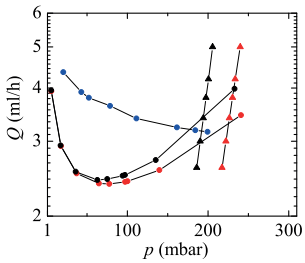

Fig. 10. Stability limits under $m = 0$ (circles) and 1 (triangles) perturbations in the simulations. The results were obtained for 5-cSt silicone oil focused by air. The nozzle shape is given by the expression (17) with $\alpha = 0.045$ (black symbols), 0.05 (red symbols), and 5 (blue symbols). The whipping instability for $\alpha = 5$ was not found. (For interpretation of the references to colour in this figure legend, the reader is referred to the web version of this article.)

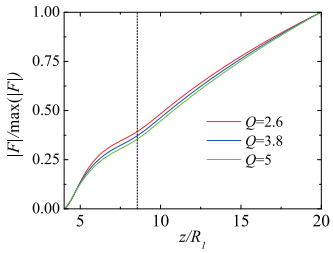

Fig. 11. Magnitude of the free surface perturbation amplitude, $|\hat{F}(z)|$, corresponding to the mode $m = 1$ for the marginally stable flows in the simulations. The results have been normalized with the maximum value for each case. The labels indicate the values of the flow rate measured in ml/h. The vertical dashed line shows the position of the nozzle neck.

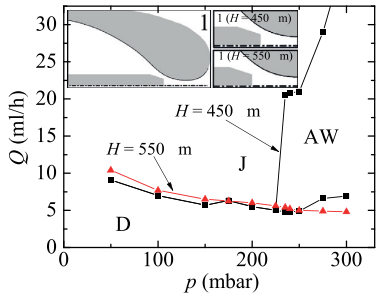

Fig. 12. Experimental stability regions for water focused with air. The black and red symbols correspond to $H = 450$ and 550 µm, respectively. Neither convective nor absolute whipping was observed for $H = 550$ µm. The insets show the shape of the nozzle and the position of the feeding capillary for the two values of H considered. (For interpretation of the references to colour in this figure legend, the reader is referred to the web version of this article.)

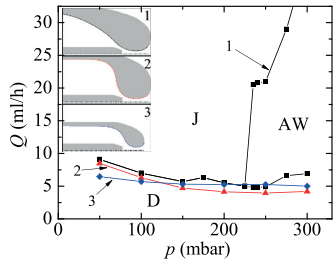

Fig. 13. Experimental stability regions for water focused with air with Nozzles 1, 2 and 3. In all the cases, H=450 µm. Nozzles 2 and 3 show neither absolute nor convective whipping. The insets show the shape of the nozzle and the position of the feeding capillary.

on the flow stability under $m = 1$ perturbations. This could have been done with the geometrical model used in Section 4.1. However, the mesh generation method used in our numerical simulations fails to adapt to that model when the nozzle convergence is increased. For this reason, we conducted numerical simulations with the (simpler) nozzle shape given by the expression (Fig. 9)

$$S(z) = R_o - (R_o - D/2)\exp[-\alpha(z - L_l)^2], \tag{17}$$

where all the distances have been made dimensionless with the capillary radius R_1. In these simulations, we considered 5-cSt silicone oil focused by air. The values of the geometrical parameters R_o, D, and L_l were the same as those in Section 4.1, while the capillary-to-neck distance was $H = 350$ µm ($H/R_1 = 4.55$). To analyze the effect of the convergence rate on the base flow stability, we carried out simulations for $\alpha = 0.045$, 0.05, and 5. As α increases, the nozzle shape approaches that of the plate-orifice configuration.

The effect of the nozzle convergence rate α on the whipping instability can be clearly appreciated in Fig. 10. As α increases, the pressure drop necessary to trigger the whipping instability increases. In fact, a small increase of α causes a significant increase in the critical pressure drop for the same liquid flow rate. We have not found whipping instability for $\alpha = 5$. The nozzle shape also affects the minimum flow rate leading to the growth of the dominant $m = 0$ mode (dripping). The focusing orifice thickness increases as α decreases, which generally enhances the focusing effect and reduces the minimum flow rate. Interestingly, the dependency of the minimum flow rate with respect to α is not monotonous. In fact, the stabilizing effect mentioned above is not observed when α decreases from 0.05 to 0.045, or when α decreases from 5 to 0.045 for $\Delta p \gtrsim 200$ mbar. The axial dependence of the free surface perturbation (Fig. 11) is very similar to that found for the nozzle considered in Section 4.1.

The neutral stability curve $m = 0$ for $\alpha = 0.045$ and 0.05 is shown to extend all the way into the region where the mode $m = 1$ becomes unstable. This means that there are parameter conditions for which both the varicose and whipping modes are unstable. In the linear regime, growing modes do not interfere with each other. If the growth rates of those modes are sufficiently different from each other, varicose (whipping) instability will be observed if the mode $m = 0$ ($m = 1$) is the dominant one. If the growth rates take similar values, then both instabilities can become noticeable at the same time. This behavior can probably be extrapolated to the nonlinear regime. In that case, we expect to observe dripping from a straight liquid thread, whipping, or dripping from a bend thread depending on the relative values of the axisymmetric and whipping growth rates. This extrapolation must be done with caution because of the interference between growing linear modes in the nonlinear regime.

5. Experimental results

In this section, we analyze experimentally the role played by both the capillary-to-neck distance and the nozzle shape on the stability of the steady jetting regime produced by a GDVN ejector. As explained in Section 3, we here distinguish the experimental realizations where both the tapering meniscus and emitted jet oscillated (absolute whipping) from those in which the instability affected only the jet (convective instability) (Fig. 5). Fig. 12 shows the stability regions in the $Q - \Delta p$ parameter plane for distilled water focused by air in Nozzle 1 (see Section 3) and two

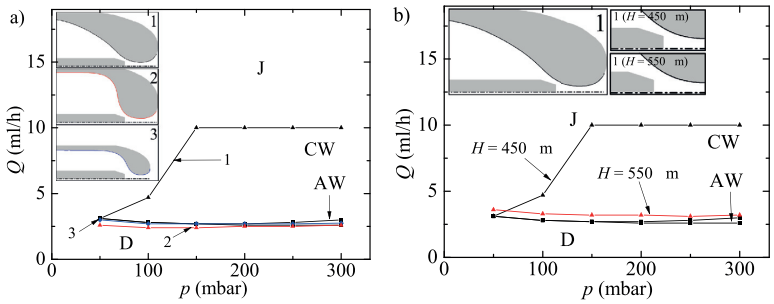

Fig. 14. Experimental stability regions for 100-cSt silicone oil focused with air. a) Effect of the nozzle shape for $H = 450$ µm. Nozzles 2 and 3 show neither absolute nor convective whipping. b) Effect of the distance H for Nozzle 1. Neither convective nor absolute whipping was observed for $H = 550$ µm. The insets show the shape of the nozzle and the position of the feeding capillary.

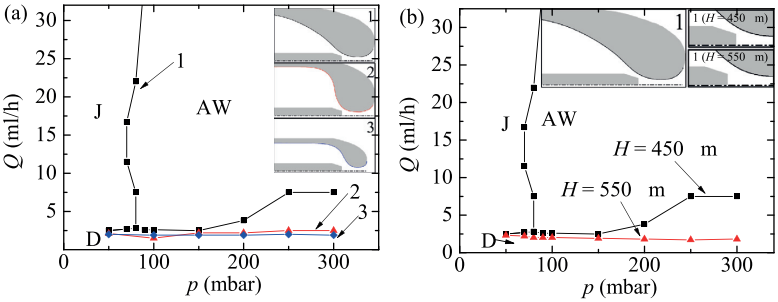

Fig. 15. Experimental stability regions for 1-cSt silicone oil focused with air. a) Effect of the nozzle shape for $H = 450$ µm. Nozzles 2 and 3 show neither absolute nor convective whipping. b) Effect of the distance H for Nozzle 1. Neither convective nor absolute whipping was observed for $H = 550$ µm. The insets show the shape of the nozzle and the position of the feeding capillary.

different values of H. The black lines/symbols correspond to the shortest distance H=450 µm, and separate the parameter regions where jetting (J), dripping (D) and absolute whipping (AW) were observed. The red line/symbols show the jetting-to-dripping transition for H= 550 µm. The figure shows the critical role played by the air speed in the absolute whipping instability. When the pressure drop Δp is sufficiently large and the distance H takes the smallest value, the outer stream causes the meniscus oscillation. This phenomenon disappears when the feeding capillary is moved away from the nozzle neck because the gap between the capillary and the nozzle increases, and, consequently, the axial speed of the air stream surrounding the meniscus decreases. In addition, the reduction of the air speed slightly increases the flow rate at the jetting-to-dripping transition for most of the applied pressure drops.

Absolute whipping can also be prevented by selecting appropriately the shape of the nozzle. This can be done with the fire-shaping method recently developed by Muñoz Sánchez et al. (2019). Fig. 13 shows the stability regions obtained for distilled water, H=450 µm, and Nozzles 1, 2 and 3, whose necks have the same diameter. Nozzles 1 and 2 have different convergence rates (distances along which the diameter reduction takes place) but practically the same shape beyond the neck (see Fig. 4). The radial component of the velocity field in front of the neck of Nozzle 2 is expected to be larger than its counterpart in Nozzle 1. In fact, the flow pattern in Nozzle 2 must be similar to that of the classical plate-orifice configuration (Gañán Calvo, 1998). As suggested by the stability analysis (Section 4.2), whipping is suppressed in Nozzle 2. Nozzle 3 is considerably smaller than the other two nozzles. Consequently, the capillary is located farther away from the nozzle inner wall for the same H. In this case, the axial component of the air velocity around the liquid meniscus is smaller, and absolute whipping is not observed.

To examine the influence of the liquid viscosity on the jetting stability, we conducted experiments with 100-cSt silicone oil. In graph (a) of Fig. 14, we compare the stability regions for the three nozzles. Absolute whipping occupies a very narrow region in the stability map. Convective whipping (CW) arises when sufficiently large pressure drops are applied to Nozzle 1. One can conclude that viscosity stabilizes the liquid meniscus in Nozzle 1 but not the emitted jet. Interestingly, and contrary to what happens to water, convective whipping disappears for $Q \gtrsim 10$ ml/h. Nozzles 2 and 3 show neither absolute nor convective whipping. Surprisingly, the nozzle shape in front of the neck affects the response of the jet far away from the discharge orifice (convective whipping). A plausible explanation for this counter-intuitive observation is that the meniscus slightly oscillates for large viscosity in Nozzle 1. This oscillation is convected and amplified downstream by the emitted jet. This would explain (i) the transition from absolute to convective instability as the viscosity increases, and (ii) the fact that convective instability is affected by the nozzle shape in front of the neck. In all the cases, the jetting-to-dripping transition takes place at flow rates much smaller than those for water. These critical flow rates hardly depend on the applied pressure drop. In graph (b) of Fig. 14, we compare the results for Nozzle 1 and two capillary-to-neck distances: H=450 µm (black symbols) and 550 µm (red symbols). The increase of the distance H reduces the air axial velocity at the jet emission point, which eliminates the whipping instability. Overall, the liquid viscosity stabilizes the tapering meniscus by reducing the flow rate leading to the jetting-to-dripping transition, and by practically suppressing the absolute whipping. However, the minimum values of the applied pressure drop that trigger the con-

vective whipping are considerably smaller than their counterparts in the low-viscosity case.

The role of the surface tension is examined in Fig. 15, which shows the results for 1-cSt silicone oil. This liquid has the same kinematic viscosity of water but a surface tension more than four times smaller than that of water. The main effect of the surface tension reduction is the enhancement of the absolute whipping in Nozzle 1. As explained in the Introduction, whipping arises when the difference between the pressures in the ridges and valleys of the deformed interface overcomes the stabilizing effect of the surface tension. Therefore, the reduction of the surface tension favors the whipping instability. The Weber number $\mathrm{We}_g = \rho_g(V_g - V_\ell)^2 R_i/\sigma$ compares the dynamic pressure associated with the gas velocity V_g relative to that of the liquid V_ℓ versus the capillary pressure σ/R_i in the tapering meniscus. In flow focusing, $V_\ell \ll V_g$, $\rho_g V_g^2 \sim \Delta p$, and thus $\mathrm{We}_g \sim \Delta p R_i/\sigma$. The comparison of Figs. 13–15 shows that the critical applied pressure for the whipping instability in Nozzle 1 has roughly decreased in the same proportion as the surface tension, which indicates that the critical Weber number takes similar values with the two liquids. The whipping instability practically prevents one from focusing low-viscosity, low-surface tension liquids with Nozzle 1. In fact, the absolute whipping observed with 1-cSt silicone oil made the tapering meniscus touch the inner wall of Nozzle 1, which continuously interrupted the liquid ejection in many experiments.

6. Conclusions

We studied the whipping instability of the tip streaming flow produced when a liquid stream is focused by a gaseous current inside a converging-diverging nozzle (GDVN ejector). We conducted the global linear stability analysis of that flow for both axisymmetric $m = 0$ and lateral $m = 1$ perturbations. For this purpose, the steady base flow was numerically calculated by solving the nonlinear Navier-Stokes equations. Then, we obtain the linear eigenmodes describing the response of that flow to small-amplitude perturbations. The parameter conditions leading to dripping and whipping are assumed to be those for which the growth rate of the $m = 0$ and $m = 1$ dominant eigenmode becomes positive, respectively. The comparison with previous experimental results (Acero et al., 2012) shows good agreement for both the jetting-to-dripping and jetting-to-whipping transitions. Under the conditions considered in those experiments, the capillary-to-neck distance affects the jetting-to-dripping transition but has a negligible effect on the whipping instability. We also examined the influence of the nozzle shape on the jetting stability. Attention was paid to the nozzle convergence rate, defined as the inverse of the distance along which the diameter reduces to its minimum value. The results show that whipping is suppressed as the convergence rate increases, which explains why whipping is much less common in the classical plate-orifice configuration (Gañán Calvo, 1998).

We also examined experimentally the influence of the ejector geometry on the jetting stability. To this end, nozzles that differed only in the convergence rate were fabricated (Muñoz Sánchez et al., 2019). The experiments allowed us to distinguish to types of lateral instabilities: absolute and whipping instabilities depending on whether the meniscus oscillates or not, respectively (Acero et al., 2012). Absolute whipping was clearly observed only when water was focused in the nozzle with the smallest convergence rate and capillary-to-neck distance. The increase of the nozzle convergence rate and capillary-to-neck distance eliminated the whipping instability. Viscosity practically suppressed the meniscus oscillation and induced the transition from absolute to convective whipping. The increase of the convergence rate and capillary-to-neck distance eliminated the whipping instability in the high-viscosity case as well. The reduction of the surface tension decreased roughly in the same proportion the critical pressure drop for absolute whipping.

Flow focusing, as most tip streaming microfluidic realizations (Montanero and Gañán Calvo, 2020), consists of two markedly different fluidic structures: a non-slender confined tapering meniscus and almost cylindrical emitted jet flying in a discharge environment. The steady jetting mode requires the stability of both structures. The theoretical and experimental results presented in this work show the complexity of the whipping phenomenon in flow focusing, as already pointed out by Acero et al. (2012). The stability map strongly depends on many parameter conditions, which prevents one from drawing general conclusions. For instance, the capillary-to-neck distance seems not to affect the whipping instability under the conditions considered in Fig. 6, while it plays a significant role in the present experiments [Figs. 12 and 14(b)]. There are also counter-intuitive results. For example, the liquid viscosity eliminates the whipping instability and enables the jetting regime for $Q \gtrsim 10$ ml/h (Fig. 14). Another example is that the shape of the converging part of the nozzle has a considerable effect on the response of the liquid jet far away from the discharge orifice. This last result can be understood if we assume that convective whipping does not take place because of the wind-induced destabilization of the jet downstream, but due to the convection and amplification of lateral waves emitted by small-amplitude oscillations of the liquid meniscus. Overall, we can probably conclude that ejector shapes closer to the plate-orifice configuration are less prone to producing whipping.

Declaration of Competing Interest

The authors declare that they have no known competing financial interests or personal relationships that could have appeared to influence the work reported in this paper.

CRediT authorship contribution statement

S. Blanco-Trejo: Investigation. **M.A. Herrada:** Software. **A.M. Gañán-Calvo:** Supervision. **A. Rubio:** Investigation. **M.G. Cabezas:** Supervision. **J.M. Montanero:** Supervision, Writing - original draft.

Acknowledgements

Partial support from the Ministerio de Economía y Competitividad and Gobierno de Extremadura (Spain) through Grant Nos. DPI2016-78887 and GR18175 are gratefully acknowledged.

References

Acero, A.J., Ferrera, C., Montanero, J.M., Gañán Calvo, A.M., 2012. Focusing liquid microjets with nozzles. J. Micromech. Microeng. 22, 065011.
Anna, S.L., Mayer, H.C., 2006. Microscale tipstreaming in a microfluidic flow focusing device. Phys. Fluids 18, 121512.
Beyerlein, K.R., Adriano, L., Heymann, M., Kirian, R., Knoska, J., Wilde, F., Chapman, H.N., Bajt, S., 2015. Ceramic micro-injection molded nozzles for serial femtosecond crystallography sample delivery. Rev. Sci. Instrum. 86, 125104.
Castro-Hernández, E., Gundabala, V., Fernández-Nieves, A., Gordillo, J.M., 2009. Scaling the drop size in coflow experiments. New J. Phys. 11, 075021.
Chapman et al., H.N., 2011. Femtosecond x-ray protein nanocrystallography. Nature 470, 73–79.
Chigier, N., Reitz, R.D., 1996. Regimes of jet breakup and breakup mechanisms (physical aspects). In: Recent Advances in Spray Combustion: Spray Atomization and Drop Burning Phenomena. AIAA, Reston, pp. 109–135.
Cohen, I., Li, H., Hougland, J.L., Mrksich, M., Nagel, S.R., 2001. Using selective withdrawal to coat microparticles. Science 292, 265–267.
Collins, R.T., Jones, J.J., Harris, M.T., Basaran, O.A., 2008. Electrohydrodynamic tip streaming and emission of charged drops from liquid cones. Nat. Phys. 4, 149–154.
Cruz-Mazo, F., Herrada, M.A., Gañán Calvo, A.M., Montanero, J.M., 2017. Global stability of axisymmetric flow focusing. J. Fluid Mech. 832, 329–344.
DePonte, D.P., Weierstall, U., Schmidt, K., Warner, J., Starodub, D., Spence, J.C.H., Doak, R.B., 2008. Gas dynamic virtual nozzle for generation of microscopic droplet streams. J. Phys. D 41, 195505.

Dharmansh, D., Chokshi, P., 2016. Axisymmetric instability in a thinning electrified jet. Phys. Rev E 93, 043124.
Dharmansh, D., Chokshi, P., 2017. Stability analysis of an electrospinning jet of a polymeric fluid. Polymer 131, 34–49.
Eggers, J., 1997. Nonlinear dynamics and breakup of free-surface flows. Rev. Mod. Phys. 69, 865–929.
Eggers, J., Villermaux, E., 2008. Physics of liquid jets. Rep. Prog. Phys. 71, 036601.
Forbes, T.P., Sisco, E., 2014. Chemical imaging of artificial fingerprints by desorption electro-flow focusing ionization mass spectrometry. Analyst 139, 2982.
Forbes, T.P., Sisco, E., 2014. Mass spectrometry detection and imaging of inorganic and organic explosive device signatures using desorption electro-flow focusing ionization. Anal. Chem. 86, 7788–7797.
Gañán Calvo, A.M., 1998. Generation of steady liquid microthreads and micron-sized monodisperse sprays in gas streams. Phys. Rev. Lett. 80, 285–288.
Gañán Calvo, A.M., López-Herrera, J.M., Riesco-Chueca, P., 2006. The combination of electrospray and flow focusing. J. Fluid Mech. 566, 421–445.
Gañán Calvo, A.M., Montanero, J.M., Martín-Banderas, L., Flores-Mosquera, M., 2013. Building functional materials for health care and pharmacy from microfluidic principles and flow focusing. Adv. Drug Deliv. Rev. 65, 1447–1469.
Gordillo, J.M., Pérez-Saborid, M., 2005. Aerodynamic effects in the break-up of liquid jets: on the first wind-induced break-up regime. J. Fluid Mech. 541, 1–20.
Gordillo, J.M., Sevilla, A., Campo-Cortés, F., 2014. Global stability of stretched jets: conditions for the generation of monodisperse micro-emulsions using coflows. J. Fluid Mech. 738, 335–357.
Herrada, M.A., Montanero, J.M., 2016. A numerical method to study the dynamics of capillary fluid systems. J. Comput. Phys. 306, 137–147.
Herrada, M.A., Montanero, J.M., Ferrera, C., Gañán Calvo, A.M., 2010. Analysis of the dripping-jetting transition in compound capillary jets. J. Fluid Mech. 649, 523–536.
Hofmann, E., Krüger, K., Haynl, C., Scheibel, T., Trebbin, M., Förster, S., 2018. Microfluidic nozzle device for ultrafine fiber solution blow spinning with precise diameter control. Lab Chip 18, 2225–2234.
Khorrami, M.R., 1989. Application of spectral collocation techniques to the stability of swirling flows. J. Comput. Phys. 81, 206–229.
Lasheras, J.C., Hopfinger, E.J., 2000. Liquid jet instability and atomization in a coaxial gas stream. Annu. Rev. Fluid Mech. 32, 275–308.
Montanero, J.M., Gañán Calvo, A.M., 2020. Dripping, jetting and tip streaming. Rep. Prog. Phys.. in press
Montanero, J.M., Rebollo-Muñoz, N., Herrada, M.A., Gañán Calvo, A.M., 2011. Global stability of the focusing effect of fluid jet flows. Phys. Rev. E 83, 036309.
Muñoz Sánchez, B.N., Gañán Calvo, A.M., Cabezas, M.G., 2019. A new fire shaping approach to produce highly axisymmetric and reproducible nozzles. J. Mater. Process. Tech. 270, 241–253.
Piotter, V., Klein, A., Plewa, K., Beyerlein, K.R., Chapman, H.N., Bajt, S., 2018. Development of a ceramic injection molding process for liquid jet nozzles to be applied for x-ray free-electron lasers. Microsyst. Technol. 24, 1247–1252.
Ponce-Torres, A., Montanero, J.M., Vega, E.J., Gañán Calvo, A.M., 2016. The production of viscoelastic capillary jets with gaseous flow focusing. J. Non-Newton. Fluid Mech. 229, 8–15.
Ponce-Torres, A., Ortega, E., Rubio, M., Rubio, A., Vega, E.J., Montanero, J.M., 2019. Gaseous flow focusing for spinning micro and nanofibers. Polymer 178, 121623.
Ponce-Torres, A., Vega, E.J., Castrejón-Pita, A.A., Montanero, J.M., 2017. Smooth printing of viscoelastic microfilms with a flow focusing ejector. J. Non-Newton. Fluid Mech. 249, 1–7.
Sauter, U.S., Buggisch, H.W., 2005. Stability of initially slow viscous jets driven by gravity. J. Fluid Mech. 533, 237–257.
Stan et al., C.A., 2016. Liquid explosions induced by x-ray laser pulses. Nat. Phys. 12, 966–971.
Si, T., Li, F., Yin, X.Y., Yin, X.Z., 2009. Modes in flow focusing and instability of coaxial liquid-gas jets. J. Fluid Mech. 629, 1–23.
Si, T., Li, G.B., an Z. Q. Zhu, Q.W., Luo, X.S., Xu, R.X., 2016. Optical droplet vaporization of nanoparticle-loaded stimuli-responsive microbubbles. Appl. Phys. Lett. 108, 111109.
Tammisola, O., Lundell, F., Soderberg, L.D., 2012. Surface tension-induced global instability of planar jets and wakes. J. Fluid Mech. 713, 632–658.
Taylor, G., 1964. Disintegration of water drops in electric field. Proc. R. Soc. Lond. A 280, 383–397.
Theofilis, V., 2011. Global linear instability. Annu. Rev. Fluid Mech. 43, 319–352.
Thompson, J.F., Warsi, Z.U.A., 1982. Boundary-fitted coordinate systems for numerical solution of partial differential equations-a review. J. Comput. Phys. 47, 1–108.
Vasireddi, R., Kruse, J., Vakili, M., Kulkarni, S., Keller, T.F., Monteiro, D.C.F., Trebbi, M., 2019. Solution blow spinning of polymer/nanocomposite micro-/nanofibers with tunable diameters and morphologies using a gas dynamic virtual nozzle. Sci. Rep. 9, 14297.
Vega, E.J., Montanero, J.M., Herrada, M.A., Gañán Calvo, A.M., 2010. Global and local instability of flow focusing: the influence of the geometry. Phys. Fluids 22, 64105.
Wiedorn et al., M.O., 2018. Megahertz serial crystallography. Nat. Commun. 9, 4025.
Zahoor, R., Bajt, S., Sarler, B., 2018. Influence of gas dynamic virtual nozzle geometry on micro-jet characteristics. Int. J. Multiphase Flow 104, 152–165.

8.3 Paper III: Global stability analysis of flexible channel flow with a hyperelastic wall

Authors:
Miguel Ángel Herrada, Sergio Blanco Trejo, Jenns Eggers, and Peter S. Stewart.

Paper published in:
Journal of Fluid Mechanics , Volume 934 , 10 March 2022 , A28
DOI: https://doi.org/10.1017/jfm.2021.1131

J. Fluid Mech. (2022), *vol*. 934, A28, doi:10.1017/jfm.2021.1131

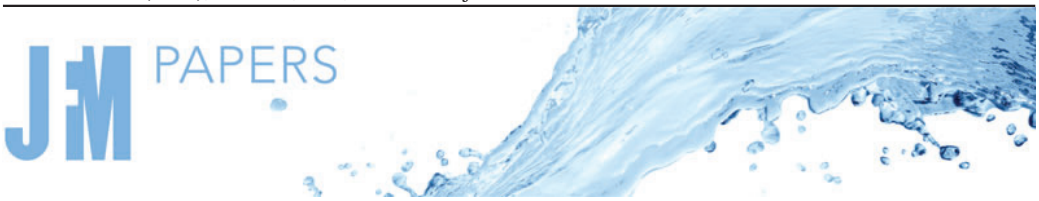

Global stability analysis of flexible channel flow with a hyperelastic wall

M.A. Herrada[1], S. Blanco-Trejo[1], J. Eggers[2] and P.S. Stewart[3],†

[1]E.S.I., Universidad de Sevilla, Camino de los Descubrimientos s/n, 41092, Spain

[2]School of Mathematics, University of Bristol, Fry Building, Bristol BS8 1UG, UK

[3]School of Mathematics and Statistics, University of Glasgow, Mathematics and Statistics Building, University Place, Glasgow G12 8QQ, UK

(Received 29 January 2021; revised 20 October 2021; accepted 12 December 2021)

We consider the stability of flux-driven flow through a long planar rigid channel, where a segment of one wall is replaced by a pre-tensioned hyperelastic (neo-Hookean) solid of finite thickness and subject to a uniform external pressure. We construct the steady configuration of the nonlinear system using Newton's method with spectral collocation and high-order finite differences. In agreement with previous studies, which use an asymptotically thin wall, we show that the thick-walled system always has at least one stable steady configuration, while for large Reynolds numbers the system exhibits three co-existing steady states for a range of external pressures. Two of these steady configurations are stable to non-oscillatory perturbations, one where the flexible wall is inflated (the upper branch) and one where the flexible wall is collapsed (the lower branch), connected by an unstable intermediate branch. We test the stability of these steady configurations to oscillatory perturbations using both a global eigensolver (constructed based on an analytical domain mapping technique) and also fully nonlinear simulations. We find that both the lower and upper branches of steady solutions can become unstable to self-excited oscillations, where the oscillating wall profile has two extrema. In the absence of wall inertia, increasing wall thickness partially stabilises the onset of oscillations, but the effect remains weak until the wall thickness becomes comparable to the width of the undeformed channel. However, with finite wall inertia and a relatively thick wall, higher-frequency modes of oscillation dominate the primary global instability for large Reynolds numbers.

Key words: flow-vessel interactions

† Email address for correspondence: peter.stewart@glasgow.ac.uk

1. Introduction

Human physiology includes a wide number of examples of fluid flow through flexible-walled conduits including blood flow through the circulation (from rapid flow in the heart and large arteries to slow viscous flows through the capillaries), air flow through the lungs and upper airways, urine flows in the excretory system and peristaltic flows through the colon. In some circumstances these flows can exhibit instability, where the flow can interact with the flexible wall in a non-trivial way. Of particular interest in this study is the onset of self-excited oscillations, where the flow and the wall can spontaneously transition to an oscillatory limit cycle; in some cases this oscillation can even become chaotic. These oscillations manifest in physiological problems such as blood pressure measurement in the form of audible Korotkoff noises (Bertram, Raymond & Butcher 1989), and wheezing in the lung airways (Gavriely *et al.* 1989).

Self-excited oscillations in flexible-walled vessels can be studied experimentally using a Starling resistor, a deceptively simple device featuring liquid flow driven through a section of externally pressurised flexible tubing mounted between two rigid pipes. Originally used as a flow resistor in cardiac experiments (Knowlton & Starling 1912), it has since become a canonical experiment for investigating fluid–structure interaction in its own right. In these experiments flow is driven using either a prescribed pressure or a prescribed flow rate, and the choice of set-up heavily influences the structure of the resulting oscillations. Results from the experiments are well summarised elsewhere (e.g. Bertram 2003; Grotberg & Jensen 2004; Heil & Hazel 2011), but we note that these self-excited oscillations occur in distinct frequency bands (Bertram, Raymond & Pedley 1990), and exhibit complicated nonlinear limit cycles which can be characterised using the methods of dynamical systems (Bertram, Raymond & Pedley 1991). Note that these experiments are typically conducted with relatively thick-walled tubes. For example, Bertram *et al.* (1990, 1991) used tubes of wall thickness to baseline radius ratio of 0.3, while Bertram & Castles (1999) used tubes with a thickness to radius ratio of 0.37.

There have been a number of theoretical studies of the Starling resistor set-up in an attempt to explain the underlying mechanisms leading to these different families of oscillation. Formulation of the full three-dimensional fluid structure interaction problem in a collapsible tube involves coupling unsteady Newtonian flow to a fully deformable elastic tube. While most theoretical models treat the tube wall as a thin shell, slightly reducing the complexity of the system, these models still require vast computational resources to resolve the unsteady oscillatory flow (Heil & Boyle 2010). Some analytical progress can be made in the limit of large membrane tension (where oscillations are high frequency, Whittaker *et al.* 2010), but this formulation is restricted to a state where the tube wall is almost uniform that has not yet been realised experimentally.

The flexible tubing used in Starling resistor experiments is typically much thicker than is appropriate to model using thin shell theory. To date, the only theoretical studies which incorporate a thick-walled tube have been restricted to steady flow configurations (Marzo, Luo & Bertram 2005; Zhang, Luo & Cai 2018). In this paper we seek to address the stability of flow in a Starling resistor analogue with a thick hyperelastic wall, and investigate the role of wall thickness in promoting or inhibiting instability.

Given the computational difficulty and expense of full three-dimensional unsteady models, theoretical study has often focused on empirical lumped parameter or cross-sectionally averaged models for flow in collapsible tubes (e.g. Shapiro 1977; Bertram & Pedley 1982; Jensen 1990; Armitstead, Bertram & Jensen 1996), which have replicated many of the features noted in Starling resistor experiments, such as non-uniform steady profiles and spontaneous transition to self-excited oscillations in distinct

oscillation frequencies. However, the flow field in these models is still approximate and misses many of the subtleties of flow separation and energy dissipation.

To make progress in understanding the mechanisms of instability driving self-excited oscillations, a compromise system is needed which is less complicated than fully three-dimensional flow, but reduces the number of empirical assumptions needed for the lumped models. Pedley (1992) proposed a two-dimensional analogue of the Starling resistor, consisting of a planar rigid channel where a section of one wall has been replaced by a flexible sheet. This set-up has since become the subject of a wide variety of computational (e.g. Luo & Pedley 1995, 1996, 1998, 2000; Heil 2004) and theoretical studies (e.g. Jensen & Heil 2003; Guneratne & Pedley 2006; Stewart *et al.* 2010; Pihler-Puzović & Pedley 2013). Despite reduced computational cost compared with the three-dimensional tube system, a full exploration of the parameter space for this collapsible channel analogue has not yet been attempted, although progress toward quantifying the mechanisms of instability has been made in various regions of the parameter space. For example, in the case of prescribed upstream flux (the subject of this study), Xu, Billingham & Jensen (2014) quantified the mechanism driving 'sawtooth' oscillations in the asymptotic limit of a long downstream rigid section, where the nonlinear oscillation is driven by the resonance of two distinct modes of perturbation (mode-1 and mode-2) of similar frequency and the same wavelength, coupled by sloshing flow in the downstream rigid section. Furthermore, Huang (2001) simplified the flux-driven collapsible channel system by imposing an external pressure gradient on the flexible wall, which facilitated decomposition of the oscillatory flow into a sum of sinusoidal modes. This analysis reveals an alternative mechanism of oscillatory instability, driven by an imbalance between (unstable) downstream propagating waves (which transfer energy from the flow to the wall) and (stable) upstream propagating waves (which transfer energy back from the wall to the fluid).

Further insights into the mechanisms of instability in these collapsible channel flows have been obtained using approximate one-dimensional models of the asymmetric channel system (derived using a flow-profile assumption, Stewart, Waters & Jensen 2009; Stewart *et al.* 2010; Xu, Billingham & Jensen 2013; Xu *et al.* 2014; Xu & Jensen 2015; Stewart 2017). In particular, a detailed exploration of the parameter space for flux-driven oscillations with constant external pressure was presented by Stewart (2017), where he found that when the fluid is inviscid, steady states only exist above a critical value of the membrane tension (for all other parameters held fixed), with a stable branch and an unstable branch (where the unstable branch is more collapsed than the stable branch). This critical point appears to be an organising centre of the dynamical system, in that many of the unsteady features of the system originate close to this point (such as the neutral curves for the two different families of self-excited oscillations). The importance of the critical point for inviscid steady states has previously been elucidated by Xu *et al.* (2013), who used an external pressure gradient. Stewart (2017) also described another branch of steady solutions maintained by viscous effects, which becomes increasingly collapsed as the wall tension is reduced. As the Reynolds number increases this viscous branch of steady solutions merges with one of the (essentially) inviscid branches. When the viscous branch merges smoothly with the stable inviscid branch then the stable steady state is unique. However, the other possibility is that the viscous branch merges with the unstable inviscid branch in a limit point bifurcation, where the system then exhibits three co-existing steady states across a narrow region of the parameter space: the stable inviscid solutions become the upper branch, the unstable inviscid solutions become the intermediate branch and the stable viscous solutions become the lower branch.

Stewart (2017) also showed that the lower branch of steady solutions can become unstable to two distinct families of self-excited oscillation, with high and low frequency, respectively. However, in addition to the flow-profile assumption, this study considered the flexible wall to be a thin (massless) pre-stressed membrane with no bending rigidity. To overcome these simplifications, this study revisits the predictions of Stewart (2017) by modelling the flexible wall as a pre-tensioned hyperelastic solid, using the finite element method to compute the fully two-dimensional steady wall and flow profiles, and test their stability to time-dependent perturbations using a fully two-dimensional eigensolver. Our new model includes the wall thickness and wall mass as explicit parameters, and we investigate their influence on the predictions below.

Another approach for theoretical modelling of this collapsible channel system has very recently been presented by Wang, Luo & Stewart (2021*a*,*b*), who treat the flexible wall as an asymptotically thin beam with resistance to both bending and stretching but with no pre-tension (based on an earlier model by Cai & Luo 2003; Luo *et al.* 2008). Using fully nonlinear simulations of this model, they identified a similar three-branch steady system for some parameters, showing that both the upper and lower branches of oscillation could (independently) become unstable to self-excited oscillations (Wang *et al.* 2021*a*) and these families of oscillations could merge together for low external pressures (Wang *et al.* 2021*b*). In this case the upper branch instability is restricted to a region in the near neighbourhood of that which exhibits multiple steady states (Wang *et al.* 2021*b*). In this study we also isolate a family of upper branch instabilities, but show that these are not limited to the region with multiple steady states but are instead unstable well away from the region of parameter space which exhibits instabilities of the lower steady branch (see § 3.4 below).

The role of wall mass in the onset of self-excited oscillations in flexible-walled vessels has already been considered for the flexible wall modelled as a thin membrane. For example, in the asymmetric channel system, Luo & Pedley (1998) coupled the heavy membrane to fully two-dimensional (unsteady) flow, showing that increasing the wall mass expands the region of parameter space where the system exhibits the primary global instability, and also results in an additional high-frequency oscillatory mode (superimposed on the fundamental mode) which eventually grows to dominate the lower-frequency mode. Also, Pihler-Puzović & Pedley (2014) investigated this channel system using interactive boundary layer theory, showing that wall mass drives an oscillatory instability which is always unstable in the presence of a cross-stream pressure gradient across the core flow (the system is always neutrally stable with no cross-stream gradient). Finally, Walters, Heil & Whittaker (2018) considered the role of wall mass in a thin shell model of flow in a collapsible tube in the limit of large pre-stress (where the tube is almost uniform), finding that wall inertia destabilises the primary mode of instability of the system while also lowering the corresponding oscillation frequency.

In this paper we consider the planar channel analogue of the Starling resistor introduced by Pedley (1992), and propose a new numerical method to solve the combined fluid and solid problem based on that developed by Snoeijer *et al.* (2020) (which already has application to viscoelastic fluids, Eggers, Herrada & Snoeijer 2020). The model formulation is described in § 2, highlighting the novel features of the numerical method. In particular, we treat the elastic solid as a pre-tensioned hyperelastic material of uniform initial thickness with non-negligible density and subject to a uniform external pressure. We validate this numerical method against the steady predictions of Heil (2004), who considered an identical set-up with a thin shell model for the wall (§ 3.1), use unsteady simulations to examine the transition between the upper and lower branches of steady solutions (§ 3.2), examine the onset of self-excited oscillations from these steady solutions

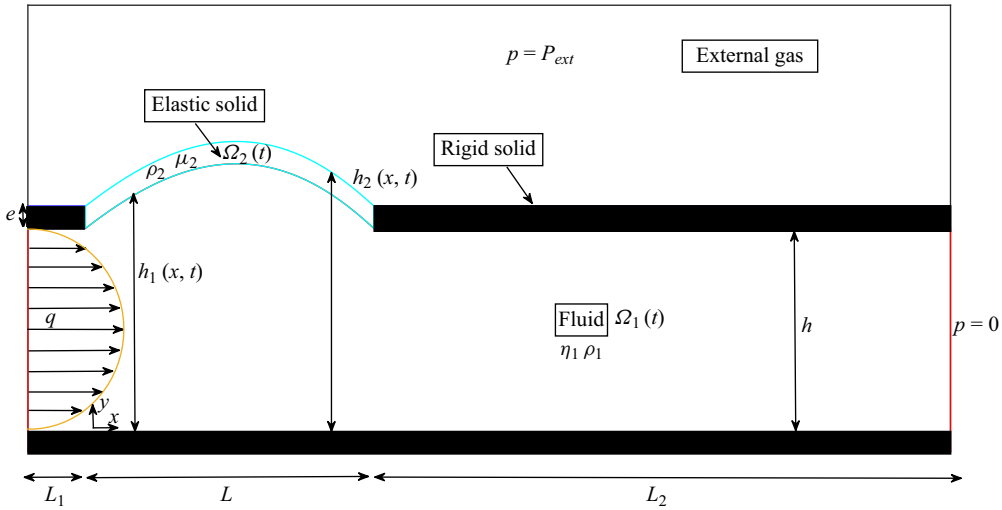

Figure 1. Sketch of the flow geometry considered in this study.

(§ 3.3), before using our new model to examine the role of membrane pre-tension (§ 3.4), the dynamics of oscillations growing from the upper branch of steady solutions (§ 3.5) as well as the role of wall thickness (§ 3.6) and wall inertia (§ 3.7) on the nonlinear steady solutions and the accompanying onset of oscillation.

2. Model formulation

We consider the configuration sketched in figure 1, where an incompressible Newtonian fluid is flowing through a planar rigid (two-dimensional) channel of uniform internal width h. An interior section of length L is removed from the upper wall of the channel and replaced by a pre-tensioned elastic solid of (initially) uniform thickness e, subject to a passive external gas at uniform pressure, P_{ext}. This elastic wall can be deformed by the load of the external gas and by the fluid traction. The rigid sections upstream and downstream of the compliant segment are of length L_1 and L_2, respectively. In this case the flow is driven by a prescribed upstream flux q, while the fluid pressure at the downstream end of the channel can be set to zero without loss of generality. The stability of this fluid–structure interaction problem has already been studied extensively using reduced models for the elastic wall (e.g. Luo & Pedley 1996; Jensen & Heil 2003; Luo *et al.* 2008; Stewart 2017). In this work, we model the wall as a continuum hyperelastic solid of finite thickness, with no simplifications or reductions. Our formulation is based on first-order elasticity (elastic strain energy function dependent on the strain tensor), which places some restrictions on the boundary conditions that can be imposed.

2.1. *Equations of motion*

The fluid domain Ω_1 is described by the planar coordinates $\boldsymbol{x} = x\boldsymbol{e}_x + y\boldsymbol{e}_y$, where x parametrises the lower wall of the channel, with $x = 0$ at the intersection between the upstream rigid segment and the compliant segment, while y parametrises the direction normal to the entirely rigid wall pointing into the fluid (in the plane of the channel). The solid domain Ω_2 is measured relative to a reference configuration parametrised by the

coordinates $\boldsymbol{X} = X\boldsymbol{e}_x + Y\boldsymbol{e}_y$, where X parametrises the lower surface of the flat wall and Y parametrises the direction pointing into the wall (in the plane of the channel).

The conservation of mass and momentum equations in the fluid ($i = 1$) and solid ($i = 2$) subdomains are given by

$$\boldsymbol{\nabla} \cdot \boldsymbol{v}_i = 0, \quad (i = 1, 2), \tag{2.1a}$$

$$\rho_i \left(\frac{\partial \boldsymbol{v}_i}{\partial t} + (\boldsymbol{v}_i \cdot \boldsymbol{\nabla})\, \boldsymbol{v}_i \right) = \boldsymbol{\nabla} \cdot \boldsymbol{\sigma}_i, \quad (i = 1, 2), \tag{2.1b}$$

where ρ_i is the density, $\boldsymbol{I}$ is the identity tensor, $\boldsymbol{v}_i$ the velocity field and $\boldsymbol{\sigma}_i$ is the stress tensor of material i ($i = 1, 2$). Each stress tensor depends on the characteristics of the material through a constitutive model. In region 1 we consider an incompressible Newtonian fluid, where this stress tensor takes the form

$$\boldsymbol{\sigma}_1 = -p_1 \boldsymbol{I} + \eta_1 \left(\boldsymbol{\nabla} \boldsymbol{v}_1 + \boldsymbol{\nabla} \boldsymbol{v}_1^{\mathrm{T}} \right), \tag{2.1c}$$

where p_1 is the fluid pressure and η_1 is the fluid viscosity. In region 2 we consider a neo-Hookean (hyperelastic) solid which has a pre-stress, $\boldsymbol{\sigma}_{2p}^{(0)}$, in the initial undeformed state, where the stress tensor is given by (Snoeijer *et al.* 2020)

$$\boldsymbol{\sigma}_2 = -p_2 \boldsymbol{I} + \mu_2 \left(\boldsymbol{F} \cdot \boldsymbol{F}^T - \boldsymbol{I} \right) + \boldsymbol{F} \cdot \boldsymbol{\sigma}_{2p}^{(0)} \cdot \boldsymbol{F}^{\mathrm{T}}, \tag{2.1d}$$

where p_2 is the solid pressure, μ_2 is the elastic shear modulus, $\boldsymbol{x}(\boldsymbol{X}, t)$ is the position of a material point after deformation of the solid and $\boldsymbol{F} = \partial \boldsymbol{x}/\partial \boldsymbol{X}$ is the deformation gradient tensor. In the initial state, $\boldsymbol{x} = \boldsymbol{X}$ and $\boldsymbol{F} \cdot \boldsymbol{F}^{\mathrm{T}} = \boldsymbol{I}$. To make a connection between the Eulerian formulation for the conservation of mass and momentum equations for the solid ((2.1) with $i = 2$) and the Lagrangian formulation for the elastic stress, we need to determine the deformation generated by transport by the solid velocity $\boldsymbol{v}_2$. This is achieved using the inverse Lagrangian map $\boldsymbol{X}(\boldsymbol{x}, t)$ (Kamrin, Rycroft & Nave 2012), which satisfies

$$\frac{\partial \boldsymbol{X}}{\partial t} + \boldsymbol{v}_2 \cdot \boldsymbol{\nabla} \boldsymbol{X} = 0, \tag{2.1e}$$

because the reference coordinates are invariant under the flow.

Given the bi-dimensionality of the problem, the material points can be expressed in Cartesian coordinates and so the velocity vectors can be written as

$$\boldsymbol{v}_i = v_{yi}\boldsymbol{e}_y + v_{xi}\boldsymbol{e}_x, \quad (i = 1, 2), \tag{2.1f}$$

while the stress tensors can be written as

$$\boldsymbol{\sigma} = \sigma_{yy}\boldsymbol{e}_y \otimes \boldsymbol{e}_y + \sigma_{yx}\boldsymbol{e}_y \otimes \boldsymbol{e}_x + \sigma_{xy}\boldsymbol{e}_x \otimes \boldsymbol{e}_y + \sigma_{xx}\boldsymbol{e}_x \otimes \boldsymbol{e}_x, \tag{2.1g}$$

and finally the deformation tensor in the solid can be written as

$$\boldsymbol{F} = \frac{\partial y}{\partial Y}\boldsymbol{e}_y \otimes \boldsymbol{e}_y + \frac{\partial y}{\partial X}\boldsymbol{e}_y \otimes \boldsymbol{e}_x + \frac{\partial x}{\partial Y}\boldsymbol{e}_x \otimes \boldsymbol{e}_y + \frac{\partial x}{\partial X}\boldsymbol{e}_x \otimes \boldsymbol{e}_x. \tag{2.1h}$$

In the undeformed position the elastic solid is subject to an initial longitudinal tension, T_o, and therefore the initial stress is $\boldsymbol{\sigma}_{2p}^{(0)} = (T_0/e)\boldsymbol{e}_x \otimes \boldsymbol{e}_x$.

For the elastic domain, it is convenient to replace the incompressibility equation based on the velocity field ((2.1*a*) with $i = 2$) by a constraint involving the deformation tensor $\boldsymbol{F}$ (Snoeijer *et al.* 2020) in the form

$$\det(\boldsymbol{F}) = \left(\frac{\partial y}{\partial Y}\frac{\partial x}{\partial X} - \frac{\partial y}{\partial X}\frac{\partial x}{\partial Y} \right) = 1. \tag{2.1i}$$

To impose the upstream flux boundary condition for the liquid, we impose a Poiseuille profile at the channel entrance, $x = -L_1$, in the form

$$v_{1x} = \frac{6q}{h^3}\, y(h-y), \quad v_{1y} = 0, \quad (x = -L_1, 0 \leqslant y \leqslant h). \tag{2.1j}$$

At the channel exit, $x = L + L_2$, we impose zero fluid pressure, $p_1 = 0$. Along the entirely rigid wall we apply no-slip conditions in the form

$$v_{x1} = v_{y1} = 0, \quad (y = 0, -L_1 \leqslant x \leqslant L + L_2). \tag{2.1k}$$

Similarly, along the rigid parts of the upper wall we apply no-slip boundary conditions in the form

$$v_{x1} = v_{y1} = 0, \quad (y = h, -L_1 \leqslant x \leqslant 0, x \geqslant L). \tag{2.1l}$$

We assume that the flexible surface (where the elastic solid and the fluid interact) can be written as a function of x (i.e. the surface does not overturn or expand beyond the range $0 \leqslant x \leqslant L$), so that $y = h_1(x, t)$. Across this interface we impose that the velocity field must be continuous, in the form

$$v_{x1} = v_{x2}, \quad v_{y1} = v_{y2}, \quad (y = h_1, 0 \leqslant x \leqslant L), \tag{2.1m}$$

and impose a balance of normal and tangential stresses between the solid and the fluid, in the form

$$\boldsymbol{n}_1 \cdot (\boldsymbol{\sigma}_1 - \boldsymbol{\sigma}_2) \cdot \boldsymbol{n}_1 = 0, \quad \boldsymbol{t}_1 \cdot (\boldsymbol{\sigma}_1 - \boldsymbol{\sigma}_2) \cdot \boldsymbol{n}_1 = 0, \tag{2.1n}$$

where

$$\boldsymbol{n}_1 = \frac{\boldsymbol{e}_y - \boldsymbol{e}_x h_{1,x}}{(1 + h_{1,x}^2)^{1/2}}, \quad \boldsymbol{t}_1 = \frac{\boldsymbol{e}_x + \boldsymbol{e}_y h_{1,x}}{(1 + h_{1,x}^2)^{1/2}}, \tag{2.1o}$$

are normal and tangential vectors to the surface $y = h_1(x, t)$, respectively, and the subscript x represents a derivative with respect to x. In this first-order elasticity approach we enforce no deformation along the surfaces where the elastic material is adhered to the rigid walls (i.e. the displacement of the solid is clamped along two edges of the rectangle in contact with the rigid walls), in the form

$$v_{2x} = v_{2y} = 0, \quad Y = y, \quad X = x, \quad (x = 0, x = L \text{ with } h \leqslant y \leqslant h + e). \tag{2.1p}$$

However, our approach does not replicate the resistance to bending of a classical Euler–Bernoulli beam. This would require second-order (or strain gradient) elasticity, where the elastic strain energy function is assumed to depend on both the strain tensor and the strain gradient tensor (Bertram & Forest 2020). In that case one must impose additional constraints on the contact between the beam and the rigid wall e.g. conditions on the derivatives of displacement, such as prescribed slope or torque. Finally, we denote

the external surface of the flexible wall as $y = h_2(x, t)$, $(0 \leqslant x \leqslant L)$ and impose that the normal and tangential elastic stresses are balanced with the external pressure, in the form

$$\boldsymbol{n}_2 \cdot (\boldsymbol{\sigma}_2 - P_{ext}\boldsymbol{I}) \cdot \boldsymbol{n}_2 = 0, \quad \boldsymbol{t}_2 \cdot (\boldsymbol{\sigma}_2) \cdot \boldsymbol{n}_2 = 0, \tag{2.1q}$$

where

$$\boldsymbol{n}_2 = \frac{\boldsymbol{e}_y - \boldsymbol{e}_x h_{2,x}}{(1 + h_{2,x}^2)^{1/2}}, \quad \boldsymbol{t}_2 = \frac{\boldsymbol{e}_x + \boldsymbol{e}_y h_{2,x}}{(1 + h_{2,x}^2)^{1/2}}, \tag{2.1r}$$

are normal and tangential vectors to the surface $y = h_2(x, t)$.

2.2. *Mapping technique*

The numerical technique used in this study is a variation of that developed by Herrada & Montanero (2016) for interfacial flows and extended by Snoeijer *et al.* (2020) to apply to hyperelastic solids. The spatial domain occupied by the fluid, $\Omega_1(t)$, is mapped onto a rectangular domain (parametrised by Cartesian coordinates ξ_1 and χ_1, where ξ_1 parametrises the lower rigid wall and χ_1 parametrises the channel inlet) by means of a non-singular mapping

$$y = f_1(\xi_1, \chi_1, t), \quad x = g_1(\xi_1, \chi_1, t), \quad [-L_1 \leqslant \xi_1 \leqslant L + L_2] \times [0 \leqslant \chi_1 \leqslant 1], \tag{2.2}$$

where the shape functions f_1 and g_1 are obtained as part of the solution. In order to capture large anisotropic deformations, the following quasi-elliptic transformation (Dimakopoulos & Tsamopoulos 2003) was applied:

$$g_{22}\frac{\partial^2 f_1}{\partial \xi_1^2} + g_{11}\frac{\partial^2 f_1}{\partial \chi_1^2} - 2g_{12}\frac{\partial^2 f_1}{\partial \xi_1 \partial \chi_1} = Q, \tag{2.3a}$$

$$g_{22}\frac{\partial^2 g_1}{\partial \xi_1^2} + g_{11}\frac{\partial^2 g_1}{\partial \chi_1^2} - 2g_{12}\frac{\partial^2 g_1}{\partial \xi_1 \partial \chi_1} = 0, \tag{2.3b}$$

where the coefficients take the form

$$g_{11} = \left(\frac{\partial g_1}{\partial \xi_1}\right)^2 + \left(\frac{\partial f_1}{\partial \xi_1}\right)^2, \quad g_{22} = \left(\frac{\partial g_1}{\partial \chi_1}\right)^2 + \left(\frac{\partial f_1}{\partial \chi_1}\right)^2, \quad g_{12} = \frac{\partial g_1}{\partial \chi_1}\frac{\partial g_1}{\partial \xi_1} + \frac{\partial f_1}{\partial \chi_1}\frac{\partial f_1}{\partial \xi_1}, \tag{2.4a–c}$$

with

$$Q = -\left(\frac{\partial D_1}{\partial \chi_1}\frac{\partial f_1}{\partial \xi_1} - \frac{\partial D_1}{\partial \xi_1}\frac{\partial f_1}{\partial \chi_1}\right)\frac{J}{D_1}, \quad J = \frac{\partial g_1}{\partial \chi_1}\frac{\partial f_1}{\partial \xi_1} - \frac{\partial g_1}{\partial \xi_1}\frac{\partial f_1}{\partial \chi_1}, \tag{2.5a,b}$$

and

$$D_1 = \epsilon_p \sqrt{\left[\left(\frac{\partial f_1}{\partial \xi_1}\right)^2 + \left(\frac{\partial g_1}{\partial \xi_1}\right)^2\right] \Big/ \left[\left(\frac{\partial f_1}{\partial \chi_1}\right)^2 + \left(\frac{\partial g_1}{\partial \chi_1}\right)^2\right]} + (1 - \epsilon_p). \tag{2.6}$$

In the above expressions, ϵ_p is a free parameter between 0 and 1 where the case $\epsilon_p = 0$ corresponds to the classical elliptical transformation. All the simulations in this work were conducted using $\epsilon_p = 0.2$. Although there is no overturning in the wall profiles for the cases analysed in this work, this transformation of the liquid domain facilitates the analysis of more complicated geometries. For example, it has been successfully used to describe pinch-off in pendant drops (Ponce-Torres *et al.* 2020).

The spatial domain occupied by the elastic solid in the current stage, $\Omega_2(t)$, and in the initial stage, Ω_{2o}, are also mapped onto rectangular domains (parametrised by Cartesian coordinates ξ_2 and χ_2, where ξ_2 parametrises the lower surface of the flexible wall and χ_2 parametrises the edges in contact with the rigid segments of the channel) by means of non-singular mappings in the form

$$\left.\begin{array}{c} y = f_2(\xi_2, \chi_2, t), \quad x = g_2(\xi_2, \chi_2, t), \\ Y = F_2(\xi_2, \chi_2, t), \quad X = G_2(\xi_2, \chi_2, t), \quad [0 \leqslant \xi_2 \leqslant L] \times [0 \leqslant \chi_2 \leqslant 1], \end{array}\right\} \tag{2.7}$$

where again the functions f_2, g_2, F_2 and G_2 should be obtained as a part of the solution. To determine these functions, the following equations have been used:

$$g_2 = \xi_2, \tag{2.8a}$$

$$F_2 = h + e\chi_2. \tag{2.8b}$$

Note that (2.8*a*) guarantees that the discretisation used for the variable ξ_2 is automatically applied to variable x. Finally, (2.8*b*) indicates that at the initial stage the elastic part of the upper channel wall is a perfect rectangle of uniform width e.

Some additional boundary conditions for the shape functions are needed to close the problem. At the channel entrance, we impose

$$g_1 = -L_1, \quad f_1 = h\chi_1, \quad (x = \xi_1 = -L_1), \tag{2.9a}$$

while at the channel exit, we use

$$g_1 = L + L_2, \quad f_1 = h\chi_1, \quad (x = \xi_1 = L + L_2). \tag{2.9b}$$

On the lower wall, we impose

$$g_1 = \xi_1, \quad f_1 = 0, \quad (y = \chi_1 = 0), \tag{2.9c}$$

while on the rigid parts of the upper channel wall, we use

$$g_1 = \xi_1, \quad f_1 = h, \quad (-L_1 \leqslant x = \xi_1 \leqslant 0,\ x = \xi_1 \geqslant L,\ y = h). \tag{2.9d}$$

At the flexible surface, we also impose

$$f_1 = f_2, \quad g_1 = g_2, \quad (0 \leqslant x = \xi_1 = \xi_2 \leqslant L, y = h_1(x, t), \chi_1 = 1, \chi_2 = 0). \tag{2.9e}$$

Finally, we enforce no displacement of the elastic solid along the two edges of the rectangle in contact with the rigid walls, in the form

$$\left.\begin{array}{c} g_2 = G_2 = \xi_2, \quad f_2 = F_2 = h + e\chi_2, \\ (x = \xi_2 = 0, x = \xi_2 = L, h \leqslant y \leqslant (h + e), 0 \leqslant \chi_2 \leqslant 1). \end{array}\right\} \tag{2.9f}$$

Figure 2 shows an example of the mappings used in this work. The green (magenta) lines represent the liquid (solid) mesh in the real space (bottom panel) and in the computational domain (top panel). The unknown variables in the liquid domain are f_1, g_1, p_1, v_{1x} and v_{1y} while the unknown variables in the solid domain are f_2, g_2, p_2, v_{2x}, v_{2y}, F_2 and G_2. All the derivatives appearing in the governing equations are expressed in terms of χ, ξ and t. These mappings are applied to the governing equations (2.1) and the resulting equations are discretised in the χ-direction with n_{χ_1} and n_{χ_2} Chebyshev spectral collocation points in the liquid and solid domains, respectively. Conversely, in the ξ-direction we use fourth-order finite differences with n_{ξ_1} and n_{ξ_2} equally spaced points in the liquid and solid domains, respectively. The results presented in this work were carried out using $n_{\xi_1} = 641$, $n_{\xi_2} = 201$, $n_{\chi_1} = 19$ and $n_{\chi_2} = 14$. In the Appendix we demonstrate that the eigenvalues characterising the linear modes do not change significantly when the number of grid points is increased.

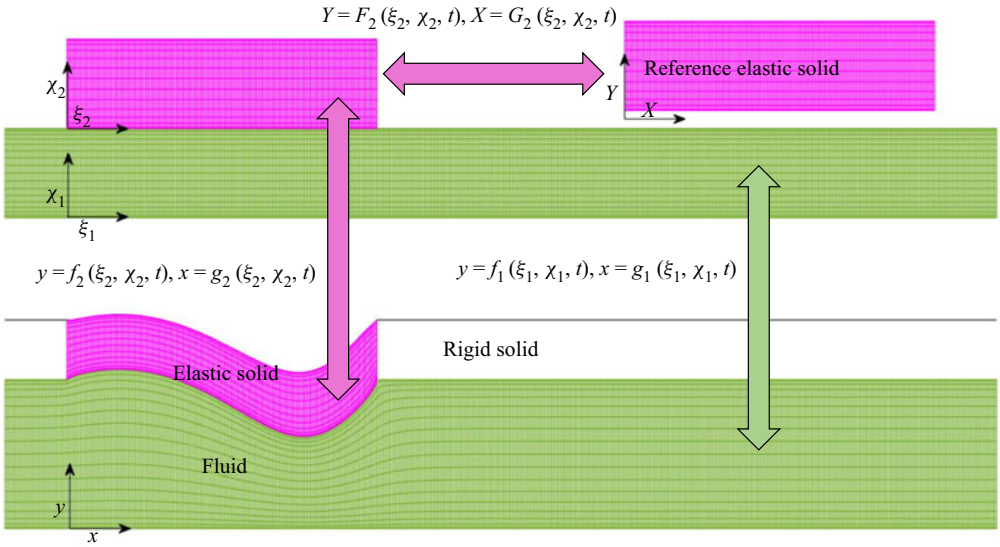

Figure 2. Computational subdomains and grids for the original and mapped variables.

2.3. *Steady solutions*

Steady solutions of the nonlinear equations (2.1) with all variables independent of time are obtained by solving all equations simultaneously (a so-called monolithic scheme) using a Newton–Raphson technique. One of the main characteristics of this procedure is that the elements of the Jacobian matrix $\mathcal{J}^{(p,q)}$ of the discretised system of equations are obtained by combining analytical functions and collocation matrices. This allows us to take advantage of the sparsity of the resulting matrix to reduce the computation time on each Newton step.

We denote the steady solution of the system with the subscript b. We trace the steady solutions as a function of the model parameters and quantify using the minimal and maximal positions of the lower surface of the flexible wall, denoted as

$$\hat{h}_{min} = \min_x \left(\frac{h_{1b}}{h} \right) \quad \text{and} \quad \hat{h}_{max} = \max_x \left(\frac{h_{1b}}{h} \right). \tag{2.10a,b}$$

2.4. *Small amplitude perturbations*

To test the stability of a given steady state we calculate the linear two-dimensional global modes by assuming the temporal dependence

$$\Psi(x, y; t) = \Psi_b(x, y) + \epsilon\, \delta\Psi(x, y) \mathrm{e}^{-\mathrm{i}\omega t}, \quad (\epsilon \ll 1), \tag{2.11}$$

where $\Psi(x, y; t)$ represents any dependent variable while $\Psi_b(x, y)$ and $\delta\Psi(x, y)$ denote the base (steady) solution and the spatial dependence of the eigenmode for that variable, respectively, while $\omega = \omega_r + \mathrm{i}\omega_i$ is the frequency (an eigenvalue). Both the eigenfrequencies and the corresponding eigenmodes are calculated as a function of the governing parameters. The dominant eigenmode is that with the largest growth factor ω_i. If that growth factor is positive, the base flow is asymptotically unstable.

As explained by Herrada & Montanero (2016), the numerical procedure used to solve the steady problem can be easily adapted to solve the eigenvalue problem which determines the linear global modes of the system. In this case, the temporal derivatives are

computed assuming the temporal dependence (2.11). The spatial dependence of the linear perturbation $\delta\Psi^{(q)}$ is the solution to the generalised eigenvalue problem $\mathcal{J}_b^{(p,q)}\delta\Psi^{(q)} = i\omega\mathcal{Q}_b^{(p)}\delta\Psi^{(q)}$, where $\mathcal{J}_b^{(p,q)}$ is the Jacobian of the system evaluated with the basic solution $\Psi_b^{(q)}$, and $\mathcal{Q}_b^{(p,q)}$ accounts for the temporal dependence of the problem. This generalised eigenvalue problem is solved using MATLAB eigs function.

2.5. *Fully nonlinear dynamical simulations*

The numerical method can be extended to compute unsteady solutions of the full nonlinear equations (2.1). Temporal derivatives are discretised using second-order backwards differences and at each time step the resulting system of (nonlinear algebraic) equations is solved using the Newton–Raphson technique (as in § 2.3). Simulations employ the same mesh as the steady simulations with a fixed timestep of $\Delta t = 0.0125$ required to capture the strong oscillations observed in the fully saturated nonlinear regime (this translates into approximately 640 timesteps per period for the oscillation shown in figure 12 below). We have verified that the nonlinear predictions are unchanged when the timestep is reduced to $\Delta t = 0.0075$. Given the large number of timesteps required, these simulations are much more computationally expensive than the global stability eigensolver and so only two relevant cases will be considered to support the global stability analysis (see figures 6 and 12 below). For example, the nonlinear simulation described in § 3.5 takes more than one week to reach the corresponding nonlinear limit cycle, while for the same machine the computation of the eigenvalues takes just a few minutes.

2.6. *Control parameters*

To non-dimensionalise the system we scale all lengths on the baseline channel width h, velocities on the mean inlet speed q/h, time on h^2/q, the fluid stress on the viscous scale $\eta_1 q/h^2$ and the solid stress on the elastic shear modulus μ_2. The solutions are characterised by the dimensionless profile of the interface between fluid and solid $\hat{h}_{b1} = h_{b1}/h$, the dimensionless frequency $\hat{\omega} = \omega q/h^2$ and the dimensionless eigenfunction profile of the surface between the fluid and the solid, denoted $\widehat{\delta h}_1 = (\delta h_1)/h$. As is conventional in this literature, a wall profile is termed as mode-n if $\widehat{\delta h}_1$ has n extrema across the compliant segment. The resulting problem is governed by six dimensionless parameters,

$$Re = \frac{\rho_1 q}{\eta_1}, \quad Q = \frac{\eta_1 q}{h^2\mu_2}, \quad \hat{p}_{ext} = \frac{P_{ext}}{\mu_2}, \quad \hat{T}_0 = \frac{T_0}{h\mu_2}, \quad \hat{e} = \frac{e}{h}, \quad \hat{\rho} = \frac{\rho_2 q^2}{h^2\mu_2}, \tag{2.12a–f}$$

representing the Reynolds number, the ratio of the viscous stresses in the fluid to the elastic shear stresses in the wall, the dimensionless external pressure, the dimensionless longitudinal pre-tension, the dimensionless thickness of the flexible wall and the ratio between the inertial and the elastic forces in the solid. The dimensionless system also involves three geometrical factors,

$$\hat{L}_1 = \frac{L_1}{h}, \quad \hat{L} = \frac{L}{h}, \quad \hat{L}_2 = \frac{L_2}{h}, \tag{2.13a–c}$$

which will be held constant throughout this study.

3. Results

In this section we predict the stability of flow through a flexible-walled channel with a hyperelastic wall. We first validate our model against published results for steady flow through channels with thin flexible walls presented by Heil (2004) (§ 3.1) and then examine the unsteady transition from beyond the upper branch limit point to the lower branch of steady solutions (§ 3.2). We then consider the onset of self-excited oscillations associated with these steady states across the parameter space spanned by Reynolds number and external pressure (§ 3.3), before examining the role of wall pre-tension (§ 3.4), the nonlinear limit cycles of oscillations which grow from the upper branch of steady solutions (§ 3.5), as well as the role of wall thickness (§ 3.6) and the role of wall inertia (§ 3.7) in the onset of these oscillations. Following Heil (2004), in all simulations we hold $\hat{L}_1 = 1$, $\hat{L} = 5$, $\hat{L}_2 = 10$ and fix the fluid–structure interaction parameter as $Q = 0.01$, indicating that elastic stresses dominate viscous stresses. In the results below we vary the Reynolds number Re, external pressure $\hat{p}_{ext}$, the wall pre-tension $\hat{T}_0$ (§ 3.4), the wall thickness $\hat{e}$ (§ 3.6) and the wall inertia parameter $\hat{\rho}$ (§ 3.7).

3.1. *Steady flow with thin flexible walls*

We first compare the predictions from our numerical method against the predictions of Heil (2004), who studied the flow through the geometry shown in figure 1 but where his elastic wall was modelled using (geometrically nonlinear) shell theory, intended to capture large displacements in the elastic solid. Our choice of non-dimensionalisation is identical to Heil (2004), with the exception that he defines a membrane pre-stress σ_0, which is related to our membrane pre-tension parameter through

$$\sigma_0 = \frac{\hat{T}_0}{\hat{e}}. \tag{3.1}$$

To compare with the predictions of Heil (2004), we consider a small wall thickness $\hat{e} = 0.01$. We then use pre-tension $\hat{T}_0 = 10$ to ensure that $\sigma_0 = 1000$, as used by Heil (2004). Since the inertia of the solid was neglected in that work we also set $\hat{\rho} = 0$ in our simulations in this section (we consider non-zero wall inertia in § 3.7 below).

In order to compare the predictions of our model with those of Heil (2004), in figure 3 we illustrate the steady flow field computed using our method (figure 3*a*) and the steady flow field obtained using the model of Heil (2004) (figure 3*b*). We observe excellent quantitative agreement between the two approaches, not only in the pressure distribution but also in the streamlines, where both exhibit a recirculating flow separation region downstream of the point of strongest wall collapse. Quantitatively, we compute the relative error in the maximal (minimal) fluid pressure as 0.2028 % (0.2089 %) between our approach and the data from Heil (2004) for these parameter values.

Following Heil (2004), in figure 4 we characterise the steady solutions of the system by the minimal ($\hat{h}_{min}$) and maximal ($\hat{h}_{max}$) channel width as a function of the model parameters. Similar to previous studies in collapsible channels (Luo & Pedley 2000; Heil 2004; Stewart 2010, 2017) and collapsible tubes (Heil & Boyle 2010), we find that for sufficiently large Reynolds numbers the system can admit multiple steady solutions at the same point in parameter space. For example, figure 4(*a*) shows that the minimum dimensionless channel width ($\hat{h}_{min}$), when plotted as a function of the external pressure, $\hat{p}_{ext}$, lies on a curve with three branches connected by two limit points (or fold bifurcations), where these three branches are labelled I, II and III. In order to quantify

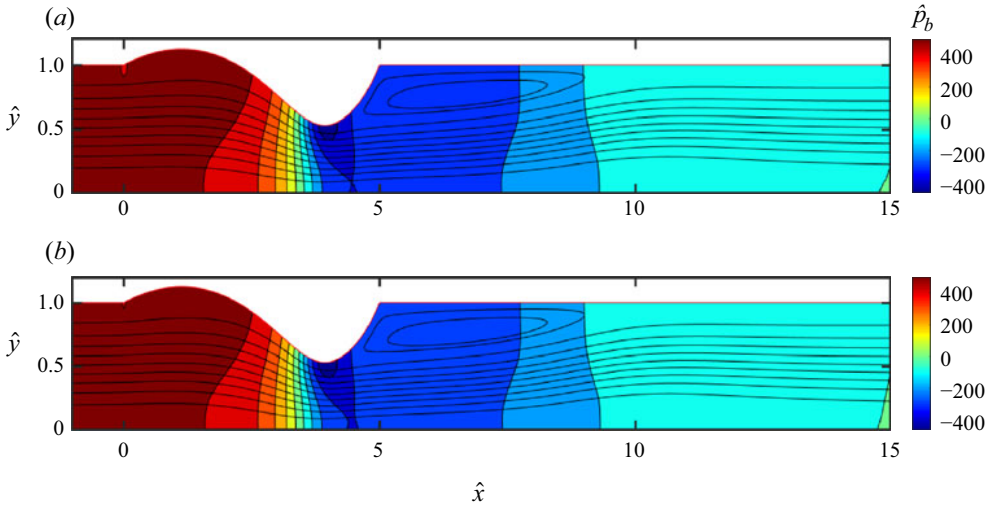

Figure 3. Streamlines and pressure contours for the steady solution computed at fixed Reynolds number ($Re = 500$) and fixed external pressure ($\hat{p}_{ext} = 3.204$) obtained from: (*a*) the present model; (*b*) the model of Heil (2004). Here, $\hat{T}_0 = 10$, $\hat{e} = 0.01$ and $\hat{\rho} = 0$.

the difference between our results and those of Heil (2004), figure 4(*b*) compares our prediction of the intermediate and lower steady branches as a function of external pressure with those depicted in figure 4 of Heil (2004) (for the same parameter values). We observe excellent quantitative agreement, although the two approaches do diverge slightly for larger external pressures when the channels are significantly more collapsed, which we attribute to the increased prominence of the differences between the wall models. Furthermore, we also produce the same plot for a smaller Reynolds number ($Re = 250$) for which the wall profile is unique for all external pressures. Again we see excellent quantitative agreement between the models, with a slight divergence as the channel becomes increasingly collapsed.

Along branch I (solid black line in figure 4), whose points correspond to a flow field like the one depicted in figure 5(*a*), where the wall is entirely bulged outwards: this branch was termed the upper branch of steady solutions by Stewart (2017). This upper branch persists as external pressure increases until an upper branch limit point is reached (denoted $\hat{p}_{ext} = \hat{p}_{ext1}$). For values of external pressure larger than $\hat{p}_{ext1}$ the elastic wall instantaneously collapses and the steady solution jumps catastrophically towards branch III (solid yellow line), where the wall is highly collapsed and the steady flow has separated beyond the constriction (figure 5*c*); this entirely collapsed branch was termed the lower branch of steady solutions by Stewart (2017). This re-circulating region is a prominent feature of branch III flow fields (figure 5*c*). We explore the transition from the upper branch limit point toward the lower steady branch in § 3.2 below, showing the birth of the re-circulation region as the channel becomes more collapsed. However, such a re-circulation region may not necessarily be a requirement for multi-valued steady solutions, since *ad hoc* one-dimensional models (which employ a flow-profile assumption which does not allow flow separation) also exhibit these multiple steady states (Stewart 2010, 2017) The lower branch (branch III) persists as we decrease the external pressure below $\hat{p}_{ext1}$ until the lower branch limit point is reached (denoted $\hat{p}_{ext} = \hat{p}_{ext2}$, where $\hat{p}_{ext2} < \hat{p}_{ext1}$). For even lower external pressures the system jumps to the upper branch, the recirculating region disappears and the channel wall bulges outward (figure 4*a*). The upper

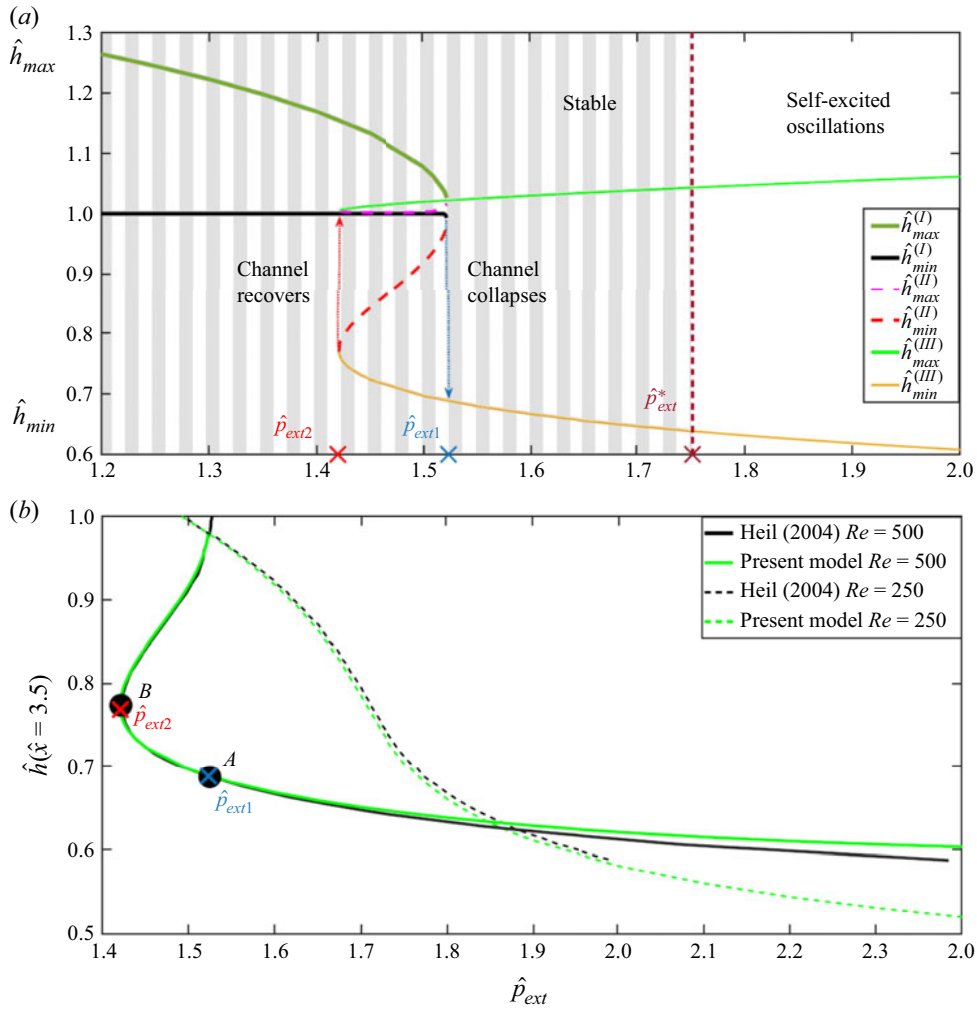

Figure 4. Nonlinear steady solutions of the model for fixed Reynolds number ($Re = 500$) and pre-tension ($\hat{T}_0 = 10$) showing: (*a*) the maximal and minimal channel widths as a function of the external pressure; (*b*) the channel width at $\hat{x} = 3.5$ as a function of the external pressure (black line), compared with the prediction from figure 4 in Heil (2004) (green line). The dotted lines in (*b*) show the comparison the present model (black) with Heil (2004) (green) for a smaller Reynolds number, $Re = 250$, where the steady state is unique. Here, $\hat{e} = 0.01$ and $\hat{\rho} = 0$.

and lower branches (I and III) are connected by an intermediate branch termed branch II, which we trace by numerical continuation. Below we confirm the observation of previous studies that this intermediate branch is always unstable to perturbations. A typical flow field for a solution along this intermediate branch is shown in figure 5(*b*).

3.2. *Transition from the upper branch limit point*

As the external pressure increases beyond the upper branch limit point the system abruptly transitions to the lower branch steady state. This transition is explored in figure 6, where we plot the unsteady evolution of the system from the upper branch limit point when the external pressure is instantaneously increased. In particular, we consider an unsteady simulation from the upper branch limit point at $R = 500$ for $\hat{T}_0 = 10$, displacing the

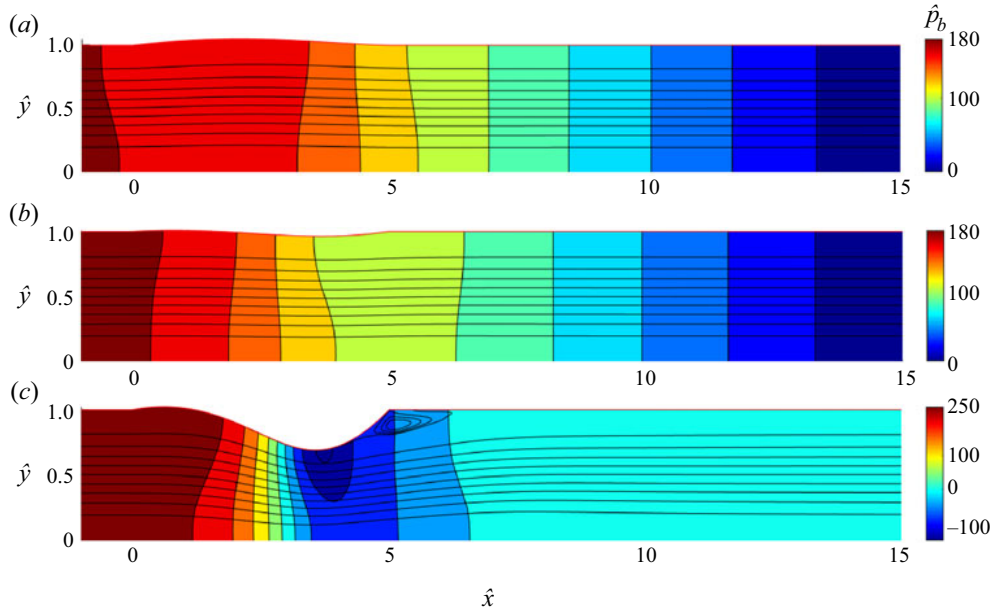

Figure 5. Streamlines and pressure contours for three branches of steady solutions for fixed Reynolds number ($Re = 500$) and fixed external pressure $\hat{p}_{ext} = 1.52$: (*a*) the upper branch (branch I); (*b*) the intermediate branch (branch II); (*c*) the lower branch (branch III). Here, $\hat{T}_0 = 10$, $\hat{e} = 0.01$ and $\hat{\rho} = 0$.

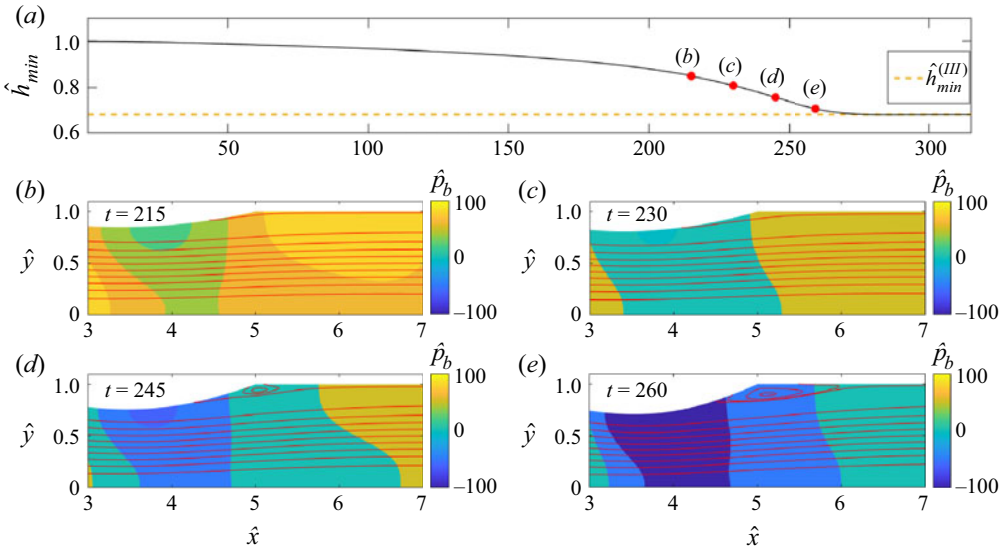

Figure 6. Unsteady transition from the upper branch limit point to the lower steady branch for a thin wall ($\hat{e} = 0.01$) with no wall inertia ($\hat{\rho} = 0$): (*a*) time trace of the minimal channel width ($\hat{h}_{min}$); streamlines and pressure colour map of the channel close to the outlet of the compliant segment at four selected times: (*b*) $t = 215.0$; (*c*) $t = 230.0$; (*d*) $t = 245.0$; (*e*) $t = 260.0$. The time points plotted in (*b–e*) are marked in panel (*a*). Here, $\hat{p}_e = 1.54$, $Re = 500$ and $\hat{T}_0 = 10$..

external pressure from $\hat{p}_{ext} = 1.52$ to $\hat{p}_{ext} = 1.54$ (marked with a cross in figure 8). Over time the channel wall collapses monotonically toward the lower branch steady state (figure 6*a*). Initially, the rate of collapse is slow and the flow is laminar (figure 6*b*),

but as the channel becomes increasingly constricted the rate of collapse increases and boundary layer separation takes place (figure 6*c*), where a re-circulation region becomes evident close to the downstream outlet of the compliant segment of the channel (figure 6*d*), creating a region of much lower pressure (figure 6*e*). A movie showing the entire transition is provided in the online supplementary material available at https://doi.org/10.1017/jfm.2021.1131.

There is an interesting analogy between these observations and those reported for swirling flows in pipes (see for e.g. Lopez 1994; Herrada, Pérez-Saborid & Barrero 2003), where fluid flows with a significant azimuthal velocity component through a rigid circular tube with an axisymmetric (fixed) sinusoidal indentation over a finite length. In this analogy the indentation of the pipe mirrors the collapse of the compliant segment of the channel, while the azimuthal fluid velocity component (and to some extent the compressibility of the fluid) extracts energy from the mean flow in a similar way to the compliance of the elastic wall. These swirling flows exhibit multiple (stable) steady solutions for a given set of parameters (when the Reynolds number is larger than a critical one) and the steady solutions can be described using bifurcation diagrams with three branches of steady solutions and two limit points, analogous to those presented in figure 4; this behaviour was recently termed 'double hysteresis' (Shtern 2018). These swirling flows also exhibit an unsteady transition from a nearly columnar flow to a recirculating flow when the swirling parameter is larger than a critical value (vortex breakdown), analogous to the spontaneous collapse of the channel we observe as the external pressure increases above the critical value ($\hat{p}_{ext1}$). In the former case, centrifugal forces generate an adverse axial pressure gradient that induces a recirculating flow, whereas the channel collapse generates an adverse pressure gradient that drives detachment of the boundary layer adjacent to the flexible wall. The flow structures in figures 6–9 of Herrada *et al.* (2003) are reminiscent of the transition observed in figure 6, where in both cases the vortex breakdown occurs just downstream of the point of greatest indentation. The only significant difference comes in the cross-stream location of vortex shedding: the symmetry of the cylindrical geometry in the swirling flows results in vortex shedding near the axis of the tube, while in the collapsible channel the vortex shedding occurs near the flexible wall.

3.3. *Linear stability results*

Having computed the steady configurations of the system, we now analyse the temporal linear stability of the three different steady solution branches depicted in figure 4. For this large value of pre-tension ($\hat{T}_0 = 10$) we find that the steady solutions along the section of the upper branch tested are globally stable to time-dependent perturbations (all the eigenvalues have $\omega_i < 0$) for all external pressures greater than the outlet pressure (i.e. $\hat{p}_{ext} \geqslant 0$), while the solutions along the intermediate branch are always unstable (at least one eigenvalue has $\omega_i > 0$ with $\omega_r = 0$). Figure 7 illustrates the stability of the lower steady branch, showing the eigenvalue spectrum of the frequency ω for several values of the external pressure, $\hat{p}_{ext}$. In this case (and in figure 11 below) we focus only on the most unstable eigenvalues, illustrating those with $\omega_i > -0.5$. We find that the lower branch is stable for sufficiently small external pressure, becoming globally unstable via a Hopf bifurcation when the external pressure exceeds a critical value, $\hat{p}^*_{ext} \approx 1.752$ (i.e. a pair of complex conjugate eigenvalues cross the real axis with non-zero ω_r). At this critical point, the corresponding steady state is shown in figure 7(*b*), where it is inflated at the upstream end and collapsed at the downstream end (termed mode-2). The corresponding eigenfunction of the wall profile for the neutrally stable mode is shown in figure 7(*c*), which has two extrema (mode-2). We label the oscillatory modes associated with the

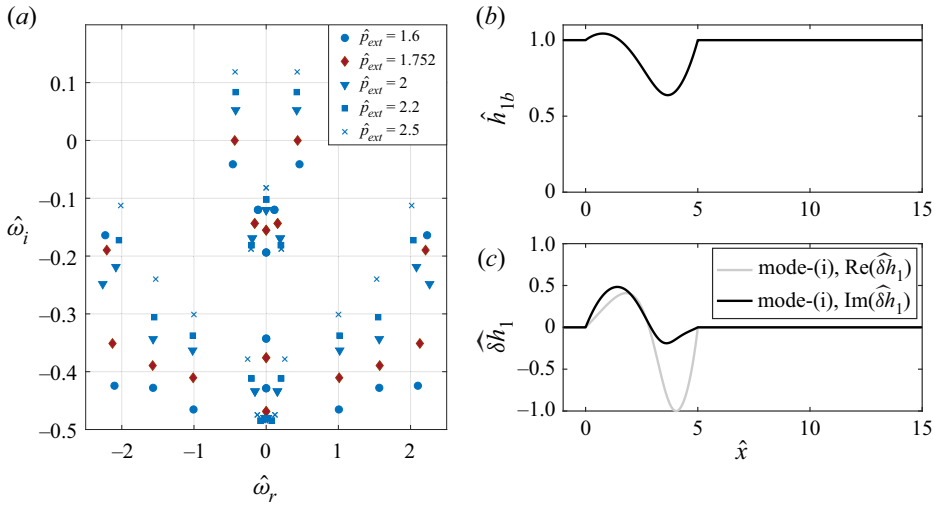

Figure 7. Stability of the lower steady branch to time-dependent perturbations for fixed Reynolds number ($Re = 500$) and fixed pre-tension ($\hat{T}_0 = 10$): (*a*) five eigenvalue spectra in the ω-plane for increasing values of $\hat{p}_{ext}$; (*b*) profile of the lower surface of the steady wall at neutral stability ($\hat{p}_{ext} \approx 1.752$); (*c*) real and imaginary parts of the wall profile eigenfunction at neutral stability ($\hat{p}_{ext} \approx 1.752$). Here, $\hat{e} = 0.01$ and $\hat{\rho} = 0$.

lower branch with lower case Roman numerals (i), (ii), (iii) ... in the order of increasing frequency, which is generally the order they become unstable as the external pressure increases, and so this primary instability is denoted mode-(i). These stability predictions agree well with the results presented by Heil (2004), where his figure 5 shows that the flow becomes unsteady and exhibits self-excited oscillations for $\hat{p}_{ext} = 2.5$, well inside our unstable regime. These results are also qualitatively similar to the predictions of the one-dimensional model of Stewart (2017), who showed that his lower branch of steady solutions becomes unstable to a mode-2 oscillation as the primary global instability of the system as the external pressure increases.

We overview the parameter space in figure 8 to summarise the regions of interest. We illustrate the region with multiple steady solutions by tracing the value of the external pressure at the limit points of the upper and lower steady branches ($\hat{p}_{ext1}$ and $\hat{p}_{ext2}$, analogous to those found in figure 4) as a function of the Reynolds number; similar to Stewart (2017), we find that this region with multiple steady states exists for Reynolds numbers greater than a threshold ($Re > Re_{cusp} \approx 330$). We further plot the critical external pressure for the onset of oscillatory instability, $\hat{p}^*_{ext}$, as a function of the Reynolds number, finding that for the range of Reynolds numbers explored here the neutral stability curve lies entirely within the range where there is a unique steady solution along the lower steady branch, so $\hat{p}^*_{ext} > \hat{p}_{ext1}$. Note that we observe no instability of the upper steady branch for this choice of the wall pre-tension ($\hat{T}_0 = 10$) across the range $0 \leqslant \hat{p}_{ext} \leqslant \hat{p}_{ext1}$. It emerges below that this branch only becomes unstable for $\hat{p}_{ext} < 0$ for this value of $\hat{T}_0$, which is not considered here. For large Reynolds number we might expect the neutral stability curve to enter the region of parameter space with multiple steady states (in a similar manner to Stewart 2017), but this possibility is discussed in more detail below.

3.4. *The influence of the pre-tension in the solid*

When the pre-tension of the elastic wall is reduced, we observe a decrease in the critical Reynolds number beyond which multiple steady flows exist, and the steady state

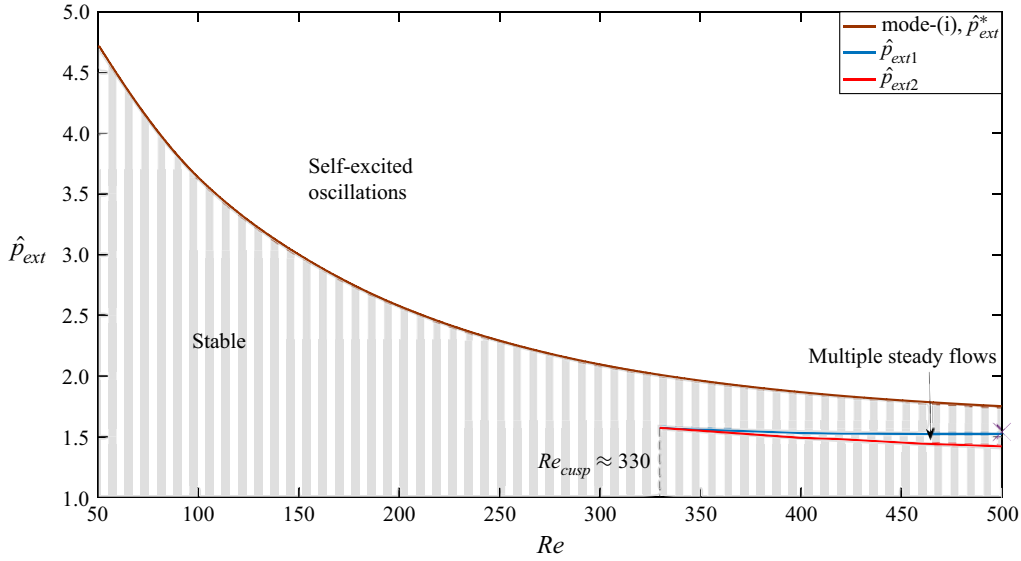

Figure 8. Overview of the critical conditions for self-excited oscillations for pre-tension $\hat{T}_0 = 10$, plotting the critical external pressure for instability as a function of the Reynolds number. The cross symbol indicates the point in parameter space which corresponds to the unsteady simulation shown in figure 6. Here, $\hat{e} = 0.01$, $\hat{\rho} = 0$.

bifurcation diagram and neutral stability curves become more complicated. To illustrate this complexity, in figure 9 we characterise the multiplicity of steady solutions that exist for a lower value of the pre-tension ($\hat{T}_0 = 5$) while holding the Reynolds number fixed ($Re = 500$), plotting the minimal ($\hat{h}_{min}$) and maximal ($\hat{h}_{max}$) widths of the steady channel as a function of the external pressure, for the upper and lower branches of steady solutions, obtained following the same procedure as § 3.1. Similar to the case we considered in figure 4 ($\hat{T}_0 = 10$), when the external pressure increases beyond a certain value, $\hat{p}_{ext} = \hat{p}_{ext1}$, there is a jump from a solution on the upper branch to a solution on the lower branch (where the channel becomes much more collapsed). In the same way, as we decrease the external pressure along the lower branch below a certain value, $\hat{p}_{ext} = \hat{p}_{ext2}$, there is a jump back to the upper branch.

To overview these steady solutions across the parameter space, in figure 10 we plot the external pressure at the limit points of the steady solutions ($\hat{p}_{ext1}$ and $\hat{p}_{ext2}$) as a function of the Reynolds number for a lower value of the pre-tension ($\hat{T}_0 = 5$), where we find that the critical Reynolds number for multi-valued solutions has reduced ($Re_{cusp} \approx 275$ in this case). To further illustrate the stability of these steady solutions, in figure 10 we also trace the critical external pressure for the onset of instability as a function of the Reynolds number, finding again that the lower branch of steady solutions (branch III) becomes unstable for external pressures greater than a critical value, $\hat{p}^*_{ext}$, and is stable otherwise (figure 10). This observation is similar to our observation for large pre-tension ($\hat{T}_0 = 10$), with the only difference that now the loss of stability is closer to the region of multiplicity of steady solutions, with the two bounding curves almost overlapping for the largest Reynolds numbers considered. Tracing these curves to larger Reynolds numbers is an interesting direction of future work, where we might expect the neutral stability curve and the trace of the lower branch limit point to eventually intersect. Such an intersection was previously observed by Stewart (2017), where the Hopf bifurcation (associated with the

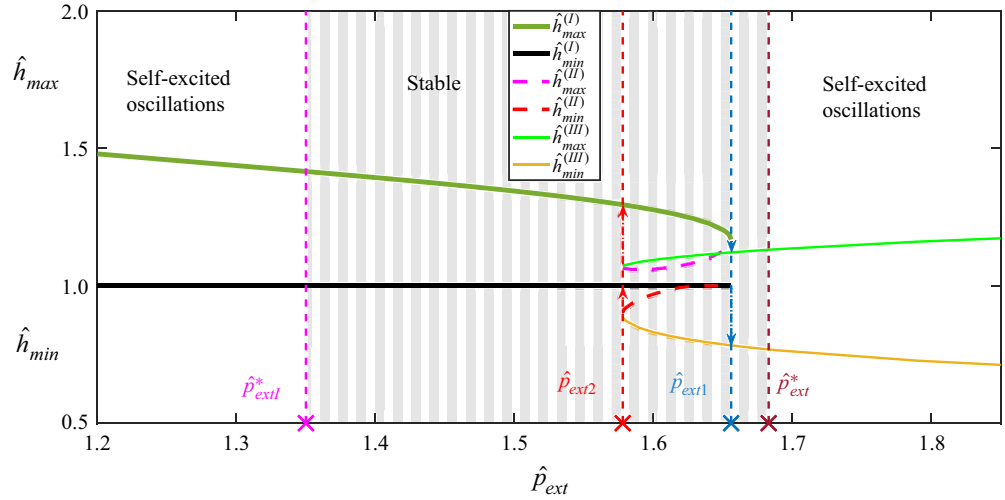

Figure 9. Nonlinear steady solutions of the model for fixed Reynolds number ($Re = 500$) and pre-tension ($\hat{T}_0 = 5$), showing the maximal and minimal channel widths as a function of the external pressure $\hat{p}_e$. Here, $\hat{e} = 0.01$ and $\hat{\rho} = 0$.

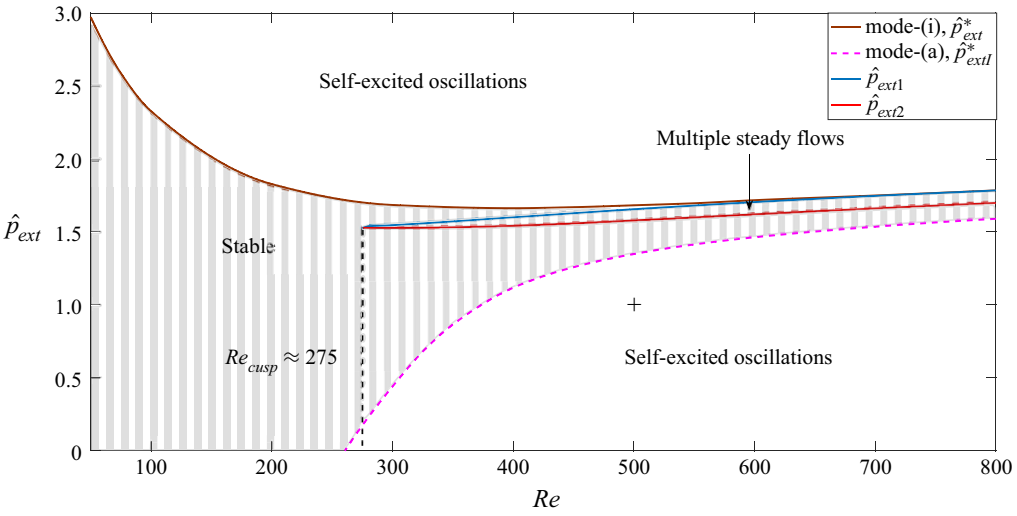

Figure 10. Overview of the critical conditions for self-excited oscillations for lower pre-tension $\hat{T}_0 = 5$, plotting the critical external pressure for instability as a function of the Reynolds number. The plus symbol indicates the point in parameter space which corresponds to the nonlinear portrait of the upper branch instability shown in figure 12. Here, $\hat{e} = 0.01$, $\hat{\rho} = 0$.

oscillation) and the saddle node bifurcation (associated with the steady solutions) interact in a co-dimension 2 bifurcation, suggesting a nearby homoclinic orbit (Glendinning 1994).

However, for this lower value of the pre-tension we also observe that steady solutions along the upper branch (branch I in figure 9) also become temporally unstable for external pressures below a critical value, denoted $\hat{p}^{*}_{extI}$, and are stable otherwise (see figure 10). This means that for $Re > Re_{cusp}$ there is only a narrow interval of external pressures compatible with a steady stable flow, focused around the region with multiple steady solutions. Instability of the upper branch of steady solutions has recently been noted by

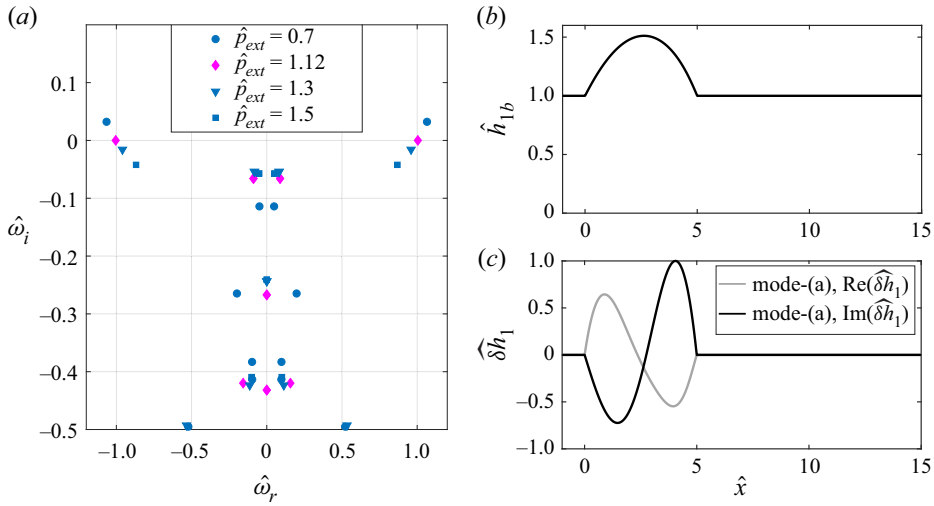

Figure 11. Exploration of the lower branch instability for lower pre-tension $\hat{T}_0 = 5$: (*a*) five eigenvalue spectra in the ω plane for increasing external pressure; (*b*) steady wall profiles for the choice of external pressure where the system is neutrally stable; (*c*) real and imaginary parts of the corresponding eigenfunction of the wall profile at neutral stability. Here, $\hat{e} = 0.01$ and $\hat{\rho} = 0$.

Wang *et al.* (2021*a*) using a flexible wall modelled as a thin nonlinear beam, but in their case the region of instability is located within and directly adjacent to the region with multiple steady solutions (Wang *et al.* 2021*b*), in contrast to that noted here. The fully developed limit cycles also exhibit some significant differences (see § 3.5 below).

To further explore this upper branch instability for lower pre-tension ($\hat{T}_0 = 5$) and fixed Reynolds number ($Re = 400$), in figure 11(*a*) we plot the corresponding eigenvalue spectra for several values of the external pressure, where a complex conjugate pair of eigenvalues cross into the upper half-plane for $\hat{p} < \hat{p}^*_{extI} \approx 1.12$ (Note that $\hat{p}^*_{ext} \approx 1.66$), consistent with a Hopf bifurcation. At neutral stability the steady configuration of the flexible wall is entirely inflated with a single hump (termed mode-1, see figure 11*b*), while the neutrally stable eigenfunction of the oscillating wall profile is mode-2 (figure 11*c*), similar to the instability of the lower branch. Note that the frequency of oscillation along the upper branch is generally larger than the corresponding instability along the lower branch. Given that this oscillation also has a mode-2 structure of the wall shape eigenfunction, we label modes associated with the upper branch using Roman letters (a),(b),... in order of increasing frequency, which is generally the order they become unstable as the Reynolds number increases. The primary oscillatory mode associated with the upper branch is therefore labelled mode-(a). It is interesting to note that the instability of the mode-1 steady state exhibits a mode-2 eigenfunction profile, presumably because the prescribed upstream flux suppresses modes that induce large volume changes in the flexible segment of the channel (such as the mode-1 oscillations observed with prescribed upstream pressure e.g. Jensen & Heil 2003; Stewart *et al.* 2009, 2010).

The upper branch neutral stability point, $\hat{p}^*_{extI}$, can be traced (by numerical continuation) to larger values of the wall pre-tension; we find that the critical external pressure must become negative to induce instability for $\hat{T}_0 = 10$, explaining why it was not observed in figures 7 and 8, where we restrict attention to external pressures larger than the channel outlet pressure ($\hat{p}_{ext} > 0$).

We note that the neutral stability curves associated with both the upper and lower steady branches trace close to the region with multiple steady solutions as the Reynolds number increases, suggesting this region plays a key role in the structure of the dynamical system. Stewart (2017) showed that the limit point on the upper steady branch (traced by the blue curve in figures 8 and 10) asymptotes to the saddle node bifurcation point for steady solutions of the inviscid system as the Reynolds number increases. Indeed, both Xu *et al.* (2013) and Stewart (2017) identified the threshold where inviscid steady states emerge as an organising centre of the dynamical system, consistent with our observation. Conversely, the lower branch of steady solutions is entirely maintained by the fluid viscosity (Stewart 2017), and is thus absent in the inviscid limit.

3.5. *Limit cycles of upper branch instability*

Fully nonlinear simulations of self-excited oscillations growing from the lower branch of steady solutions have been widely reported elsewhere (e.g. Heil 2004; Luo *et al.* 2008). An instability of the upper branch of steady solutions was recently reported by Wang *et al.* (2021*a*), who considered flow through a similar two-dimensional collapsible channel system modelling the flexible wall as a thin (nonlinear) beam with resistance to both bending and stretching (with no pre-stress), and the nonlinear limit cycles were explored using fully nonlinear simulations. However, the upper branch oscillations evident from the present model exhibit a significant difference in structure: for the oscillations reported by Wang the unstable region restabilises as the upper branch limit point is reached (Wang *et al.* 2021*a*) and remains confined to the neighbourhood of the region with multiple steady states (Wang *et al.* 2021*b*), whereas for the present model the system is stable in the neighbourhood of the upper branch limit point and instead the unstable region extends over a wide range of external pressures away from the region with multiple steady states (figure 10).

Given the difference in structure between our predictions and those of Wang *et al.* (2021*a*), in figure 12 we examine the underlying dynamics of our upper branch oscillations using fully nonlinear simulations of our model (method described in § 2.5) at a point in parameter space within the upper branch neutral stability curve. In this case we choose $Re = 500$, $\hat{p}_{ext} = 1$ and $\hat{T}_0 = 5$, marked with a plus inside the unstable region in figure 10. Initiating the simulation on the upper branch steady solution, numerical noise is enough to trigger an oscillatory instability evident in the time trace of the maximal channel width (see figure 12(*a*) with growth rate and frequency consistent with the global linear stability eigensolver), eventually saturating into a complicated nonlinear limit cycle (one period shown in figure 12*b*). A movie showing the flow field and vorticity over several periods of this limit cycle is provided in the online supplementary material.

Over a period of this limit cycle the wall profile grows a single hump at the downstream end of the compliant segment (figure 12*c*); this hump propagates upstream reaching a global maximum (figure 12*d*) before being reflected back downstream again by the upstream rigid segment, where its amplitude subsequently decreases. As this hump propagates downstream a second hump appears at the downstream end of the compliant segment (figure 12*e*) which eventually dominates the first (figure 12*f*). However, these two humps do not coalesce but instead the x-location of the maximum wall deflection changes discontinuously at the global minimum of $\hat{h}_{max}$ (figure 12(*f*), explaining the cusp in figure 12(*b*) at $t \approx 1138.2, 1145.5, 1152.8$). This second hump grows in amplitude, engulfing the remains of the first hump and shedding a low pressure vortex into the downstream rigid segment (figure 12*g*). This propagating vortex creates a so-called

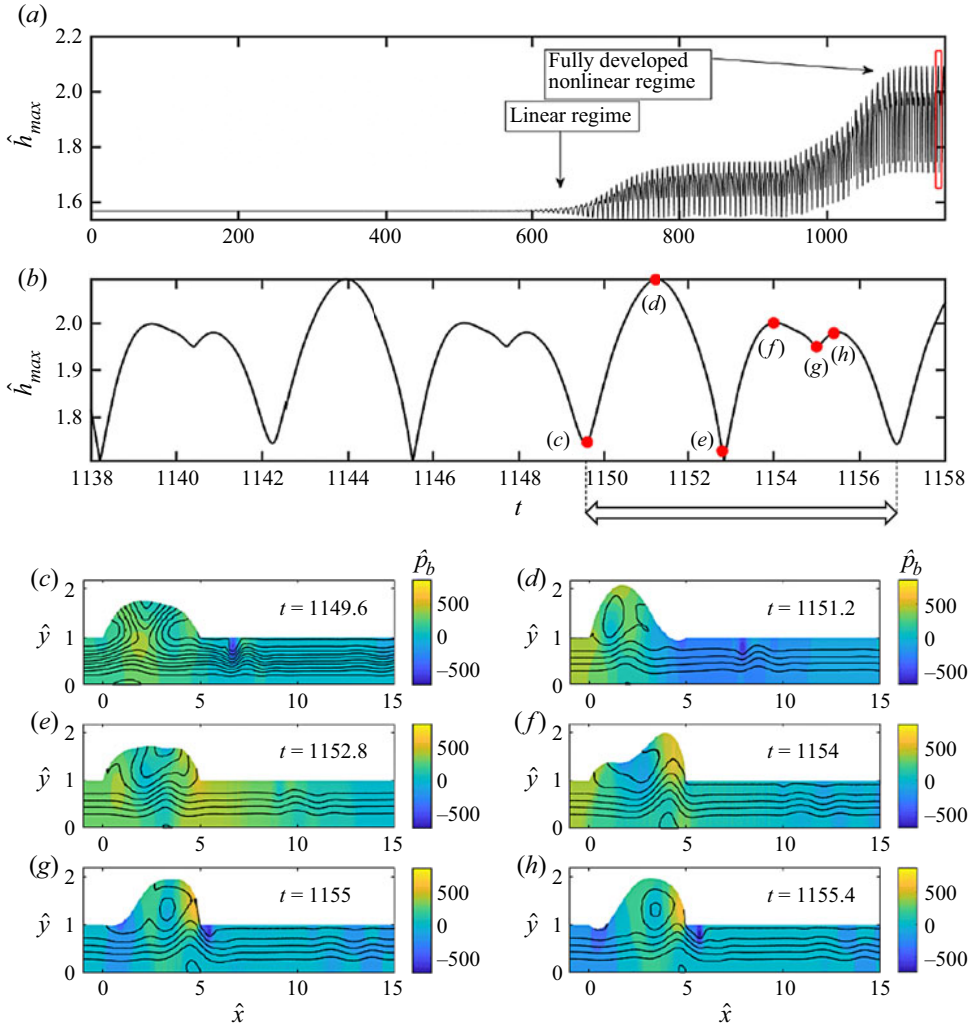

Figure 12. The mechanism of upper branch instability for a thin hyperelastic wall ($\hat{e} = 0.01$) with no wall inertia ($\hat{\rho} = 0$): (*a*) the maximal channel width $\hat{h}_{max}$ as a function of time; (*b*) zoom-in over panel (*a*) over one period of oscillation; streamlines and pressure colour map of the channel close to the outlet of the compliant segment at six selected times over a period of oscillation including: (*c*) $t = 1149.6$; (*d*) $t = 1151.2$; (*e*) $t = 1152.8$; (*f*) $t = 1154$; (*g*) $t = 1155$; (*h*) $t = 1155.4$. The fully developed limit cycle of interest is enclosed in the red box in (*a*). The times corresponding to the snapshots in panels (*c–h*) are labelled in (*b*). Here, $Re = 500$, $\hat{p}_{ext} = 1$ and $\hat{T}_0 = 5$.

vorticity wave in the downstream rigid segment (particularly evident in figure 12*c*,*g*,*h*) while the large hump at the downstream end of the compliant segment drives a short region of channel collapse at the upstream end. As this vorticity wave propagates downstream, the single hump in the compliant segment propagates upstream, repeating the cycle. The nature of this oscillation exhibits many of the features of the nonlinear upper branch oscillations described by Wang *et al.* (2021*a*), including the development of an upstream propagating hump. However, for their upper branch oscillations this hump is annihilated by the upstream rigid segment (not reflected) and the flow remains entirely laminar throughout, with no evidence of low pressure vortex shedding. However, the present model is restricted by the assumption of first-order elasticity, meaning that we cannot apply as

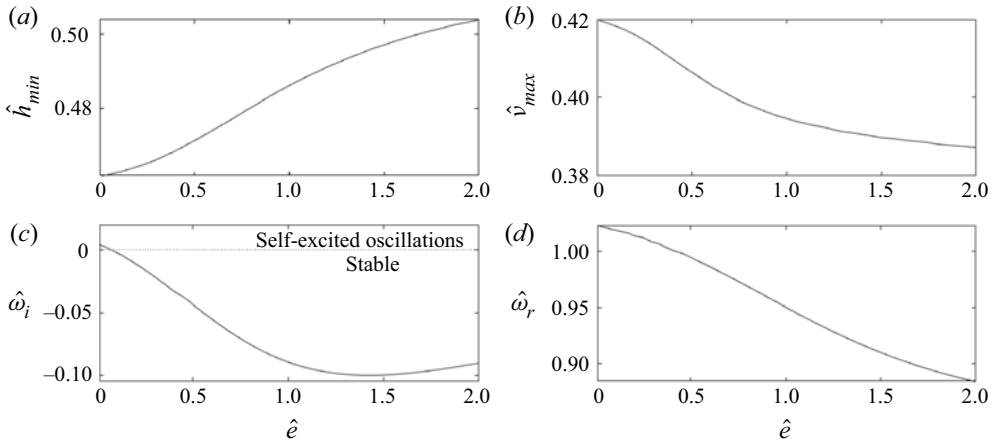

Figure 13. The influence of the wall thickness on the steady and oscillatory solutions in the absence of wall inertia ($\hat{\rho} = 0$): (*a*) the minimal steady channel width $\hat{h}_{min}$ as a function of the wall thickness; (*b*) the maximal steady flow speed v_{max} as a function of the wall thickness; (*c*) the growth rate of the primary oscillatory mode as a function of the wall thickness (mode-(i)); (*d*) the frequency of the primary oscillatory mode (mode-(i)) as a function of the wall thickness. Here, $\hat{T}_0 = 5$, $\hat{p}_{ext} = 2.98$ and $Re = 50$.

many boundary conditions at each end of the beam as Wang *et al.* (2021*a*) (who applied zero slope conditions at the end of the beam in addition to the clamped conditions).

These vorticity waves have previously been observed in channel flows with self-excited oscillations from a collapsed (lower branch) steady state (Luo & Pedley 1996; Luo *et al.* 2008) or with prescribed (oscillatory) wall motion in one compartment (Stephanoff *et al.* 1983; Pedley & Stephanoff 1985).

3.6. *The influence of the wall thickness*

In this subsection we analyse the influence of the dimensionless wall thickness, $\hat{e}$, on the model predictions. We consider a particular case holding the pre-tension, external pressure and Reynolds number fixed ($\hat{T}_0 = 5$, $\hat{p}_{ext} = 2.98$ and $Re = 50$). For these parameters, with wall thickness $\hat{e} = 0.01$, the system has a unique steady wall shape where the external pressure is sufficiently large to collapse the channel wall ($\hat{h}_{min} < 1$). These parameters are chosen so that the system is just inside the unstable regime for lower branch oscillations ($Re = 50$ and $\hat{T}_0 = 5$ which has critical $\hat{p}^*_{ext} \approx 3.001$). In figure 13 we characterise how an increase in the wall thickness influences the underlying steady flow (figure 13*a*,*b*) and the critical conditions for the onset of lower branch oscillations (figure 13*c*,*d*). Considering the steady system first, figure 13(*a*) shows that the increase in wall thickness has little effect on the overall shape of the flexible wall for this value of Reynolds number; the channel becomes slightly less constricted as the wall thickness increases. Similarly, figure 13(*b*) shows that increasing wall thickness slightly reduces the maximal streamwise velocity through the constriction, $\hat{v}_{max} = \max_{x,y}(\hat{v}_{1xb})$ (as expected by conservation of mass). However, the wall thickness plays a more significant role in determining the stability of these steady solutions. The increase of the wall thickness results in the initially unstable solution (for $\hat{e} = 0.01$) becoming stable for a critical value of the wall thickness $\hat{e} \gtrsim 0.08$ (figure 13*c*), with a corresponding decrease in the frequency of oscillation (figure 13*d*).

In order to quantify the effect of increasing the wall thickness on the stability of the system across the parameter space, in figure 14 we plot the critical external pressure

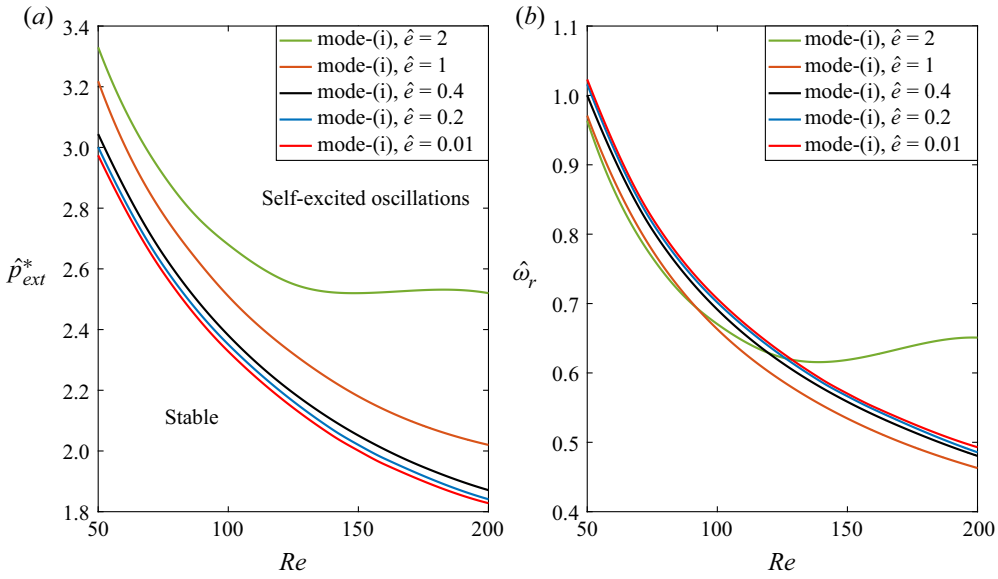

Figure 14. Overview of the critical conditions required for the onset of oscillations while changing the wall thickness, plotting the critical external pressure for the onset of oscillation $\hat{p}^*_{ext}$ as a function of the Reynolds number for five different wall thicknesses ($\hat{e} = 0.01$, $\hat{e} = 0.2$, $\hat{e} = 0.4$, $\hat{e} = 1$ and $\hat{e} = 2$). Here, $\hat{T}_0 = 5$.

for the onset of the primary oscillatory instability of the lower branch (mode-(i)), denoted as $\hat{p}^*_{ext}$, as function of the Reynolds number for fixed pre-tension ($\hat{T}_0 = 5$) and five different wall thicknesses ($\hat{e} = 0.01, 0.2, 0.4, 1, 2$). Note that we have limited our investigation to values of the Reynolds numbers smaller than the critical value required for multiple steady solutions (Re_{cusp}), so the steady profile is unique. In the absence of wall inertia ($\hat{\rho} = 0$) the effect of the wall thickness on the critical conditions for instability remains weak for relatively thin walls ($\hat{e} = 0.01, 0.2, 0.4$): the steady flow remains almost unchanged (figure 13*a*,*b*) and there is only a mild stabilisation of the instability, characterised by an increase in the critical pressure needed to generate self-excited oscillations (figure 14). It emerges that the thickness of the wall must be of the order of the channel width (i.e. $\hat{e} \sim 1$) before there is any significant difference in the stability threshold. For example, for $\hat{e} = 1$ and $\hat{e} = 2$ the critical pressure for the onset of instability is more appreciably increased compared with $\hat{e} = 0.01$ (figure 14*a*), while the oscillation frequency is decreased (figure 14*b*). Furthermore, for $\hat{e} = 2$ the critical external pressure and oscillation frequency both saturate as the Reynolds number becomes large (figure 14). We show in § 3.7 below that changes to the stability of the system are even more prominent when we include wall inertia.

3.7. *The influence of wall inertia*

We now examine the influence of increasing wall inertia. It should be noted that the steady version of the full nonlinear equations (2.1) is independent of the wall inertia parameter $\hat{\rho}$, and so all steady results are unchanged from those reported above. To study the additional influence of wall inertia on the onset of self-excited oscillations growing from the lower branch of static solutions, in figure 15 we trace the growth rate (figure 15*a*) and frequency (figure 15*b*) of the mode-(i) instability from figures 8

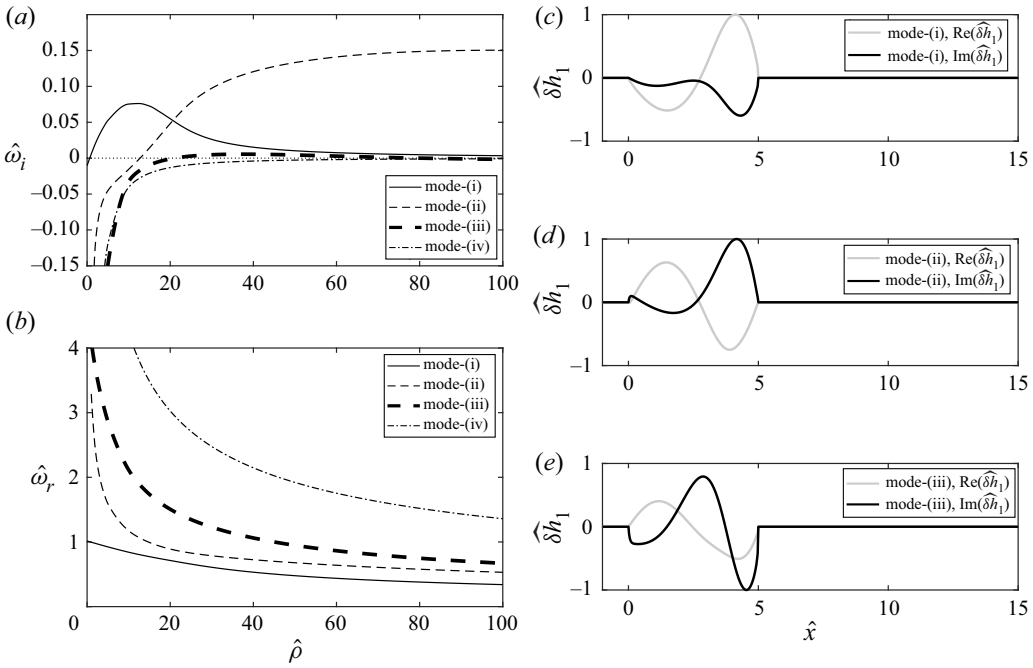

Figure 15. The role of increasing wall inertia in the growth rate and frequency of self-excited oscillations for fixed wall thickness $\hat{e} = 0.2$: (*a*) the growth rate of the first four oscillatory modes as a function of the wall inertia parameter; (*b*) the corresponding frequency of the first four oscillatory modes as a function of the wall inertia parameter; spatial profiles of real and imaginary parts of the eigenfunctions at neutral stability for (*c*) mode-(i) ($\hat{\rho} = 0.631$); (*d*) mode-(ii) ($\hat{\rho} = 12.73$); (*e*) mode-(iii) ($\hat{\rho} = 21.02$). Here, $\hat{T}_0 = 5$, $\hat{p}_{ext} = 2.98$ and $Re = 50$.

and 10 as a function of the wall inertia parameter $\hat{\rho}$; at neutral stability the eigenfunction profile of the oscillatory mode has two (three) extrema in the real (complex) part of the wall profile (figure 15*c*), meaning the number of extrema can change over a period of oscillation for these walls of finite thickness. For this choice of parameters the primary oscillatory mode of the lower branch (mode-(i)) is stable for $\hat{\rho} = 0$, becoming unstable as the wall inertia parameter, $\hat{\rho}$, increases (figure 15*a*), while the corresponding oscillation frequency decreases (figure 15*b*). The perturbation growth rate for lower branch mode-(i) exhibits a local maximum at $\hat{\rho} \approx 10$ before asymptoting toward zero as the wall inertia parameter continues to increase. Hence, this mode of instability approaches stability with decreasing oscillation frequency as the wall gets heavier. However, as the wall inertia parameter increases a second mode of oscillation also becomes unstable at $\hat{\rho} \approx 12.72$ (figure 15*a*) with larger frequency than mode-(i) (figure 15*b*); we term this mode-(ii), which also has a perturbation wall profile with two extrema (figure 15*d*) albeit with a narrow boundary layer at the upstream end of the profile. Unlike the primary mode, the growth rate of this instability continues to increase as $\hat{\rho}$ increases for these parameter values, while the corresponding oscillation frequency again approaches zero (figure 15*b*). As the wall mass parameter becomes even larger, we eventually observe another mode becoming destabilised for $\hat{\rho} \approx 21.02$ with larger frequency (figure 15*b*) which we term mode-(iii), where the wall profile again exhibits two extrema with a narrow upstream boundary layer (see eigenfunction wall profile in figure 15*e*). Further increases in the wall inertia parameter destabilises mode-(iv) (figure 15*a*,*b*). Note that, in accordance with our naming convention, the oscillation

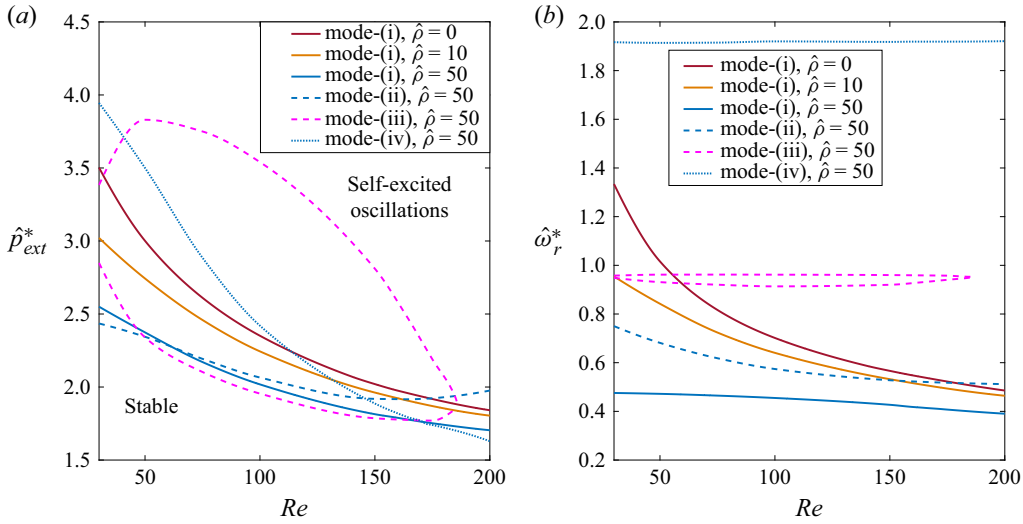

Figure 16. An overview of the critical conditions for the onset of instability for fixed wall thickness $\hat{e} = 0.2$ for three different values of the wall inertia parameter $\hat{\rho} = 0, 10, 50$: (*a*) the critical external pressure for the onset of the four most unstable modes of the system (modes-(i) to (iv)) as a function of the Reynolds number; (*b*) the corresponding neutrally stable oscillation frequency of these four modes as a function of the Reynolds number. Here, $\hat{T}_0 = 5$.

frequency of each mode increases with increasing mode number (figure 15*b*). In summary, increasing the wall inertia parameter, for all other parameters held fixed, destabilises the primary global instability of the system, but also destabilises higher modes of instability.

In order to summarise the influence of increasing wall inertia across the parameter space, in figure 16 we plot the critical external pressure for the onset of lower branch oscillations, $\hat{p}^*_{ext}$, as a function of the Reynolds number for constant wall thickness ($\hat{e} = 0.2$) and fixed pre-tension ($\hat{T}_0 = 5$) for three different values of the wall inertia parameter ($\hat{\rho} = 0, 10, 50$). For small values of the wall inertia parameter ($\hat{\rho} = 0, 10$) we find only mode-(i) across the section of parameter space considered (a direct continuation of mode-(i) identified in the absence of wall inertia); this mode becomes increasingly unstable as $\hat{\rho}$ increases (figure 16*a*), while the corresponding frequency of oscillation decreases (figure 16*b*). This observation is consistent with the work of Luo & Pedley (1998), who found that increasing wall mass enlarges the unstable region of parameter space. However, consistent with figure 15, as the wall inertia parameter increases, additional (higher-frequency) modes of instability also arise in the system. In particular, we identify modes (i), (ii), (iii) and (iv), labelled in order of increasing frequency. In fact, it emerges that for $\hat{\rho} = 50$, for the parameters investigated the mode-(ii) oscillation is more unstable than mode-(i) until $Re \approx 46$. Beyond this critical value mode-(iii) becomes the most unstable mode, while for even larger Reynolds numbers ($Re \gtrsim 166$) there is another cross-over in parameter space and mode-(iv) becomes the most unstable mode. Note that the frequency of the oscillation increases with increasing mode number (figure 16*b*). These observations are again consistent with the predictions of Luo & Pedley (1998), who found that a higher-frequency oscillatory mode eventually dominated the fundamental mode as the wall inertia parameter increased.

Figure 16(*a*) also highlights that the structure of the neutral stability curve for mode-(iii) oscillations is somewhat different to the traces of mode-(i), (ii) and (iv), exhibiting a

maximal Reynolds number and a two-branch structure analogous to the tongue structures seen in other collapsible channel systems (Luo *et al.* 2008; Stewart 2017).

4. Discussion

In this paper we have developed a model for the flow of Newtonian fluid through a finite-length (asymmetric) flexible-walled channel, as a planar analogue of flow through a Starling resistor experiment. The flexible wall of the channel was assumed to be a pre-tensioned hyperelastic material of finite thickness, overcoming the limitation with more approximate models that require the elastic wall to be asymptotically thin (such as a membrane (e.g. Luo & Pedley 1996), a nonlinear beam (e.g. Luo *et al.* 2008; Wang *et al.* 2021*a*) or an elastic shell (e.g. Heil 2004)) and providing a much closer resemblance to the experiments where the tube walls are typically of the order of the tube radius (e.g. Bertram *et al.* 1990, 1991; Bertram & Castles 1999). It should be noted that in the limit of an asymptotically thin wall our hyperelastic model can be rationally reduced to either a membrane or an elastic shell depending on the assumptions. Flow through the channel is driven by a prescribed upstream flux against a prescribed downstream pressure, while the compliant segment of the channel is externally pressurised. This model is validated against previous predictions which approximated the wall using nonlinear shell theory (Heil 2004), showing excellent agreement (figures 3, 4).

The numerical method used in this study is based on an arbitrary Lagrangian–Eulerian approach (Hirt, Amsden & Cook 1974; Donea *et al.* 2004; Hron & Turek 2006; Basting *et al.* 2017; Ryzhakov *et al.* 2020), in that one can either move with the fluid (Lagrangian description) or view the flow from a fixed position (Eulerian description). The novelty of our method lies in the use of non-singular mappings between these two descriptions, in which all fields are solved simultaneously and which allow the method to be fully implicit. At the same time, we use high-order (fourth-order) finite differences or spectral Chebyshev collocation to discretise the transformed domains. Thus, while there are other such monolithic methods (e.g. Hron & Turek 2006; Ryzhakov *et al.* 2020), we are able to construct a stable method with high spatial accuracy. The numerical method used herein is well suited for solving other fluid–structure interaction problems (e.g. Bungartz & Schäfer 2006) since it can handle large deformation of the solid with the help of these non-singular mappings; many standard implementations of fluid–structure interaction fail due to excessive mesh deformation.

The model predicts that at least one steady configuration of the system exists for all values of the parameters. For sufficiently large Reynolds numbers the system exhibits three co-existing steady states for a narrow range of the parameters. These states are connected by a pair of limit points, similar to earlier predictions using more approximate models (Luo & Pedley 2000; Stewart 2017) with two stable configurations (figures 4, 9): an upper branch (where the channel wall is entirely inflated) and a lower branch (where the channel wall is collapsed). Beyond the upper limit point the system transitions (dynamically) from the upper branch of steady solutions to the lower, where the wall profile becomes increasingly collapsed, the flow separates beyond the constriction and a low pressure vortex is shed into the downstream rigid segment (figure 6); such an observation has many similarities to swirling flows in pipes and open jets (Lopez 1994; Shtern & Hussain 1996; Herrada *et al.* 2003).

Similar to previous studies (Heil 2004; Stewart 2017), we found an instability of the lower branch of steady solutions via a Hopf bifurcation when either the Reynolds number or the external pressure becomes sufficiently large (figures 8, 10). For the parameter values considered in this study we did not observe the neutral stability curve entering the region

of multiple steady states. However, in line with observations of Stewart (2017), we expect that the neutral stability curve will eventually terminate when it intersects the line of limit points along the lower branch of steady solutions.

However, our model also predicted that the upper branch of steady solutions could become unstable via a Hopf bifurcation to an entirely separate branch of mode-2 instabilities when the pre-tension is sufficiently low (figure 10). Note that an analogous instability of the upper branch has very recently been found in a model of Newtonian flow in a collapsible channel with a nonlinear elastic beam (Wang *et al.* 2021*a*). The fully developed limit cycle of our upper branch oscillations bears many similarities to those described by Wang *et al.* (2021*a*), exhibiting a hump propagating upstream along the compliant segment and interacting with flow in the upstream rigid segment (figure 12); however, in our oscillations the hump is reflected by the upstream rigid segment and the flow sheds a low pressure vortex which drives a vorticity wave into the downstream rigid segment (Stephanoff *et al.* 1983; Pedley & Stephanoff 1985).

Our new hyperelastic formulation provides an opportunity to investigate the role of wall thickness on the onset of instability. Previous studies of flow in thick-walled tubes or channels have been restricted to steady configurations (Marzo *et al.* 2005; Zhang *et al.* 2018), while unsteady systems have typically considered asymptotically thin walls (Luo & Pedley 1996; Jensen & Heil 2003; Luo *et al.* 2008). We found that, in the absence of wall inertia, increasing the wall thickness alone makes negligible difference to either the steady solutions (figure 13*a*,*b*) or the onset of oscillations (figures 13*c*,*d*, 14) until the wall thickness becomes comparable to the channel thickness (in this case the aspect ratio of the wall is relatively small $h/L \lesssim 0.2$ and so thin-wall approximations are still appropriate). For even larger wall thicknesses the critical pressure for the onset of instability is significantly increased compared with the thin walls (figure 14), while the oscillation frequency is decreased (figure 14*b*). Furthermore, for the largest wall thickness considered the critical external pressure and oscillation frequency both saturate as the Reynolds number becomes large (figure 14).

The dimensionless parameter $\hat{\rho}$ describes the strength of wall inertia compared with the internal elastic stress, but also represents an eigen-frequency of the elastic wall compared with the characteristic (inverse) time scale of the flow past the elastic wall. It is therefore important to characterise how these natural frequencies of wall vibration correlate to the other modes of self-excited oscillation of this system. Wall mass also plays an important role in physiological applications such as human phonation (Mittal, Erath & Plesniak 2013). We found that increasing the wall inertia parameter promotes the onset of self-excited oscillation by enlarging the unstable region of the primary (mode-2) global instability in the space spanned by Reynolds number and external pressure (figure 16); inertia-driven destabilisation was previously noted by Luo & Pedley (1998). In addition, increasing the wall inertia parameter also destabilises higher-frequency modes of instability, which eventually dominate the primary global instability as the wall inertia parameter increases (figure 16), again consistent with the observations of Luo & Pedley (1998). However, it turns out that the value of the parameter $\hat{\rho}$ is typically small for the silicone rubber tubes used in Starling resistor experiments; these tubes have been estimated to have a Young's modulus and Poisson ratio of $E = 3.8$ MPa and $\nu = 0.423$, respectively (Bertram 1987), resulting in a shear modulus of $\mu_2 = 1.335$ MPa (assuming an isotropic material). Silicone rubber also has an average density of $\rho_2 = 1240$ kg m^{-3}. Starling resistor experiments in a tube with internal diameter 12 mm and a flow rate of the order of 60 ml s^{-1} (Bertram & Tscherry 2006), exhibit a flow velocity of approximately 0.531 m s^{-1}. Flow of this velocity in a channel of thickness 1 mm corresponds to a flow

rate per unit length in the out-of-plane direction of $q = 5.31 \times 10^{-4}$ m^2 s^{-1}. Using all this information, we estimate $\hat{\rho} \approx 2.62 \times 10^{-4} \ll 1$ for a compliant channel formed from silicone rubber.

Our hyperelastic formulation assumed first-order elasticity, with elastic stress proportional to the gradient of the strain energy function with respect to the strain tensor. We imposed lateral boundary conditions of no displacement along the face of the elastic solid in contact with the rigid wall. This approach cannot reproduce the resistance to bending of an elastic beam, since this would require strain gradient (second-order) elasticity, where the elastic stress has additional contributions due to the derivative of the strain energy function with respect to the strain gradient tensor; this approach would also require additional boundary conditions at the edges of the compliant segment. Indeed, Luo and coworkers considered a collapsible channel model where the (asymptotically thin) elastic wall exhibited resistance to both bending and stretching but no pre-tension, imposing clamped and zero slope conditions at each end of the flexible wall (Luo *et al.* 2008; Wang *et al.* 2021*a*,*b*). Their wall profiles accommodated this zero slope condition over very narrow boundary layers at each end of the compliant segment (see examples in Wang *et al.* 2021*a*). Furthermore, Wang *et al.* (2021*b*) noted that increasing the resistance to bending of the beam narrowed the region of multiple steady states, and eventually suppressed the onset of self-excited oscillation. Similar to the present study, the model of Wang *et al.* (2021*a*,*b*) predicted self-excited oscillations growing from both the upper and lower branches of static solutions. However, their lower branch oscillations were typically of higher frequency and re-stabilised for sufficiently large external pressure (Wang *et al.* 2021*b*) (contrary to the present system where lower branch instability persisted as the external pressure increased, figures 8, 10). Both systems exhibited an upper branch instability of $O(1)$ frequency, but in Wang *et al.* (2021*a*,*b*) the unstable zone remained localised to the neighbourhood of the upper branch limit point (contrary to the present system where the upper branch instability persisted to low external pressures, figure 10). However, it is unclear if these discrepancies are due to the differences in the constitutive assumptions between the two systems, or due to the absence of pre-tension in the work of Wang *et al.* (2021*a*,*b*). A more expansive comparison will be pursued in future work.

Supplementary movie. Supplementary movie is available at https://doi.org/10.1017/jfm.2021.1131.

Acknowledgements. Helpful discussions with Professor J.H. Snoeijer (University of Twente) are very gratefully acknowledged. We are very grateful to Professor M. Heil (University of Manchester) for providing the data used to plot figure 3(*b*).

Funding. M.A.H. and S.B.T. acknowledge funding from the Spanish Ministry of Economy, Industry and Competitiveness under Grants DPI2016-78887 and PID2019-108278RB and from the Junta de Andalucía under Grant P18-FR-3623. P.S.S. acknowledges funding from Engineering and Physical Sciences Research Council (UK) grants EP/P024270/1, EP/N014642/1 and EP/S030875/1.

Declaration of interests. The authors report no conflict of interest.

Supporting data. Supporting data for this paper can accessed at https://dx.doi.org/10.5525/gla.researchdata.1113.

Author ORCIDs.
M.A. Herrada https://orcid.org/0000-0003-0388-8001;
J. Eggers https://orcid.org/0000-0002-0011-5575;
P.S. Stewart https://orcid.org/0000-0002-0971-8057.

ξ_1	ξ_2	χ_1	χ_2	$\hat{\omega}_r$	$\hat{\omega}_i$
641	**201**	**19**	**14**	**1.052**	**0.0232**
641	201	19	19	1.054	0.02229
641	201	25	14	1.053	0.02404
641	201	25	19	1.055	0.02314
721	226	19	14	1.051	0.02064
721	226	25	14	1.051	0.02140
801	251	21	19	1.054	0.02239

Table 1. Mesh sensitivity for an unstable case on the upper branch of steady solutions for a thin wall ($\hat{e} = 0.01$) with no wall inertia ($\hat{\rho} = 0$), listing the real and imaginary parts as a function of the discretisation parameters ξ_1, ξ_2, χ_1 and χ_2. The row listed in bold corresponds to the parameters used for the simulations in the main text. Here $\hat{T}_0 = 5$, $\hat{p}_{ext} = 0.82$ and $Re = 400$.

Appendix. Convergence study of the numerical method

To illustrate the mesh independence of the numerical results we compute the real and imaginary components of the eigenvalue $\hat{\omega}$ obtained from the global linear stability eigensolver for different discretisations of the domain, changing the number of mesh points ξ_1, ξ_2, χ_1 and χ_2 (listed in § 2.2). A typical example for an unstable point on the upper branch of steady solutions is provided in table 1, where we find that the real and imaginary parts of $\hat{\omega}$ show only negligible variations as the mesh is refined. The data listed in boldface correspond to the numerical mesh used in this work.

References

Armitstead, J.P., Bertram, C.D. & Jensen, O.E. 1996 A study of the bifurcation behaviour of a model of flow through a collapsible tube. *Bull. Math. Biol.* **58** (4), 611–641.

Basting, S., Quaini, A., Canic, S. & Glowinski, R. 2017 Extended ALE method for fluid-structure interaction problems with large structural displacements. *J. Comput. Phys.* **331**, 312–336.

Bertram, A. & Forest, S. 2020 *Mechanics of Strain Gradient Materials*. Springer.

Bertram, C.D. 2003 Experimental studies of collapsible tubes. In *Flow Past Highly Compliant Boundaries and in Collapsible Tubes* (ed. P.W. Carpenter & T.J. Pedley), pp. 51–65. Springer.

Bertram, C.D. & Castles, R.J. 1999 Flow limitation in uniform thick-walled collapsible tubes. *J. Fluids Struct.* **13** (3), 399–418.

Bertram, C.D. & Pedley, T.J. 1982 A mathematical model of unsteady collapsible tube behaviour. *J. Biomech.* **15** (1), 39–50.

Bertram, C.D. 1987 The effects of wall thickness, axial strain and end proximity on the pressure-area relation of collapsible tubes. *J. Biomech.* **20** (9), 863–876.

Bertram, C.D., Raymond, C.J. & Butcher, K.S.A. 1989 Oscillations in a collapsed-tube analog of the brachial artery under a sphygmomanometer cuff. *Trans. ASME J. Biomech. Engng* **111** (3), 185–191.

Bertram, C.D., Raymond, C.J. & Pedley, T.J. 1990 Mapping of instabilities for flow through collapsed tubes of differing length. *J. Fluids Struct.* **4** (2), 125–153.

Bertram, C.D., Raymond, C.J. & Pedley, T.J. 1991 Application of nonlinear dynamics concepts to the analysis of self-excited oscillations of a collapsible tube conveying a fluid. *J. Fluids Struct.* **5** (4), 391–426.

Bertram, C.D. & Tscherry, J. 2006 The onset of flow-rate limitation and flow-induced oscillations in collapsible tubes. *J. Fluids Struct.* **22** (8), 1029–1045.

Bungartz, H.J. & Schäfer, M. 2006 *Fluid-Structure Interaction: Modelling, Simulation, Optimisation*. Springer.

Cai, Z.X. & Luo, X.Y. 2003 A fluid–beam model for flow in a collapsible channel. *J. Fluids Struct.* **17** (1), 125–146.

Dimakopoulos, Y. & Tsamopoulos, J. 2003 A quasi-elliptic transformation for moving boundary problems with large anisotropic deformations. *J. Comput. Phys.* **192** (2), 494–522.

DONEA, J., HUERTA, A., PONTHOT, J.-PH. & RODRIGUEZ-FERRAN, A. 2004 Arbitrary Lagrangian–Eulerian methods. In *Encyclopedia of Computational Mechanics*. John Wiley and Sons. https://doi.org/10.1002/0470091355.ecm009.

EGGERS, J., HERRADA, M.A. & SNOEIJER, J.H. 2020 Self-similar breakup of polymeric threads as described by the Oldroyd-B model. *J. Fluid Mech.* **887**, A19.

GAVRIELY, N., SHEE, T.R., CUGELL, D.W. & GROTBERG, J.B. 1989 Flutter in flow-limited collapsible tubes: a mechanism for generation of wheezes. *J. Appl. Physiol.* **66** (5), 2251–2261.

GLENDINNING, P. 1994 *Stability, Instability and Chaos: An Introduction to the Theory of Nonlinear Differential Equations*, vol. 11. Cambridge University Press.

GROTBERG, J.B. & JENSEN, O.E. 2004 Biofluid mechanics in flexible tubes. *Annu. Rev. Fluid Mech.* **36**, 121–147.

GUNERATNE, J.C. & PEDLEY, T.J. 2006 High-Reynolds-number steady flow in a collapsible channel. *J. Fluid Mech.* **569**, 151–184.

HEIL, M. 2004 An efficient solver for the fully coupled solution of large-displacement fluid-structure interaction problems. *Comput. Meth. Appl. Mech. Engng* **193** (1–2), 1–23.

HEIL, M. & BOYLE, J. 2010 Self-excited oscillations in three-dimensional collapsible tubes: simulating their onset and large-amplitude oscillations. *J. Fluid Mech.* **652**, 405–426.

HEIL, M. & HAZEL, A.L. 2011 Fluid-structure interaction in internal physiological flows. *Annu. Rev. Fluid Mech.* **43**, 141–162.

HERRADA, M.A. & MONTANERO, J.M. 2016 A numerical method to study the dynamics of capillary fluid systems. *J. Comput. Phys.* **306**, 137–147.

HERRADA, M.A., PÉREZ-SABORID, M. & BARRERO, A. 2003 Vortex breakdown in compressible flows in pipes. *Phys. Fluids* **15** (8), 3468–3477.

HIRT, C.W., AMSDEN, A.A. & COOK, J.L. 1974 An arbitrary Lagrangian–Eulerian computing method for all flow speeds. *J. Comput. Phys.* **14**, 227–253.

HRON, J. & TUREK, S. 2006 A monolithic FEM/multigrid solver for an ALE formulation of fluid-structure interaction with applications in biomechanics. In *Fluid-Structure Interaction*, Lecture Notes in Computational Science and Engineering, vol. 53, pp. 146–170. Springer.

HUANG, L. 2001 Viscous flutter of a finite elastic membrane in Poiseuille flow. *J. Fluids Struct.* **15**, 1061–1088.

JENSEN, O.E. 1990 Instabilities of flow in a collapsed tube. *J. Fluid Mech.* **220**, 623–659.

JENSEN, O.E. & HEIL, M. 2003 High-frequency self-excited oscillations in a collapsible-channel flow. *J. Fluid Mech.* **481**, 235–268.

KAMRIN, K., RYCROFT, C.H. & NAVE, J.C. 2012 Reference map technique for finite-strain elasticity and fluid-solid interaction. *J. Mech. Phys. Solids* **60** (11), 1952–1969.

KNOWLTON, F.P. & STARLING, E.H. 1912 The influence of variations in temperature and blood-pressure on the performance of the isolated mammalian heart. *J. Physiol.* **44** (3), 206.

LOPEZ, J.M. 1994 On the bifurcation structure of axisymmetric vortex breakdown in a constricted pipe. *Phys. Fluids* **6** (11), 3683–3693.

LUO, X.Y., CAI, Z.X., LI, W.G. & PEDLEY, T.J. 2008 The cascade structure of linear instability in collapsible channel flows. *J. Fluid Mech.* **600**, 45–76.

LUO, X.Y. & PEDLEY, T.J. 1995 A numerical simulation of steady flow in a 2-D collapsible channel. *J. Fluids Struct.* **9** (2), 149–174.

LUO, X.Y. & PEDLEY, T.J. 1996 A numerical simulation of unsteady flow in a two-dimensional collapsible channel. *J. Fluid Mech.* **314**, 191–225.

LUO, X.Y. & PEDLEY, T.J. 1998 The effects of wall inertia on flow in a two-dimensional collapsible channel. *J. Fluid Mech.* **363**, 253–280.

LUO, X.Y. & PEDLEY, T.J. 2000 Multiple solutions and flow limitation in collapsible channel flows. *J. Fluid Mech.* **420**, 301–324.

MARZO, A., LUO, X.Y. & BERTRAM, C.D. 2005 Three-dimensional collapse and steady flow in thick-walled flexible tubes. *J. Fluids Struct.* **20** (6), 817–835.

MITTAL, R., ERATH, B.D. & PLESNIAK, M.W. 2013 Fluid dynamics of human phonation and speech. *Annu. Rev. Fluid Mech.* **45**, 437–467.

PEDLEY, T.J. 1992 Longitudinal tension variation in collapsible channels: a new mechanism for the breakdown of steady flow. *Trans. ASME J. Biomech. Engng* **114** (1), 60–67.

PEDLEY, T.J. & STEPHANOFF, K. 1985 Flow along a channel with a time-dependent indentation in one wall: the generation of vorticity waves. *J. Fluid Mech.* **160**, 337–367.

PIHLER-PUZOVIĆ, D. & PEDLEY, T.J. 2013 Stability of high-Reynolds-number flow in a collapsible channel. *J. Fluid Mech.* **714**, 536–561.

PIHLER-PUZOVIĆ, D. & PEDLEY, T.J. 2014 Flutter in a quasi-one-dimensional model of a collapsible channel. *Proc. R. Soc. Lond.* A **470** (2166), 20140015.

PONCE-TORRES, A., RUBIO, M., HERRADA, M.A., EGGERS, J. & MONTANERO, J.M. 2020 Influence of the surface viscous stress on the pinch-off of free surfaces loaded with nearly-inviscid surfactants. *Sci. Rep.* **10** (1), 16065.

RYZHAKOV, P.B., ROSSI, R., IDELSOHN, S.R. & ONATE, E. 2020 A monolithic Lagrangian approach for fluid–structure interaction problems. *Comput. Mech.* **46**, 883–899.

SHAPIRO, A.H. 1977 Steady flow in collapsible tubes. *Trans. ASME J. Biomech. Engng* **99** (3), 126–147.

SHTERN, V. 2018 Models of fold-related hysteresis. *Phys. Fluids* **30** (5), 2–7.

SHTERN, V. & HUSSAIN, F. 1996 Hysteresis in swirling jets. *J. Fluid Mech.* **309**, 1–44.

SNOEIJER, J.H., PANDEY, A., HERRADA, M.A. & EGGERS, J. 2020 The relationship between viscoelasticity and elasticity. *Proc. R. Soc. Lond.* A **476**, 20200419.

STEPHANOFF, K., PEDLEY, T.J., LAWRENCE, C. & SECOMB, T.W. 1983 Fluid flow along a channel with an asymmetric oscillating constriction. *Nature* **305**, 692–695.

STEWART, P.S. 2010 Flows in flexible channels and airways. PhD thesis, University of Nottingham.

STEWART, P.S. 2017 Instabilities in flexible channel flow with large external pressure. *J. Fluid Mech.* **825**, 922–960.

STEWART, P.S., HEIL, M., WATERS, S.L. & JENSEN, O.E. 2010 Sloshing and slamming oscillations in a collapsible channel flow. *J. Fluid Mech.* **662**, 288–319.

STEWART, P.S., WATERS, S.L. & JENSEN, O.E. 2009 Local and global instabilities of flow in a flexible-walled channel. *Eur. J. Mech. (*B*/Fluids)* **28** (4), 541–557.

WALTERS, M.C., HEIL, M. & WHITTAKER, R.J. 2018 The effect of wall inertia on high-frequency instabilities of flow through an elastic-walled tube. *Q. J. Mech. Appl. Maths* **71** (1), 47–77.

WANG, D., LUO, X.Y. & STEWART, P.S. 2021*a* Energy analysis of collapsible channel flow with a nonlinear fluid-beam model. *J. Fluid Mech.* **926**, A2.

WANG, D., LUO, X.Y. & STEWART, P.S. 2021*b* Multiple steady and oscillatory solutions in a collapsible channel flow. *Intl J. Appl. Mech.* **13** (4), 2150058.

WHITTAKER, R.J., HEIL, M., JENSEN, O.E. & WATERS, S.L. 2010 Predicting the onset of high-frequency self-excited oscillations in elastic-walled tubes. *Proc. R. Soc. Lond.* A **466** (2124), 3635–3657.

XU, F., BILLINGHAM, J. & JENSEN, O.E. 2013 Divergence-driven oscillations in a flexible-channel flow with fixed upstream flux. *J. Fluid Mech.* **723**, 706–733.

XU, F., BILLINGHAM, J. & JENSEN, O.E. 2014 Resonance-driven oscillations in a flexible-channel flow with fixed upstream flux and a long downstream rigid segment. *J. Fluid Mech.* **746**, 368–404.

XU, F. & JENSEN, O.E. 2015 A low-order model for slamming in a flexible-channel flow. *Q. J. Mech. Appl. Maths* **68** (3), 299–319.

ZHANG, S., LUO, X.Y. & CAI, Z. 2018 Three-dimensional flows in a hyperelastic vessel under external pressure. *Biomech. Model. Mechanobiol.* **17** (4), 1187–1207.